Dissertation with the aim
of achieving a doctoral degree

The impact of sea salt emissions on the air quality in the North Sea and Baltic Sea regions

Faculty of Mathematics, Informatics and Natural Sciences
Department of Earth Sciences
Universität Hamburg

Daniel Neumann

2016 in Hamburg

Day of oral defense: 14/07/2016, 2 p.m.
The following evaluators recommend the admission of the dissertation:
Dr. Volker Matthias, Institute of Coastal Research, Helmholtz-Zentrum Geesthacht
Prof. Dr. Kay-Christian Emeis, Institute of Geology, Universität Hamburg

Schon wieder zu spät? – Ausnahmsweise mal nicht!

Abstract

The Northwestern European coastal areas are subject to considerable anthropogenic activities yielding emissions of pollutants into the atmosphere. In particular, air pollution by fine sulfate particles, formation of acid deposition by nitric and sulfuric acid, and atmospheric nitrogen input into water bodies are major threats for human health and the ecosystem functioning. Anthropogenic emissions of sulfur compounds and nitrogen oxides have been considerably reduced by approximately 80 % and 50 %, respectively, in the European Union in the last 25 years. However, their magnitude is still of great concern. The coastal areas are also characterized by natural marine emissions, particularly of sea salt. Sea salt particles interact with air pollutants and influence their deposition by contributing to the particulate sulfate budget, by providing particle surface area for condensation of acids and bases, and by altering dry deposition patterns. The impacts are characterized by strong spatio-temporal variability. This variability depends on the amount of sulfur emitted by anthropogenic sources, on the availability of the base NH_3, and on the presence of other atmospheric particles and their size distribution. Laboratory experiments and measurement campaigns support quantifying this impact, but lack a detailed spatial resolution.

Therefore, the contribution of sea salt sulfate to the atmospheric sulfate loading and the effect of sea salt particles on atmospheric nitrate and nitrogen deposition were assessed in this thesis for Northwestern Europe by means of the chemistry transport model CMAQ.

Additionally, three different sea salt particle emission parameterizations and their variable interaction with air pollutants were compared with each other and with measurements. They are abbreviated as GO03, SP13, and OV14. The parameterizations were selected, because they produce different sea salt particle size distributions and depend on different input parameters. The standard parameterization in CMAQ (GO03) depends on wind speed and was extended by a dependence on salinity in this thesis. The SP13 parameterization is additionally based on SST and the OV14 parameterization on SST and wave data. OV14 yields more particles than GO03 but smaller ones and less particle mass. In contrast, SP13 yields higher number and mass emissions than GO03. The size distributions of the emitted sea salt particles govern their atmospheric transport distance because they impact the particles' dry deposition velocities: The OV14 parameterization led to the lowest particulate sodium concentrations at coastal stations but the highest at some inland stations. Sodium PM_{10} measurements were best reproduced by the OV14 and GO03 parameterizations. In this context, the extension of GO03 by a dependence on salinity considerably improved the modeled particulate sodium concentrations in the Baltic Sea region.

The impact of sea salt on nitrate concentrations was assessed. The equilibrium between gaseous nitric acid and particulate nitrate was shifted towards nitrate in the presence of sea salt particles because of increased particle surface area for condensation. The nitrate condensation was further enhanced through sea salt chloride because hydrochloric acid evaporates when nitric acid condenses and, thus, buffers the liquid phase pH value. As a result, the re-volatilization of nitrate is inhibited. However, the effectiveness of this process was reduced because of the high availability of NH_3 in Northwestern Europe. In parallel, the nitrate concentrations were reduced because sea salt particles are larger and heavier on average than most other particles in the particular region and, hence, increased the dry deposition velocity of nitrate and other compounds condensed on them. The wet deposition velocities were not impacted but nitrogen deposition into water bodies was increased. The shape of the sea salt size distribution clearly impacted the size distribution of particulate nitrate and its concentrations: Among the three

parameterizations, SP13 yielded the highest nitrate $PM_{2.5}$ concentrations, whereas OV14 the highest nitrate PM_{10} concentrations. The latter ones even exceeded the nitrate concentrations in the absence of particulate sea salt at most stations. In winter, the nitrate PM_{10} concentrations of all model cases were closer to each other. This is because, first, the particle loading in winter was higher providing more surface area for condensation and, second, the lower temperatures shifted the HNO_3-NO_3^- equilibrium towards nitrate.

In the year of investigation, 2008, sea salt was simulated to account for up to 9 % of the total nitrogen deposition into the North Sea. The percentage depended on the used sea salt emission parameterization. The standard CMAQ setup (GO03) yielded contributions of 2.5 % to 7 %, whereas OV14 contributed 0 % to 3.5 % and SP13 up to 9 %. In the Baltic Sea, the contribution of sea salt in summer was negligible but all three parameterizations contributed approximately 3.5 % in winter. The total nitrogen deposition in summer and winter did not deviate much.

The contribution of sea salt, energy-production, and shipping related emissions to the atmospheric particulate sulfate concentrations was assessed, treating the contribution of other anthropogenic sectors as one emission sector. Approximately half of the atmospheric sea salt mass was in the coarse particle mode ($> 2.5\,\mu m$) and the other half in the fine mode ($\leq 2.5\,\mu m$). In contrast, anthropogenically caused particles consisted of approximately 80 % fine particle mass. Hence, sea salt particle emissions led to a relative increase of the coarse particle fraction increasing the dry deposition velocity of condensed compounds such as nitrate. Sea salt emissions were one of the major contributors to sulfate PM_{10} and $PM_{2.5}$ concentrations at coastal stations. They contributed a share of up 30 % to sulfate PM_{10} concentrations in the standard sea salt setup of CMAQ (GO03). At most stations the share was below 20 %. The alternative sea salt emission parameterization OV14 yielded lower shares at coastal stations but was on the same level as GO03 at inland ones. The energy-production sector had the highest share in sulfate PM_{10} (15–30 %) concentrations among the individually regarded sectors. However, approximately 50 % of the sulfate was accounted to the not-differentiated other anthropogenic sectors. This high share is remarkable because half of the anthropogenic sulfur emissions were caused by the energy-production sector. The shift of the share is due to the fact that power plants emit their exhaust gases in altitudes above 100 m in order to reduce their impact on the local air quality. Additionally, their emissions consisted of nearly any particulate sulfate but mainly of SO_2. In contrast, the not-differentiated sectors yielded relatively more particulate sulfate. The latter fact is clearly visible in the modeled SO_2 concentrations, which were dominated by power plant SO_2. The shipping sector contributes approximately a third of the particulate sulfate in summer but less than a tenth in winter. The reason for this is an enhanced conversion of SO_2 to H_2SO_4 and SO_4^{2-} in summer because the availability of oxidizing compounds is higher because of more solar radiation.

Zusammenfassung

Die Küstenregionen Nordwesteuropas sind durch hohe anthropogene Aktivität, die zur Emission von Schadstoffen in die Atmosphäre führt, gekennzeichnet. Die Luftverschmutzung durch feine Sulfatpartikel, die Bildung saurer Deposition durch Salpeter- und Schwefelsäure und die Deposition von Stickstoffverbindungen in Gewässer stellen eine besondere Gefährdung der menschlichen Gesundheit und der Funktion von Ökosystemen dar. Obwohl die anthropogenen Emissionen von Schwefelverbindungen und Stickoxiden in der Europäischen Union in den vergangenen 25 Jahren um 80 % bzw. 50 % zurückgegangen sind, sind sie immer noch bedenklich hoch. Küstenregionen zeichnen sich außerdem durch natürliche marine Emissionen – speziell von Seesalz – aus. Seesalzpartikel wechselwirken mit Luftschadstoffen und ihrer Deposition. Dies geschieht indem sie zum atmosphärischen Sulfatbudget beitragen, Teilchenoberfläche für die Kondensation von Säuren und Basen bieten und die räumliche Verteilung der Trockendeposition beeinflussen. Der Einfluss von Seesalz variiert regional, weil er von der Menge der anthropogen emittierten Schwefelverbindungen, von der Verfügbarkeit an NH_3 und von der Anzahl und Größenverteilung anderer atmosphärischer Partikel abhängt. Laborexperimente und Messkampagnen tragen zur Quantifizierung dieses Einflusses bei, bieten aber keine räumlich detaillierte Auflösung.

Daher wurden in dieser Dissertation der Beitrag von Seesalzsulfat zum atmosphärischen Sulfatbudget und der Einfluss von Seesalzpartikeln auf atmosphärisches Nitrat und auf Stickstoffdeposition in Nordwesteuropa unter Nutzung des Chemietransportmodells CMAQ betrachtet.

Zusätzlich wurden hierbei drei verschiedene Parametrisierungen für Seesalzemissionen und ihre unterschiedliche Wechselwirkung mit Luftschadstoffen verglichen – untereinander und mit Messergebnissen. Die Parametrisierungen werden im Folgenden mit GO03, SP13 und OV14 abgekürzt. Die Parametrisierungen wurden ausgewählt, da sie sich in der Größenverteilung des emittierten Seesalzes und in den benötigten Eingangsparametern unterscheiden. Die CMAQ Standardparametrisierung GO03 hängt nur von der Windgeschwindigkeit ab und wurde in dieser Arbeit um eine Abhängigkeit von der Salinität erweitert. Die Parametrisierung SP13 hängt zusätzlich von der Meeresoberflächentemperatur ab, während die Parametrisierung OV14 darüber hinaus Wellendaten nutzt. OV14 emittiert mehr, aber kleinere Seesalzpartikel und eine geringere Masse als GO03. Im Gegensatz produziert SP13 mehr Partikel und eine höhere Masse. Da die Größenverteilung der Partikel Einfluss auf ihre Depositionsgeschwindigkeit hat, beeinflusst sie die Entfernung, die Partikel zurücklegen bevor sie deponieren: OV14 führte an Küstenstationen zu den niedrigsten Natrium PM_{10} Konzentrationen, aber bei einigen inländischen Stationen zu den höchsten. Die Natriumkonzentration wurde am besten von den OV14 und GO03 Parametrisierungen reproduziert. In diesem Zusammenhang führte die Erweiterung der GO03 Parametrisierung um die Salinität als Eingangsparameter zu einer deutlichen Verbesserung der simulierten Natriumkonzentrationen im Osterseeraum im Vergleich zu Messergebnissen.

Der Einfluss von Seesalz auf Nitrat wurde evaluiert. Das Verteilungsgleichgewicht zwischen gasförmiger Salpetersäure und partikelgebundenem Nitrat wird durch die Anwesenheit von Seesalzpartikeln zum Nitrat verschoben, da eine größere Partikeloberfläche für die Kondensation zur Verfügung steht. In Anwesenheit von Chlorid, welches während der Kondensation von Salpetersäure als Salzsäure verdampft, kommt es zu einer pH-Wert-Pufferung des Partikelwassers wodurch das Nitrat an einer erneuten Verdampfung gehindert wird. Dies verstärkt die Verschiebung des Verteilungsgleichgewichtes. Allerdings wurde dieser Einfluss durch hohe Luftkonzentrationen von NH_3 im Nordwesten Europas gemindert. Da Seesalzpartikel im Durchschnitt größer und schwerer sind als die meisten anderen Partikel im Untersuchungsgebiet, erhöhten sie die Trockendeposition des Nitrates und anderer auf diesen Partikel kondensierter

Substanzen. Dies führte zu einer Senkung der partikulären Nitratkonzentrationen. Die Nassdeposition wurde nicht beeinflusst. Die Größenverteilung von Seesalzpartikeln hatte einen deutlichen Einfluss auf die Größenverteilung des partikulären Nitrates und dessen Konzentration. Im Vergleich der drei Parametrisierungen führte SP13 zu den höchsten Nitrat $PM_{2.5}$ Konzentrationen und OV14 zu den höchsten Nitrat PM_{10} Konzentrationen. Letztere überschritten an den meisten Stationen sogar die partikulären Nitratkonzentrationen einer Referenzsimulation ohne Seesalzemissionen. Im Winter waren die Unterschiede zwischen den Nitrat PM_{10} Konzentrationen der drei Parametrisierungen geringer als im Sommer. Gründe hierfür waren, dass zum einen eine höhere Partikelbelastung im Winter zu einer Erhöhung der gesamten Partikeloberfläche, die zur Kondensation zur Verfügung stand, führte. Zum anderen führte die geringere Lufttemperatur im Winter zu einer Verschiebung des HNO_3-NO_3^- Gleichgewichtes in Richtung des Nitrates wodurch der Einfluss von Seesalz geringer wurde.

Im simulierten Jahr, 2008, lag der indirekte Beitrag von Seesalz zur gesamten Stickstoffdeposition in die Nordsee bei 9 %. Dieser Anteil hing stark von der Parametrisierung der Seesalzemissionen ab. Die Standardparametrisierung GO03 trug 2,5 % bis 7 % bei, während OV14 0 % bis 3,5 % und SP13 bis zu 9 % beitrugen. Der Stickstoffeintrag in die Ostsee war im Sommer vernachlässigbar und betrug im Winter 3,5 % unabhängig von der Emissionsparametrisierung. Die absolut deponierte Stickstoffmenge wies zwischen Sommer und Winter nur geringe Unterschiede auf.

Der Anteil an der Konzentration an partikelförmigem Sulfat aus Seesalz-, Kraftwerks- und Schifffahrtsemissionen wurde berechnet und analysiert. Die übrigen anthropogenen Emissionen wurden als ein Sektor betrachtet. Etwa die Hälfte des Seesalzsulfates bildete grobe Partikel ($> 2{,}5\,\mu m$) und die andere Hälfte feine Partikel ($\leq 2{,}5\,\mu m$). Im Gegensatz dazu befand sich 80 % der Masse aus anthropogenen Quellen in feinen Partikeln. Daher führten Seesalzemissionen zu einem erhöhten Anteil an groben Partikeln, was zu einer erhöhten Trockendepositionsgeschwindigkeit von Nitrat und anderen auf Partikeln kondensierten Substanzen führte. In Küstengebieten waren Seesalzemissionen eine der größten Quellen für Sulfat PM_{10} und $PM_{2.5}$ Partikel. Sie trugen einen Anteil von durchschnittlich 3 % bis 20 % und in einem Fall bis zu 30 % zur Sulfat PM_{10} Konzentration bei, wenn die CMAQ Standardparametrisierung GO03 genutzt wurde. Die alternative Parametrisierung OV14 führte im Vergleich zu GO03 zu geringeren Beiträgen bei Küstenstationen, aber zum Teil zu höheren im Landesinneren. Unter den einzeln betrachteten Emissionssektoren trug der Kraftwerkssektor die höchsten Sulfat PM_{10} Konzentrationen bei (15–30 %). Allerdings stammte etwa 50 % des partikulären Sulfates von den nicht weiter differenzierten anthropogenen Emissionssektoren. Dies ist erstaunlich, weil die Hälfte der anthropogenen Schwefelemissionen von Kraftwerken ausgestoßen wird. Diese Verschiebung des Anteils lässt sich damit begründen, dass Kraftwerksabgase in Höhen oberhalb von 100 m emittiert werden um den negativen Einfluss auf die Luftqualität der direkten Umgebung gering zu halten. Weiterhin macht Sulfat in Kraftwerksemissionen nur etwa 0,5 % der Schwefelemissionen aus, wohingegen die Emissionen aus den übrigen anthropogenen Quellen einen wesentlich höheren Sulfatanteil haben. Dieses Verhältnis war in den modellierten SO_2 Konzentrationen wiederzufinden, die eindeutig von Kraftwerksemissionen dominiert wurden. Der Schifffahrtssektor trug in Küstengebieten im Sommer etwa ein Drittel zum partikulären Sulfat bei. Im Winter war es nur ein Zehntel. Der Grund für diesen saisonalen Unterschied war eine erhöhte Umwandlung von SO_2 zu H_2SO_4 und SO_4^{2-} im Sommer, die durch deutlich erhöhte Konzentrationen oxidierender Spezies angetrieben wurde. Letztere wurden durch erhöhte Sonneneinstrahlung im Sommer verursacht.

Preface

This PhD thesis consists of four studies on sea salt emissions and the interaction between sea salt particles and anthropogenically emitted air pollutants, which are framed by the general chapters *Introduction* (Chap. 1), *Scientific and Technical Background* (Chap. 2), *Summarizing Discussion* (Chap. 7), and *Conclusions* (Chap. 8). The Chaps. 1 and 2 motivate the studies, give a broad introduction, and present the background and methods that are related to all four studies: relevant atmospheric chemistry, atmospheric aerosol particles and their modeling, sea salt particle emissions and their impact, the chemistry transport model CMAQ, and measurement data for the model evaluation. These chapters are succeeded by the four studies: The first two are published research articles (Chaps. 3 and 4), the third one is a brief synthesis of the first two, and the fourth one is designed as a draft research article. Each of the three research articles has its own *Introduction*, *Material and Methods*, *Results*, *Discussion*, and *Conclusions* sections focused on the articles' topic. The Chap. 7 summarizes the *Results*, *Discussion*, and *Conclusions* sections of the previous chapters and discusses them in a broader perspective. Chapter 8 concludes the thesis and gives an outlook.

Detailed technical descriptions of programs and model output files were avoided in the main body of this thesis but they are attached as Appendices. Namely, the Appendix includes descriptions of the CMAQ OCEAN file (Apdx. H) and its creation, of the processing of EMEP measurement data for model validation (Chap. G), of program scripts for calculating sea salt emissions externally (Chap. I), and of a listing of used third-party software (Chap. J). Additionally, the appendices and supplements of the research articles are also put into this thesis' appendix (Chaps. A to E). They are slightly modified in order to avoid duplicated information.

Daniel Neumann, Geesthacht, April 2016

Contents

1 Introduction

1.1 Motivation

Europe is facing considerable air pollution caused by anthropogenic emissions. Although the emissions of air pollutants have been decreased in the last three decades [EMEP, 2015; Smith et al., 2011], large amounts of nitrogen oxides (NO_x), gaseous sulfur oxides (SO_x), ammonia (NH_3), and particulate matter are still emitted in connection with anthropogenic activities. These substances are emitted directly as particles (primary particles) and as gases that then partly form particles (secondary particles) or condense on existing ones. Furthermore, nitrogen dioxide (NO_2) enhances the formation of ozone (O_3). The inhalation of gaseous NO_2, sulfur dioxide (SO_2), and O_3 irritates the lungs which may lead to respiratory diseases [Kampa and Castanas, 2008]. Particles can be inhalated by humans and settle in the lungs favoring respiratory diseases. The smallest ones, such as ultra-fine sulfate particles, travel through the tissue into the blood and may cause cardiovascular diseases [Brunekreef and Holgate, 2002]. The commonly used classification into particulate matter below 10 µm in diameter (PM_{10}, "thoracic") and below 2.5 µm in diameter ($PM_{2.5}$, "respirable") is derived from these threat levels. Particulate and gaseous nitrogen compounds act as nutrients for algae when they deposit from the atmosphere into the water. This contributes to eutrophication in water bodies [Smith et al., 1999].

Sea salt particles are emitted ubiquitously from the sea surface, especially, in coastal regions. Atmospheric sea salt particles contain sulfate and, thus, contribute relevant amounts of sulfate to the atmospheric sulfate budget and they passively transport pollutants and nutrients that condense onto them. Sea salt particles deposit faster to the ground than most particles formed in the atmosphere because they are larger and, thus, heavier. Hence, the deposition velocity of species attached to sea salt is also higher leading to enhanced nitrogen deposition along the coast line.

Since nitrogen oxides, nitrate (NO_3^-), sulfur oxides, ammonia and particulate matter cause harm to human health and may have negative effects on aquatic ecosystems, health and environmental protection agencies – as well as non-governmental organizations (NGOs) working in this field – target the reduction of emissions of these substances. However, field studies and model experiments showed that reductions of the emission of one air pollutant may lead to increased concentrations of other air pollutants [e.g. Matthias et al., 2016, Fig. 8]. Therefore, considerable research is performed on predicting air quality in order to assess which emission reductions result in the most beneficial improvements of air quality. Here, sea salt particles play an important role for estimating the sulfate budget and atmospheric transport and deposition processes in coastal regions. Moreover, the impact of sea salt particles on atmospheric nitrogen and its deposition varies regionally [Im, 2013; Liu et al., 2015] and has not been well quantified for Northwestern Europe, yet. Therefore, it is reasonable to evaluate sea salt emissions and their impact on other atmospheric compounds which is done in this thesis via simulations with a chemistry transport model (CTM).

1.2 Sea Salt

Sea salt consists primarily of sodium (Na^+), chloride (Cl^-), and sulfate (SO_4^{2-}).[a] The chloride ions have a buffer-like effect because hydrochloric acid (HCl) is a weak acid that evaporates upon the condensation of stronger acids, namely sulfuric acid (H_2SO_4) and nitric acid (HNO_3). Sea salt particles deposit faster to the ground than fine secondary particles and, hence, increase the dry deposition velocity of compounds condensed onto them. Therefore, sea salt particles need to be considered for correctly predicting air pollution and deposition patterns by CTMs in coastal regions, such as Northwestern Europe.

Primary marine particles, also denoted as sea spray, are emitted as water droplets from the sea surface by bursting air bubbles, breaking waves, and strong winds. Sea spray consists of water, sea salt, and organic compounds. Sea spray droplets directly emitted by wave breaking are relatively large and have a too short atmospheric life time to be relevant for atmospheric chemistry processes under most weather conditions. The dominant process for sea spray production is the bursting of air bubbles [Lewis and Schwartz, 2004]. The air is entrained into the water mainly by breaking waves. Therefore, sea spray emissions depend on the wind speed and the bathymetry (water depth and shape of the sea floor) which govern wave generation and breaking. The sea surface temperature (SST) was identified to also have an impact on sea spray emissions [Mårtensson et al., 2003; Salter et al., 2015]. Wave breaking is enhanced at the coast because of a low water depth, beaches and cliffs. Thus, sea spray emissions are intensified along the coast line leading to the distinction between open ocean and surf zone emissions [de Leeuw et al., 2000]. It is important to note that a considerable mass fraction of fine sea spray consists of organic material in some regions [O'Dowd et al., 2004]. The amount of sea salt per sea salt particle depends on the availability of solved salt in the marine water. Therefore, sea salt emissions depend on the salinity. The focus in the studies presented in this thesis was on the sea salt and not the sea spray as a whole. Therefore, sea spray is not further considered.

The research on sea salt emissions and their dependence on wind, waves, temperature, and salinity is a broad field of research that dates back to the 1960s and 70s [Blanchard, 1964; Junge, 1972; Duce and Hoffman, 1976]. In the 1980s, Edward C. Monahan performed detailed studies on the wind dependence of sea salt emissions [Monahan and Muircheartaigh, 1980; Monahan et al., 1982, 1986] forming a basis for nowadays' sea salt emission parameterization. In recent years, more sophisticated sea salt emission parameterizations were derived – amongst others a parameterization by Ovadnevaite et al. [2014] based on wave model data. However, there are still large uncertainties in the size distribution of sea salt emissions (size distribution = "How much particles of which size are emitted?"). This size distribution is very important for estimating both the atmospheric life time of sea salt particles and the particle surface area. Particularly in the coastal regions, the estimation of sea salt emissions is afflicted with large uncertainties because the wave breaking is more complex to predict along the coastline due to flat bathymetry and different types of land-water boundaries such as beaches and cliffs. But it would be important to reduce these uncertainties in order to better estimate deposition patterns of sea salt particles and substances attached to them, such as nitrate and ammonium, as well as the impact of sea salt on HNO_3-NO_3^- and NH_3-ammonium (NH_4^+) equilibria.

1.3 Sulfur Oxides

Gaseous sulfur oxides (SO_x) summarize sulfur dioxide (SO_2), sulfuric acid (H_2SO_4), and sulfate (SO_4^{2-}). SO_2 and H_2SO_4 are gaseous, whereas SO_4^{2-} is solid or solved in the liquid phase. SO_2 is converted by different reaction pathways to H_2SO_4, which has a very short atmospheric life time because it directly condenses on existing particles or nucleates to new ones. The newly formed sulfate particles are very small in diameter and are denoted as nucleation mode or ultra-

[a] See Apdx. E.1 for the detailed composition.

fine particles. Their atmospheric sulfur chemistry is described in detail in Seinfeld and Pandis [2006a, Chap. 2.2].

Anthropogenic SO_x and particulate sulfate emissions have been strongly reduced in the last 30 years by (a) the usage of low sulfur fuels by cars, (b) scrubbers and filters in power plants and industrial facilities, and, recently, (c) introducing sulfur thresholds for shipping emissions [EMEP, 2015; Smith et al., 2011]. Nowadays, the major sources of atmospheric sulfate particles are the shipping sector, the energy sector (coal burning), as well as sea salt emissions [EMEP, 2015]. In remote marine regions, dimethyl sulfide (DMS), which is produced by some types of algae, considerably contributes to the atmospheric sulfur budget [Lana et al., 2011] but not in anthropogenically affected regions as a comparison of sulfur emission data shows [EMEP, 2015].

The sulfur oxides emitted from anthropogenic sources and as sea salt impact human health differently due to different resulting particle size classes. Anthropogenic sulfur oxide emissions primarily contribute to fine and ultra-fine particle fractions and not to the coarse one because, firstly, SO_2 leads to the formation of new ultra-fine sulfate particles and, secondly, particulate sulfate emissions are dominated by fine and ultra-fine particles nowadays due to improved filter techniques. In contrast, sea salt particles are a combination of fine and coarse particles whereby the total particle mass is dominated by coarse ones. Since anthropogenically sourced particles dominate the fine sulfate particle fraction and sea salt particles the coarse particle fraction, anthropogenic sulfur oxide emissions are substantially more relevant for human health considerations.

At most European background measurement stations, the inorganic constituents of PM_{10} particles are measured including sulfate. However, speciated $PM_{2.5}$ measurements are rare and the measurements of pollutants, such as sulfate, do not hold information about their exact sources. In contrast, CTMs enable the user to attribute air pollution to individual sources, source sectors, or source regions. This is important feature, because the dominant emitters of SO_x and particulate sulfate are emission point sources, namely power plants and industrial facilities, which are simpler to regulate than NO_x emission sources. In this thesis, the particulate sulfate air pollution at distinct locations in Europe was attributed to individual source sectors.

1.4 Nitrogen Compounds

All combustion processes that use air (instead of pure O_2) produce nitrogen monoxide (NO) and NO_2 as byproducts which are summarized as NO_x. NO_2 leads to the production of O_3 and NO to its degradation. Furthermore, NO_2 is oxidized to HNO_3. Nitric acid forms new particles or condenses onto existing ones as NO_3^-. Since sulfur oxide emissions have decreased strongly, nitric acid is the most relevant acidifying atmospheric species nowadays. Nitric acid and nitrate are in an equilibrium which depends on the presence of other acids and bases. At this point, NH_3 comes into play, which is primarily emitted from faeces and manure. Ammonia emissions are very high in Northwestern Germany, Denmark, and the Netherlands, because of intensive livestock farming. On the one hand, NH_3 neutralizes atmospheric acids, i.e. H_2SO_4, HNO_3, and HCl, by forming ammonium sulfate ($[NH_4]_2SO_4$), ammonium nitrate (NH_4NO_3), and ammonium chloride (NH_4Cl) reducing the acidity of rain. On the other hand, it is a nutrient when it is carried into water bodies supporting eutrophication. The atmospheric nitrogen chemistry is described in detail in Seinfeld and Pandis [2006a, Chap. 2.3] and a broader overview over terrestrial, aquatic, and atmospheric processes is given in Sutton et al. [2011].

The determination of nitrogen deposition from the atmosphere is an import step in assessing the threat of eutrophication. Measurements of nitrogen dry deposition are difficult to perform and afflicted with errors. Additionally, no fine spatial coverage of nitrogen wet deposition measurement platforms – particularly on the ocean – is available. The application of CTMs plays an important role in estimating the nitrogen deposition onto the land and into water bodies for the assessment of eutrophication.

CTMs can be employed to assess the impact of anthropogenic emissions and natural emissions on atmospheric nitrogen compounds and on nitrogen deposition. Not only emitted nitrogen that deposits again is relevant in this context, but also non-nitrogen compounds that impact atmospheric nitrogen processes and nitrogen deposition, such as sea salt particles.

1.5 Chemistry Transport Models

A CTM calculates transport processes of gaseous and particulate compounds, their chemical reactions, and physical processes taking place in the atmosphere. Thus, it enables the user to predict concentrations of air pollutants (and other atmospheric compounds) and their deposition to the ground. Meteorological data, such as wind speed, temperature, and precipitation are necessary for these predictions. These data are provided externally from observations or from meteorological models which is denoted as one-way coupling: data flows from the meteorological model into the CTM but not vice versa.

In this thesis, the Eulerian CTM Community Multiscale Air Quality (CMAQ) model was used that has been developed and is maintained by the U.S. Environmental Protection Agency (U.S. EPA) [Byun and Schere, 2006]. Meteorological input data were calculated by the meteorological model COSMO-CLM at the Helmholtz-Zentrum Geesthacht (HZG) [Rockel et al., 2008].

1.6 Study Region

The studies presented in this thesis are focussed on the air pollution in the North Sea and Baltic Sea regions. Therefore, both regions are briefly described.

The North Sea is a marginal sea to the Atlantic Ocean. Major European cities, such as London and Hamburg, are located at its coast, in river estuaries, and along rivers flowing into it. Furthermore, large industrial areas such as the Ruhr Area are located at these rivers. The rural areas are dominantly used for agriculture and livestock. Besides, one of the world's most densely used water ways connects the Atlantic Ocean with the North Sea, namely the English

Figure 1.1: Map showing northwestern Europe including the North Sea and Baltic Sea regions. Relevant oceanic regions are labeled by name.

Channel. Here, ships travel to the ports of Antwerp, Rotterdam, and Hamburg in order to supply the European population with goods from other parts of the world and vice versa. Ships that transport goods towards Eastern Europe need to pass the North Sea to access the Baltic Sea. The Baltic Sea is nearly completely enclosed by continental land masses and has only one connection to the North Sea that is denoted as Kattegat. The land bordering the Baltic Sea is also subject to agricultural and industrial use.

The input of pollutants and nutrients by these anthropogenic activities into water bodies is a cause of great concern. Hence, several legislative acts [EU, 2008, 2000] were passed to reduce these inputs. However, pollutants and nutrients are also emitted into the atmosphere and, potentially, transported to the sea. These are SO_2, H_2SO_4, SO_4^{2-}, NO_x, NO_3^-, NH_3, and volatile organic compounds (VOCs).

The spatial variation of the sea surface salinity in the North Sea and the Baltic Sea is important to include in modeling studies because the salinity governs the amount of sea salt emissions. The average salinity in the North Sea and the Atlantic Ocean is approximately 35 ‰ ($= 35\,\mathrm{g\,kg^{-1}} = 35\,\mathrm{psu} = 0.035$). It decreases towards the coast and, particularly, in river estuaries. The seasonal variation is low. The salinity in the Baltic Sea is considerably lower and has a negative gradient from west to east and from south to north. In the Kattegat it varies between 10 ‰ and 30 ‰ depending on the season and wind conditions. In German parts of the Baltic Sea the salinity is approximately 10 ‰ on annual average, in the vicinity of Gotland 7 ‰, and 5 ‰ to 1 ‰ in the Gulf of Bothnia and Gulf of Finland.

1.7 Scientific Question

Based on the given short introduction on some pollutants in Northwestern Europe the following major research question for this PhD thesis was set up:

- What is the impact of sea salt particles on the anthropogenic air pollution regime in the North Sea and Baltic Sea regions and which role does their size distribution play in this context?

This question should be assessed by means of simulations with the Community Multiscale Air Quality (CMAQ) model. Model runs are validated against concentration and deposition measurements. Since shortcomings of the sea salt emission setup were identified in the past and since surf zone emissions are afflicted with considerable uncertainty, the following sub-questions were derived:

- How well are sea salt emissions and, particularly, surf zone emissions included in CMAQ and how well are the sea salt concentrations reproduced?
- How strong does sea salt impact atmospheric nitrogen concentrations and nitrogen deposition in Northwestern Europe?
- What are the dominant contributors to fine and coarse particulate air pollution by sulfate particles at different locations in Northwestern Europe?

2 Scientific and Technical Background

The publication manuscripts in Chaps. 3, 4, and 6 have their own *Materials and Methods* sections. In order to avoid doubling of descriptions, this chapter gives a broad overview. Detailed descriptions can be found in the respective manuscripts' *Material and Methods* sections and in the Appendix.

2.1 The role of Marine Emissions in Atmospheric Chemistry

A brief description of relevant chemical and physical processes in the atmosphere is given in the Introduction. In this section, the processes are described in more detail.

2.1.1 Chemical Processes

The atmospheric acids HNO_3 and H_2SO_4 and their deprotonate counterparts are relevant for the exchange of nitrogen and sulfur between the gas and particle phase. HNO_3 is produced from NO and NO_2 and partly via the intermediate product dinitrogen pentaoxide (N_2O_5). The dominant reaction pathway is indicated by reactions R 2.1 and R 2.2. A detailed overview on the atmospheric nitrogen cycle is presented in Seinfeld and Pandis [2006a, Chaps. 2.3, 6.13, and 7.5].

$$\mathrm{NO(g) + O_3(g) \rightleftharpoons NO_2(g) + O_2(g)} \tag{R 2.1}$$

$$\mathrm{NO_2(g) + OH \rightleftharpoons HNO_3(g)} \tag{R 2.2}$$

The reaction pathways from SO_2 to H_2SO_4 and ${SO_4}^{2-}$ are diverse and some are situated in the gas phase and others in the aqueous phase of cloud droplets. Exemplary, wet sea salt particles provide space for aqueous phase reactions.

Atmospheric acids and bases condense onto atmospheric particles, dissolve in the particles' liquid phase, and exchange protons [Seinfeld and Pandis, 2006a]. Alternatively, they exchange protons in the gas phase and form new ultra-fine particles. The most common inorganic ones are H_2SO_4, HNO_3, and HCl (acids) and NH_3 (base):

$$\mathrm{2\ NH_3(g) + H_2SO_4(g) \longrightarrow 2\ {NH_4}^+(aq) + {SO_4}^{2-}(aq)} \tag{R 2.3}$$

$$\mathrm{NH_3(g) + HNO_3(g) \rightleftharpoons {NH_4}^+(aq) + {NO_3}^-(aq)} \tag{R 2.4}$$

$$\mathrm{NH_3(g) + HCl(g) \rightleftharpoons {NH_4}^+(aq) + Cl^-(aq)} \tag{R 2.5}$$

If the availability of NH_3 is limited compared to the acids, the stronger acids condense and replace deprotonate weaker acids which then evaporate into the gas phase. This exchange does not happen instantly but, first, the liquid phase pH is reduced after the condensation of a strong acid, which decreases the equilibrium concentrations of dissolved acids – particularly of weak ones – and, finally, leads to their evaporation towards their equilibrium concentrations. Hence, the ion balance does not need to be leveled continuously.

$$\mathrm{2\ NO_3{-}(aq) + H_2SO_4(g) \longrightarrow 2\ HNO_3(g) + {SO_4}^{2-}(aq)} \tag{R 2.6}$$

$$\mathrm{2\ Cl^-(aq) + H_2SO_4(g) \longrightarrow 2\ HCl(g) + {SO_4}^{2-}(aq)} \tag{R 2.7}$$

$$Cl^-(aq) + HNO_3(g) \longrightarrow HCl(g) + NO_3{}^-(aq) \quad \text{(R 2.8)}$$

The dominant component of sea salt is sodium chloride (NaCl). If the amount of available NH_3 falls below its demand required by the condensation of H_2SO_4 and HNO_3, HCl is released from sea salt particles into the atmosphere. HCl transfer the hydrogen atom to hydroxyl radical (OH) leaving a chlorine radical (Cl) that interacts with the O_3 chemistry [Cai et al., 2008; Crisp et al., 2014; Knipping and Dabdub, 2003]. In addition to HCl, nitryl chloride ($ClNO_2$) is produced by a reaction of sea salt Cl^- with gaseous N_2O_5 [Behnke et al., 1997; Knipping and Dabdub, 2003]. However, this reaction is not included in the CMAQ setup described in Sect. 2.4.1.

2.2 Aerosol Particles

2.2.1 General Features of Atmospheric Particles

An aerosol is defined as the mixture of particles in the air or another gas. These aerosol particles are objects of various shapes that have a solid core with a liquid or frozen water film at their surface or that are completely liquid.[a]. Basically, particles can be classified into the following groups. More classifications are possible but only these four are relevant for this thesis.

a) **primary or secondary particles:** Primary particles denote those particles that are emitted into the gas phase as particles. Secondary particles form in the gas phase by the clustering of single molecules to nuclei and the activation and growth of the nuclei [Seinfeld and Pandis, 2006a]. In the presence of pre-existing particles, some gas phase substances condense on the existing particles and others form new ones. During measurement campaigns, sudden nucleation events have been observed that cannot be clearly explained by the current state of research [Kulmala et al., 2004]. Some substances, which are available in very low concentrations, are discussed to enhance cluster formation and/or activation of clusters, such as iodine compounds [O'Dowd and de Leeuw, 2007; Allan et al., 2015]. Approaches to model particle formation in clear air environments in detail are available but model results still diverge considerably from measurements [Karl et al., 2012]. Detailed reviews were published by Kulmala et al. [2004], O'Dowd and Hoffmann [2005], and Holmes [2007].

b) **inorganic or organic particles:** Inorganic particles consist of inorganic compounds, such as $SO_4{}^{2-}$, $NH_4{}^+$, and silicates (dust). Organic particles consist of hydrocarbons, such as condensed VOCs. However, this exclusive distinction is often not applicable in real world situations: During the aging of particles, they coagulate with other particles and gaseous substances condense onto them resulting in mixed particles, such as primary inorganic particle cores with an organic coating.

c) **anthropogenic or natural particles**: Anthropogenic particles can be traced back to emissions of anthropogenic activities such as exhaust gases of combustion processes. Natural particles originate from natural sources such as sea spray or secondary organic aerosols from VOCs and other organic material, e.g. emitted by trees.

d) **ultra-fine, fine, and coarse particles:** Coarse particles are large particles with diameters larger than 2.5 µm. Ultra-fine particles are below a few 10 nm in diameter, whereas fine particles are in between. Measurements of coarse particle mass are often abbreviated as PM_C and measurements of fine particle mass as $PM_{2.5}$ (including ultra-fine particles), respectively. The definitions of fine and ultra-fine particles collide partly with the definition of Aitken and accumulation mode particles introduced later in Sect. 2.2.2.

[a] When the liquid particles/droplets become activated and start growing, they are denoted as cloud droplets and are not considered as aerosol particles anymore.

The particle size is relevant for estimating the atmospheric life time of particles. In this context, particles are deposited to the ground via stochastic processes – Brownian motion[b] – and by gravitational settling: The smaller and lighter particles are, the faster they move and the higher is the probability to hit an object in a certain time interval. In contrast, the larger and heavier particles are, the stronger the Earth's gravity acts on them – at same particle density – and the stronger is their gravitational settling. Therefore, coarse particles are dominantly removed from the atmosphere by gravitational settling, whereas ultra-fine and fine particles below approximately 0.1 µm are dominantly removed by stochastic motion [Seinfeld and Pandis, 2006a, Fig. 19.2]. The fine particles in between have the highest atmospheric life time and are mainly removed by wet deposition.

2.2.2 Particle Distributions

Figure 2.1 shows an idealized representation of the atmospheric particle size distribution. The distribution consists of three humps that are denoted as modes. The flat increase on the left side of the first hump from left is the nucleation mode, the first hump is the Aitken mode, the second one the accumulation mode, and the third one is the coarse mode. In some representations, nucleation and Aitken mode are summarized as one mode. The particles in the nucleation, Aitken, and accumulation modes are denoted as fine particles and the particles in the coarse mode as coarse particles. Nucleation and Aitken mode particles might also be summarized as ultra-fine particles.

The nucleation mode consist of recently nucleated secondary particles. These particles grow further to diameters of several 10 to 100 nm by condensation of further gases onto their surface and by coagulation which means that two or more particles collide and stick together. Particles in this second size range are relevant for cloud formation. They are named after the meteorologist John Aitken who did research on atmospheric particles in the late 19th century. Aitken mode particles deposit to the ground – by molecular diffusion or by wash-out through precipitation – or grow further. The growth rate of the particle diameter converges towards zero when their diameter is in the order of 1 µm. The Volume V and the diameter D of an ideal sphere are related to each other by $V \propto D^{1/3}$ and, thus, large particles need to grow considerably more in volume than small particles in order to growth by the same Δ in diameter. Hence, particles accumulate in this size range during their growth process. The resulting mode is denoted as accumulation mode. Large particles of 2.5 µm diameter and above, which form the coarse mode, are, commonly, no grown-up accumulation mode particles but they are emitted from the ground (dust), from the ocean (sea salt), by volcanos and by anthropogenic activity as coarse particles. They are subject to condensation and agglomeration as Aitken and accumulation mode particles but their growth in diameter is slow.

Atmospheric particles can be represented by their number, surface area, and volume distributions. The total particle number, surface area, and volume are relevant for different atmospheric processes[c]. While Fig. 2.1 outlines a schematic size distribution with no realistic Y-axis unit, Fig. 2.2 displays a particle number distribution and consistent surface area and volume distributions. Equations (2.1) and (2.2) show the mathematical relation between these three parameters. The particles mass distribution is calculated by Eq. (2.3), assuming that the particles consist of the species 1 to n with the densities ρ_1 to ρ_n.

[b] At his point, it is called it Brownian motion and not diffusion because diffusion denotes the emergent phenomenon on the macroscopic level while Brownian motion describes the individual particle's motion.

[c] number distribution: cloud formation; surface area distribution: condensation of pollutants onto particles and cloud formation; volume distribution: amount of chemical compounds and calculation of particle mass

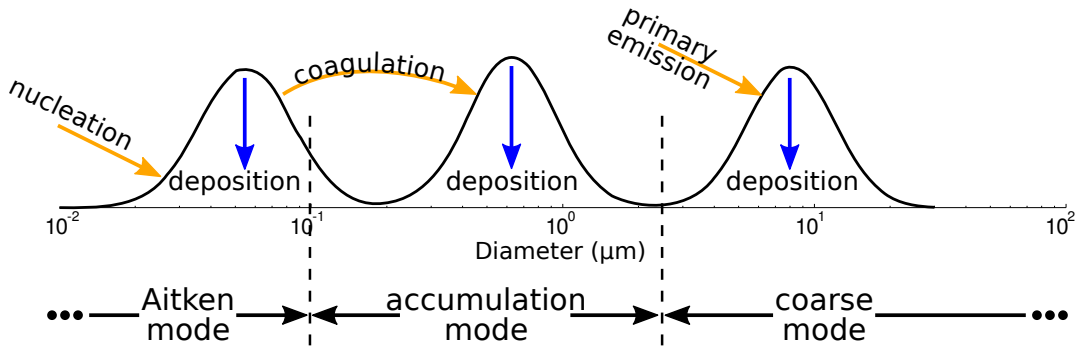

Figure 2.1: Schematic representation of three size modes of atmospheric aerosol particles derived (and modified) from Seinfeld and Pandis [2006a, Fig. 2.7,p.59] which is based on Whitby and Cantrell [1976]. The y-axis is a fictive combination of particle number and mass concentration so that the Aitken, accumulation, and coarse mode are apparent. Condensation of gaseous substances is not included. The dominant deposition processes differs between the modes: stochastic settling in the Aitken mode and gravitational settling in the coarse mode.

$$\frac{dN}{dD} \qquad \text{number distribution}$$

$$\frac{dS}{dD} = \frac{1}{4}\pi \cdot D^2 \cdot \frac{dN}{dD} \qquad \text{surface area distribution} \qquad (2.1)$$

$$\frac{dV}{dD} = \frac{1}{6}\pi \cdot D^3 \cdot \frac{dN}{dD} \qquad \text{volume distribution} \qquad (2.2)$$

$$\frac{dm}{dD} = \sum_{i=1}^{n} \left(\rho_i \cdot \frac{dV_i}{dD} \right) \qquad \text{mass distribution} \qquad (2.3)$$

The factor D^3 in Eq. (2.2) indicates that larger particles are more relevant for the volume distribution than for the number distribution. The particle number distribution is dominated by nucleation and Aitken mode particles, the surface area distribution by accumulation mode particles, and the volume distribution by coarse mode particles. The mass distribution is dominated by the coarse mode particles, too.

Integrating the distributions $\frac{dN}{dD}$, $\frac{dS}{dD}$, $\frac{dV}{dD}$ and $\frac{dm}{dD}$ from 0 to ∞ leads to the concentrations c_N, c_S, c_V, and c_m given in the Eqs. (2.4) to (2.7). These concentrations are related to the number distribution's moments. Equation (2.8) shows the mathematical definition of the k$^{\text{th}}$ moment. Thus, the concentration c_N is the 0th moment M_0 to the particle number size distribution, c_S is the 2nd moment M_2 times $\pi/2$, and c_V is the 3rd moment M_3 times $\pi/6$.

$$\mathrm{M}_0 = c_N = \int_0^\infty \frac{dN}{dD} dD \qquad (2.4)$$

$$\frac{1}{2}\pi \cdot \mathrm{M}_2 = c_S = \int_0^\infty \frac{dS}{dD} dD = \frac{1}{2}\pi \int_0^\infty D^2 \frac{dN}{dD} dD \qquad (2.5)$$

$$\frac{1}{6}\pi \cdot \mathrm{M}_3 = c_V = \int_0^\infty \frac{dV}{dD} dD = \frac{1}{6}\pi \int_0^\infty D^3 \frac{dN}{dD} dD \qquad (2.6)$$

$$c_m = \int_0^\infty \frac{dm}{dD} dD = \frac{1}{6}\pi \int_0^\infty \left(D^3 \sum_{i=1}^{n} \left(\rho_i \cdot \frac{dN_i}{dD} \right) dD \right) \qquad (2.7)$$

$$\mathrm{M}_k = \int_0^\infty D^k \frac{dN}{dD} dD \qquad (2.8)$$

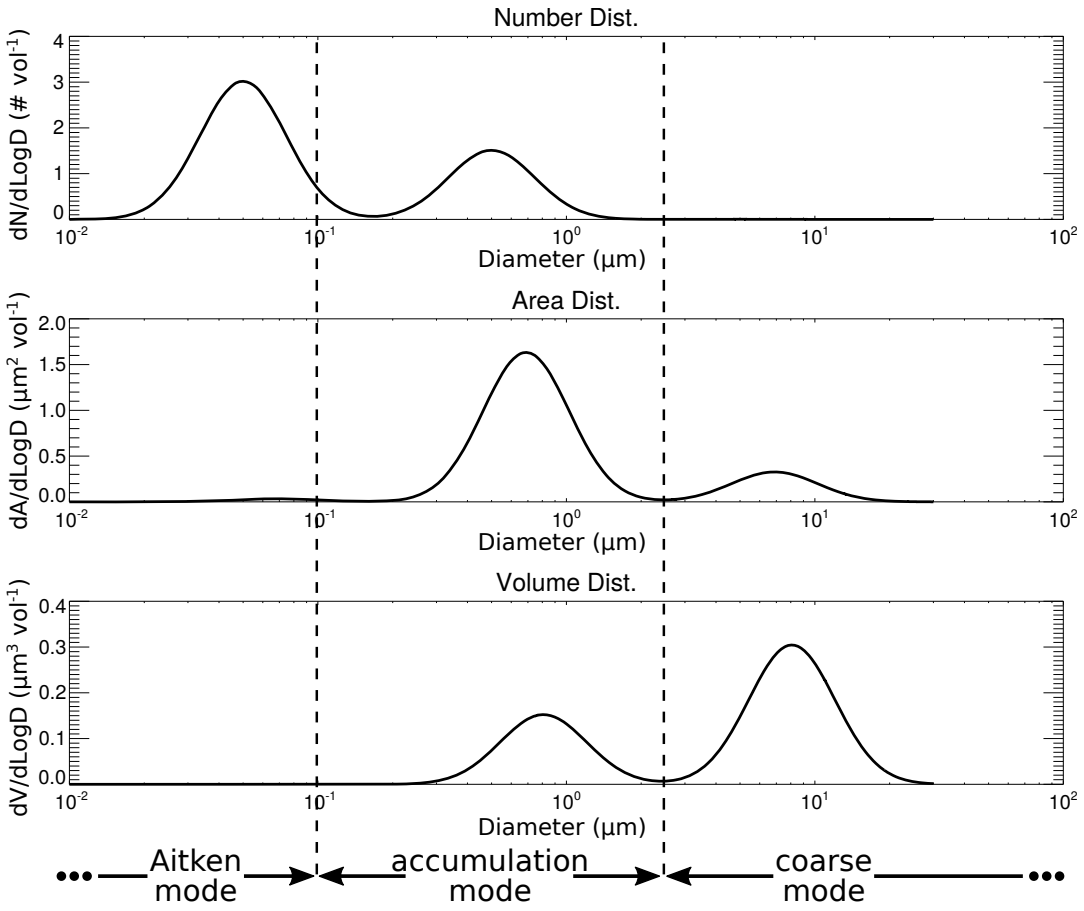

Figure 2.2: Exemplary idealized number, surface area, and volume distribution of atmospheric particles [modified version of Robinson, 2012, GNU Free Documentation License, Version 1.2].

The derivative $\frac{dN}{dD}$ can be converted into $\frac{dN}{d\ln D}$ and $\frac{dN}{d\log_{10} D}$ as shown in Eqs. (2.9) and (2.10). Please note that some authors write and plot their distributions as $\frac{d}{d\ln D}$ and others as $\frac{d}{d\log_{10} D}$ and sometimes it is not clear whether log means ln ($= \log_e$) or $\log_{10}$.

$$\frac{dN}{d\ln D} = \frac{dD}{d\ln D} \cdot \frac{dN}{dD} = D \cdot \frac{dN}{dD} \tag{2.9}$$

$$\frac{dN}{d\log D} = \frac{d\ln D}{d\log_{10} D} \cdot \frac{dN}{d\ln D} = \ln 10 \cdot \frac{dD}{d\ln D} \cdot \frac{dN}{dD} = \ln 10 \cdot D \cdot \frac{dN}{dD} \tag{2.10}$$

The individual modes of the number distribution can be approximated by each one log-normal distribution with the geometric mean μ and the standard deviation σ [Seinfeld and Pandis, 2006a]. Since μ has the same unit as particle diameter, it is often denoted as geometric mean diameter (GMD). We set $\frac{dN}{d\ln D}$ equal to the log-normal distribution in Eq. (2.11). By inserting Eq. (2.11) into Eq. (2.8) and solving it with the help of the error function, one gets a generic formula for calculating the k^{th} moment in Eq. (2.12) (see pp. 362 in Seinfeld and Pandis [2006a] for details). In both equations M_0 may be replaced by c_N.

$$\frac{dN}{d\ln D} = \frac{\mathrm{M}_0}{\sqrt{2\pi}\ln\sigma} \cdot \exp\left(-0.4\left(\frac{\ln\frac{D}{\mathrm{GMD}}}{\ln\sigma}\right)^2\right) \tag{2.11}$$

$$\mathrm{M}_k = \mathrm{M}_0 \cdot \mathrm{GMD}^k \cdot \exp\left(\frac{k^2}{2}\ln^2\sigma\right) \tag{2.12}$$

Forming an equation system by taking Eq. (2.12) for $k \in \{0, 2, 3\}$ and solving this system to geometric mean diameter (GMD) and σ, one gets Eqs. (2.13) and (2.14).

$$\sigma = \exp\left(\frac{1}{9} \cdot (\ln\mathrm{M}_0 + 2\ln\mathrm{M}_3 - 3\ln\mathrm{M}_2)^2\right) \tag{2.13}$$

$$\mathrm{GMD} = \left(\frac{\mathrm{M}_3}{\mathrm{M}_0 \cdot \exp\left(\frac{9}{2}\ln^2\sigma\right)}\right)^{1/3} \tag{2.14}$$

Thus, having Eqs. (2.12) to (2.14) one can calculate two of the five parameters M_0 ($= c_N$), M_2, M_3, GMD, and σ from the other three. Using another function than the log-normal distribution to express the particle number distribution would make the transformation and final expression more complicated. For several functions the equations might not be solvable, e.g. if the functions were not invertible. Therefore, it is beneficial for the computing time and storage space of CTMs to represent aerosol size distributions by log-normal distributions. The ideal log-normal distributions also agree well with measurements [e.g. Seinfeld and Pandis, 2006a, Sect. 8.1.6].

An alternative approach to the modal representation was to define a discrete set of size sections (bins) with given width and count the particles per section. This sectional approach is commonly not used in the standard versions of the most CTMs – here the modal approach is employed.

2.3 Sea Salt

Sea spray droplets are classified in four categories: film, jet, spume and splash droplets. Their size ranges increase from left to right: 0.5–5 µm (film), 3–50 µm (jet), > 20 µm (spume), and > 20 µm (splash). Film and jet droplets are ejected when air bubbles burst at the sea surface. The air is entrained into the water dominantly by breaking waves. Film droplets originate from the bursting bubbles surface. The bursting bubble results in a vertical pressure gradient which sucks water from the bottom of the bubble into the air forming jet droplets. Considerably more film than jet droplets are produced per bursting bubble: a few 100 versus less than 10. Splash droplets are directly emitted by breaking waves and spume droplets are torn off by the wind from wave crests at high wind speeds. Spume and splash droplets have a short atmospheric life time, because of their large diameter, and, therefore, are not relevant for most atmospheric processes. Film and jet droplets have longer atmospheric life times and contribute to the accumulation and coarse mode, respectively. It is assumed that the sea salt concentration is equal in each droplet type at the time of its formation and depends only on the sea water salinity [Mårtensson et al., 2003] and that the composition of sea salt is approximately equal in all oceanic regions (Sect. E.1). All other parameters that influence the sea salt generation affect the droplet formation process. The SST was found to have such an effect [Mårtensson et al., 2003; Salter et al., 2015]. Moreover, emissions of particles below ≈ 1 µm in diameter are differently affected than those of larger ones. Organic compounds – Water Soluble Organic Carbon (WSOC) and, particularly, Water Insoluble Organic Carbon (WIOC) – form the surface microlayer (SML) that is a fine layer at the sea surface in which these organic carbon compounds enrich. The SML alters the surface tension of the sea surface and, hence, affects the bubble bursting and droplet generation process. Film droplets tear parts of the SML with them when they are emitted.

Jet droplets, however, consist of water that is sucked from below the SML. Therefore, organic compounds are considerably enriched in film droplets compared to jet droplets [O'Dowd et al., 2004; Cavalli et al., 2004].

For modeling purposes, several sea salt emission parameterizations have been derived. The parameterizations relevant for this thesis are described in the Materials and Methods sections of chaps. 3 and 4 and the associated Appendix chapters. Extensive reviews were published by Lewis and Schwartz [2004] and O'Dowd and de Leeuw [2007]. Spada et al. [2013] and Ovadnevaite et al. [2014] are more modern modeling studies with short reviews of relevant sea salt emission parameterizations. The Tel-Aviv University (TAU) Weather Research Center (TAU WeRC) even provides an operational public sea salt aerosol forecast (`wind.tau.ac.il/salt-ina/salt.html`) based on Erickson et al. [1986].

The compounds HNO_3, H_2SO_4, and NH_3 condense onto available particle surfaces, e.g. provided by coarse sea salt particles and fine anthropogenically caused ones. Coarse particles have a higher dry deposition velocity than fine particles. Hence, these compounds deposit closer to their sources and their transport distance is reduced when coarse particles, i.e. sea salt particles, are present.

2.4 The chemistry transport model and its setup

2.4.1 Community Multiscale Air Quality Modeling System

The CMAQ model version 5 of the U.S. EPA was employed in this study [Byun and Schere, 2006]. CMAQ calculates transport of chemicals and their deposition, chemical reactions in the gas phase, at particles surfaces (heterogeneous chemistry) and in clouds (in-cloud chemistry), and particle formation and growth. Different configurations of CMAQ were used for the simulations presented in this PhD thesis. The gas phase chemistry was represented by the cb05tucl and cb05tump mechanisms and the heterogeneous chemistry by the AERO5 and AERO6 mechanisms that are described further below. Vertical diffusion is calculated by an enhanced version of the asymmetric convective model (ACM) denoted as ACM2 [Pleim and Chang, 1992; Pleim, 2007a,b] that represents, both, super-grid- and sub-grid-scale turbulent transport processes.

The cb05tucl abbreviates the Carbon Bond V (CB05) mechanism [Yarwood et al., 2005] with enhanced **t**ol**u**ene [Whitten et al., 2010] and **c**h**l**orine chemistry [Sarwar et al., 2007]. HCl can be released from sea salt particles. Therefore, the consideration of advanced chlorine chemistry is important for modeling studies in coastal regions. The cb05tump is the **m**ulti-**p**ollutant version of the cb05tucl which includes mercury compounds.

AERO5 and AERO6 are the CMAQ aerosol chemistry mechanisms and they are based on ISORROPIA v1.7 [Nenes et al., 1998, 1999] and ISORROPIA v2.1 mechanisms [Fountoukis and Nenes, 2007; Sarwar et al., 2011]. Isorropia means "equilibrium" in Greek. Both mechanisms describe the condensation of NH_3, HNO_3, H_2SO_4, and HCl on particles and their evaporation – except of H_2SO_4 that does only condense. The main difference between AERO5 and AERO6 relevant for this study, are the modeled sea salt species that are Cl^-, ${SO_4}^{2-}$, and Na^+ in AERO5 and Cl^-, ${SO_4}^{2-}$, Na^+, potassium (K^+), magnesium (Mg^{2+}), and calcium (Ca^{2+}) in AERO6.

The simulations presented in Chaps. 3 and 4 were conducted with cb05tucl and AERO5 for the year 2008, whereas the simulations presented in Chap. 6 were conducted with cb05tump and AERO6 for the year 2013. The cb05tucl gas phase chemistry mechanism is compatible with the AERO5 and AERO6 mechanisms but cb05tump requires AERO6.

2.4.2 Domain

For the simulations presented here, CMAQ was set up on a coarse $72 \times 72\,km^2$ grid (CD72) covering Europe and the northern coast of Africa and on a refined $24 \times 24\,km^2$ grid (CD24) covering north-western Europe (Fig. 2.3). Boundary conditions for the CD72 grid were taken

from global TM5 [Huijnen et al., 2010] and GEOS-5/MOZART-4 [Emmons et al., 2010] model runs for the years 2008 and 2013, respectively. Boundary conditions for the CD24 grid were generated from the CD72 simulation results. The CD24 grid is one-way nested into the CD72 grid.

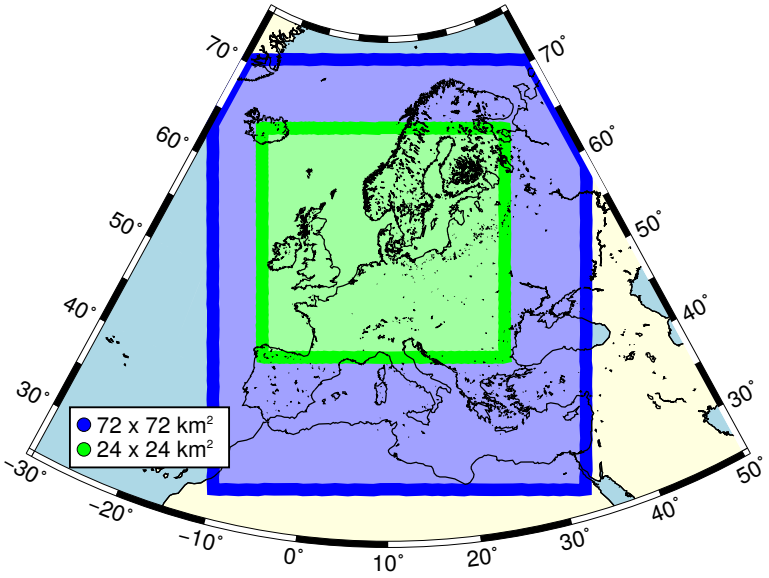

Figure 2.3: The CD72 (blue) and CD24 (green) model grid domains. The grid definitions are given in Table 2.1

The CD72 and CD24 grids are set up in a Lambert conformal conic projection. The parameters of the projection and the grids are given in Table 2.1.

Table 2.1: Parameters for the CD24 and CD72 grids. The projections parameters are: cone intersections at 30° N and 60° N; central meridian at 15° E; center at 15° E and 51° N.

grid	x origin [km]	y origin [km]	number of columns	number of rows
CD24	-1398	-1191	112	106
CD72	-1926	-2655	57	66

2.4.3 Input Data

Flows of input data and the general model set up are presented in Fig. 2.4. The content of the box (package) denoted as *CTM: CMAQ* is explained in Sect. 2.4.4.

Meteorological data needed for the CMAQ runs were produced by the COSMO-CLM model [Rockel et al., 2008]. The COSMO-model has been originally developed as Lokal-Modell to provide operational weather predictions for the German Weather Service (DWD) [Doms et al., 1998, 2011]. Nowadays, it is further developed and maintained by the Consortium for Small-scale Modeling (COSMO). The Climate Limited-area Modelling (CLM) community created a climate model version of COSMO denoted as COSMO-CLM [Déqué et al., 2005; Rockel et al., 2008; Geyer and Rockel, 2013; Geyer, 2014]. The data were converted into the CMAQ format by Beate Geyer with a modified version of CMAQ's Meteorology-Chemistry Interface Processor (MCIP) [Otte and Pleim, 2010]. Additionally to meteorological data, oceanic data – salinity (SAL), sea surface temperature (SST), and wave parameters – were used for some CMAQ simulations. SAL and SST data for the North Sea and Baltic Sea were provided by the Federal Maritime and Hydrographic Agency (BSH) from their operational model BSHcmod, and North Sea wave data

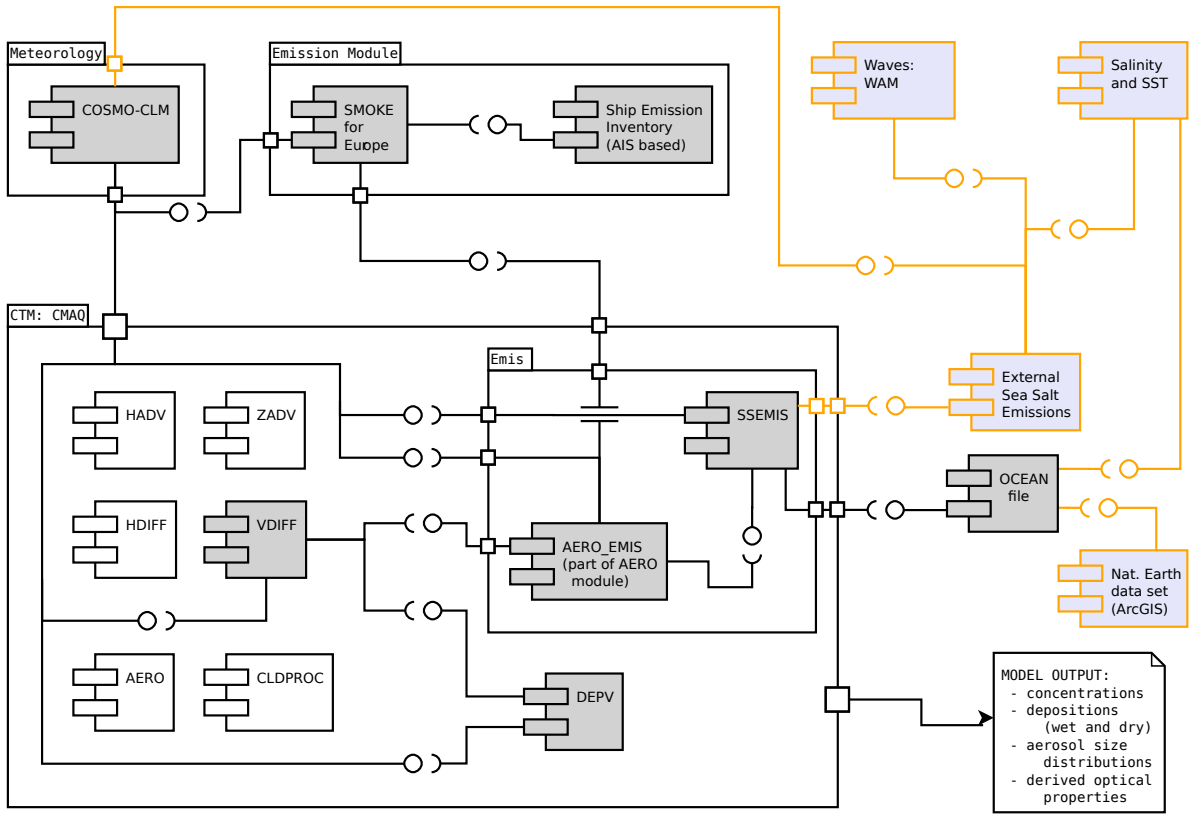

Figure 2.4: UML component diagram of the CMAQ model setup and of flows of input and output data. Some components are added for completeness which are not necessary for the descriptions here. The small labeled boxes (e.g. *CCLM*, *SSEMIS*, and *OCEAN file*) are components that represent program(parts)s and data. The connecting lines are data flows. Lines ending with a circle indicate data that is offered by the connected component. The corresponding half circles – similar to a hand grabbing vor the full circle – indicate that the data is used by the connected component. The connections and component frames colored in orange indicate modifications (additions) to the CMAQ setup performed for this thesis.

were taken from coastDatII being calculated by WAM. SST and wave data for other regions were taken from the ERA-Interim data set of the European Centre for Medium-Range Weather Forecasts (ECMWF). Detailed information on the data are enlisted in the individual chapters.

The emissions for all simulations were prepared and compiled with SMOKE for Europe [Bieser et al., 2011]. Moreover, the nitrogen emissions were improved according to Backes et al. [2016a]. The shipping emissions were calculated externally [Aulinger et al., 2016] and merged with the other emissions via SMOKE for Europe. In the standard CMAQ setup, the sea salt emissions are calculated inline based on the 10-meter wind speed (u_{10}) and on gridded open ocean and surf zone data [Kelly et al., 2010] using the parameterization of Gong [2003]. The open ocean and surf zone data is read in from the so-called OCEAN file which is described in Apdx. H in detail. The coastline and surf zone data required for creating new OCEAN files were extracted from the Natural Earth data set 3.1.0 (`www.naturalearthdata.com`) via ArcGIS.

2.4.4 Relevant technical Parts of CMAQ

For a better comprehension of CMAQ its relevant parts are illustrated in Fig. 2.4. The modules HADV and HDIFF deal with horizontal transport, the modules ZADV and VDIFF with vertical

transport, the module CHEM with gas phase chemistry, the module AERO with aerosol chemistry, and the module CLDPROC with aqueous phase chemistry. All these modules are called in the SCIPROC module (not included in Fig. 2.4 to keep it readable). If one wants to use a 1-dimensional column version of CMAQ for detailed process studies, one needs to comment the interface definitions and calls of the HADV and HDIFF modules in the SCIPROC module out. VDIFF is responsible for vertical diffusion and, additionally, for deposition and emissions via the DEPV and AERO_EMIS modules, respectively. The latter reads in SMOKE files and calls the SSEMIS and DUST_EMIS modules. The SSEMIS module accesses the meteorological input data and the OCEAN file.

2.4.5 Aerosol Particles in CMAQ

In Sect. 2.2 it was described how particle distributions can be represented. In CMAQ, the aerosol particle distribution is represented by three log-normal distributed modes [Binkowski and Roselle, 2003]: Aitken, accumulation and coarse mode. Nucleated particles are mapped to the Aitken mode. Each mode is represented by three moments (3-moment scheme). The number, the surface, and the speciated mass concentrations are the model variables in CMAQ, from which the moments are calculated when required ($\mathrm{M}_3 = 6\pi^{-1}\, c_V = 6\pi^{-1} \sum_{i=1}^{n} \rho_i^{-1} c_{m_i}$ for the species $i \in \{1, \ldots, n\}$). The GMD and σ are variable, which allows the individual modes to grow and shrink along the x-axis[d]: e.q. particle populations can grow in their diameter but their number can remain unchanged. The CMAQ calculations can be reproduced by the equations derived in Sect. 2.2. One might also have a look into [Binkowski and Roselle, 2003][e] for more details. Even though, not the current version is described, they give a detailed overview over the basic idea.

A CMAQ version with sectional aerosol representation – in contrast to modal – is CMAQ "model of aerosol dynamics, reaction, ionisation and dissolution (MADRID)" [Zhang et al., 2004]. In this study, however, the standard aerosol representation by log-normal distributed modes is employed.

2.4.6 Aerosol Emission in CMAQ

The particle emissions into have to consist of particle number, surface area, and speciated mass emissions because the particles concentrations are represented by these parameters. Dust (AERO6 only) and sea salt that are calculated inline and other particulate emissions that are calculated externally via SMOKE (or SMOKE for Europe) need to be distinguished at this point. Figure 2.5 gives an overview of the calculation procedures that are described in the following paragraph.

SMOKE calculates speciated mass emissions: neither distribution into modes, nor number emissions, nor surface area emissions. SMOKE files are read into CMAQ and the mass emissions are split into the three size modes using pre-defined modal split factors – one set of factors per species. The number and surface area emissions are calculated on the basis of invariable GMDs and standard deviations (σs) for each mode. In contrast, sea salt accumulation and coarse mode mass emissions are calculated individually based on Gong [2003]. Number and surface area emissions are derived by RH-dependent GMDs and σs from the mass emissions. The mass emissions per mode are split into speciated mass emissions by mode-dependent species split factors. These operations are performed in the SSEMIS module. The procedure for computing dust emissions is in between: Total mass emissions are calculated and split into accumulation and coarse mode mass emissions. These in turn are split into speciated mass emissions by mode-dependent split factors. M_0 and M_2 emissions are derived by invariable GMDs and σs. Dust

[d] In contrast, a 2-moment scheme would keep GMD or σ constant and a 1-moment scheme would keep both parameters constant.

[e] There is a typo in Eq. (5a) of Binkowski and Roselle [2003] that is corrected here in Eq. (2.13).

emissions are calculated in the DUST_EMIS module.

2.4.7 Sea Salt Emission in CMAQ

The implementation of sea salt emissions in CMAQ was touched briefly in some of the previous subsections. Before proceeding to extensions made with respect to sea salt emissions, the description should be summarized and extend.

Sea salt emissions are calculated on the base of the emission parameterization of Gong [2003] that extends the parameterization of Monahan et al. [1986] and describes bubble bursting generated sea salt emissions. The parameterization consists of an invariant sea salt particle size distribution flux multiplied by an u_{10}-dependent function – the whitecap coverage (W) [Monahan and Muircheartaigh, 1980]. The whitecap coverage is defined to take values between 0.0 (no bursting bubbles) and 1.0 (100 % of sea surface covered by bursting bubbles; foam). For the implementation in CMAQ, the Gong [2003] parameterization was fitted by two log-normal distributions representing the accumulation and coarse mode emissions. RH-dependent parameters of these distributions are hard-coded in the SSEMIS module in order to reduce computing time of the sea salt emission calculations. The parameters are RH dependent because wet sea salt particles are emitted – instead of dry – and the water content is assumed to be in equilibrium with atmospheric humidity. Surf zone and open ocean sea salt emissions are distinguished [Kelly et al., 2010]: Open ocean sea salt emissions are calculated as described above. In the surf zone, however, the whitecap coverage is set to 1 meaning that 100 % of the surface is covered by foam. The surf zone is assumed to be a 50 m wide stripe along the coastline. The information on open ocean and surf zone coverage is given in the OCEAN file (see Apdx. H).

The described setup is valid for the CMAQ versions 4.7 to 5.0.2. In CMAQ v5.1 the whitecap coverage in the surf zone will be set to 0.5 – implying 25 m surf zone width – and one free parameter of Gong [2003] will be adjusted. Sea salt particles consist of Cl^-, Na^+, and SO_4^{2-} when the AERO5 mechanism is employed and of Cl^-, Na^+, SO_4^{2-}, Mg^{2+}, Ca^{2+}, and K^+ when the AERO6 mechanism is employed. See Apdx. E.1 for the exact composition.

A detailed description of the implementation of the sea salt emissions in CMAQ can be found in the Materials and Methods sections of Chaps. 3 and 4.

2.4.8 New Sea Salt Emissions

For this PhD thesis, sea salt emissions were calculated based on two alternative parameterizations [Ovadnevaite et al., 2014; Spada et al., 2013] and supplied them into CMAQ. The emissions were calculated externally and read into CMAQ via a modified version of the SSEMIS module, whereby the modifications in the CMAQ code were kept as less as possible. When new CMAQ versions are released, changes made to the old version, have to be applied to the new one involving the spending of time for implementing and testing purposes. Therefore, the most reasonable approach for me was to calculate sea salt emissions externally. The emission calculation routines were chosen to be implemented in the R scripting language.

The procedure of calculating the sea salt emissions externally is shown in the activity diagram in Fig. 2.6 (same notation as Fig. 2.5). It is further described in Sect. 4.2 and Apdx. I. There are three major differences compared to the standard sea salt emissions are: (a) Aitken mode (I mode) emissions are calculated in addition to accumulation and coarse mode (J and K mode) emissions; (b) the 0^{th}, 2^{nd}, and 3^{rd} moments, which are the number, surface area, and volume/-mass emissions, respectively, are calculated in one step based on the original source function; (c) the emissions are written into files that are read in by the SSEMIS module and not calculated inline.

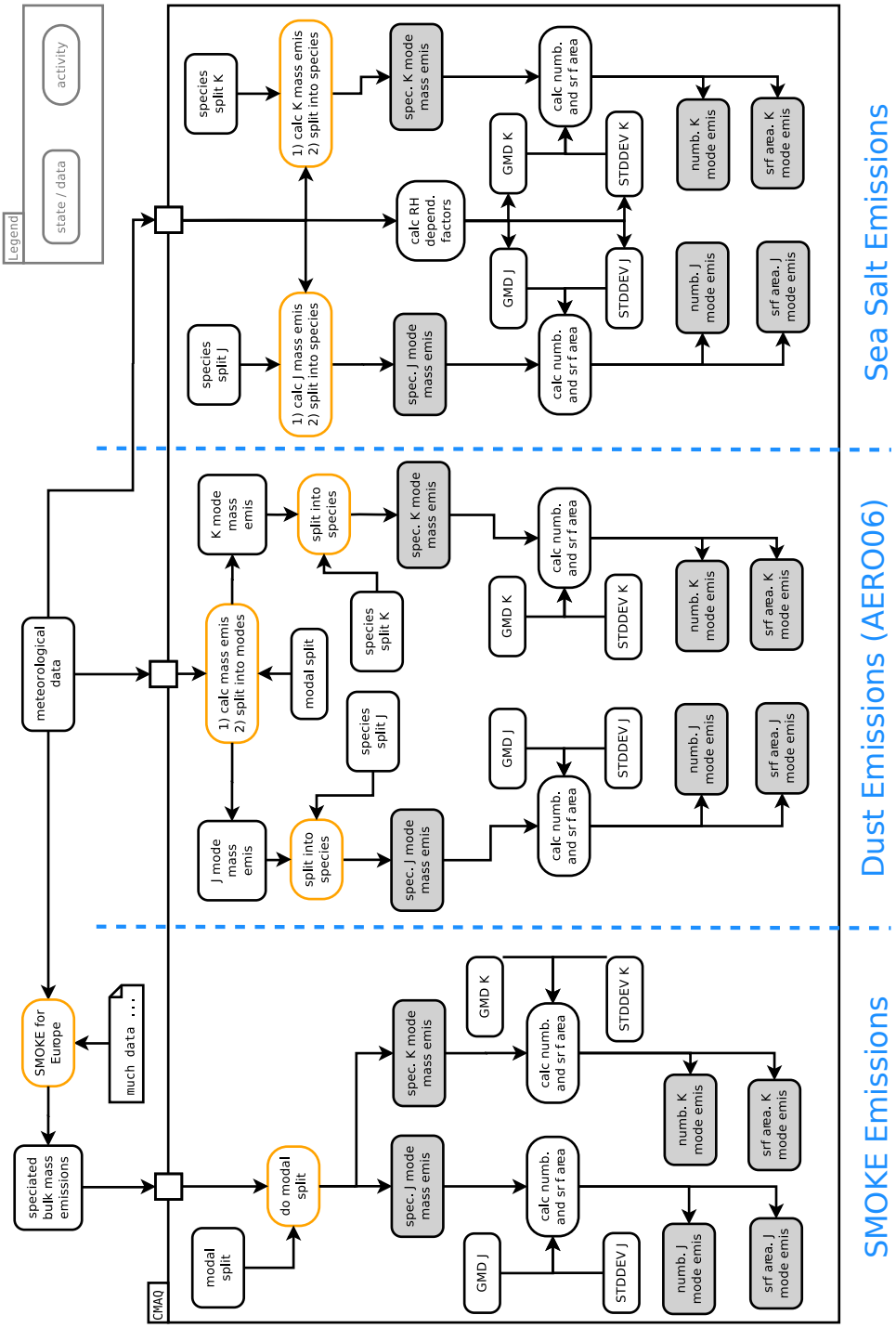

Figure 2.5: UML activity diagram showing the processing of SMOKE emissions (left), dust emissions (centre), and sea salt emissions (right). The diagram contains activities and states (see legend top right). States equal data that is used or produced. The grey filled states are the data that are needed by the aerosol mechanism. The activities are the calculation of emissions and the splitting (orange framed) of existing emissions into individual components. On the one hand, bulk mass is split into Aitken, accumulation, and coarse mode mass and, on the other hand, an unspeciated mass is split into mass per species, e.g. SO_4^{2-} and Cl^-. The accumulation and coarse modes are abbreviated as J and K modes (CMAQ notation), respectively.

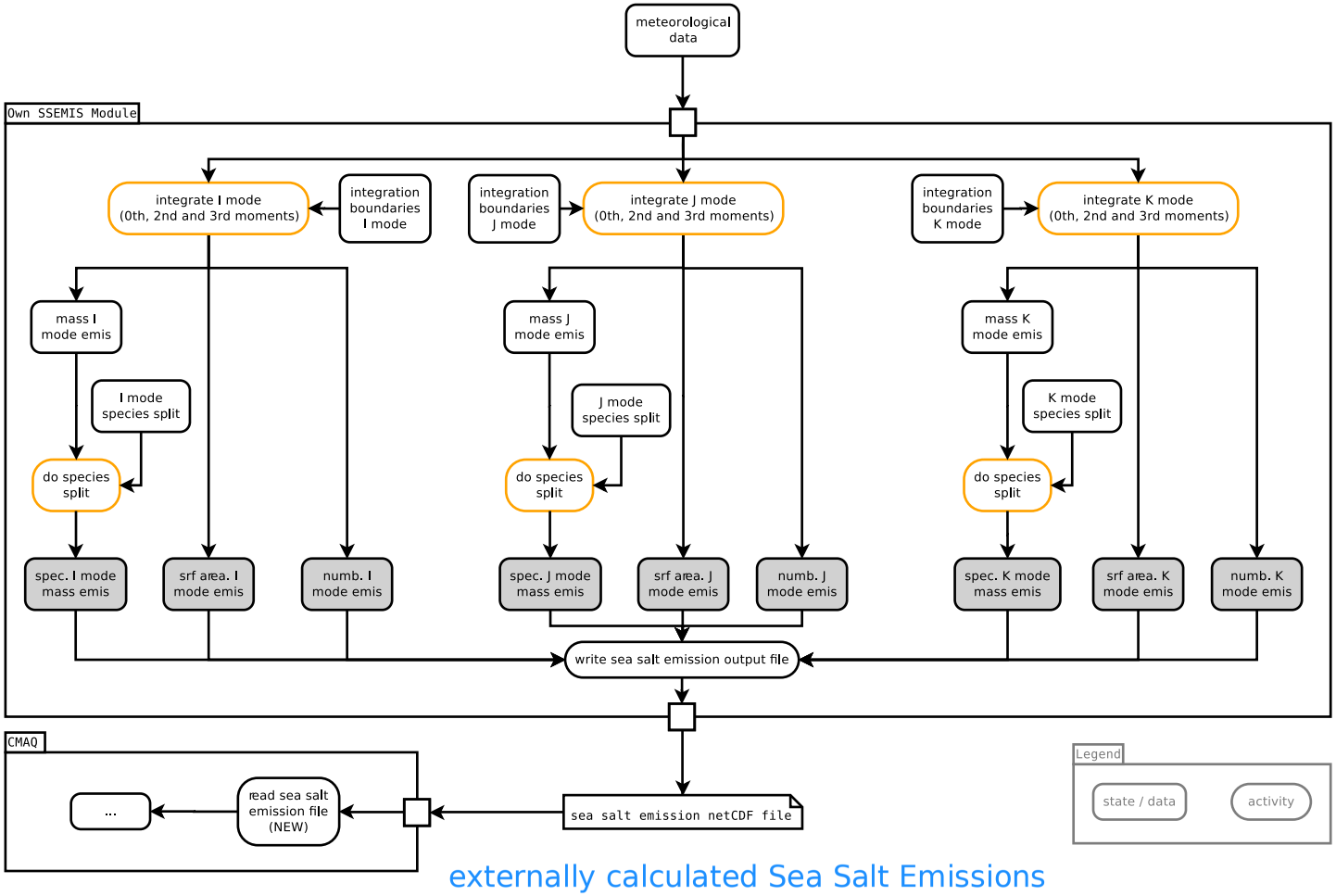

Figure 2.6: UML activity diagram (like Fig. 2.5) on the procedure of calculating sea salt emissions externally. The import into CMAQ is indicated bottm left.The Aitken mode is abbreviated as I mode. The 0^{th}, 2^{nd}, and 3^{rd} moments of the sea salt emission parameterization are calculated via integration (Eqs. (2.4) to (2.6)).

2.5 EMEP Data

Air pollutants ignore political boundaries on their journey through the atmosphere. Therefore, reducing air pollution in a region like Europe requires the cooperation of all countries in that regions with respect to emission reductions of air pollutants. Realizing this fact led to the Convention on Long-range Transboundary Air Pollution (LRTAP) that was signed in 1979 by all European countries, the USA, Canada, Russia and a few former member states of the Soviet Union. A major instrument in the implementation of Convention on Long-range Transboundary Air Pollution (LRTAP) is the European Monitoring and Evaluation Programme (EMEP) – short form of *Co-operative Programme for Monitoring and Evaluation of the Long-range Transmission of Air Pollutants in Europe*. In European Monitoring and Evaluation Programme (EMEP) five institutes and four working groups work on the tasks of (a) emission inventorization, (b) air pollution measurements, (c) regional meteorological modeling, and (d) chemistry transport modeling (`www.emep.int`).

The air pollution measurement data are provided by the member states and are collected by the Chemical Coordination Centre (CCC) that is situated at the Norwegian Institute for Air Research (NILU). The member states' measurements are performed at permanent measurement stations in order to allow the analysis of inter-annual variation and long-term trends in the air pollution. There is no predefined set of measured species (chemical components) at the EMEP stations. Also the temporal resolution and measurement instruments vary between stations. The measurements are reviewed by quality assurance managers who assign quality flags to each measurement indicating their quality and validity. The units and abbreviation in which the measurements have to be reported are defined by EMEP. The data are stored in the Norwegian Institute for Air Research (NILU)'s EBAS database and are publicly available via a web-interface (`ebas.nilu.no/`). The data are provided as text files in the EBAS version 1.1 format (in January 2016) which is derived from the NASA Ames 1001 format. A description of the data file format is given below (Sect. G.1).

The model validations presented in this PhD thesis are based on EMEP data extracted from the EBAS database. The data were managed in a local database for facilitated accessibility. The database structured and created tools to import data from the EBAS database into the local database are given in Appendix G.3. The stations at which measurement and model data are compared are given in the respective chapters.

Two pitfalls exists when working with EMEP data that should be mentioned here: (a) precipitation measurements and (b) NH_3, NH_4^+, HNO_3, and NO_3^- measurements performed with 3-filter packs.

At few measurement stations more than one wet deposition collected are placed. This may be reasonable when common air pollutants, heavy metal, and organic pollutants are collected. On the one hand, parts of the deposition collector may lead to a contamination of the samples – e.g. organic pollutants leaching from plastic parts – and, on the other hand, different institutions might analyze the samples. When one converts the measured pollutant concentrations into deposition rates via the precipitation one needs to be careful to choose the precipitation from the correct wet deposition collector: collectors might be emptied at different days or might contain different amounts of precipitation.

At most stations, the species NH_3, NH_4^+, HNO_3, and NO_3^- are collected with 3-filter packs. These filter packs [EMEP, 2014, Chap. 3.2.2] consist of an

- aerosol filter that collects particles (including particulate NO_3^-, NH_4^+, and SO_4^{2-}),
- alkaline impregnated filter that collects atmospheric acids, such as HNO_3, SO_2, HNO_2, and HCl, and
- acidic impregnated filter that collects atmospheric bases, such as NH_3.

However, gaseous nitric acid and ammonia may condense at the particle filter and particulate nitrate and ammonium may have re-volatilize from the particle filter and condense on the alkaline and acidic filters, respectively. Therefore, NH_3 and NH_4^+ as well as HNO_3 and NO_3^- should be considered as sums only, when collected by 3-filter packs [EMEP, 2014, Chap. 3]. url

3 Sensitivity of modeled atmospheric nitrogen species and nitrogen deposition to variations in sea salt emissions in the North Sea and Baltic Sea regions

Daniel Neumann[1], **Volker Matthias**[1], **Johannes Bieser**[1,2], **Armin Aulinger**[1], **and Markus Quante**[1]

[1] Helmholtz-Zentrum Geesthacht, Institute of Coastal Research, Max-Planck-Straße 1, 21502 Geesthacht, Germany
[2] Deutsches Zentrum für Luft- und Raumfahrt (DLR), Institute of Atmospheric Physics, Oberpfaffenhofen, 82234 Weßling, Germany

Published in Atmos. Chem. Phys., 16, 2921–2942, 2016, doi: 10.5194/acp-16-2921-2016
Received: 25 Sept. 2015 – Published in Atmos. Chem. Phys. Discuss.: 30 Oct. 2015
Revised: 3 Feb. 2016 – Accepted: 23 Feb. 2016 – Published: 8 Mar. 2016

Abstract

Coarse sea salt particles are emitted ubiquitously from the ocean surface by wave-breaking and bubble-bursting processes. These particles impact the atmospheric chemistry by affecting the condensation of gas-phase species and, thus, indirectly the nucleation of new fine particles, particularly in regions with significant air pollution. In this study, atmospheric particle concentrations are modeled for the North Sea and Baltic Sea regions in northwestern Europe using the Community Multiscale Air Quality (CMAQ) modeling system and are compared to European Monitoring and Evaluation Programme (EMEP) measurement data. The sea salt emission module is extended by a salinity-dependent scaling of the sea salt emissions because the salinity in large parts of the Baltic Sea is very low, which leads to considerably lower sea salt mass emissions compared to other oceanic regions. The resulting improvement in predicted sea salt concentrations is assessed. The contribution of surf zone emissions is considered separately. Additionally, the impacts of sea salt particles on atmospheric nitrate and ammonium concentrations and on nitrogen deposition are evaluated.

The comparisons with observational data show that sea salt concentrations are commonly overestimated at coastal stations and partly underestimated farther inland. The introduced salinity scaling improves the predicted Baltic Sea sea salt concentrations considerably. The dates of measured peak concentrations are appropriately reproduced by the model. The impact of surf zone emissions is negligible in both seas. Nevertheless, they might be relevant because surf zone emissions were cut at an upper threshold in this study. Deactivating sea salt leads to minor increases in $NH_3 + NH_4^+$ and $HNO_3 + NO_3^-$ and a decrease in NO_3^- concentrations. However, the overall effect on $NH_3 + NH_4^+$ and $HNO_3 + NO_3^-$ concentrations is smaller than the deviation from the measurements. Nitrogen wet deposition is underestimated by the model at most stations. In coastal regions, the total nitrogen deposition (wet and dry) is considerably affected by sea salt particles. Approximately 3–7 % of atmospheric nitrogen deposition into the North Sea is caused by sea salt particles. The contribution is lower in the Baltic Sea region.

The stations in the EMEP network provide a solid basis for model evaluation and validation. However, for a more detailed analysis of the impact of sea salt particles on atmospheric nitrogen species, size-resolved measurements of Na^+, NH_4^+, and NO_3^- are needed.

3.1 Introduction

Atmospheric sea salt particles are generated from saline water droplets emitted from the sea surface by wind-governed processes and the breaking of waves. Sea salt particle generation is influenced by sea surface temperature, salinity, and the composition of the sea surface microlayer [Mårtensson et al., 2003; Jaeglé et al., 2011; Gantt et al., 2011]. It is considerably enhanced in the surf zone, where waves break along the coast.

Sea salt particles affect the abundance and chemistry of atmospheric pollutants in various ways. Gas-phase species condense on coarse sea salt particles instead of nucleating as new ones and undergo heterogeneous reactions on the particle surfaces [Seinfeld and Pandis, 2006a, Chap. 10.4.4 and 10.4.6]. Coarse particles have higher dry deposition velocities than fine particles, which leads to faster dry deposition of those species adhering to the course particles. Additionally, hydrochloric acid (HCl) is released from sea salt particles, which affects ozone chemistry in polluted marine air [Cai et al., 2008; Crisp et al., 2014; Knipping and Dabdub, 2003]. The effect of sea salt particles on atmospheric chemistry is most relevant in coastal regions where anthropogenic and natural land-emitted species and sea salt particles coincide.

The North and Baltic Sea regions are areas of high anthropogenic activity, including heavy industry, shipping, road transport, agriculture, power generation, and residential heating. These activities emit various air pollutants, such as NO_x, SO_2, NH_3, and particulate matter. Although emissions have been reduced over the past 30 years [Lövblad et al., 2004; Crippa et al., 2015], their effects on human health and their environmental impact are still significant. In this air pollution regime, sea salt is expected to play an important role in affecting the deposition and heterogeneous chemistry of relevant pollutants. The target of this study was to evaluate the following questions for the central European domain using the EPA's Community Multiscale Air Quality (CMAQ) modeling system:

a. What effects do sea salt emissions have on atmospheric ammonium and nitrate concentrations and on nitrogen deposition?

b. How strongly do surf zone emissions contribute to total sea salt and what influence do these emissions have on (a)?

c. Are sea salt emissions well represented in CMAQ for this region?

These analyses were conducted by setting up four sea salt emission cases and comparing the model results to each other and to European Monitoring and Evaluation Programme (EMEP) measurement data. Manders et al. [2010] recently evaluated sea salt measurements from various EMEP stations. Modeling air quality in the Eastern Mediterranean Sea using CMAQ, Im [2013] found a strong impact of sea salt emissions on atmospheric nitrate concentrations and considered surf zone emissions to be important. Liu et al. [2015] also found a large impact of sea salt particles on nitrate in a modeling study in the Pearl River Delta, China.

In models, sea salt emissions are parameterized by wind speed and other meteorological and oceanic parameters. Several current parameterizations are based on the wind dependence derived by Monahan and Muircheartaigh [1980] and Monahan et al. [1986]. Spada et al. [2013] and Lewis and Schwartz [2004] provided a useful overview and comparison of available sea salt emission parameterizations. Additionally, Jaeglé et al. [2011] and Ovadnevaite et al. [2014] recently published improved approaches that include wind speed, salinity, sea surface temperature (SST), and wave data. However, sea salt emissions are still not well parameterized in the surf zone, an area of increased wave breaking along the coastline. CMAQ employs a parameterization published by Gong [2003] that expands the Monahan et al. [1986] parameterization to smaller particle diameters. This study adds a dependence on salinity.

3.2 Materials and Methods

3.2.1 Target Region

The study region is located in the northeastern corner of the Atlantic Ocean and includes the North Sea and Baltic Sea. The North Sea is directly connected to the Atlantic Ocean via the English Channel to the southwest and via the Norwegian Sea to the north. The English Channel is a region of major shipping activity because nearly all ships traveling from outer Europe to the large North European ports, such as Antwerp, Rotterdam, and Hamburg, pass through it. In addition to shipping, considerable anthropogenic activity occurs on land, such as industry, agriculture, and road traffic. The North Sea has a salinity of approximately 35 ‰, which is similar to the Atlantic Ocean. The Baltic Sea is connected to the North Sea via a natural passage between Denmark and Norway/Sweden. In the Baltic Sea, the salinity is approximately 20 ‰ in the western parts and decreases to below 8 ‰ in the eastern parts. During winter, northeastern parts of the Baltic Sea are covered by sea ice. High anthropogenic activity also occurs on the land and water. However, shipping activity is not as pronounced as in the North Sea.

3.2.2 Model Setup

The simulations were performed with the CMAQ modeling system, which was developed and maintained by the US EPA. Version 5.0.1 was used for this study. The cb05tucl mechanisms, i.e., the Carbon Bond 05 mechanism by Yarwood et al. [2005] with updated toluene [Whitten et al., 2010] and chlorine chemistry [Tanaka et al., 2003; Sarwar et al., 2007], represented the gas-phase chemistry. Heterogeneous chemistry is covered by the AERO05 mechanism, which is based on the ISORROPIA 1.7 [Nenes et al., 1998, 1999] mechanism. Among other processes, this mechanism governs the condensation of HCl, NH_3, HNO_3, and H_2SO_4 on particles and the nucleation of new particles. HCl, NH_3, and HNO_3 may evaporate back into the gas phase, whereas H_2SO_4 does not. The aerosol phase is modeled by three lognormal-distributed modes that are each represented by three moments [Binkowski and Roselle, 2003]. The AERO05 mechanism is described in

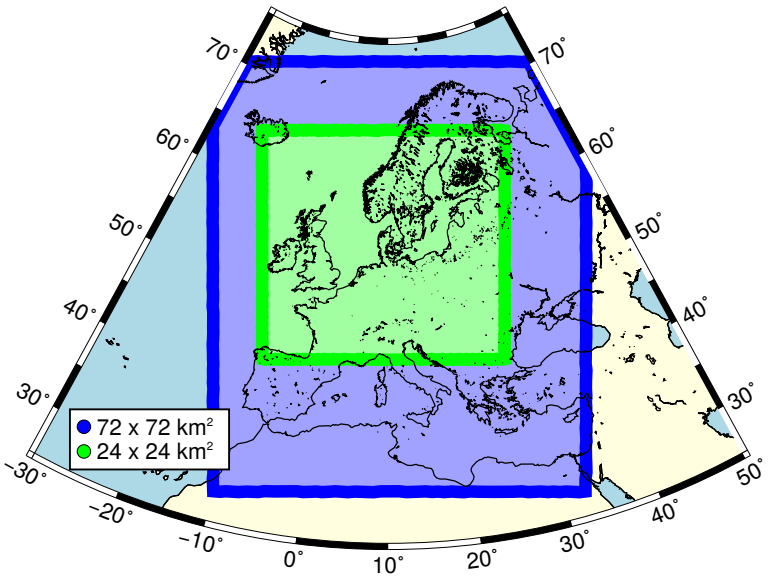

Figure 3.1: Study region and size of the model grids. The coarse grid (blue) includes Europe and parts of northern Africa. The first nested grid (green) includes northwestern Europe, including the North and Baltic seas.

the CMAQ Wiki (`www.airqualitymodeling.org/cmaqwiki`). CMAQ also includes in-cloud chemistry.

The study region is covered by a grid with a resolution of 24 km × 24 km and is enclosed by a grid with a resolution of 72 km × 72 km covering Europe (Fig. 3.1). The boundary conditions of the outer grid are taken from monthly means of the TM5 global chemistry transport model system [Huijnen et al., 2010], and the boundary conditions of the 24 km grid are taken from the enclosing 72 km grid. Wind-blown dust is not included in the outer boundary conditions.

Two 3-month periods – January to February and July to August 2008 – denoted as winter and summer, respectively, are considered. No model input data were available for December 2007, and no German EMEP measurement data were available for September to December 2008. Therefore, it was decided to represent winter and summer by 2 months each. A 10-day spin-up phase, which was initiated from standardized spatially homogeneous initial conditions, preceded each of the two periods.

3.2.3 Input Data

Meteorological input data were calculated by COSMO-CLM (Consortium for Small-scale Modeling in Climate Mode) version 4.8 on a rotated long–lat grid of 0.22° resolution with hourly output [Geyer and Rockel, 2013; Geyer, 2014]. The model grid covers Europe, parts of Greenland, and the southern coast of the Mediterranean Sea. The data were remapped onto the CMAQ grid, and relevant variables were extracted and converted using a modified version of CMAQ's Meteorology-Chemistry Interface Processor (MCIP) [Otte and Pleim, 2010].

The European land-based emissions were compiled with SMOKE for Europe [Bieser et al., 2011], and agricultural emissions were updated according to Backes et al. [2016a,b]. Shipping emissions were calculated on the basis of Automated Identification System (AIS) data [Aulinger et al., 2016]. Sea salt emissions were calculated inline [Kelly et al., 2010; Gong, 2003] and scaled by annual average salinity. Details on the sea salt emissions are given in the next section. The salinity data were taken from runs of a hydrodynamic model based on HAMSOM (HAMburg Shelf Ocean Model). A detailed description of the hydrodynamic model and recent updates were published by Schrum and Backhaus [1999] and Barthel et al. [2012], respectively.

3.2.4 Sea Salt Emissions

Physically, sea salt particles are dried sea water droplets that are ejected from the sea surface into the atmosphere [Lewis and Schwartz, 2004]. Under most weather conditions, the generation of sea salt particles is dominated by bubble bursting: air is mixed into sea water by breaking waves and forms air bubbles that rise to the sea surface and burst. Small water droplets are ejected from the breaking hull of the bubble (film droplets). Through the abruptly changing pressure within the bursting bubble, some water is sucked from below the bubble into the air (jet droplets). The fraction of sea surface covered by bursting bubbles is denoted as whitecap coverage. Droplets, which are emitted primarily when waves break and are torn by the wind from wave crests, are termed splash and spume droplets, respectively. High wind speeds of larger than approximately $10\,\mathrm{m\,s^{-1}}$ are needed for both processes to be relevant for atmospheric sea salt particle generation. The naming conventions for spume and splash droplets are not consistent throughout the literature.

The amount of sea salt per droplet and the resulting sea salt particle size are governed by the sea surface salinity [Mårtensson et al., 2003]. Sea surface temperature, biofilms, and other surfactants affect the sea salt particle size spectra [Mårtensson et al., 2003; Gantt et al., 2011]. In the surf zone, sea salt emissions are enhanced due to a higher number of breaking waves. Additionally, sea salt particles may be electrically charged [Gathman and Hoppel, 1970; Bowyer et al., 1990].

Sea Salt Emission Parameterizations in CMAQ

Edward Monahan and colleagues [Monahan et al., 1982; Monahan and Muircheartaigh, 1980] derived a parameterization that describes the generation of sea salt particles by bursting bubbles. A sea salt particle number flux distribution was estimated for 100 % whitecap coverage and multiplied by the whitecap coverage (W), which is fitted by a power law to the 10 m wind speed (u_{10}) as given in Eq. (3.1) [Monahan et al., 1986, Eq. 12]. Sea salt emissions in CMAQ are calculated following Gong [2003], an enhancement of Monahan et al. [1982] that incorporates smaller radii (see Eq. (3.2)). Particle number, dry surface, dry mass flux, and water content at an ambient relative humidity (RH) are calculated explicitly in CMAQ. Water content is calculated using a polynomial fit published by Zhang et al. [2005]. The total emitted dry sea salt mass is split into 7.55 % SO_4^{2-}, 53.98 % Cl^-, and 38.56 % Na^+ [Kelly et al., 2010]. The model Na^+ represents Na^+, Mg^{2+}, K^+, and Ca^{2+}.

$$W = 3.84 \times 10^{-6} \times u_{10}^{3.41} \tag{3.1}$$

$$\begin{aligned}\frac{\mathrm{d}F}{\mathrm{d}r_{80}} &= W \times 3.5755 \times 10^5 \times r_{80}^{-A} \times \left(1 + 0.057 \times r_{80}^{3.45}\right) \\ &\quad \times 10^{1.607 \times e^{-B^2}} \\ &= 1.373 \times u_{10}^{3.41} \times r_{80}^{-A} \times \left(1 + 0.057 \times r_{80}^{3.45}\right) \\ &\quad \times 10^{1.607 \times e^{-B^2}}\end{aligned} \tag{3.2}$$

$$A = 4.7 \times (1 + \theta \times r_{80})^{-0.017 \times r_{80}^{-1.44}}$$

$$B = \frac{0.433 - \log(r_{80})}{0.433}$$

In the above equations, r_{80} (µm) is the particle radius at 80 % RH, u_{10} ($\mathrm{m\,s^{-1}}$) is the 10 m wind speed and θ is an adjustable parameter, which is set to 30. The term $\mathrm{d}F/\mathrm{d}r$ is the number flux (number $\mathrm{m^{-2}\mu m^{-1}s^{-1}}$) of sea salt particles. The parameterization is valid in a size range of $0.06\,\mu\mathrm{m} \leq r_{80} \leq 20\,\mu\mathrm{m}$.

Surf Zone Emissions

In the surf zone, the sea salt particle number flux is considerably higher than in the open ocean. Addressing surf zone emissions is quite difficult because they depend on the direction of waves and the wind, as well as on local coastal features, such as steep cliffs and flat beaches. In the employed CMAQ version, the surf zone is parameterized by setting the white cap coverage W to 1. The surf zone area is proposed to be a 50 m wide strip along the coastline [Kelly et al., 2010]. CMAQ simulations in parts of Florida performed well with this definition of surf zone [Kelly, 2014, personal communication]. Equation (3.3) shows a modified emission function in cooperating surf zone and open ocean fractions. These fractions need to be pre-calculated for each model domain.

$$\frac{\mathrm{d}F_{\mathrm{eff}}}{\mathrm{d}r_{80}} = (W \times \mathrm{open} + \mathrm{surf}) \times \frac{1}{W} \times \frac{\mathrm{d}F}{\mathrm{d}r_{80}} \tag{3.3}$$

For this study, the ratios of open ocean and surf zone surface per grid cell were calculated by ArcGIS based on the Natural Earth data set. The surf zone area was obtained by placing a 50 m wide strip along the coastline and calculating the area of that strip. Overlapping areas were ignored. Grid cells with long fragmented coastlines and many islands do not necessarily have a large surf zone area because some parts of the coastline and islands are protected by others. Therefore, the surf zone fraction per grid cell was cut at a threshold (see Appendix H for details).

Salinity Dependence

The salinity in large parts of the Baltic Sea is less than 10 ‰, in contrast to the North Sea value of 35 ‰. Therefore, the sea salt emissions must be corrected to account for differences in salinity. The open ocean and surf zone coverage data were scaled by the salinity S ($S/0.035$, with 0.035=35 ‰) to obtain salinity-dependent sea salt emissions [Mårtensson et al., 2003]. CMAQ sea salt emissions would otherwise not depend on salinity. Sea ice cover is not considered. Finally, Eq. (3.4) for sea salt emissions was obtained:

$$\frac{\mathrm{d}F_{\mathrm{eff}}}{\mathrm{d}r_{80}} = \frac{S}{0.035} \times (W \times \mathrm{open} + \mathrm{surf}) \times \frac{1}{W} \times \frac{\mathrm{d}F}{\mathrm{d}r_{80}}. \tag{3.4}$$

The technical procedure of including salinity dependence is described in the Appendix Sect. H and references to the modeled salinity are given in Sect. 3.2.3. Annual average salinity data from the year 1993 were used. Annual averages were taken because the oceanic data are time independent in CMAQ. In the central, eastern, and northern parts of the Baltic Sea, the seasonal variability of the salinity is low – on the scales relevant for sea salt emissions. In contrast, in the Kattegat the seasonal variation can be up to ±10 ‰ with respect to the annual average.

Unfortunately, data for the year 2008 were not available to the authors when the CMAQ model runs were performed. According to Matthäus et al. [1997] and Nausch et al. [2009], the difference in the sea surface salinity between the years 1993 and 2008 is low. The interannual and seasonal affects on the sea salt emissions are low compared to the difference between salinity-scaled and non-salinity-scaled sea salt emissions (for example, see Fig. H.3 in the Appendix). Therefore, we assume that employing salinity data from the year 1993 instead of 2008 has no relevant impact on the results of this study.

Sea Salt Emission Scenarios

Four different sea salt emission cases are investigated in this study: base, noSurf, zero, and full. The base case corresponds to the standard CMAQ sea salt emissions extended by the salinity scaling described in Sect. 3.2.4. The zero case contains no sea salt emissions. In the noSurf case, the surf zone is treated as the open ocean. In the full case, the standard CMAQ sea salt emissions without any extensions are used (no salinity scaling). The cases are listed in Table 3.1.

Table 3.1: Sea salt emission cases.

Case	Description
Base	Standard CMAQ sea salt emissions but scaled by salinity: 50 m surf zone, coast line from Natural Earth data set, linearly scaled with salinity
NoSurf	Like base but surf zone is treated like open ocean
Zero	No sea salt
Full	Standard CMAQ sea salt emissions (like base case but no salinity scaling)

3.2.5 Evaluation Procedure

The CMAQ simulation results were evaluated against concentration measurements performed at EMEP stations. The data were obtained via EBAS (`ebas.nilu.no/`). The stations were chosen according to the availability of data for comparison (Fig. 3.2). Three stations – Westerland (DE0001R), Waldhof (DE0002R), and Zingst (DE0009R) – are described in detail in Sect. 3.3; the data from the other stations are evaluated only statistically and the original data are included in the Supplement. The Westerland station is located directly on the North Sea coast, Zingst is located on the Baltic Sea coast, and Waldhof is located approximately 200 km inland. Thus,

Figure 3.2: The EMEP stations chosen for the comparison to the CMAQ data. Red circles indicate the station data, which are plotted in Sect. 3.3.

these stations' measurements cover three different sea salt emission regimes. All stations are divided into coastal (within 50 km downwind to the coast) and inland stations.

Species including Na^+, $NH_3 + NH_4^+$, and $HNO_3 + NO_3^-$ were compared. Sea salt emissions are the major source of atmospheric sodium cations (Na^+). Na^+ does not evaporate from sea salt particles in contrast to Cl^- and it does not condense onto particles in contrast to HCl and H_2SO_4. Therefore, Na^+ is a good tracer for sea salt particles and is considered for evaluating sea salt particle predictions. Ammonium (NH_4^+) and ammonia (NH_3) as well as nitrate (NO_3^-) and nitric acid (HNO_3) are considered as sums only. Because these substances were collected with three-stage filter packs at most of the considered EMEP stations in 2008, the individual measurements of NH_4^+, NH_3, NO_3^-, and HNO_3 are subject to large uncertainties, whereas the sums are accurately determined (see Apdx. F and EMEP [2014, Chap. 3]).

Daily mean concentrations are compared as plotted time series and box plots and via three statistical metrics (Eqs. (A.1), (A.2), and (A.3)): residual absolute error (RAE), mean normalized bias (MNB), and Spearman's correlation coefficient (R). See Schlünzen and Sokhi [2008] for descriptions of these figures. The box plots contain data from only those days for which measurement data are available.

Nitrogen deposition is considered in Sect. 3.3.3. It is calculated according to Eqs. (A.4) to (A.6). The nitrogen wet deposition is compared to measurement data at most of the stations in Fig. 3.2 (where available) via R and the mean values (μ_{sim} and μ_{obs}). Spearman's correlation coefficient (R) was only calculated when more than ten measurements were available. Measured rain water concentrations were converted into nitrogen deposition per area by the measured amount of rain water. No validation of total nitrogen deposition (wet + dry) against measurement data is performed due to the lack of dry deposition measurement data.

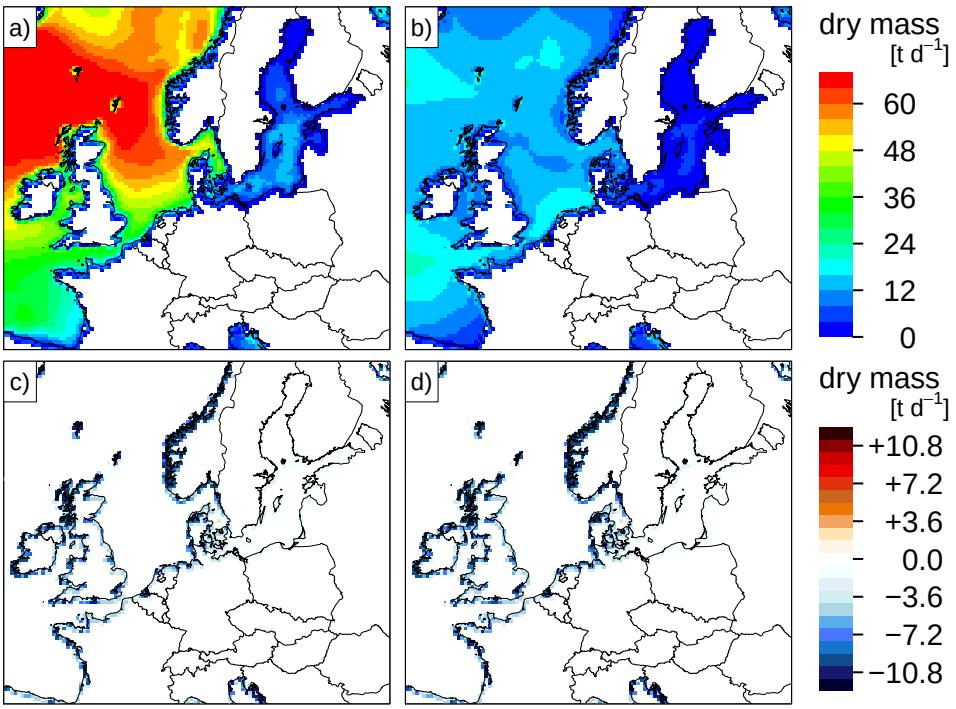

Figure 3.3: Average total sea salt emissions in t/d of the base case (top row) in winter 2008 **(a)** and summer 2008 **(b)**. The difference to the noSurf case (noSurf – base) is shown in the bottom row **(c, d)**.

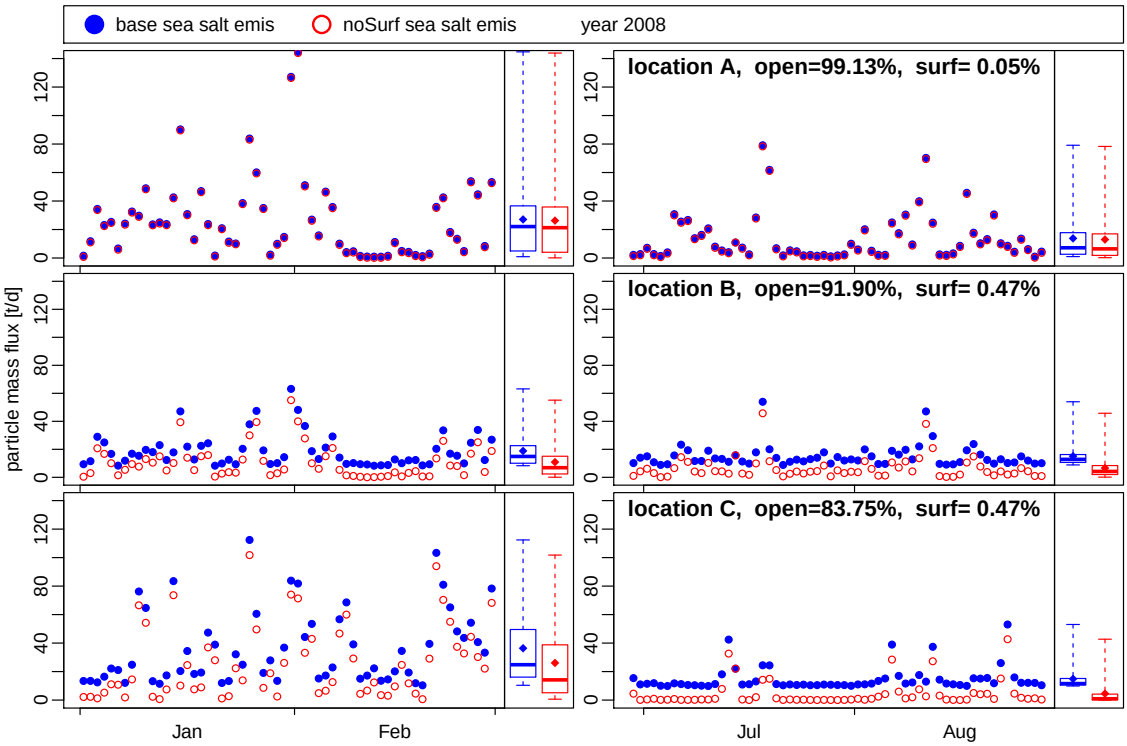

Figure 3.4: Daily averaged sea salt emission flux in t/d in three example coastal grid cells (one per row) in winter 2008 (left) and summer 2008 (right). The fraction of open ocean and surf zone is listed in the plots on the right. The remaining share is land. Location A is located on the Dutch coast, location B is on the German coast, and location C is on the Norwegian Atlantic coast.

3.3 Results

3.3.1 Emissions

Figure 3.3 shows modeled monthly averaged sea salt emissions for the base emission case (top row) in winter and summer (left and right columns, respectively). The bottom row shows the differences between the noSurf and base cases.

According to Fig. 3.3, winter sea salt emissions are 2 to 5 times higher than summer sea salt emissions due to higher wind speeds. In the Baltic Sea, sea salt emissions are considerably lower than in the North Sea, which is caused by the salinity-dependent downscaling of the sea salt emissions. Because wind speeds decrease towards the coast and are highest above open waters, sea salt emissions decrease towards the coast as well. Comparing the base and noSurf sea salt emissions, the greatest differences are observed along the Norwegian and British Atlantic coasts, and lowest differences are observed along the Baltic Sea coast.

Figure 3.4 shows daily averaged sea salt emissions in three coastal grid cells. Although the surf zone covers only a small fraction of the grid cell surface, surf zone emissions contribute a considerable share of sea salt emissions in low wind speed situations. This result emphasizes the importance of correctly parameterizing surf zone sea salt emissions.

3.3.2 Concentrations

The modeled and measured concentrations of two 60-day time series (summer and winter) at 16 EMEP stations are analyzed in this section based on key statistical figures. Three of these EMEP stations, i.e., Westerland (DE0001R), Waldhof (DE0002R), and Zingst (DE0009R), are described and discussed in more detail by considering the actual time series and box plots of the data. For the box plots, only the modeling data points that had corresponding measurement data points were used. The corresponding raw data from the stations are attached as Supplement.

Sodium

The concentration time series in Fig. 3.5 shows that the dates of peaks are consistent across all three stations. The correlation coefficient is greater than 0.75 in winter and greater than 0.70 in summer. However, the magnitudes of the peak values do differ in most situations. The model overestimates these values. During winter, overestimations of peak concentrations occur at all stations, which is indicated by the box plots (Fig. 3.5) and the bias values (Table 3.2). Coastal and inland station cannot be distinguished via the MNB during winter, but the RAE is higher at coastal stations than at inland ones. The correlation coefficient is nearly 0.6 or above at all stations except at Ulborg, Keldsnor, and Virolahti II. During summer, sea salt is moderately overestimated at coastal stations (Westerland and Zingst) and underestimated inland (Waldhof), as indicated by the plots and bias values. The MNBs of the other stations, except those of Tange and Keldsnor, support this finding. The measured base line concentrations, i.e., when no peaks are present, are well matched by the model. Winter sodium concentrations are approximately twice as high as summer concentrations (see scale in Fig. 3.5). The RAE and the MNB values are lower at most stations during summer than during winter, whereas R does not show any tendency between the two seasons.

Deactivating surf zone emissions leads to a reduction in the modeled concentrations most of the time. MNB is reduced at all stations. This reduction leads to a lower bias in situations when concentrations are overestimated in the base case. However, the concentrations are further underestimated in situations when concentrations are already underestimated in the base case. Surf zone emissions lead to a slight improvement in R and the RAE. No clear differences between the effects of summer and winter are visible through deactivating surf zone emissions. Surf zone emissions have an important impact in certain low-emission periods, such as in mid-February

and at the end of July, when surf zone emissions contribute more than the half of the atmospheric sodium.

The zero case is not considered here. The orange asterisks represent a simulation without salinity-dependent scaling of sea salt emissions denoted as the full case. The simulation considerably overestimated sodium concentrations at Zingst (Baltic Sea coast). At all coastal stations, the full case leads to higher MNB values than the base case. The impacts on the two Finish stations Utö and Virolahti II on the eastern Baltic Sea coast are particularly strong. Salinity scaling of emissions is therefore important. Because sodium concentrations are not underestimated at Zingst and not as overestimated as in the non-salinity-scaling case, we assume that the applied linear salinity scaling of the sea salt emissions in the Baltic Sea is a valid procedure as a first-order correction.

Table 3.2: Statistical values (RAE, MNB, and R) for the comparison of measured and modeled (base and noSurf scenarios) sodium concentrations at all considered stations (Fig. 3.2) and during two time periods (winter and summer 2008).

Na^+		Winter 2008				Summer 2008			
Station	Case	n	RAE	MNB	R	n	RAE	MNB	R
Westerland	base	60	1.89	1.01	0.76	61	0.72	2.37	0.70
DE0001R	noSurf	60	1.84	0.65	0.75	61	0.63	1.17	0.79
Coast	full	60	2.01	1.31	0.75	61	0.87	3.51	0.49
Waldhof	base	55	0.42	1.75	0.67	60	0.18	−0.33	0.70
DE0002R	noSurf	55	0.40	1.02	0.74	60	0.20	−0.43	0.71
Inland	full	55	0.45	2.51	0.63	60	0.18	−0.21	0.65
Neuglobsow	base	60	0.30	1.27	0.76	59	0.18	−0.36	0.71
DE0007R	noSurf	60	0.29	0.66	0.81	59	0.19	−0.47	0.73
Inland	full	60	0.35	2.40	0.69	59	0.17	−0.16	0.68
Zingst	base	60	0.72	1.24	0.79	61	0.26	0.20	0.69
DE0009R	noSurf	60	0.64	0.69	0.82	61	0.31	−0.16	0.62
Coast	full	60	1.40	3.28	0.69	61	0.70	1.75	0.36
Melpitz	base	59	0.25	0.43	0.66	61	0.11	−0.35	0.69
DE0044R	noSurf	59	0.25	0.32	0.67	61	0.12	−0.43	0.70
Inland	full	59	0.25	0.54	0.66	61	0.11	−0.24	0.65
Tange	base	56	1.03	1.12	0.67	61	0.44	0.88	0.65
DK0003R	noSurf	56	0.96	0.56	0.74	61	0.41	0.02	0.74
Inland	full	56	1.11	1.37	0.60	61	0.50	1.50	0.46
Keldsnor	base	60	1.26	0.75	0.48	56	0.46	0.21	0.26
DK0005R	noSurf	60	1.07	0.11	0.65	56	0.50	−0.32	0.53
Coast	full	60	1.64	1.47	0.39	56	0.85	1.03	0.09
Anholt	base	59	1.26	0.51	0.81	51	0.60	0.05	0.69
DK0008R	noSurf	59	1.19	0.32	0.82	51	0.67	−0.23	0.70
Coast	full	59	1.61	0.75	0.77	51	0.62	0.36	0.66
Ulborg	base	60	1.41	1.63	0.77	54	0.68	1.22	0.52
DK0031R	noSurf	60	1.22	0.38	0.85	54	0.48	−0.03	0.76
Coast	full	60	1.48	1.83	0.75	54	0.75	1.66	0.48
Utö	base	59	0.59	1.26	0.59	61	0.24	0.24	0.67
FI0009R	noSurf	59	0.52	0.92	0.62	61	0.26	−0.29	0.74
Coast	full	59	3.16	6.09	0.57	61	0.99	4.79	0.41
Virolahti II	base	60	0.24	1.50	0.37	60	0.12	0.07	0.74
FI0017R	noSurf	60	0.21	1.05	0.42	60	0.14	−0.16	0.70
Coast	full	60	1.01	6.27	0.23	60	0.34	2.61	0.73
Birkenes	base	60	0.89	5.77	0.57	61	0.26	1.12	0.35
NO0001R	noSurf	60	0.81	4.31	0.58	61	0.23	−0.14	0.60
Mixed	full	60	0.92	6.13	0.57	61	0.27	1.34	0.29
Hurdal	base	59	0.49	3.80	0.30	55	0.10	0.23	0.51
NO0056R	noSurf	59	0.42	2.80	0.42	55	0.10	−0.22	0.51
Inland	Inland	59	0.52	4.17	0.28	55	0.10	0.56	0.43

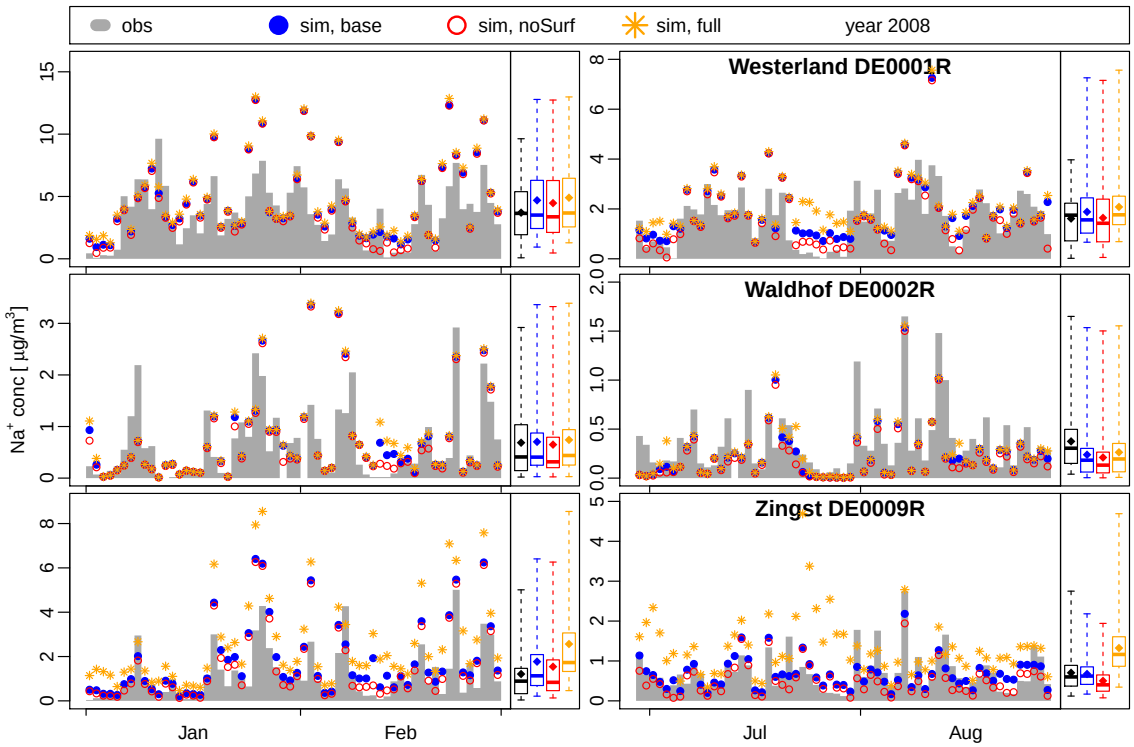

Figure 3.5: Measured (gray bars and black box plots) and modeled (colored symbols) sodium concentrations at three stations (top to bottom) during winter 2007/08 (left) and summer 2008 (right). The orange line indicates sodium concentrations without salinity-dependent downscaling of sea salt emissions. On the left of each plot, the time series of the data are plotted. To the right of each time series, box plots showing the minimum, 25 % percentile, median, 75 % percentile, maximum, and mean values (rhombus) are shown.

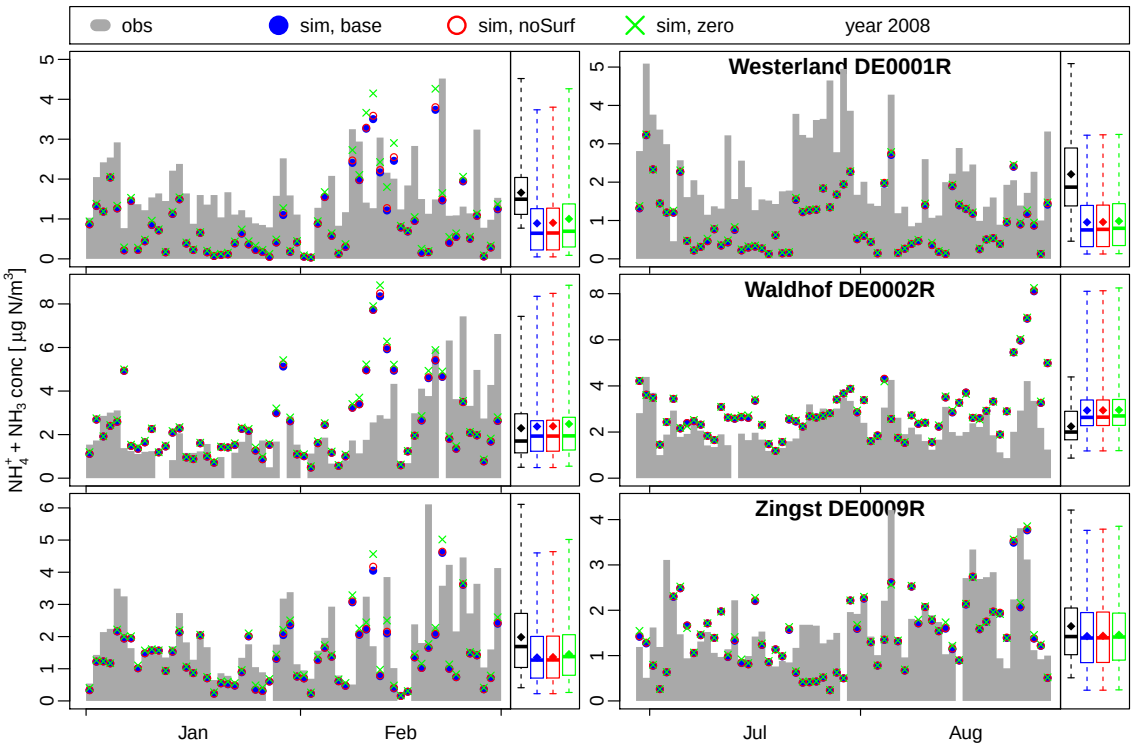

Figure 3.6: Similar to Fig. 3.5 but showing sNH_4 values of the base, noSurf, and zero sea salt emission cases.

Ammonia and Ammonium

$NH_3 + NH_4^+$ (sNH_4, s = sum) concentrations are slightly underestimated at Westerland, as shown in the time series (Fig. 3.6) and indicated by the box plots and the MNB (Table 3.3). During summer, the absolute MNB value is high, but the correlation is strong, which can also be observed directly in the time series in Fig. 3.6: the shape is well matched, but the predicted magnitude is generally too low. In winter, certain peak concentrations are overestimated, which improves the MNB and RAE values but decreases R. At Waldhof, baseline concentrations are well matched, but peak concentrations are overestimated. In winter, the MNB is lower than

Table 3.3: Similar to Table 3.2 but showing sNH_4 ($NH_3 + NH_4^+$) concentrations. Three sea salt emissions scenarios – base, noSurf, and zero – are considered.

sNH_4		Winter 2008				Summer 2008			
Station	Case	n	RAE	MNB	R	n	RAE	MNB	R
Westerland	base	58	1.00	−0.46	0.60	61	1.29	−0.57	0.69
DE0001R	noSurf	58	0.99	−0.45	0.61	61	1.29	−0.56	0.69
Coast	zero	58	0.96	−0.39	0.60	61	1.27	−0.55	0.69
Waldhof	base	54	1.28	0.25	0.59	60	0.88	0.39	0.63
DE0002R	noSurf	54	1.28	0.26	0.59	60	0.88	0.39	0.63
Inland	zero	54	1.31	0.31	0.59	60	0.89	0.40	0.62
Neuglobsow	base	57	1.01	0.21	0.63	59	0.93	0.68	0.36
DE0007R	noSurf	57	1.01	0.22	0.63	59	0.93	0.68	0.36
Inland	zero	57	1.04	0.28	0.64	59	0.94	0.69	0.35
Zingst	base	57	0.81	−0.19	0.72	59	0.60	−0.02	0.46
DE0009R	noSurf	57	0.81	−0.19	0.72	59	0.60	−0.01	0.46
Coast	zero	57	0.77	−0.12	0.71	59	0.60	0.00	0.47
Tange	base	60	1.23	3.84	0.56	55	1.28	0.72	0.40
DK0003R	noSurf	60	1.24	3.86	0.56	55	1.29	0.73	0.41
Inland	zero	60	1.31	4.13	0.57	55	1.32	0.75	0.40
Keldsnor	base	59	0.71	0.01	0.66	55	0.70	0.17	0.38
DK0005R	noSurf	59	0.71	0.02	0.66	55	0.71	0.18	0.38
Coast	zero	59	0.70	0.09	0.65	55	0.71	0.20	0.37
Anholt	base	59	0.40	−0.06	0.78	51	0.24	0.38	0.67
DK0008R	noSurf	59	0.41	−0.05	0.78	51	0.24	0.39	0.67
Coast	zero	59	0.41	0.07	0.78	51	0.26	0.44	0.66
Ulborg	base	60	0.48	0.08	0.79	55	0.68	0.51	0.80
DK0031R	noSurf	60	0.49	0.09	0.79	55	0.68	0.52	0.79
Coast	zero	60	0.53	0.21	0.78	55	0.70	0.56	0.79
Utö	base	59	0.32	0.93	0.81	61	0.13	0.08	0.57
FI0009R	noSurf	59	0.32	0.95	0.81	61	0.13	0.08	0.57
Coast	zero	59	0.33	1.25	0.82	61	0.14	0.12	0.55
Virolahti II	base	60	0.39	2.00	0.75	60	0.18	0.54	0.64
FI0017R	noSurf	60	0.39	2.03	0.74	60	0.18	0.54	0.64
Coast	zero	60	0.43	2.32	0.75	60	0.19	0.57	0.64
Birkenes	base	51	0.22	1.11	0.52	53	0.25	0.02	0.40
NO0001R	noSurf	51	0.23	1.14	0.52	53	0.25	0.04	0.40
Mixed	zero	51	0.28	1.61	0.50	53	0.26	0.10	0.36
Hurdal	base	53	0.72	3.71	0.19	58	0.17	0.24	0.31
NO0056R	noSurf	53	0.73	3.78	0.18	58	0.18	0.25	0.31
Inland	zero	53	0.80	4.17	0.18	58	0.18	0.29	0.32
Jarczew	base	58	1.25	−0.44	0.69	56	1.24	−0.29	0.44
PL0002R	noSurf	58	1.25	−0.43	0.69	56	1.24	−0.29	0.44
Inland	zero	58	1.21	−0.41	0.68	56	1.24	−0.29	0.44
Leba	base	60	0.74	−0.43	0.78	61	0.43	0.06	0.46
PL0004R	noSurf	60	0.74	−0.42	0.77	61	0.43	0.06	0.46
Coast	zero	60	0.69	−0.37	0.78	61	0.42	0.08	0.45
Råö	base	60	0.33	0.22	0.68	61	0.26	0.31	0.38
SE0014R	noSurf	60	0.33	0.23	0.68	61	0.26	0.32	0.38
Coast	zero	60	0.34	0.45	0.67	61	0.28	0.37	0.36

during summer due to a strongly underestimated time period at the end of February. The correlation coefficient is 0.59 in winter and increases slightly in summer to 0.63. At Zingst, the measured concentrations are most consistent in terms of the order of magnitude, which is represented by MNB ≈ 0 and by a low RAE. The occurrence of peaks is well matched, but the correlation coefficient is less than 0.5 in summer. This pattern is caused by peak concentrations that are sometimes over- and sometimes underestimated. For example, in late July, CMAQ predicts a decrease in concentrations, but measured concentrations increase. This episode will be analyzed in more detail in Sect. 3.4.3. At most of the 16 stations, the correlation is better and the RAE is worse in winter compared to summer.

The effect of surf zone sea salt emissions on sNH_4 is negligible, as indicated by the plots and statistics. During winter, zero case sNH_4 concentrations increase slightly, particularly when peak concentrations occur. Because these peak concentrations are already overestimated in the base case, deactivating sea salt emissions does not improve the predictions. The impact of deactivating sea salt emissions on the MNB, the RAE and R values is low and no clear increase or decrease of the MNB or R are induced. The RAE rather decreases at coastal stations and rather increases at inland stations.

Nitrate and Nitric Acid

At Westerland, several measured sNO_3 concentrations in the EMEP database are marked as "under detection limit", which leaves only 21 comparable values in winter and 26 in summer. In mid-February, very high concentrations are predicted, even though the measured values were below the detection limit. Due to the low number of valid measurements, Westerland was not analyzed further.

At Waldhof, the average concentrations are well represented, as indicated by box plots (Fig. 3.7) and MNB (Table 3.4). In winter, the timing of peaks is well matched, but their heights are overestimated in some situations and underestimated in others. This leads to a high RAE value

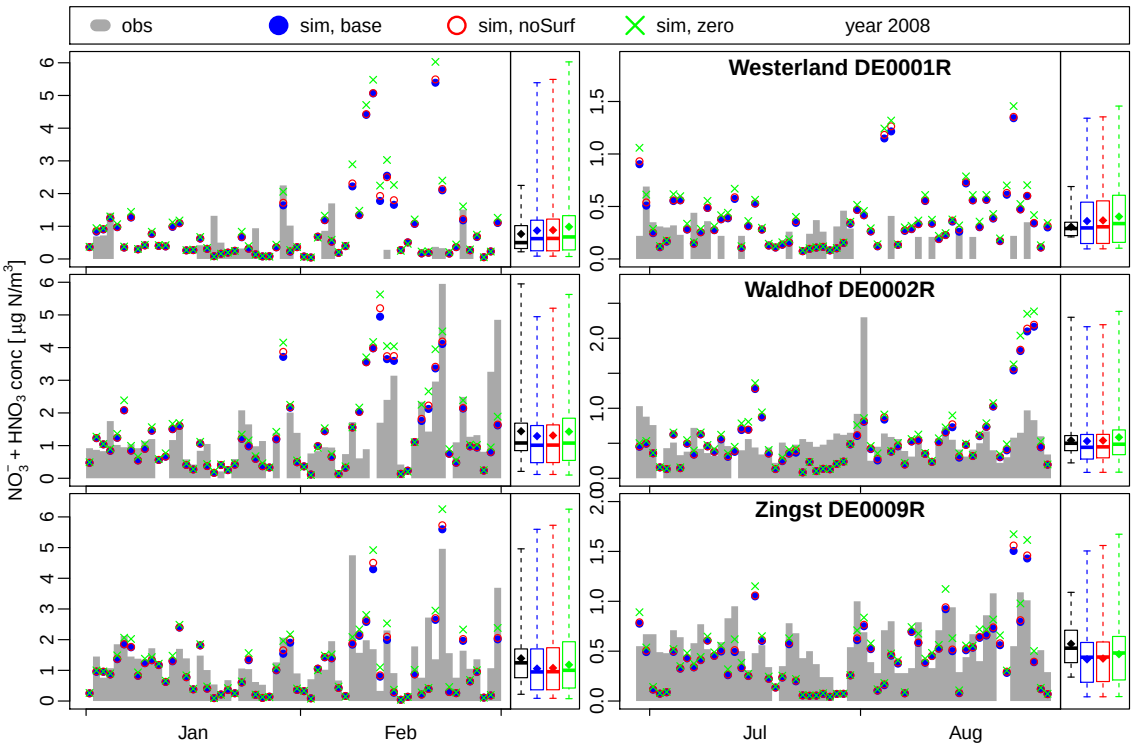

Figure 3.7: Similar to Fig. 3.6 but showing sNO_3 values.

of approximately 0.7. Additionally, in mid-February, one wide and high peak is considerably overestimated. In summer, the RAE improves. However, the correlation coefficient decreases from 0.64 to 0.34 due to two quite poorly matched peaks at the beginning and end of August. The winter concentrations at Zingst are very well represented by CMAQ. The time series plots and box plots agree with each other, yielding an R value of 0.76. In summer, the correlation decreases. A period of highly underestimated sNO_3 concentrations exists in late July at Zingst and Waldhof. Comparing all the stations, R and the RAE are higher in winter meaning that the correlation improves but the error worsens from summer to winter. During winter, the sNO_3 concentrations are underestimated at several stations, as indicated by negative MNBs. In

Table 3.4: Similar to Table 3.2 but showing sNO_3 ($HNO_3 + NO_3^-$) concentrations. Three sea salt emissions scenarios – base, noSurf, and zero – are considered.

sNO_3		Winter 2008				Summer 2008			
Station	Case	n	RAE	MNB	R	n	RAE	MNB	R
Westerland	base	21	0.76	1.17	0.10	26	0.25	0.41	−0.14
DE0001R	noSurf	21	0.76	1.19	0.10	26	0.26	0.43	−0.14
Coast	zero	21	0.81	1.48	0.11	26	0.28	0.57	−0.13
Waldhof	base	50	0.67	0.00	0.64	59	0.31	0.05	0.34
DE0002R	noSurf	50	0.67	0.01	0.64	59	0.31	0.06	0.34
Inland	zero	50	0.68	0.10	0.67	59	0.32	0.16	0.34
Neuglobsow	base	53	0.59	0.39	0.63	54	0.25	0.04	0.39
DE0007R	noSurf	53	0.59	0.40	0.63	54	0.25	0.05	0.39
Inland	zero	53	0.62	0.50	0.65	54	0.26	0.16	0.41
Zingst	base	54	0.56	−0.17	0.76	56	0.26	−0.23	0.55
DE0009R	noSurf	54	0.57	−0.16	0.76	56	0.26	−0.22	0.55
Coast	zero	54	0.58	−0.08	0.77	56	0.26	−0.14	0.55
Tange	base	60	0.33	0.44	0.77	61	0.23	−0.43	0.52
DK0003R	noSurf	60	0.33	0.47	0.77	61	0.23	−0.42	0.51
Inland	zero	60	0.37	0.76	0.77	61	0.20	−0.29	0.52
Keldsnor	base	60	0.52	−0.04	0.66	56	0.32	−0.30	0.57
DK0005R	noSurf	60	0.53	−0.02	0.66	56	0.32	−0.28	0.58
Coast	zero	60	0.57	0.07	0.64	56	0.30	−0.20	0.58
Anholt	base	59	0.38	−0.08	0.76	51	0.26	−0.39	0.49
DK0008R	noSurf	59	0.39	−0.06	0.76	51	0.26	−0.38	0.50
Coast	zero	59	0.42	0.08	0.74	51	0.24	−0.28	0.46
Ulborg	base	60	0.34	−0.25	0.74	55	0.23	−0.48	0.59
DK0031R	noSurf	60	0.35	−0.23	0.74	55	0.22	−0.47	0.60
Coast	zero	60	0.38	−0.09	0.75	55	0.21	−0.38	0.59
Utö	base	59	0.26	0.85	0.71	61	0.19	−0.63	0.57
FI0009R	noSurf	59	0.27	0.88	0.71	61	0.19	−0.62	0.57
Coast	zero	59	0.31	1.06	0.72	61	0.18	−0.58	0.61
Virolahti II	base	59	0.35	1.41	0.58	61	0.12	−0.45	0.68
FI0017R	noSurf	59	0.36	1.45	0.58	61	0.12	−0.45	0.69
Coast	zero	59	0.39	1.64	0.60	61	0.11	−0.39	0.69
Birkenes	base	60	0.19	1.24	0.45	52	0.17	−0.30	0.18
NO0001R	noSurf	60	0.19	1.25	0.45	52	0.17	−0.28	0.20
Mixed	zero	60	0.25	1.79	0.48	52	0.16	−0.11	0.17
Hurdal	base	60	0.34	1.86	0.44	52	0.11	−0.36	0.34
NO0056R	noSurf	60	0.35	1.90	0.45	52	0.11	−0.35	0.35
Inland	zero	60	0.39	2.15	0.43	52	0.11	−0.22	0.34
Jarczew	base	58	0.45	−0.14	0.67	61	0.14	−0.19	0.49
PL0002R	noSurf	58	0.45	−0.14	0.66	61	0.14	−0.19	0.49
Inland	zero	58	0.44	−0.09	0.66	61	0.13	−0.13	0.50
Leba	base	60	0.34	0.13	0.75	61	0.14	−0.03	0.51
PL0004R	noSurf	60	0.35	0.14	0.76	61	0.14	−0.01	0.50
Coast	zero	60	0.37	0.24	0.75	61	0.16	0.10	0.52
Råö	base	60	0.41	0.05	0.60	61	0.24	−0.39	0.54
SE0014R	noSurf	60	0.41	0.07	0.60	61	0.24	−0.38	0.53
Coast	zero	60	0.43	0.30	0.58	61	0.22	−0.30	0.54

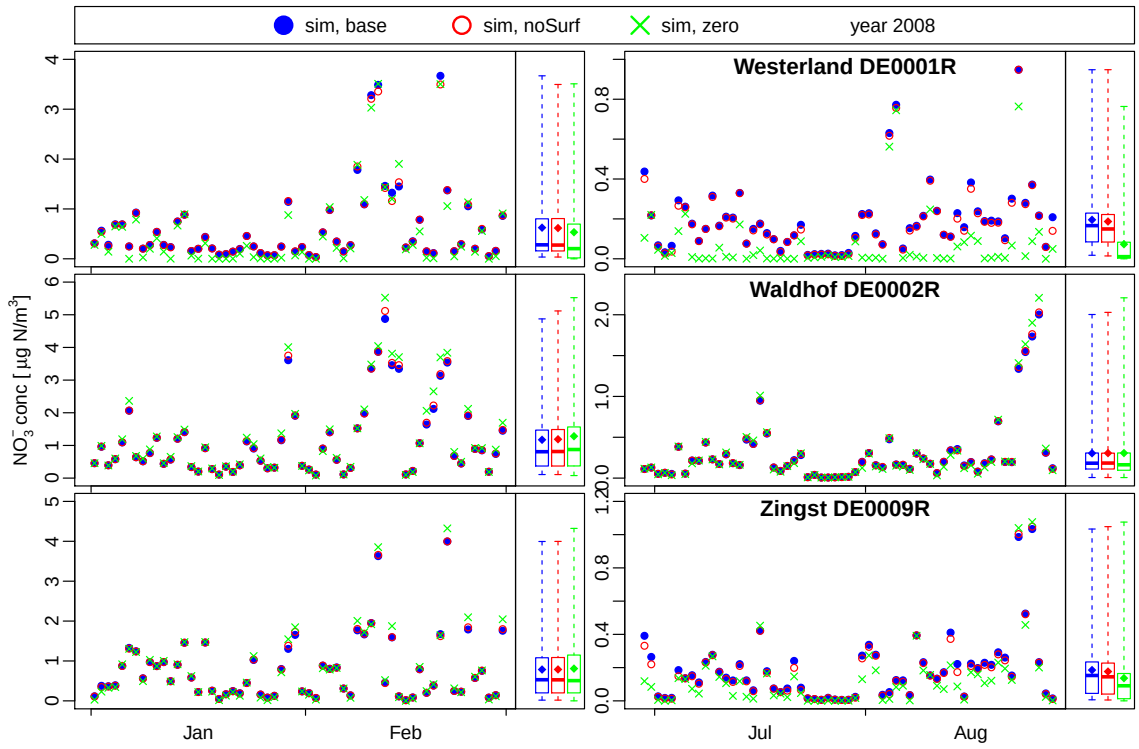

Figure 3.8: Similar to Fig. 3.6 but showing NO_3^- values.

summer, the MNBs are positive at all stations.

In the no surf zone case, sNO_3 concentrations are slightly higher than those of the base case (higher MNB) but R does not change by more ±0.01. Deactivating sea salt emissions increases predicted sNO_3 concentrations at most stations as indicated by the higher MNB values. The RAE and R values show no tendency. The prediction quality, i.e., R and MNB, increases at Waldhof and Zingst because slightly underestimated concentrations are increased, which automatically improves MNB.

Because sNO_3 concentrations do not necessarily represent NO_3^- concentrations, Fig. 3.8 shows the NO_3^- concentrations at the three known stations, and Table 3.5 shows the bias of the zero case NO_3^- and sNO_3 concentrations with respect to the base case concentrations. Usable measurement data were only available for Melpitz. Therefore, no comparison to measurement data is performed here.

The MNB for NO_3^- concentrations is negative with a few exceptions. Thus, nitrate concentrations are commonly higher in the presence of sea salt. The exceptions are inland stations at which positive MNBs occur. In contrast, the MNB values for sNO_3 concentrations are positive at all stations throughout the year which indicates the increase in sNH_3 concentrations in the absence of sea salt, as noted above.

Table 3.5: MNB values of hourly NO_3^- and sNO_3 concentrations in the zero case with respect to the base case. Base case concentrations are considered as observations for the MNB calculation (see Eq. (A.2)). Thus, positive values indicate the zero case concentrations exceed base case concentrations and negative concentrations indicate the opposite.

Station	Winter		Summer	
	NO_3^-	sNO_3	NO_3^-	sNO_3
DE0001R	−0.55	0.09	−0.79	0.13
DE0002R	0.05	0.12	−0.19	0.11
DE0007R	0.00	0.11	−0.31	0.14
DE0009R	−0.19	0.10	−0.54	0.12
DE0044R	−0.02	0.10	−0.25	0.10
DK0003R	0.03	0.24	−0.35	0.25
DK0005R	−0.17	0.12	−0.52	0.14
DK0008R	−0.40	0.15	−0.75	0.16
DK0031R	−0.35	0.20	−0.58	0.20
FI0009R	−0.66	0.13	−0.85	0.15
FI0017R	−0.49	0.11	−0.61	0.13
NO0001R	−0.57	0.17	−0.76	0.30
NO0056R	−0.28	0.07	−0.61	0.16
PL0002R	−0.19	0.07	−0.36	0.10
PL0004R	−0.34	0.09	−0.62	0.13
SE0014R	−0.50	0.15	−0.80	0.16

3.3.3 Nitrogen Deposition

Figure 3.9a and b show the nitrogen deposition in the base case during winter and summer, respectively. In most regions, nitrogen deposition is higher during summer than during winter – up to twice as high and in some regions even higher. During winter, the deposition is highest in western France, the Netherlands, Belgium, northwestern Germany, and northern Italy (Po Valley). During summer, the greatest deposition occurs in the same regions and, additionally, above the northern part of the Alps. The Po Valley deposition is on the same order of magnitude during both seasons, but the deposition in the other regions exhibits the described seasonal pattern.

The nitrogen deposition difference between the noSurf and the base case (Fig. 3.9c and d, noSurf – base) shows that deactivating surf zone emissions leads to a strong reduction in the nitrogen deposition along the coast line of the southern North Sea and the western Baltic Sea. The nitrogen deposition is slightly increased far from the coast in inland regions and above the ocean. The differences are higher in summer than during winter. The differences are also higher in regions with high nitrogen deposition.

Deactivating sea salt emissions completely (Fig. 3.9e and f; note the different scales compared

Table 3.6: Nitrogen deposition into the North Sea and Baltic Sea in $kt\,N\,d^{-1}$ in the base, noSurf, zero, and full cases during winter and summer. The North Sea and Baltic Sea cover 6.50×10^{11} and $4.13 \times 10^{11}\,m^2$, respectively, in this study's model setup. The exact regions considered are plotted in Sect. B.5 of the Appendix.

Region	Season	Base	NoSurf	Zero	Full	
North Sea	winter	1.01	1.00	0.94	1.01	$kt\,N\,d^{-1}$
	summer	1.08	1.08	1.05	1.08	
Baltic Sea	winter	0.57	0.56	0.55	0.58	$kt\,N\,d^{-1}$
	summer	0.60	0.60	0.60	0.61	
North Sea	winter	100.0 %	99.7 %	93.1 %	99.9 %	rel. to base
	summer	100.0 %	99.7 %	97.4 %	100.0 %	
Baltic Sea	winter	100.0 %	99.8 %	96.6 %	103.2 %	rel. to base
	summer	100.0 %	99.9 %	100.0 %	101.2 %	

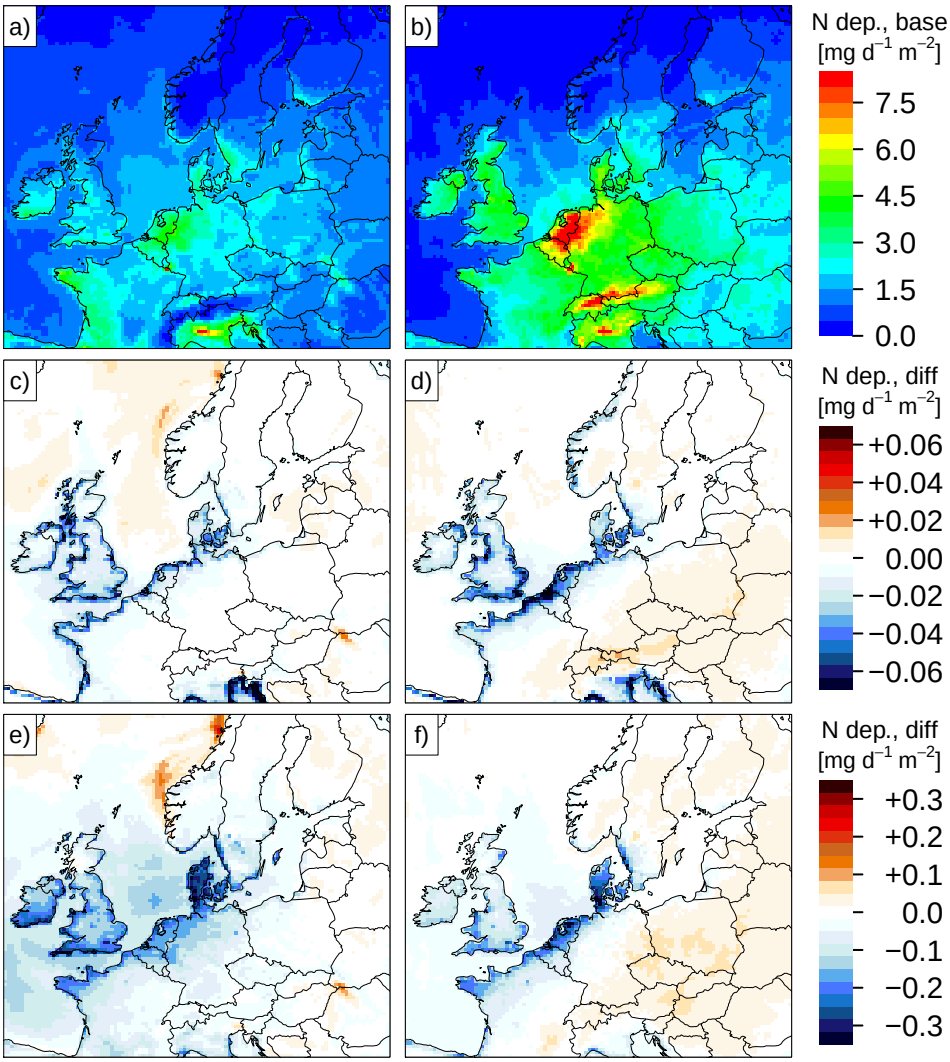

Figure 3.9: Total nitrogen deposition (dry plus wet deposition) in mg N m^{-2} d^{-1} in the study region during winter **(a, c, e)** and during summer **(b, d, f)**. **(a, b)** Nitrogen deposition in the base case; **(c, d)** nitrogen deposition difference between noSurf and base case (noSurf – base); **(e, f)** nitrogen deposition difference between zero and base case (zero – base). Note: The color scale of the plots **(c)** and **(d)** is different from that of the plots **(e)** and **(f)**.

to panels c and d) considerably reduces the nitrogen deposition in large parts of Denmark, the Netherlands, Belgium, and the southern UK by up to 10 % and even more in a few regions. The nitrogen deposition into the southern North Sea is reduced as well. In turn, the nitrogen deposition increases considerably along the Norwegian Atlantic coast during winter and moderately in Eastern Europe during summer.

Table 3.6 shows the summed nitrogen deposition into the North and Baltic Sea in the four emission cases during winter and summer. The nitrogen deposition into the North Sea is approximately 7 % higher during summer than during winter. In the Baltic Sea region, this difference is 6 %.

In the noSurf case, nitrogen deposition is reduced by less than 1 % compared to the base case. In the zero case during winter, however, the nitrogen deposition into the North Sea is reduced by approximately 7 % ($\approx 22\,\mathrm{kt\,N\,a^{-1}}$). During summer, it is reduced by only 2.6 %. The deposition difference for the Baltic Sea is considerably lower, with values of 3.4 and 0 % for winter and

Table 3.7: Similar to Table 3.2 but showing R and mean values of model (μ_{sim}) and observational data (μ_{obs}) of nitrogen wet deposition ($kg\,N\,ha^{-1}\,d^{-1}$) for the base case. Reduced nitrogen and oxidized nitrogen are not shown individually. R of time series with a length of 10 or shorter is not shown. The length of the measurement intervals at the individual stations varies between 1 day, 1 week, and 2 weeks. Therefore, the number of measurements intervals for the comparison differs considerably between the stations.

Station	Winter				Summer			
	n	R	μ_{sim}	μ_{obs}	n	R	μ_{sim}	μ_{obs}
DE0001R	7	–	0.009	0.020	7	–	0.013	0.040
DE0002R	19	0.56	0.023	0.059	30	0.20	0.016	0.046
DE0007R	22	0.42	0.017	0.034	22	0.10	0.013	0.050
DE0009R	7	–	0.008	0.014	7	–	0.016	0.019
DE0044R	6	–	0.008	0.016	8	–	0.014	0.032
DK0005R	3	–	0.006	0.010	4	–	0.013	0.024
DK0008R	3	–	0.011	0.013	4	–	0.018	0.015
DK0031R	3	–	0.007	0.023	4	–	0.013	0.018
FI0017R	7	–	0.006	0.019	8	–	0.008	0.012
NO0001R	36	0.68	0.012	0.079	27	0.66	0.019	0.032
NO0056R	25	0.60	0.000	0.054	28	0.54	0.008	0.028
PL0002R	24	0.71	0.010	0.045	17	−0.34	0.008	0.079
PL0004R	31	0.55	0.013	0.030	28	0.59	0.020	0.035
SE0014R	38	0.62	0.013	0.038	26	0.20	0.032	0.033

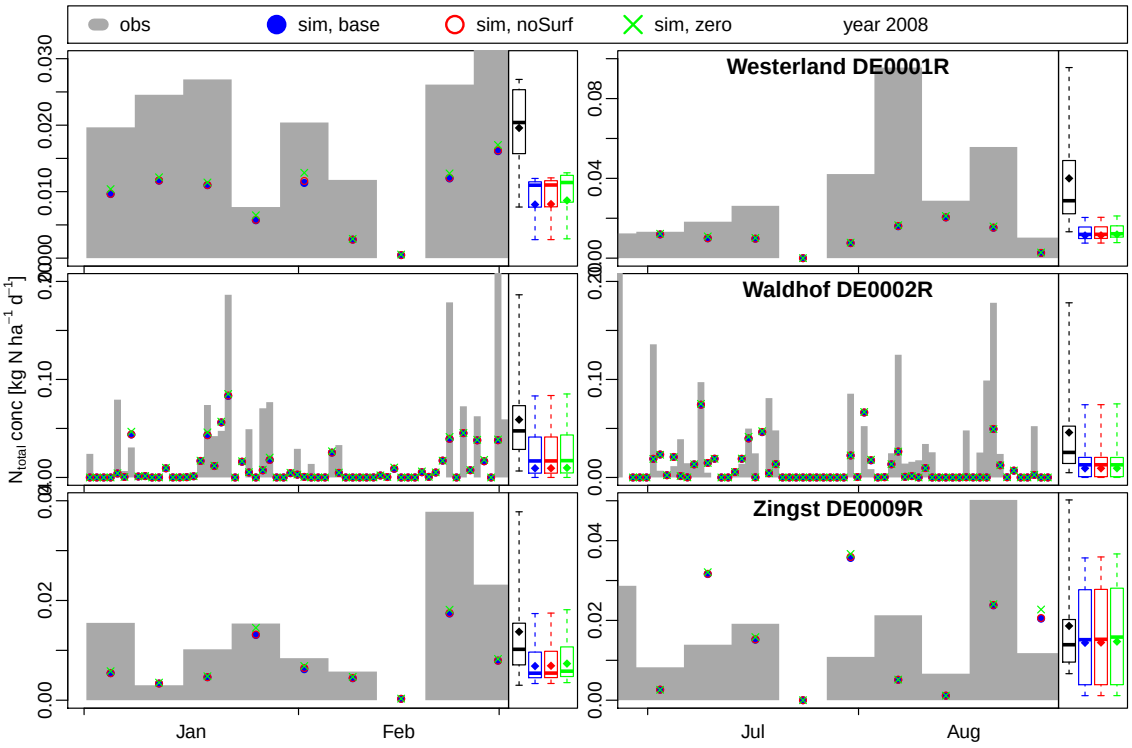

Figure 3.10: Similar to Fig. 3.6 but showing nitrogen (reduced and oxidized) deposition ($kg\,N\,ha^{-1}\,d^{-1}$). The different interval length is due to different measurement intervals at the individual stations.

summer, respectively. The deposition into the North Sea is not affected by applying salinity scaling (full case). However, nitrogen deposition into the Baltic Sea is slightly higher when no salinity scaling is applied.

Figure 3.10 and Table 3.7 show the nitrogen wet deposition in $\mathrm{kg\,N\,ha^{-1}\,d^{-1}}$ at the known EMEP stations. Oxidized and reduced nitrogen is not individually considered here but given in the Supplement. The nitrogen deposition is underestimated in most measurement periods as the plots in Fig. 3.10 indicate. In a few situations, nitrogen deposition are overestimated at Waldhof and Zingst.

A comparison of the mean values in Table 3.7 confirms that the model considerably underestimates nitrogen wet deposition also at most other stations. Exceptions are the stations Zingst and Råö at which the nitrogen depositions are only slightly underestimated. The correlation coefficient is higher during winter than during summer. During summer, it is below 0.5 at four of seven stations. The Norwegian stations Birkenes and Hurdal and the Polish station Leba show the highest correlations throughout the year.

3.4 Discussion

3.4.1 Salinity Dependence and Particle Size Spectra

The salinity dependence of sea salt emissions was analyzed by Mårtensson et al. [2003] in laboratory studies. They found that for particles below 0.1 µm dry radius, the number flux remains roughly unchanged, but the number flux distribution was shifted to smaller radii by a factor of $(S/0.035)^{1/3}$ [Mårtensson et al., 2003, Fig. 5]. Thus, the volume flux is reduced by $S/0.035$ and the surface flux by $(S/0.035)^{2/3}$. For particles larger than 0.1 µm (dry radius), they found that the number flux was reduced by an order of magnitude. In the approach chosen in this study, the number, surface, and volume fluxes are all scaled by $S/0.035$. Technically, this process was performed by scaling the fractions of the open ocean and surf zone in one input file by $S/0.035$. The resulting salinity dependence is not in accordance with the findings of Mårtensson et al. [2003], in terms of either the fine particles or the coarse ones. However, this method was the only way to include basic salinity dependence without modifying the CMAQ code. Thus, the chosen solution is easily applicable to other CMAQ versions and by other CMAQ users. Changing the CMAQ code would have meant that the changes needed to be applied in each new CMAQ version.

Two different sea salt fluxes exist: the sea salt surface flux and the effective sea salt flux. The effective sea salt flux represents the sea salt particles emitted from the sea surface that do not fall back into the ocean immediately. The surface flux represents all particles emitted from the sea surface. The effective flux is a combination of the surface flux and the atmospheric behavior of the sea salt particles which represents the surface emissions flux minus instant dry deposition. Mårtensson et al. [2003] measured the surface flux, whereas Gong [2003] described the effective flux. The shift in the number flux distribution of particles less than 1 µm in size due to salinity variations, which Mårtensson et al. [2003] observed, might not be directly applicable to the effective flux. The shape of the distribution might change as well. Changes in the RH might alter the particle size distribution, as well. Additionally, de Leeuw et al. [2000, Sect. 6] noted that the bubble-bursting process itself might be affected by low-salinity conditions. Therefore, scaling bulk sea salt emissions by functions dependent upon salinity and RH is not necessarily a correct approach. Changes in the shape of the distribution need to be evaluated in the laboratory and in real-world studies.

3.4.2 Discussion of the Sea Salt Results

The sodium concentrations were well matched in terms of the order of magnitude and the temporal occurrence of peaks. Measurements at Zingst, Utö, and Virolahti II showed that sea salt emissions were considerably overestimated in this region when salinity scaling was not applied. Therefore, salinity downscaling is important. Further studies should investigate whether an improved downscaling procedure (see Sect. 3.4.1) improves predicted sea salt concentrations.

Sodium concentrations are overpredicted at all stations during summer. During winter, however, sea salt concentrations tend to be overpredicted at coastal stations and underpredicted at inland stations. The inland station Tange shows overpredictions throughout the year. Amongst the inland stations, Tange is located closest to the coast. The pattern of overpredictions at the coast and underpredictions inland may be due to a combination of overpredicted sea salt emissions and overpredicted dry deposition velocities for coarse sea salt particles. Additionally, certain peaks are better matched in terms of magnitude than others. This difference may be attributable to meteorological conditions, droplet generation processes missing from Gong's sea salt emission parameterization, the SST, and the sea surface micro layer (SML).

Based on laboratory studies, Mårtensson et al. [2003] found that the sea salt emission size spectrum depends on SST. Jaeglé et al. [2011] and Gantt et al. [2015] improved sea salt particle model results by applying SST dependence to sea salt source functions. The results of

Mårtensson et al. [2003], Jaeglé et al. [2011], Callaghan et al. [2014], and Salter et al. [2015] clearly show that sea salt emissions decrease when the SST decreases. The Na^+ concentrations might be overestimated at coastal stations during winter because Gong [2003] does not consider the SST when calculating sea salt emissions. However, this factor does not explain the general overestimation in summer.

The SML that is formed by mainly surface active organic compounds affects the bubble-bursting process and, thus, sea salt emissions. Because the marine biological activity is higher during summer than during winter, one might expect that the SML affects sea salt emissions more during summer than during winter. This could explain the general overestimation of Na^+ concentrations during summer. However, the impact of the SML on sea salt emissions is currently poorly understood and little investigated.

Because Gong's parameterization lacks SST and SML dependence, splash, and spume droplet generation, and non-wind-related bubble bursting, repeating the simulations with other sea salt emission parameterizations might yield interesting results. To analyze the impact of the SML, satellite-derived chlorophyll *a* data could be correlated with the deviations between the measured and modeled results. However, chlorophyll *a* data may not be the ideal proxy [Fuentes et al., 2010].

Under low wind conditions, surf zone emissions are a major source of atmospheric sea salt in the coastal grid cells. The contribution of these emissions decreases under high wind conditions (Fig. 3.4). In this study, the maximum fraction of surf zone per grid cell (24 km × 24 km grid) was capped at 0.47 % to reduce the amount of surf zone emissions. Commonly, this parameter is not capped. Without capping, the fraction of surf zone was considerably greater in certain coastal grid cells, particularly along the Norwegian Atlantic coast, with its numerous fjords and islands. Not capping the surf zone would have led to considerably higher surf zone emissions. Along the Dutch, German, and western Danish coast, most grid cells were not affected by the capping (see Appendix, Fig. H.1 (c)). De Leeuw et al. (2000) found through measurements at a beach in late January that surf zone emissions can contribute approximately 10 times more to ambient atmospheric sea salt concentrations than open ocean emissions. However, at other times, surf zones contribute just 0.1 times as much as the open ocean. The surf zone emissions in grid cells with a large proportion of surf zone, without capping, might be comparable to the maximum-contribution situations observed in de Leeuw et al. [2000]. However, the observed high contributions did not occur continuously. Additionally, the measurements were collected in January, when winds are stronger than those in summer. Therefore, the modeled surf zone emissions were reduced by capping the surf zone fraction. Mechanistically, modifying the whitecap coverage would have been more correct. In the new CMAQ v5.1 release, surf zone emissions will be reduced by 50 % by setting the whitecap coverage to 0.5. This step was not included in this study because changes in the CMAQ code were avoided in order to make the chosen procedure simpler and more applicable in other CMAQ versions. As an alternative, one might choose another parameterization for the surf zone emissions. For example, de Leeuw et al. [2000] and Chomka and Petelski [1997] presented alternative surf zone emission parameterizations. In their study, which was discussed above, de Leeuw et al. [2000] analyzed measured surf-zone-related sea salt concentrations, meteorological data, and video data of the surf zone. They found no correlation between surf zone width or wave height and the surf zone production of sea salt.

Im [2013] estimated a considerably higher contribution of surf zone emissions to atmospheric sea salt concentrations. In that study, the surf zone fraction per grid cell was not capped and was calculated by multiplying the length of the coastlines by 50 m (and dividing by grid cell area). In our study, the surf zone size was calculated in a way so as to not count overlapping surf zones twice. Additionally, the Greek coastal waters contain more islands and the coastline is less straight than the man-made coastlines of the Netherlands and Germany. Therefore, the surf zone contribution estimated in this study is lower.

Salinity in coastal waters is commonly lower than in open ocean water due to freshwater inflow. Thus, surf zone emissions are indirectly scaled down in this study. Im [2013] and Kelly et al. [2010, 2014] do not consider salinity. Hence, this study's surf zone emissions are reduced compared to those in the named studies due to salinity-dependent scaling.

Sea ice is not considered in this study. If the sea surface is covered with sea ice, no sea salt particles are emitted by bursting bubbles. Therefore, sea salt emissions can be deactivated in regions with sea ice cover. For the study region, sea surface salinity is very low in areas with significant sea ice cover (northeastern Baltic Sea). Additionally, these areas are commonly downwind relative to the considered EMEP stations, except the two Finish stations Utö and Virolahti II. Therefore, the overestimation of sea salt emissions introduced by not considering sea ice is expected to be negligible. Moreover, sea salt particles have been found to be re-emitted by wind-blown snow from sea ice [Tian-Kunze et al., 2009; Yang et al., 2008]. Additionally, the edges of sea ice required a similar treatment as the surf zone. Therefore, deactivating sea salt emissions above sea ice would not necessarily improve sea salt emission prediction quality.

3.4.3 Discussion of atmospheric Nitrogen Compounds

The concentrations of sNH_4 were found to be well matched at Zingst, underpredicted at Westerland, and overpredicted at Waldhof. Because land-based NH_3 emissions are not the topic of this paper, Waldhof will not be discussed further. Backes et al. [2016a] described and discussed the employed NH_3 emissions in detail.

A 1-week episode of northeasterly winds during the end of July corresponds in the time series plots to a strong decline in sNH_4 concentrations at Zingst and a strong increase at Westerland. The increase at Westerland is due to NH_3-rich air from Denmark. Although modeled concentrations increased considerably, measured concentrations increased even more. This result might be due to underpredicted emissions or overpredicted NH_3/NH_4^+ deposition. The discrepancy is not caused by sea salt. Remarkably, at Zingst, the modeled sNH_4 concentrations decreased, whereas the measured concentrations increased during this episode. No major landmasses are on the route between the Swedish coast and Zingst, the path by which the air masses likely traveled. If we consider the measured NH_3 and NH_4^+ concentrations individually (which one should not do; EMEP, 2014, Chap. 3), the measured sNH_4 consists primarily of NH_3 ($> 95\,\%$ by mass, not shown here). Because NH_3 has a short atmospheric lifespan, we assume that most sNH_4 is transported over a short distance and does not originate from Sweden. The NH_3 may be emitted from the sea surface [Barrett, 1998; Paulot et al., 2015]. Norman and Leck [2005] found oceanic emissions to be relevant contributors to atmospheric NH_3 in remote marine regions. These oceanic NH_3 emissions would explain the generally underpredicted concentrations at coastal stations. However, these emissions are approximately 2 to 3 orders of magnitude lower than land-based emissions. Additionally, a brief examination of chlorophyll *a* data [Lavender et al., 2015] does not indicate the presence of algae blooms. Therefore, marine NH_3 cannot account for the entire difference at Zingst. Another reason might be incorrectly predicted wind directions caused by sea and land breezes and planetary boundary layer height [e.g., Miao et al., 2009]. Sea and land breezes during day and night do not form in COSMO-CLM with the given setup, version, and grid resolution [Schultze, 2015, personal communication]. Furthermore, certain land-based NH_3 sources, which are located close to the measurement station, might not be considered by the employed emission data set. This topic needs to be considered further.

Predicted and measured sNO_3 concentrations are not well correlated at Westerland in either seasons and at all stations in summer. Approximately half of the measurements at Westerland were under the detection limit and not in the EMEP database. Thus, the peak concentrations were measured and compared. Comparing peak concentrations is biased because they are often over- or underestimated, e.g., via smoothing in the discretization. Therefore, an analysis of the sNO_3 Westerland data is problematic. Additionally, peaks arise in the model results that do not exist in the measurements. This effect may be due to the employed shipping emission inventory,

which contains the weekly averaged shipping emissions of 2011 (whereas the model year is 2008) or due to problems with the measurements.

Surf zone emissions of sea salt have a negligible impact on atmospheric sNH_4 and sNO_3 concentrations at most EMEP stations. Deactivating sea salt emissions completely showed that sea salt particles slightly affect the sNH_4 and sNO_3 concentrations: these concentrations rose when sea salt was deactivated, which means that the presence of sea salt particles decreases them. NO_3^- concentrations, in contrast, increase in the presence of sea salt at most stations throughout the year. At some inland stations, sea salt particles lead to a decrease in NO_3^- concentrations. Additionally, the negative MNB values of other inland stations are closer to 0 than those of coastal stations. Thus, the impact of sea salt particles on NO_3^- decreases with distance from the coast. This pattern is expected because sea salt concentrations decrease from the coast to inland locations. As Fig. 3.8 indicates, the zero case NO_3^- peak concentrations are higher than base case peak concentrations although the MNBs are negative. Therefore, the impact of sea salt on NO_3^- is not as clear as one might assume from the table of MNB values.

Im [2013], Liu et al. [2015] and Kelly et al. [2014] found that sea salt has a significant impact on atmospheric nitrate concentrations. In Im [2013] and Liu et al. [2015], particulate nitrate concentrations considerably increased when sea salt was added. They increased even more when surf zone emissions were activated [Im, 2013, Table 4]. For summer months, their results agree completely with the results of this study but inland stations deviate during winter. Additionally, the peak concentrations differ from the MNBs in this study and the result of other studies. The emission and meteorological regimes in the Mediterranean and Pearl River Delta regions are different from those in the North Sea region, which may account for the different behavior. Due to high agricultural activity in the North Sea region, sufficient fine particles and ammonia are available in summer months for the condensation of ammonium nitrate onto existing particles. As described above, ammonium and nitrate concentrations correlate well in the model but are less correlated in reality. If the nitrate condensation is NH_3 limited in the Mediterranean region, modeled nitrate may condense on particles only in exchange for the release of HCl. According to the other studies, HCl displacement is a relevant process in those regions. Hence, comparing the NH_3/NH_4^+ concentrations would be interesting. Additionally, Saharan dust is blown from the boundaries into the model domain of Im [2013]. The dust may have an indirect effect on atmospheric chemistry that is not present in this study because desert dust is not included in the boundary conditions of this study.

3.4.4 Discussion of Nitrogen Deposition

The nitrogen deposition is higher during summer because the nitrogen emissions are higher during summer, too. While anthropogenic NO_x emissions are higher in winter due to residential heating, NH_3 emissions are considerably higher during summer due to animal husbandry and agricultural activities (involving, for example, fertilizers and manure). The Po Valley is an exception. It is one of the largest and densest industrialized regions in Europe and features high NO_x emissions throughout the year leading to the high nitrogen depositions.

A comparison of modeled and measured nitrogen wet depositions showed that the wet deposition is underestimated by the model by up to a factor of two.

The nitrogen deposition into the North Sea was $1.01\,\mathrm{kt\,N\,d^{-1}}$ ($369\,\mathrm{kt\,N\,a^{-1}}$) during winter and $1.08\,\mathrm{kt\,N\,d^{-1}}$ ($395\,\mathrm{kt\,N\,a^{-1}}$) during summer in the year 2008. The literature values are $622\,\mathrm{kt\,N\,a^{-1}}$ [de Leeuw et al., 2003], $709\,\mathrm{kt\,N\,a^{-1}}$ [Hertel et al., 2002], and $430\,\mathrm{kt\,N\,a^{-1}}$ [Bartnicki and Fagerli, 2008] for the whole years 2003, 1999, and 2005, respectively. These literature annual values are considerably higher than the winter and summer results in this study. The North Sea is defined similar to the OSPAR region II in the cited publications and in this study. Thus, the English Channel (until approximately 5° W) and the Skagerrak are considered to be parts of the North Sea. Therefore, the considered North Sea area is comparable between the studies. In this study, the Baltic Sea featured nitrogen deposition of $0.57\,\mathrm{kt\,N\,d^{-1}}$ ($207\,\mathrm{kt\,N\,a^{-1}}$)

during winter and 0.60 kt N d^{-1} (220 kt N a^{-1}) during summer, whereas 264 kt N a^{-1} [HELCOM, 2005], 204 kt N a^{-1} [Bartnicki and Fagerli, 2008], 201–300 kt N a^{-1} [Langner et al., 2009], and $\approx$ 200 kt N a^{-1} [Bartnicki et al., 2011] were found in other studies for the years 2000, 2005, 1992–2001, and 2006, respectively. Although Bartnicki and Fagerli [2008] and Bartnicki et al. [2011] obtained results similar to those in this study, HELCOM [2005] and Langner et al. [2009] estimated deposition rates that were considerably higher and similar to those of the North Sea.

One reason for lower nitrogen deposition in this study compared to other ones might be that the nitrogen deposition in other months was considerably higher. Additionally, interannual variation in the meteorological conditions and nitrogen emissions might have contributed to the low results in this study. The nitrogen deposition might be generally underestimated in the model setup because of the underestimation in the wet deposition. However, it is not known whether the dry deposition compensates the latter underestimation. The nitrogen deposition along the coastline is considerably higher than at the open ocean (see Fig. 3.9) which is caused by the coincidence of marine coarse sea salt particles and nitrogen species emitted on the land. Thus, the procedure of dividing the nitrogen deposition between deposition into water and deposition onto land in coastal regions might lead to differences in the stated nitrogen deposition.

The surf zone sea salt emissions do affect nitrogen deposition in coastal regions, but the effect is very small (Fig. 3.9). The impact of the surf zone emissions on the nitrogen deposition into the entire North Sea and Baltic Sea is negligible (Table 3.6).

In general, sea salt particles considerably increase the nitrogen deposition in coastal regions and, particularly, in Denmark. Additionally, the nitrogen deposition above the open ocean is affected. The Po Valley nitrogen deposition is nearly unaffected by sea salt emissions because the sea salt concentrations are very low in this region due to its geographic location.

The impact of sea salt emissions on the nitrogen deposition into the Baltic Sea is generally small. Because the full and base case lead to quite similar nitrogen depositions, we assume that the low impact is not caused by the salinity-scaled sea salt emissions and is instead due to low nitrogen emissions upwind of the Baltic Sea. However, a comparison of the zero, base, and full cases indicates that sea-salt-induced nitrogen deposition would be twice as high if no salinity scaling was applied.

The salinity scaling (base vs. full) is not relevant for nitrogen deposition into the North Sea. However, sea-salt-induced nitrogen deposition is higher than in the Baltic Sea region. During winter, $\approx$ 7 % is induced by sea salt. Unfortunately, we are not aware of comparable studies on the impact of sea salt particles on nitrogen deposition into the North Sea.

3.5 Conclusions

Measured sea salt concentrations are fairly well represented in the given model setup. Commonly, sea salt peak concentrations are overestimated. The current parameterization might overestimate sea salt emissions under strong wind conditions during the winter. This overestimation should be evaluated in future studies. A few peak concentrations are underestimated, indicating that one or more sea salt particle generation processes are not considered in the current sea salt emission parameterizations. These parameterizations should be tested with alternative sea salt emission source functions to determine whether these alternatives provide better predictions in these situations. However, the underestimated peak concentrations may be due to differences between the modeled meteorology and the real-world meteorology, as well. The evaluation of the Zingst, Utö, and Virolahti II data in Fig. 3.5 and Table 3.2 clearly shows that salinity-dependent scaling of sea salt emissions is important in marginal seas with salinities that differ from 35 ‰.

Surf zone emissions do not generally improve or deteriorate estimated sea salt concentrations in the presented model setup. Their effect on sNH_4, sNO_3, and NO_3^- on its own is negligible. At a finer grid resolution, however, the impact of surf zone emissions might be relevant due to a relatively higher surf zone fraction. The concentrations of sNH_4 and sNO_3 increased when

sea salt emissions were deactivated, although the effect is small. In contrast, the MNBs for the NO_3^- time series decreased except at inland stations during winter where the MNBs increased. However, NO_3^- peak concentrations in the absence of sea salt emissions often exceeded the peak concentrations in the presence of sea salt emissions, which contradicts the MNB values. Im [2013], Liu et al. [2015] and Kelly et al. [2014] found that sea salt had a strong negative impact on nitrate, which agrees with the summer MNB results but disagrees with the winter results at inland stations and with peak concentrations. We assume that this difference is due to different emission and air pollution regimes, especially with respect to NH_3 emissions. In one 10-day episode in late July, sNH_4 concentrations were considerably underestimated by the model. The reason for this is unclear. However, this underestimation is not related to sea salt particles.

Surf zone sea salt emissions have a negligible effect on the nitrogen deposition. However, sea salt emissions in general have a relevant impact on nitrogen deposition in some regions, and this impact varies intra-annually. Therefore, sea salt emissions need to be considered in nitrogen deposition studies. The literature values on the modeled total nitrogen deposition into the North Sea are up to a factor of 2 as high as the nitrogen deposition in this study. The nitrogen wet deposition is underestimated in this study's model setup which might lead to an underestimation of the total nitrogen deposition. However, it is unknown how accurate the model predicts the nitrogen dry deposition and whether the model tends to over- or underestimate the dry deposition.

For an improved validation, it would be favorable to have individual measurements of NO_3^-, HNO_3, NH_4^+, and NH_3 available. Data from both coastal and inland stations are needed to evaluate whether either the emission parameterization or modeled atmospheric transport processes lead to observed discrepancies. Size-resolved sea salt measurements would be of high value for this process. Finally, more experimental work is needed to determine parameterizations for surf zone emissions.

Acknowledgements

Beate Geyer provided COSMO-CLM meteorology data which can be accessed via the Climate and Environmental Retrieval and Archive (CERA) of the German Climate Computing Centre (DKRZ). Salinity data were extracted from ECOSMO simulations by Corinna Schrum. We thank Anna Backes, Matthias Karl, and Markus Schultze from our institute of discussions on the model results. Additionally, Anna Backes provided GIS-related data for this study. Uma Shankar, James Kelly, and Brett Gantt (U.S. EPA) provided very detailed answer to questions about the inline sea salt emissions of CMAQ. A general thanks goes out to the U.S. EPA and the CMAQ development team for providing this high-quality chemistry transport model as an open-source product. The EMEP measurement data were extracted from the EBAS database which is maintained and further developed by the Norwegian Institute for Air Research (NILU). Statistical evaluation and most plotting were performed using R. The remaining plots were created with the Generic Mapping Tools (GMT) developed and maintained by Paul Wessel, Walter H. F. Smith, Remko Scharroo, Joaquim Luis, and Florian Wobbe. The simulation data were processed with the Climate Data Operators (cdo) by Uwe Schultz-Weider from the Max Planck Institute for Meteorology and with the netCDF Operators (NCO) by Charlie Zender and Henry Butowsky. Parts of the study were funded by the project "Measurements of shipping emissions in the marine troposphere" (MeSMarT) of the German Federal Maritime and Hydrographic Agency (Bundesamt für Seeschifffahrt und Hydrographie).
The article processing charges for this open-access publication were covered by a Research Centre of the Helmholtz Association.

Edited by: M. C. Facchini

3.6 Addon: Nitrogen Dioxide Concentrations

The atmospheric sNO_3 concentrations (NO_3^-+HNO_3) are underestimated in the CMAQ simulations presented in Sect. 3.3.2. HNO_3 is a produced from atmospheric NO_2 (Sect. 2.1.1). Too slow NO_2-HNO_3 conversion or too low NO_2 concentrations might be reasons for underestimated HNO_3 concentrations. As Table 3.8 clearly displays, the NO_2 concentrations are underestimated by the model at most stations during both seasons.

Table 3.8: Similar to Table 3.2 but showing NO_2 concentrations. Two sea salt emission cases – base and zero – are considered.

NO_2		Winter 2008				Summer 2008			
Station	Case	n	RAE	MNB	R	n	RAE	MNB	R
Westerland	base	51	2.41	-0.41	0.71	59	1.48	-0.76	0.66
DE0001R	zero	51	2.40	-0.40	0.70	59	1.48	-0.76	0.66
Waldhof	base	57	1.83	-0.08	0.61	61	1.02	-0.54	0.62
DE0002R	zero	57	1.83	-0.08	0.61	61	1.02	-0.54	0.62
Neuglobsow	base	58	1.44	0.23	0.59	61	0.81	-0.53	0.56
DE0007R	zero	58	1.44	0.24	0.58	61	0.81	-0.53	0.56
Zingst	base	55	1.13	-0.13	0.68	61	1.10	-0.60	0.53
DE0009R	zero	55	1.13	-0.13	0.68	61	1.10	-0.60	0.52
Keldsnor	base	59	1.31	-0.14	0.79	53	1.19	-0.44	0.45
DK0005R	zero	59	1.31	-0.13	0.79	53	1.18	-0.44	0.44
Anholt	base	60	0.95	-0.20	0.76	61	0.90	-0.63	0.61
DK0008R	zero	60	0.95	-0.20	0.76	61	0.90	-0.63	0.62
Utö	base	60	1.02	-0.52	0.69	46	0.59	-0.75	0.04
FI0009R	zero	60	1.02	-0.52	0.69	46	0.59	-0.75	0.04
Virolahti II	base	60	0.84	-0.16	0.48	61	0.42	-0.53	0.40
FI0017R	zero	60	0.84	-0.16	0.49	61	0.42	-0.53	0.40
Birkenes	base	60	0.36	1.19	0.77	61	0.16	0.23	0.30
NO0001R	zero	60	0.36	1.20	0.77	61	0.16	0.23	0.31
Hurdal	base	60	2.29	2.72	0.59	59	0.84	3.79	0.32
NO0056R	zero	60	2.29	2.72	0.59	59	0.83	3.79	0.32
Jarczew	base	56	1.37	-0.12	0.66	59	2.43	-0.81	0.28
PL0002R	zero	56	1.37	-0.12	0.66	59	2.43	-0.81	0.27
Leba	base	60	0.75	-0.25	0.84	61	0.85	-0.74	0.03
PL0004R	zero	60	0.74	-0.25	0.83	61	0.85	-0.73	0.03
Råö	base	60	0.88	-0.28	0.68	61	0.44	-0.42	0.44
SE0014R	zero	60	0.87	-0.28	0.67	61	0.43	-0.42	0.44

4 A comparison of sea salt emission parameterizations in Northwestern Europe using a chemistry transport model setup

Daniel Neumann[1], **Volker Matthias**[1], **Johannes Bieser**[1,2], **Armin Aulinger**[1], **and Markus Quante**[1]

[1] Helmholtz-Zentrum Geesthacht, Institute of Coastal Research, Max-Planck-Straße 1, 21502 Geesthacht, Germany
[2] Deutsches Zentrum für Luft- und Raumfahrt (DLR), Institute of Atmospheric Physics, Oberpfaffenhofen, 82234 Weßling, Germany

Published in Atmos. Chem. Phys. Discuss., doi: 10.5194/acp-2015-946
Received: 22 Nov. 2015 – Accepted: 22 Feb 2016 – Published: 23 Feb. 2016
Revised version published in Atmos. Chem. Phys. (not included here), doi: 10.5194/acp-16-9905-2016

Abstract

Atmospheric sea salt particles affect chemical and physical processes in the atmosphere. They provide surface area for condensation and reaction of nitrogen, sulfur, and organic species and are a vehicle of transport for these species. Additionally, HCl is released from sea salt. Hence, sea salt has a relevant impact on air quality, particularly in coastal regions with high anthropogenic emissions such as in the North Sea region. Therefore, the integration of sea salt emissions in modeling studies in these regions is necessary. However, it was found that sea salt concentrations are not represented with necessary accuracy in some situations.

In this study, three sea salt emission parameterizations depending on different combinations of wind speed, salinity, sea surface temperature, and wave data were implemented and compared: GO03 [Gong, 2003], SP13 [Spada et al., 2013], and OV14 [Ovadnevaite et al., 2014]. The aim is to improve modeled atmospheric sea salt concentrations by identifying the parameterization that predicts the sea salt PM_{10} mass concentrations at different distances to the source regions most accurately and that represents atmospheric sea salt particle size distributions most appropriately in the region under consideration.

While the GO03 emissions yielded overestimations in the PM_{10} concentrations at coastal stations and underestimations of those at inland stations, OV14 emissions, vice versa, led to underestimations at coastal stations and overestimations at inland stations. Because of differently shaped particle size distributions of the GO03 and OV14 emission cases, the deposition velocity of the coarse particles differs between both cases which yields this distinct behavior at inland and coast stations. PM_{10} concentrations produced by the SP13 emissions generally overestimated measured concentrations. With respect to the size distribution, OV14 produced most accurate coarse particle concentrations, whereas GO03 produced most accurate fine particle concentrations. Overall, GO03 and OV14 produced most accurate results, but both parameterizations still reveal weaknesses in some situations.

4.1 Introduction

Sea salt particles affect atmospheric chemistry [Seinfeld and Pandis, 2006a, Chap. 10] and cloud formation. They are emitted as water droplets from the sea surface as a result of strong wind,

the breaking of waves and the bursting of air bubbles. The parameterization of sea salt emissions has a long history [e.g., Blanchard and Woodcock, 1980; Fairall et al., 1983; Monahan and Muircheartaigh, 1980] because such parameterizations are necessary in chemistry transport models (CTMs) and climate models because of their impact on atmospheric processes. However, as shown by Gantt et al. [2015], Im [2013], and Neumann et al. [2016], sea salt concentrations are still not satisfactorily reproduced by CTMs in all situations; thus, improvements to sea salt emission parameterizations are necessary. Extensive reviews of sea salt emissions and emission parameterizations have been published in recent years [Lewis and Schwartz, 2004; de Leeuw et al., 2011; O'Dowd and de Leeuw, 2007; Spada et al., 2013].

Sea salt particle generated by the bursting of bubbles are the most relevant for atmospheric chemistry because they are smaller than sea salt particles produced by other processes and, thus, they have the longest atmospheric lifetime: Air is entrained into the sea water by the breaking of waves, which is primarily wind driven, and forms air bubbles, which then rise to the surface where they burst [Monahan et al., 1986]. Organic surfactants at the surface, the sea surface temperature (SST) and the sea surface salinity (SAL) affect these processes [Mårtensson et al., 2003; Salter et al., 2015; Blanchard, 1964; Donaldson et al., 2006]. A large number of parameterizations relating sea salt emissions to wind speed and other parameters have been published in recent decades. Several were derived from a wind-speed-based parameterization published by Monahan and Muircheartaigh [1980] and Monahan et al. [1986]. Nevertheless, atmospheric sea salt concentrations are not always predicted with sufficient accuracy [Tsyro et al., 2011; Spada et al., 2013; Neumann et al., 2016], and improving these predictions remains an objective of ongoing research [Ovadnevaite et al., 2014; Gantt et al., 2015; Petelski et al., 2014; Salter et al., 2015; Long et al., 2011].

Sea salt particles provide a surface for the condensation of gaseous atmospheric species and for heterogeneous reactions. The dry deposition velocity of particles is dependent on size and differs from the dry deposition velocities of gases. Thus, the condensation of pollutants, such as nitric acid (HNO_3), sulfuric acid (H_2SO_4) and ammonia (NH_3), onto sea salt affects their atmospheric lifetimes and deposition patterns. The latter are important for quantifying the input of pollutants and nutrients into water bodies, e.g., for studying eutrophication. The condensation of strong acids (e.g., H_2SO_4 and HNO_3) onto sea salt particles reduces the pH of the particles, leading to the release of sea salt chloride (Cl^-) as hydrochloric acid (HCl) into the atmosphere. This HCl affects the ozone chemistry in polluted marine air by the release of Cl radicals through oxidation by OH radicals [Cai et al., 2008; Crisp et al., 2014; Knipping and Dabdub, 2003]. The relevance of this process depends on the availability of atmospheric bases (e.g., NH_3), which increase the pH of the aerosols.

The North and Baltic Sea regions are areas of high anthropogenic activity giving rise to the emission of various air pollutants such as NO_x, SO_2, NH_3 and primary particulate matter, which lead to the formation of HNO_3, H_2SO_4 and secondary particulate matter. Sea salt plays an important role in affecting the deposition and heterogeneous chemistry of relevant pollutants in this air pollution regime. Thus, when modeling air pollution in Northwestern Europe, sea salt emissions must be adequately parameterized.

Therefore, the purpose of this study is to improve the modeling of atmospheric sea salt concentrations in Northwestern Europe by evaluating various open-ocean sea salt emission parameterizations. This is done by comparing three different sea salt emission parameterizations [Gong, 2003; Spada et al., 2013; Ovadnevaite et al., 2014] with each other and with measurements from stations within the network of the European Monitoring and Evaluation Programme (EMEP). Gong [2003], which describes sea salt emissions by bubble bursting, is a widely used parameterization depending only on the wind speed. Spada et al. [2013] compared several parameterizations from which MA03/MO86/SM93 is used here. This parameterization depends on wind speed and SST. In addition to Gong [2003], Spada et al. [2013] describes the emission of spume droplets for high wind speeds: Ovadnevaite et al. [2014] is a quite new parameterization that depends on

wind speed, SST, salinity (SAL), and wave data and that should cover all sea salt production processes. It was not used in a CTM setup in the study region up till now. For this study, the parameterizations of Gong [2003] and Spada et al. [2013] were extended to depend on salinity.

There have been a few recent studies on sea salt in the Northwestern European region. Manders et al. [2010] evaluated sea salt measurements from various EMEP stations. Other studies addressed data from Mace Head [Cavalli et al., 2004; Ovadnevaite et al., 2014]. Tsyro et al. [2011] compared five open ocean sea salt emission parameterizations, which depended on the wind speed only, in Europe. In this study comparing three sea salt emission parameterizations, the impact of SAL on sea salt particles generation as well as the contribution of surf zone emissions are considered. Additionally, with the employment of the parameterization of Ovadnevaite et al. [2014], an explicitly wave-dependent function is considered in this study.

4.2 Materials and Methods

4.2.1 Chemistry Transport Model

The simulations were performed using the Community Multiscale Air Quality (CMAQ) modeling system, which is developed and maintained by the U.S. EPA. Version 5.0.1 was used in this study. The study region was enclosed by a grid with dimensions of $24 \times 24\,\mathrm{km}^2$, which was one-way nested in a coarse grid with dimensions of $72 \times 72\,\mathrm{km}^2$ (Fig. 4.1). The outer boundary conditions were taken from TM5 model runs [Huijnen et al., 2010]. The cb05tucl mechanism [Yarwood et al., 2005; Whitten et al., 2010; Tanaka et al., 2003; Sarwar et al., 2007] was used to represent the gas-phase chemistry, and the AERO5 mechanism [Nenes et al., 1998, 1999] was used to represent the particle-phase chemistry. CMAQ also includes in-cloud chemistry.

The aerosol phase is represented by three log-normally distributed modes: the Aitken, accumulation and coarse modes. Each size mode is represented by three moments (3-moment scheme): the total particle number (0th moment), the total particle surface area (2π of the 2nd moment), and the total particle mass ($\frac{4}{3}\pi \times \rho_{ss}$ of the 3rd moment; ρ_{ss} = sea salt dry density). The total mass is split into speciated mass fractions, but the total number and surface area emissions are not. The standard deviation and geometric mean diameter (GMD) of each size

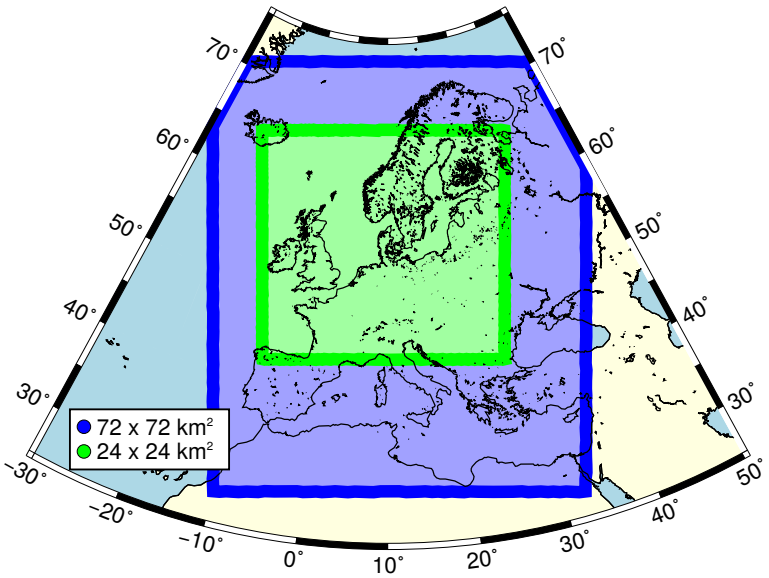

Figure 4.1: Study region and size of the model grids. The coarse grid (blue) includes Europe and parts of northern Africa. The first nested grid (green) includes Northwestern Europe, including the North and Baltic Seas.

mode are not fixed but rather are calculated from the moments when necessary. Binkowski and Roselle [2003] and the CMAQ Wiki (`www.airqualitymodeling.org/cmaqwiki`) describe the CMAQ aerosol mechanism in greater detail.

4.2.2 Sea Salt Emissions

In this section, sea salt emissions are described from three perspectives: (1) the physical processes related to sea salt emissions, (2) the sea salt emission parameterizations compared in this study, and (3) the technical implementation of the sea salt emission parameterizations for CMAQ.

Physical Processes

Water droplets are emitted from the sea surface by the bursting of bubbles (film and jet droplets), by the breaking of waves (splash droplets) and by high wind speeds (spume droplets). The droplet water evaporates until the droplet water content is in equilibrium with the ambient relative humidity. This droplet is denoted as wet sea salt particles.

When air is mixed into sea water by processes such as the breaking of waves, the air forms bubbles, which then rise to the sea surface where they burst. Small water droplets are ejected from the breaking hull of a bubble (film droplets). Because of the abrupt change in pressure within the bursting bubble, water is also sucked from below the bubble into the air (jet droplets). The bursting of bubbles is the most relevant process for sea salt particle production. An increase in wind speed increases wave generation, wave breaking, and, consequently, bubble-bursting-generated sea salt emissions. Sea salt particles from spume and splash droplets are very large and commonly fall back into the ocean within a short time after their emission. They are only relevant at high wind speeds [Lewis and Schwartz, 2004]. The SST affects the formation and bursting of air bubbles [Mårtensson et al., 2003; Callaghan et al., 2014; Grythe et al., 2014], thereby altering the size distribution of the sea salt particles thus produced. Changing the SAL also alters the particle size - a lower salinity leads to smaller particles [Mårtensson et al., 2003]. Moreover, organic species are relevant to sea salt emissions, but their actual impact has not yet been well quantified.

In the surf zone, which is the region along a coast line where waves break, sea salt emissions are enhanced because of the higher number of breaking waves in this relatively small region. Addressing surf zone emissions is quite difficult because they depend on the direction of the waves, the direction of the wind, and local coastal features such as steep cliff coasts and flat beaches.

Sea Salt Emission Parameterizations

The existing sea salt emission parameterizations and their historical development have been extensively described and compared in Lewis and Schwartz [2004], O'Dowd and de Leeuw [2007], de Leeuw et al. [2011], Tsyro et al. [2011], and Spada et al. [2013].

Three parameterizations, developed by Gong [2003], Spada et al. [2013], and Ovadnevaite et al. [2014], and a reference case without any sea salt emissions are compared in this study. They are abbreviated as GO03, SP13, OV14, and zero, respectively. GO03 is the standard parameterization in CMAQ [Kelly et al., 2010]. SP13 consists of three existing parameterizations proposed by Mårtensson et al. [2003] (MA03), Monahan et al. [1986] (MO86), and Smith et al. [1993] (SM93). Table 4.1 presents an overview of these parameterizations. Relevant aspects thereof are described below. They are plotted in Fig. 4.2 and their formulas are provided in the Appendix (Eqs. (C.1) to (C.7)). A more detailed description of the formulas and of their implementation are provided in the Sect. D.1.

All three parameterizations describe the size distribution of sea salt particle emissions in terms of number. For their implementation in CMAQ, log-normal distributions are preferred. GO03

Table 4.1: Overview of sea salt emission parameterizations GO03, SP13, and OV14.

Parameterization	Functional Relation	Wind Dependence	Surf Zone	Parameters	Range of Validity	Reference
GO03	two log-normal distributions	MO80	KE10	u_{10}, SAL[a]	$0.07\,\mu m \leq D_{dry} \leq 20\,\mu m$	Gong [2003]
SP13	mixed	mixed	mixed	u_{10}, SST, SAL[a]	$0.02\,\mu m \leq D_{dry} \leq 30\,\mu m$	Spada et al. [2013]
MA03	three polynomials	MO80	KE10	u_{10}, SST, SAL[a]	$0.02\,\mu m \leq D_{dry} \leq 2.8\,\mu m$	Mårtensson et al. [2003]
MO86	special function	MO80	KE10	u_{10}, SAL[a]	$2.8\,\mu m \leq D_{dry} \leq 8\,\mu m$ [b]	Monahan et al. [1986]
SM93	two log-normal distributions	own: wind	no	u_{10}, SAL[a]	$2.8\,\mu m \leq D_{dry} \leq 30\,\mu m$ and $u_{10} \geq 9\,m\,s^{-1}$	Smith et al. [1993]
OV14	five log-normal distributions	own: wind and waves	no	u_{10}, H_s, u_* SAL, SST	$0.015\,\mu m \leq D_{dry} \leq 6\,\mu m$ $Re_{Hw} \geq 10 \times 10^5$ [c]	Ovadnevaite et al. [2014]

[a] Originally, the parameterization does not depend on the SAL. The SAL dependence was added in this study.

[b] MO86 is valid on the size range $2.8\,\mu m \leq D_{dry} \leq 8\,\mu m$ if it is not used in this context.

[c] The fifth mode is only valid for $Re_{Hw} \geq 2 \times 10^5$.Abbreviations: MO80 refers to Monahan and Muircheartaigh [1980], KE10 refers to Kelly et al. [2010], $u_{10} = 10\,m$ wind speed, SAL = sea surface salinity, SST = sea surface temperature, H_s = significant wave height, u_* = friction velocity at sea surface, D_{dry} = dry sea salt particle diameter.

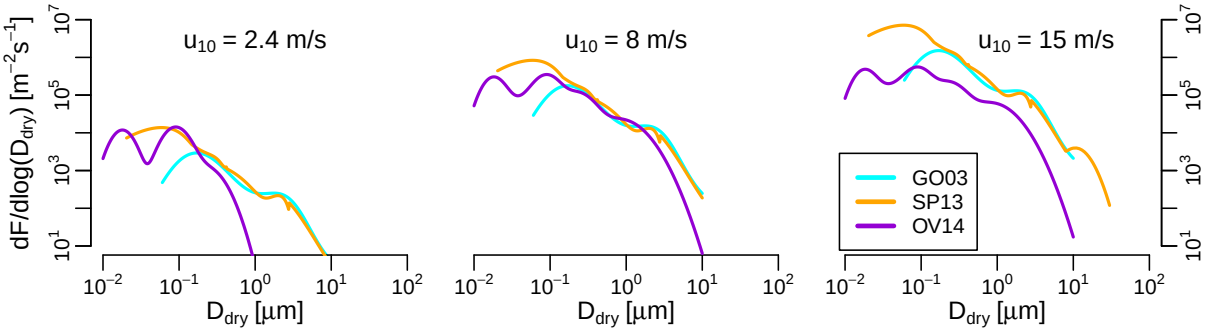

Figure 4.2: Comparison of the source functions and their wind speed dependence. The largest size mode of OV14 is deactivated for $\mathrm{Re_{Hw}} \leq 2 \times 10^5$, and all modes are deactivated for $\mathrm{Re_{Hw}} \leq 1 \times 10^5$ (see Eq. (C.7) for the definition of $\mathrm{Re_{Hw}}$). In SP13, a spume-droplet-generated mode represented by SM93 is activated for $u_{10} \geq 9\,\mathrm{m\,s^{-1}}$. The parameters used were as follows: SST = 283 K, SAL =35 ‰, $C_D = 2.15 \times 10^{-3}$, H_s = 1.23 m, and $\nu_W = 1.34 \times 10^{-6}\,\mathrm{m^2\,s^{-1}}$

represented by two log-normal distributions, in CMAQ, and describes the bubble-generated production of sea salt particles. SP13 consists of a combination of different types of functions and cannot be simply represented using log-normal distributions. It describes the production of sea salt particles generated by bursting bubbles (MA03 and MO86) and spume droplets (SM93). Spume droplet production is activated at wind speeds above $9\,\mathrm{m\,s^{-1}}$ [Monahan et al., 1986]. MA03 is based on laboratory studies. Finally, OV14 is a linear combination of five log-normal distributions. It describes bubble-bursting- and spume-droplet-generated sea salt emissions and is based on measurements recorded at Mace Head, Ireland.

The wind speed dependence (Fig. 4.2) of GO03 and SP13 (MA03 and MO86) is described by the whitecap coverage parameterization proposed by Monahan and Muircheartaigh [1980]. It relates the 10 m wind speed, u_{10} $\left[\mathrm{m\,s^{-1}}\right]$, to the fraction of the sea surface covered by whitecaps, denoted by the whitecap coverage (W). Bubble bursting and, consequently, sea salt production depend linearly on the whitecap coverage. W (Eq. (4.1)) scales the distribution functions but does not alter their shape. OV14 employs another wind speed dependence. Each of the five modes is scaled by an individual power-law function depending on a Reynolds number, $\mathrm{Re_{Hw}}$, which is calculated from the friction velocity at the sea surface, u_* $\left[\mathrm{m\,s^{-1}}\right]$; the significant wave height, H_s [m]; and the sea water kinetic viscosity, ν_W $\left[\mathrm{m^2\,s^{-1}}\right]$. The parameter u_* is calculated from u_{10} and a wave drag coefficient, C_D. The parameter ν_W depends on the SST and SAL and is calculated in accordance with Eqs. (8) and (22) in Sharqawy et al. [2010].

$$W = 3.84 \times 10^{-6} \times u_{10}^{3.41} \tag{4.1}$$

In the surf zone, the sea salt particle number flux is considerably enhanced compared with that in the open ocean. Kelly et al. [2010] proposed the approach to addressing surf zone emissions that is used in CMAQ, namely, the whitecap coverage W is set to 1 in the surf zone which is assumed to have a width of 50 m. CMAQ simulations of parts of Florida performed well with this definition of the surf zone [Kelly, 2014].

Technical Implementation

The aerosol particles in CMAQ are represented by particle number, surface area, and mass concentrations (see Sect. 4.2.1). Therefore, the total particle number, surface area, and mass emissions per size mode must be provided in CMAQ. However, non-sea-salt-particle emissions are read in only as total mass emissions via external input files. These mass emissions are split into the three size modes using pre-defined splitting factors. The number and surface area

emissions are calculated on the basis of standardized geometric mean diameters (GMDs) and standard deviations for each mode. By contrast, for sea salt emissions in the standard CMAQ setup, all three values are calculated online in the sea salt emission module based on Gong [2003]. The parameterization is fitted to two log-normal distributions (Fig. 4.3), with the GMD, the standard deviation, and the 0th and 3rd moments being prescribed in the sea salt emission module of CMAQ. The number, surface area, and mass emissions are calculated from these prescribed parameters. One of the distributions represents the accumulation mode, and the other represents the coarse mode. For the GO03 emission case, this portion of the implementation was left unchanged. By contrast, the SP13 and OV14 emissions (number, surface area, and mass) were calculated externally and read by CMAQ at run time.

Because OV14 consists of five log-normally distributed modes, the two finest size modes were assigned to the Aitken mode in CMAQ, the third and fourth finest size modes were assigned to the accumulation mode, and the largest size mode was assigned to the coarse mode. Because SP13 is not based on log-normally distributed modes, it was integrated within fixed boundaries to split it into the Aitken, accumulation, and coarse modes. The boundary between the Aitken and accumulation modes was set to $D_{\mathrm{dry}} = 0.1\,\mu\mathrm{m}$, and the boundary between the accumulation and coarse modes was set to the intersection between the accumulation and coarse modes for GO03 ($D_{\mathrm{dry}} \approx 1.5\,\mu\mathrm{m}$), which depends somewhat on the relative humidity (see Sect. D.4.1 in the Appendix).

The SAL in the Baltic Sea is very low - below 10 ‰ throughout large regions - which requires the inclusion of an SAL dependence in the sea salt emission calculation. For GO03, the approach described in Neumann et al. [2016] was applied: number, surface area, and mass emissions were multiplied by $\frac{\mathrm{SAL}}{35\,‰}$. OV14 already includes salinity as a parameter. For SP13, we added an SAL dependence based on plots published by Mårtensson et al. [2003]: the size of the emitted sea salt particles was scaled by $\left(\frac{\mathrm{SAL}}{35\,‰}\right)^{1/3}$. Graphically, the number emission distribution (Fig. 4.3 center and Fig. 4.2 orange line) shifts to the left as the SAL decreases (Fig. D.1). The Aitken/accumulation and accumulation/coarse mode integration boundaries were held constant, leading to a decrease in the coarse-mode number emissions with a decreasing SAL. Detailed information on the salinity dependence is provided in the Appendix (Sect. D.3). The surf zone is treated differently in the three parameterizations. In CMAQ (GO03), the surf zone is treated in accordance with Kelly et al. [2010] by setting the whitecap coverage W is set to 1 in the surf zone. In this study, calculations of the surf zone size were performed for a 50 m wide surf zone by ArcGIS avoiding double-counting of overlapping surf zone stripes [Neumann et al., 2016]. The procedure of setting W to 1 can also be applied for SP13 because MA03 and MO86 depend on the same whitecap coverage parameterization as does GO03 (see Sect. D.2). However, the

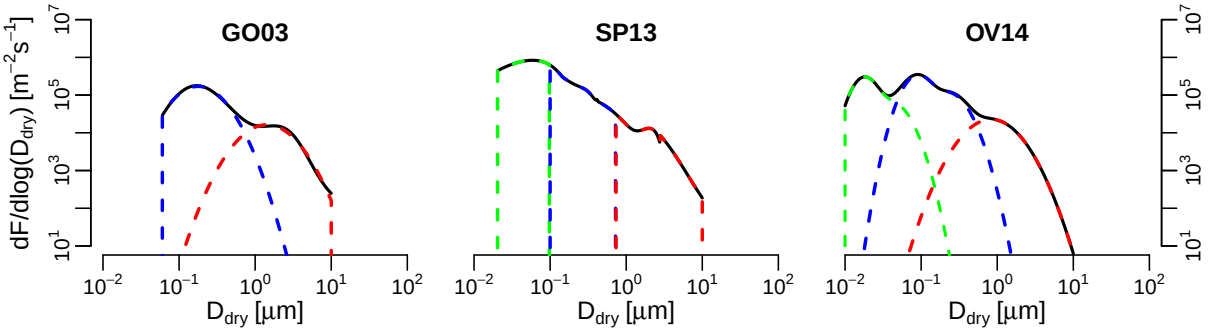

Figure 4.3: Modal splitting of the sea salt emission parameterizations GO03 (left), SP13 (center), and OV14 (right). The color indicates the size mode in which the sea salt is emitted: green corresponds to the Aitken mode, blue to the accumulation mode and red to the coarse mode.

SM93 coarse emissions remain unchanged. This approach cannot be applied to OV14 without modification because the wind speed dependence of OV14 is not based on the whitecap coverage approach. Therefore, no surf zone treatment for OV14 was introduced. The total emitted sea salt mass was split into 7.6 % SO_4^{2-}, 53.9 % Cl^-, and 38.6 % Na^+ [Kelly et al., 2010]. The Na^+ in the model includes Na^+, Mg^{2+}, K^+, and Ca^{2+}; only 78 % of the Na^+ in the model is true Na^+. This split was applied for all three parameterizations. In addition to dry sea salt, water is also emitted. For GO03, the water content was calculated according to Zhang et al. [2005], and for SP13 and OV14, it was calculated according to Lewis and Schwartz [2006]. Both relations are based on data from Tang et al. [1997]. The new sea salt emissions were calculated externally and read at run time by CMAQ. The CMAQ sea salt emission module (SSEMIS.F) was modified for this purpose. In the modified version, sea salt emissions can be calculated internally or read in from an external source. Currently, no Aitken-mode sea salt particles are considered in standard CMAQ. The sea salt emission and aerosol emission modules (AERO_EMIS .F) were modified to consider Aitken-mode sea salt emissions in addition to those considered in the standard implementation. The modified CMAQ modules are attached as supplementary material (DVD) and briefly documented in Sect. D.7.

4.2.3 Geophysical Input and Emission Data

The land-based emissions were compiled by SMOKE for Europe [Bieser et al., 2011] with the agricultural emissions in accordance with Backes et al. [2016a,b]. Dust emissions were not included. Shipping emissions were calculated bottom up using ship movement and ship characteristics data [Aulinger et al., 2016].

The meteorological input data were generated by COSMO-CLM (Consortium for Small-scale Modeling in Climate Mode) [Geyer and Rockel, 2013; Geyer, 2014]. The used data set is part of the coastDatII database of the Helmholtz-Zentrum Geesthacht [Weisse et al., 2015] (`www.coastdat.de/`). The coastDatII database also contains modeled data for wave and ocean currents, which are forced by COSMO-CLM meteorology. The model grid spans the entire model domain. The data were remapped onto the CMAQ grid, and relevant variables were extracted

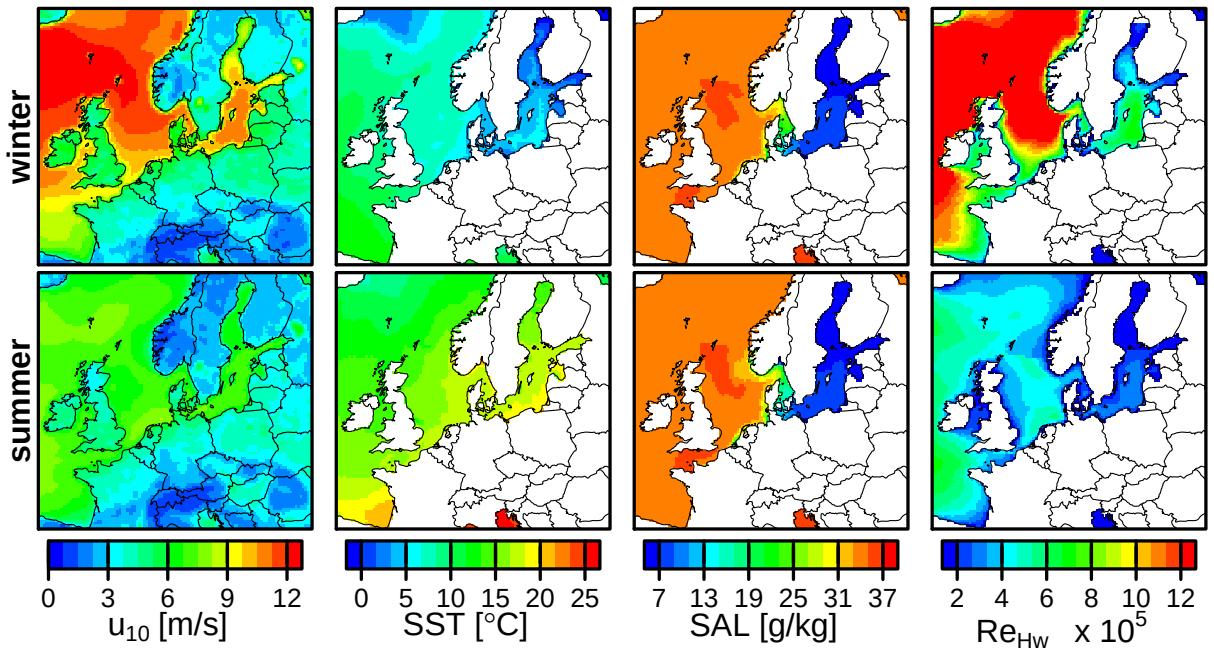

Figure 4.4: Two-month average u_{10}, SST, SAL, and Re_{Hw} data are plotted for winter (top) and summer (bottom). Re_{Hw} was calculated according to Eq. (C.7).

and converted using a modified version of CMAQ's Meteorology-Chemistry Interface Processor (MCIP) [Otte and Pleim, 2010].

Wave data (H_s and u_*), SAL values, and SST values are required for calculating the new sea salt emissions. For the North Sea, H_s and u_* were obtained from the coastDatII database modeled by the Wave Model (WAM) [Groll et al., 2014]. However, Baltic Sea wave data were not available from this database. The significant wave height data for the other seas were acquired from the ERA-Interim wave data set, which was calculated by WAM for a global domain [Dee et al., 2011]. No friction velocity data, u_*, were available from that data set; hence, the values of this quantity were calculated from u_{10} [Wu, 1982] using Eqs. (D.8) and (D.9).

No SAL and SST fields are present in coastDatII. For the North and Baltic Seas, these data were acquired from operational model runs of the German Federal Maritime and Hydrographic Agency (Bundesamt f"r Seeschifffahrt und Hydrographie, BSH) at two different resolutions (see Fig. D.2) produced by their model BSHcmod. For the other seas, ERA-Interim SST data were used. The SAL was set to 35 ‰ in the Atlantic Ocean, 37 ‰ in the Mediterranean Sea, and 18 ‰ in the Black Sea.

A detailed listing of the input data sets (Table D.6) and their spatial extend (Fig. D.2) are given in the Appendix (Sect. D.5).

4.2.4 Model Evaluation

The modeled sodium concentrations were compared with the sodium concentrations measured at 11 EMEP stations. The EMEP data [Tørseth et al., 2012] were obtained from the EBAS database (`ebas.nilu.no/`). The sodium concentration is an accurate representation of the sea salt concentration because sea salt is the major source of atmospheric sodium and sodium does not evaporate into the gas phase. Data from winter (January and February) and summer (July and August) of 2008 were considered.

The stations considered in the comparison are plotted in Fig. 4.5 and listed in Table 4.2. The last column in Table 4.2 indicates whether each station is located on the coast or inland

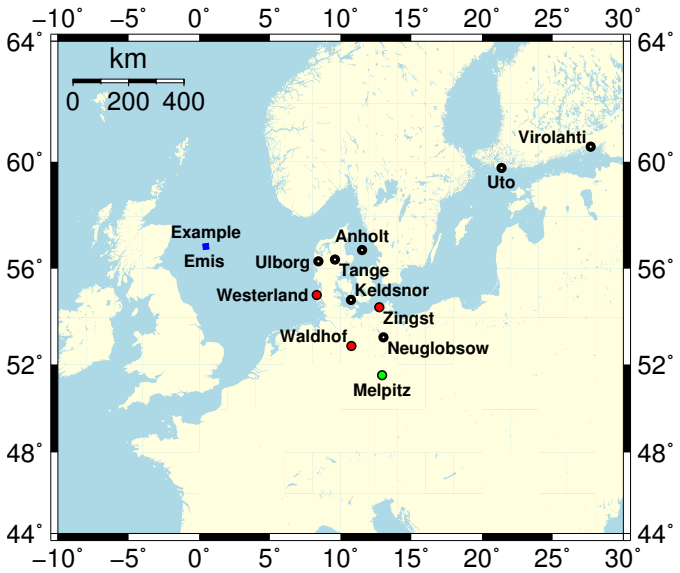

Figure 4.5: Locations of the EMEP stations at which measured and modeled daily average sodium PM_{10} data were compared. Red circles: In addition to statistical data being provided, plots are shown and described in detail. Green circle: An additional comparison of $PM_{2.5}$ data is presented (DE0044R). Blue box: Location of a grid cell which sea salt emissions are presented.

Table 4.2: EMEP stations that were considered for comparison with the modeled data.

Station ID	Station Name	Data	Lon	Lat	Height [m]	Location
DE0001R	Westerland	PM_{10}	8.31	54.93	12	Coast
DE0002R	Waldhof	PM_{10}	10.76	52.80	74	Inland
DE0007R	Neuglobsow	PM_{10}	13.03	53.17	62	Inland
DE0009R	Zingst	PM_{10}	12.73	54.43	1	Coast
DE0044R	Melpitz	PM_{10}, $PM_{2.5}$	12.93	51.53	86	Inland [a]
DK0003R	Tange	PM_{10}	9.60	56.35	13	Inland
DK0005R	Keldsnor	PM_{10}	10.73	54.73	10	Coast
DK0008R	Anholt	PM_{10}	11.52	56.72	40	Coast
DK0031R	Ulborg	PM_{10}	8.43	56.28	10	Coast
FI0009R	Utö	PM_{10}	21.38	59.78	7	Coast
FI0017R	Virolahti II	PM_{10}	27.69	60.53	4	Coast

[a] located far inland but often influenced by coastal air

(more than 50 km distance to the next coast in upwind direction). Daily average PM_{10} measurement data are available at all of the stations. In addition, at Melpitz, $PM_{2.5}$ measurements are available and compared against model data. All stations were compared on the basis of statistical parameters: the residual absolute error (RAE), the mean normalized bias (MNB), and Spearman's correlation coefficient (R). The formulas for the RAE, the MNB, and R are given in the appendix as Eqs. (A.1) to (A.3), respectively. In addition, the data from the Westerland (DE0001R), Waldhof (DE0002R), Zingst (DE0009R) (PM_{10}, each), and Melpitz (PM_{10} and $PM_{2.5}$) stations were compared graphically.

For the comparison of model and measurement data, PM_{10}, $PM_{2.5}$ and PM_C (= PM_{10} - $PM_{2.5}$) data were extracted from the model simulation results. PM_{10} equals the whole modeled particle mass, $PM_{2.5}$ sums the particle mass of each model mode which is below 2.5 µm, and PM_C is the difference between PM_{10} and $PM_{2.5}$. PM_C does not equal the modeled coarse-mode mass and $PM_{2.5}$ does not equal the sum of Aitken- and accumulation-mode mass.

4.3 Results and Discussion

The first part of this section offers a review of the sea salt emissions produced by the parameterizations. The second part presents a review of the resulting atmospheric concentrations. Finally, the section closes with a summary.

4.3.1 Sea Salt Emissions

In this section, sea salt mass (Sect. 4.3.1), surface area (4.3.1), and number emissions (4.3.1) are described and discussed. The particle surface area is the most important of the three parameters because it governs the impact of the sea salt particles on the atmospheric chemistry: a larger surface area yields a stronger condensation of gases onto sea salt. However, this parameter is not measured. By contrast, measurements of the speciated particle mass are standardized and available at several measurement stations. Particle number measurements are more complicated to perform, only available at a few stations and not divided into species but given as bulk number concentration. In order to describe the atmospheric behavior of particle distributions accurately, particle mass, surface area and number data are needed. Therefore, considering all three types of emissions is relevant.

Figure 4.6 shows plots of dry sea salt mass emissions. Plots a to f show two-month average dry mass sea salt emissions in winter (left column) and summer (right column) produced with GO03 (1st row), SP13 (2nd row), and OV14 (3rd row). Figure 4.6 g shows box plots of the sea salt mass emissions split into Aitken, accumulation and coarse modes (left to right) at a location in the German Bight (blue square in Fig. 4.5) that is representative of the open ocean. Figures 4.7

and 4.8 are similar but show sea salt surface area and number emissions, respectively. The time series corresponding to the box plots in the three figures are given in the Appendix (Sect. D.8, Figs. D.3 to D.5).

Sea Salt Mass Emissions

The SP13 sea salt mass emissions are considerably higher than those produced by GO03 and OV14. The winter emissions are higher than the summer emissions because of higher wind speeds. The sea salt mass emissions in the Baltic Sea region are quite low because of the SAL scaling. In addition, the difference in emissions between the North and Baltic Seas is partly caused by differences in wind speed. SP13 emits the most mass per mode, and OV14, the least (Fig. 4.6, a-f). In the coarse and accumulation modes, the GO03 mass emissions lie between those of SP13 and OV14 but closer to the SP13 emissions. The SP13 mass emissions strongly decrease from winter to summer. As indicated in Fig. 4.2, an additional coarse particle mode exists in SP13 for high wind speeds ($u_{10} > 9\,\mathrm{m\,s^{-1}}$). The strong decrease in the SP13 mass emissions in summer originates from a reduced production of spume droplets due to fewer occurrences of threshold exceedance by the wind speed. The coarse-mode mass emissions are considerably higher than those in the accumulation and Aitken modes. Therefore, they dominate the mass

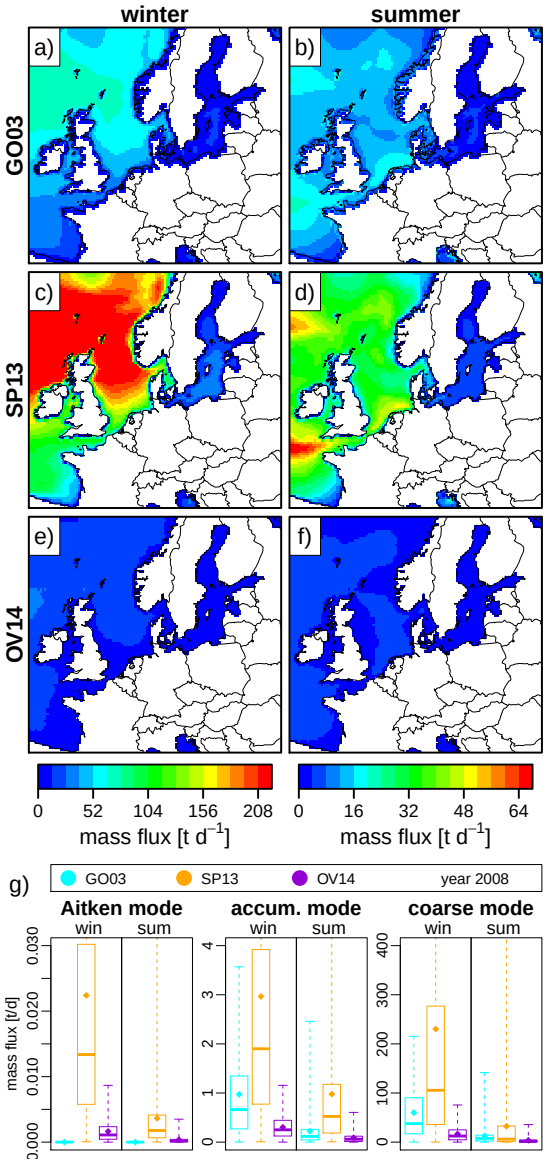

Figure 4.6: Sea salt mass emissions in tons of sea salt per day and grid cell $\left[\mathrm{t\,d^{-1}}\right]$ (total mass of sea salt and not mass of sodium). **a-f**: two-month average mass emissions in winter (left column) and summer (right column). The emissions were calculated using the GO03, SP13, and OV14 (top to bottom) emission parameterizations. The color scale is the same for all plots in the same column. **g**: box plots of mass emissions in the Aitken, accumulation and coarse modes (left to right) at one location in the German Bight (Fig. 4.5) during summer and winter 2008.

emissions depicted in Fig. 4.6 g.

Sea Salt Surface Area Emissions

In Fig. 4.7 a-f, the SP13 dry sea salt particle surface area emissions exceed the GO03 and OV14 emissions. However, the GO03 and OV14 surface area emissions are higher than their mass emissions in relation to the respective SP13 emissions. The surface area emissions are not relevant for the comparisons presented in this study because no measurement data are available. However, they are relevant when considering condensation processes and the formation of NO_3^-, NH_4^+ and SO_4^{2-}. According to Fig. 4.7 g, the coarse-mode surface area emissions of GO03 and SP13 are similar to each other, but those of SP13 are slightly higher. The SP13 accumulation-mode emissions are approximately twice as high as the corresponding GO03 emissions. For all

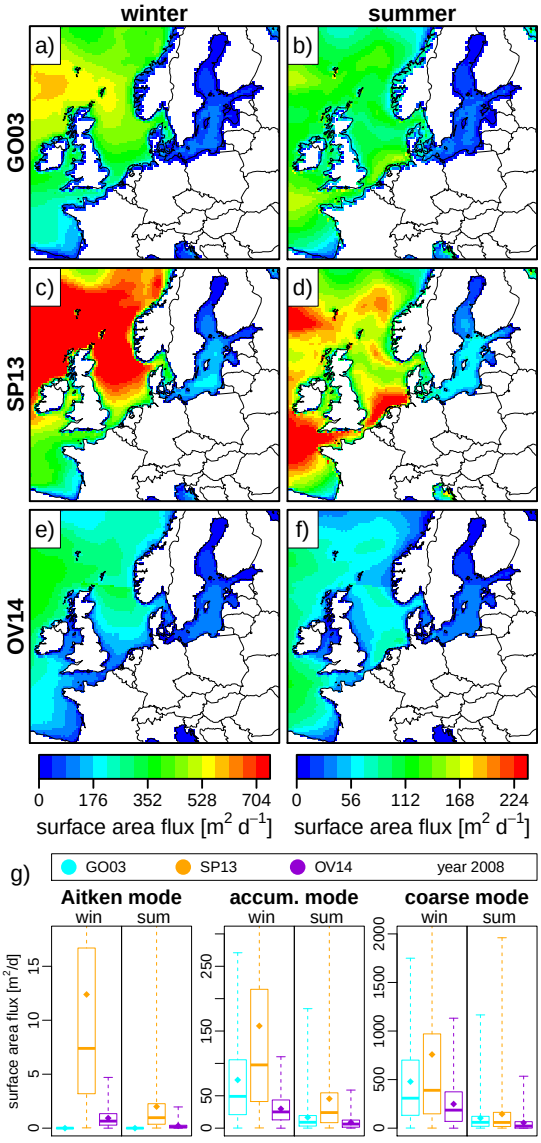

Figure 4.7: Similar to Fig. 4.6 but showing sea salt surface area emissions. **a-f**: two-month average surface area emissions **g**: box plots of surface area emissions.

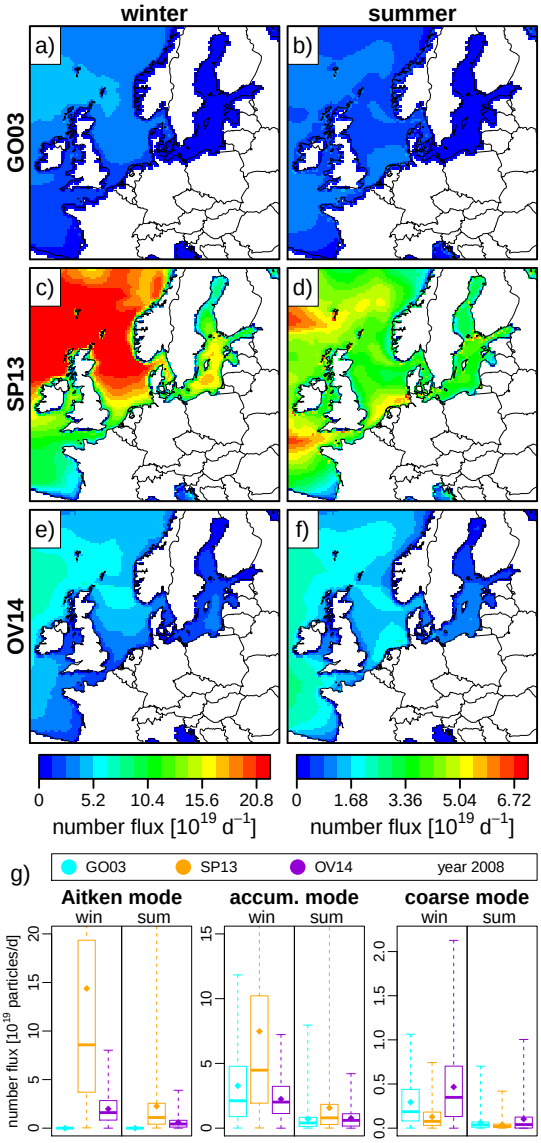

Figure 4.8: Similar to Fig. 4.6 but showing sea salt number emissions. **a-f**: two-month average number emissions **g**: box plots of number emissions.

three parameterizations, OV14 produces the lowest emissions in all three modes. The coarse-mode emissions are four to five times as high as the accumulation-mode emissions and ten to fifty times as high as the Aitken-mode emissions. Hence, the coarse-mode surface area emissions represent the greatest contribution to the total surface area emissions shown in plots a–f.

Sea Salt Number Emissions

The highest total number emissions are calculated using SP13. This is because of the large number of ultra-fine particles on the far left of the distribution in the emission parameterization ($D_{\mathrm{dry}} < 0.1\,\mu\mathrm{m}$), as shown in Fig. 4.2. For the SP13 parameterization, the relative difference between the Baltic Sea and North Sea number emissions is lower than between the Baltic Sea and North Sea mass emissions. This is because the total mass emissions are scaled by SAL/35 ‰ and the total number emissions are scaled by 1. Investigation of the modal emissions reveals that the highest coarse-mode number emissions are produced by the OV14 parameterization, followed by GO03. In the accumulation mode, the SP13 number emissions are higher than the corresponding GO03 and OV14 emissions. In the Aitken mode, the SP13 emissions are considerably higher than the respective OV14 emissions. The total number emissions are dominated by the Aitken and accumulation modes. Therefore, SP13 produces the highest total sea salt number emissions and GO03 the least highest. GO03 would probably yield considerably higher particle numbers than OV14 if GO03 included Aitken mode particles. Because OV14 produces the highest coarse-mode number emissions, one might assume that it also produces the highest coarse-mode surface area and mass emissions. The reason why this is not the case is because the OV14 coarse mode (Fig. 4.3) consists of particles with a smaller diameter than those in the other two source functions, as confirmed by the GMD (Fig. D.6).

4.3.2 Sea Salt Concentrations

PM10 Concentrations

The modeled daily average sodium PM_{10} concentrations were compared with the concentrations measured at 11 EMEP stations. Figure 4.9 shows the sodium concentrations at three German EMEP stations (Westerland, Waldhof and Zingst) in winter and summer. Table 4.3 reports the corresponding statistical data for all 11 stations. These stations include both coastal and inland stations (see Table 4.2), whereas the Melpitz station is located far inland.

At Westerland and Zingst (coastal stations), the SP13 case considerably overestimates the Na^+ concentrations and the OV14 case underestimates them. The winter baseline concentrations at Zingst are somewhat well reproduced by all three parameterizations, whereas the highest values (peaks) are not. GO03 overestimates the peak concentrations at Westerland and Zingst. The correlation coefficients for all three parameterizations are similar to each other at both stations and in both seasons. However, the MNB is closest to 0 for the OV14 case, followed by GO03 and then SP13. The MNB of OV14 is usually negative, whereas it is positive for the other two cases. The RAE is highest for SP13, and the RAEs of GO03 and OV14 are similar. For all coastal stations in Table 4.3, the correlation coefficient decreases from winter to summer, whereas the MNBs and RAEs improve. For Westerland and Zingst, the MNBs and RAEs are highest for SP13. At most coastal stations, the MNBs for the SP13 and GO03 cases are positive and those for the OV14 case are negative. It can be concluded that SP13 and GO03 overestimate the sea salt concentrations at coastal stations, whereas OV14 underestimates them. Based on the MNB and RAE, GO03 and OV14 produce more accurate sodium concentrations than does SP13. The correlation coefficients are quite similar to each other and do not indicate a clear ranking. Notably, at Keldsnor (DK0005R), the correlation coefficients are particularly low.

At Waldhof, which is located approximately 200 km inland, the modeled concentrations are more similar to each other than at the other stations. In winter, SP13 and GO03 overestimate several peak concentrations but the baseline concentrations are well reproduced by all three

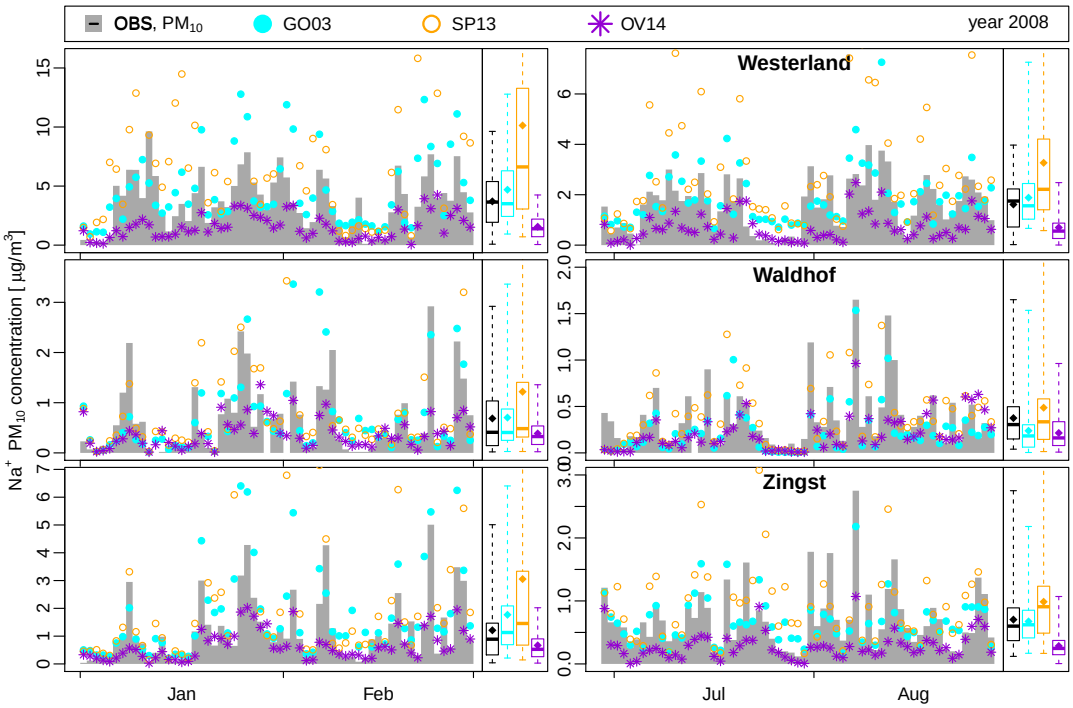

Figure 4.9: Sodium concentrations at three representative EMEP stations (Westerland, Waldhof and Zingst). The black box plot represents the observations. For the box plots of the modeled data, only the daily model values with corresponding measured values are considered.

parameterizations. In summer, GO03 underestimates the baseline concentration and SP13 appears to yield the best reproduction of the observations. Inland stations exhibit high correlation coefficients of between 0.6 and 0.8. The SP13 emissions yield the highest correlation coefficients. However, the difference to the correlation coefficients of the GO03 and OV14 cases is small. The inland MNBs of the GO03 and SP13 cases are smaller than those at the coastal stations, indicating less overestimation of the sodium concentrations at inland stations. For the OV14 case, the MNB is positive in approximately half of the inland cases - particularly during winter - whereas it is typically negative at all coastal stations. Thus, OV14 produces fewer underestimations at inland stations. The RAE is often below 0.5 at inland stations, with the exception of Tange (DK0003R). Commonly, the winter MNB and RAE values are higher than those in summer. The MNBs and RAEs for Tange deviate most strongly from those for the other stations in this group. Tange is the station that is located closest to the coast. At Melpitz, the MNB of OV14 is positive in both winter and summer. In winter, the MNBs of SP13 and GO03 at Melpitz are lower than those at the other stations.

The sodium concentrations at coastal stations, such as Westerland and Zingst, are highest for the SP13 emissions and lowest for the OV14 emissions. For locations farther inland, the SP13 and GO03 concentrations decrease more rapidly than the OV14 concentrations, as indicated by the MNBs. At the far-inland station of Melpitz, the SP13 and OV14 cases yield similar sodium concentrations (MNBs, Table 4.3) that are higher than the GO03 concentrations. In a similar study, Tsyro et al. [2011] also reported slight overestimations at coastal stations and underestimations at inland stations for GO03 sea salt emissions. This indicates that the particle dry deposition velocities for the SP13 and GO03 emission cases are higher than those for OV14 emission case. The different size distributions of the three parameterizations, which are probably responsible for this effect, are described in Sect. 4.3.2.

At the coastal station of Keldsnor (DK0005R), the correlation coefficients are very low. During

Table 4.3: Statistical evaluation for the comparisons between the modeled and measured Na^+ concentrations at 11 EMEP stations in the vicinity of the North and Baltic Seas during winter (left) and summer (right).

Station	Case	winter				summer			
		n	RAE	MNB	R	n	RAE	MNB	R
Westerland	GO03	60	1.89	1.01	0.76	61	0.72	2.37	0.70
DE0001R	SP13	60	6.75	2.22	0.71	61	1.83	3.36	0.73
Coast	OV14	60	2.21	-0.36	0.75	61	1.00	-0.11	0.70
Waldhof	GO03	55	0.42	1.75	0.67	60	0.18	-0.33	0.70
DE0002R	SP13	55	0.75	2.27	0.76	60	0.25	0.36	0.71
Inland	OV14	55	0.39	0.64	0.73	60	0.20	-0.34	0.68
Neuglobsow	GO03	60	0.30	1.27	0.76	59	0.18	-0.36	0.71
DE0007R	SP13	60	0.66	1.71	0.83	59	0.18	0.32	0.72
Inland	OV14	60	0.35	0.43	0.77	59	0.19	-0.32	0.65
Zingst	GO03	60	0.72	1.24	0.79	61	0.26	0.20	0.69
DE0009R	SP13	60	1.91	1.85	0.81	61	0.46	0.69	0.59
Coast	OV14	60	0.63	-0.09	0.77	61	0.43	-0.56	0.76
Melpitz	GO03	59	0.25	0.43	0.66	61	0.11	-0.35	0.69
DE0044R	SP13	59	0.39	1.27	0.67	61	0.12	0.58	0.67
Inland	OV14	59	0.27	0.11	0.65	61	0.13	0.12	0.57
Tange	GO03	56	1.03	1.12	0.67	61	0.44	0.88	0.65
DK0003R	SP13	56	2.97	2.03	0.74	61	0.84	1.22	0.74
Inland	OV14	56	0.96	-0.22	0.73	61	0.44	-0.32	0.67
Keldsnor	GO03	60	1.26	0.75	0.48	56	0.46	0.21	0.26
DK0005R	SP13	60	2.91	1.19	0.68	56	0.76	0.51	0.37
Coast	OV14	60	1.31	-0.50	0.46	56	0.75	-0.63	0.39
Anholt	GO03	59	1.26	0.51	0.81	51	0.60	0.05	0.69
DK0008R	SP13	59	4.44	1.49	0.82	51	0.91	0.31	0.68
Coast	OV14	59	1.61	-0.53	0.71	51	1.07	-0.67	0.59
Ulborg	GO03	60	1.41	1.63	0.77	54	0.68	1.22	0.52
DK0031R	SP13	60	4.87	1.82	0.83	54	1.15	1.07	0.79
Coast	OV14	60	1.33	-0.33	0.79	54	0.62	-0.40	0.71
Utö	GO03	59	0.59	1.26	0.59	61	0.24	0.24	0.67
FI0009R	SP13	59	1.86	3.10	0.64	61	0.33	0.91	0.64
Coast	OV14	59	0.32	0.23	0.61	61	0.33	-0.30	0.57
Virolahti II	GO03	60	0.24	1.50	0.37	54	0.09	0.16	0.75
FI0017R	SP13	60	0.50	2.71	0.49	54	0.13	1.10	0.72
Coast	OV14	60	0.18	0.74	0.33	54	0.12	0.34	0.55

winter, the RAEs are higher than those at the other stations. The RAEs during summer and the MNBs are in the same range as those at the other stations. Thus, the order of magnitude of the sodium concentrations is well reproduced, but the temporal occurrences of the peak concentrations are not well reproduced with respect to the other stations. Keldsnor is located on an island that is not resolved by the model, as is Anholt (DK0008R). However, Anholt is located on a small island that is surrounded only by water, whereas Keldsnor is located on a larger island in a region of several islands. Therefore, the local wind fields near Keldsnor may not be correctly predicted and consequently, sub-grid deposition processes may not be correctly reproduced by CMAQ, thereby causing the quality of the modeled sea salt concentrations to decline.

Particle Size Distribution

We noted in Sect. 4.3.2 that sodium PM_{10} mass concentrations were overestimated at coastal stations and underestimated at inland stations in the GO03 case, whereas in the OV14 case the concentrations were underestimated at coastal stations and overestimated at inland stations. This behavior was assumed to be caused by different atmospheric particle size distributions in the three emission cases inducing different dry deposition velocities. Therefore, in this section,

the sea salt particle size distributions in the GO03, SP13, and OV14 cases and their evolution from their source regions towards inland are analyzed. In addition, we are interested in how well the modeled size distributions represent measurements. This is done by considering the $PM_{2.5}$ and PM_C sodium concentrations (PM_C=PM_{10}−$PM_{2.5}$) and the modeled coarse mode GMDs at the stations Westerland, Waldhof, and Melpitz. Unfortunately, $PM_{2.5}$ measurement data for validating model data were only available at the station Melpitz. The modeled and measured $PM_{2.5}$ and PM_C concentrations from Melpitz are analyzed first (Fig. 4.10) followed by an evaluation of the modeled PM data at the three stations (Figs. 4.11 to 4.13).

For the $PM_{2.5}$ concentrations in summer (Fig. 4.10, center right), GO03 best reproduces the measured concentrations with respect to their magnitude. SP13 and OV14 yield considerable overestimations. During winter, all parameterizations underestimate the $PM_{2.5}$ peak concentrations, but SP13 overestimates the baseline concentrations, and positive MNBs indicate overestimations in all three cases. The average concentrations are best predicted by OV14, but the MNB is lowest for GO03. The correlation coefficient for OV14 is lower than those for GO03 and SP13 (Table 4.4). Thus, GO03 produces the best sodium $PM_{2.5}$ predictions, followed by OV14. Because OV14 is based on a highly detailed particle size distribution data set and considers ultra-fine particles (the Aitken mode), it might be expected that this parameterization would yield the best predictions of the $PM_{2.5}$ particle concentrations.

The temporal occurrences of peak PM_C concentrations are not consistently predicted by the three parameterizations, i.e., GO03 and SP13 predict several peaks that are not predicted by OV14, and OV14 also predicts peaks that are not predicted by the other two models. The PM_C concentrations are underestimated by GO03 in summer (MNB = −0.4), which leads to underestimation of the PM_{10} concentrations. In summer, OV14 and SP13 slightly underestimate the coarse particles but moderately overestimate the PM_{10} concentrations because of a considerable overestimation of $PM_{2.5}$. In particular, OV14 considerably overestimates the PM_C concentrations in late August for approximately a week, whereas the other parameterizations predict lower and more accurate concentrations. If this period were to be neglected, a more pronounced negative MNB for OV14 during summer would result. In winter, the coarse particles are overestimated by all parameterizations (MNB > 0); this overestimation is lowest for OV14 and highest for SP13. The correlation coefficients and RAEs for each season are quite similar to each other and provide no clear indication of which parameterization yields better results. Thus, based on the R values and the RAEs, no parameterization produces a clearly superior prediction of PM_C concentrations. However, according to the MNBs, OV14 produces the best results when winter and summer are considered together.

In summary, GO03 produces the best $PM_{2.5}$ concentrations, and OV14 produces the best PM_C concentrations at Melpitz. This size-resolved comparison indicates that PM_{10} concentrations are not necessarily appropriate for validating sea salt emission parameterizations but that size-

Table 4.4: Similar to Table 4.3 but for the Melpitz station only and for different particle sizes.

Size	Case	winter				summer			
		n	RAE	MNB	R	n	RAE	MNB	R
PM_{10}	GO03	59	0.25	0.43	0.66	61	0.11	-0.35	0.69
	SP13	59	0.39	1.27	0.67	61	0.12	0.58	0.67
	OV14	59	0.27	0.11	0.65	61	0.13	0.12	0.57
$PM_{2.5}$	GO03	58	0.09	0.19	0.64	56	0.03	0.08	0.50
	SP13	58	0.10	1.37	0.64	56	0.07	2.28	0.45
	OV14	58	0.10	0.39	0.52	56	0.06	1.27	0.31
PM_C [a]	GO03	56	0.20	0.69	0.64	52	0.11	-0.40	0.53
	SP13	56	0.35	1.42	0.65	52	0.13	0.15	0.50
	OV14	56	0.19	0.19	0.65	52	0.11	-0.27	0.48

[a] PM_C is calculated as PM_{10}−$PM_{2.5}$. In rare situations, PM_{10}<$PM_{2.5}$ exists in the measurements. In these situations, the resulting PM_C value is not considered.

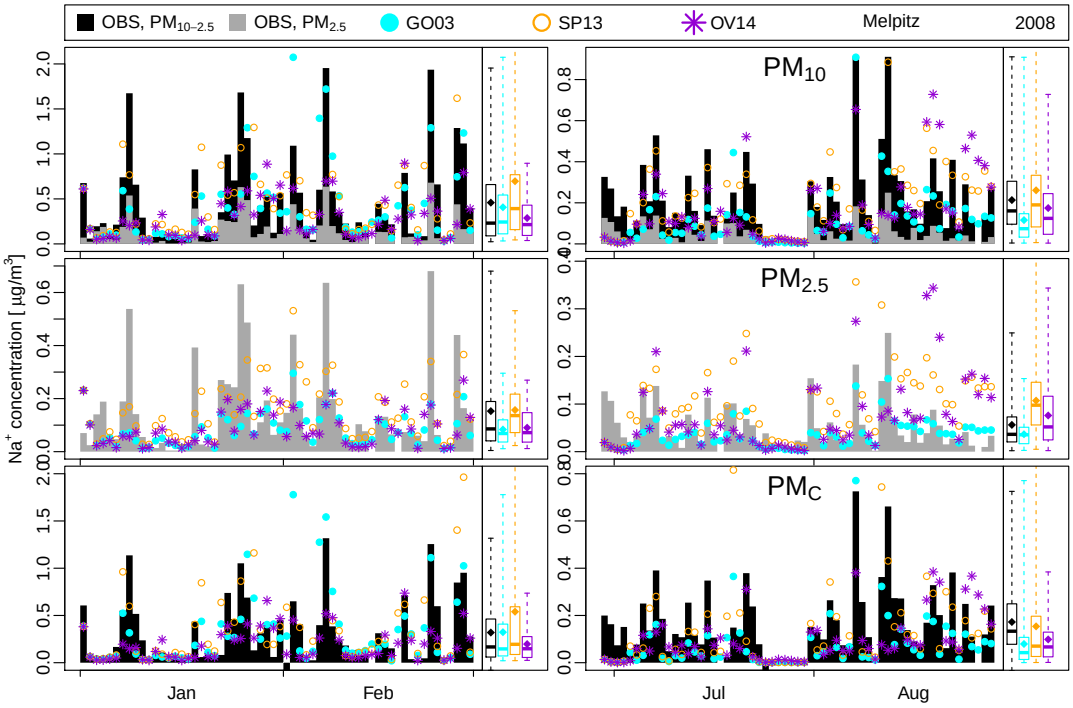

Figure 4.10: Daily average measured and modeled sodium concentrations at the EMEP station at Melpitz. The PM_{10}, $PM_{2.5}$ and PM_C concentrations are plotted in the top, center and bottom rows, respectively, for winter (left) and summer (right). The black box plot represents the observations. For the box plots of the modeled data, only the daily model values with corresponding measured values are considered.

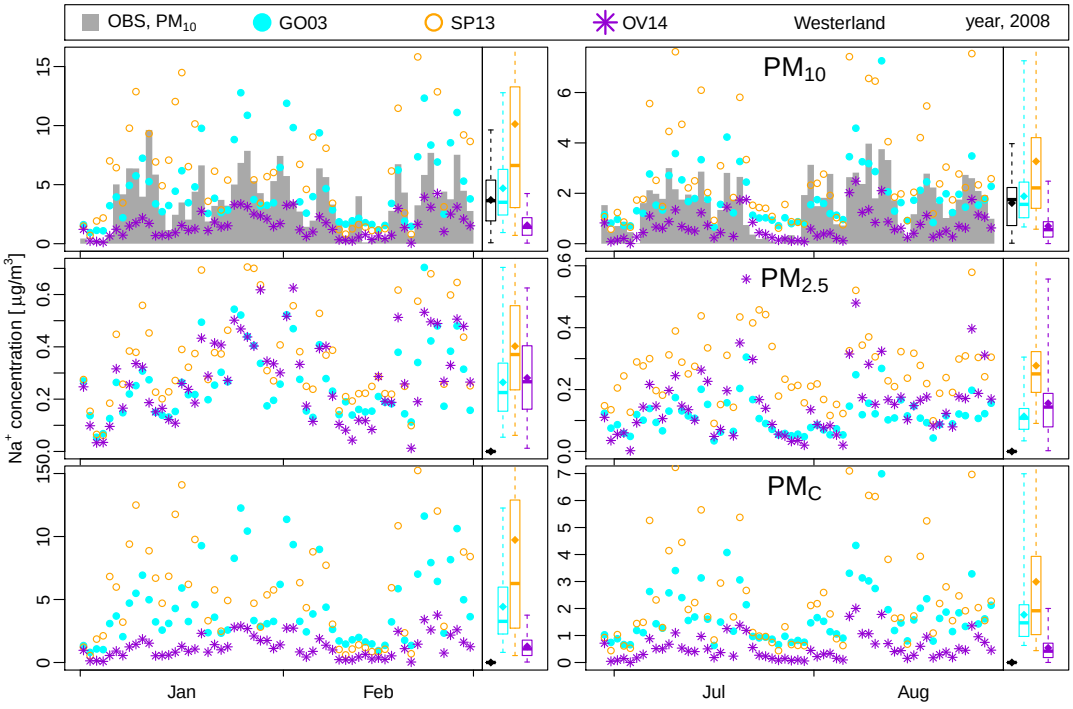

Figure 4.11: Similar to Fig. 4.10 but showing data for Westerland. No $PM_{2.5}$ data were available and no PM_C concentrations were calculated.

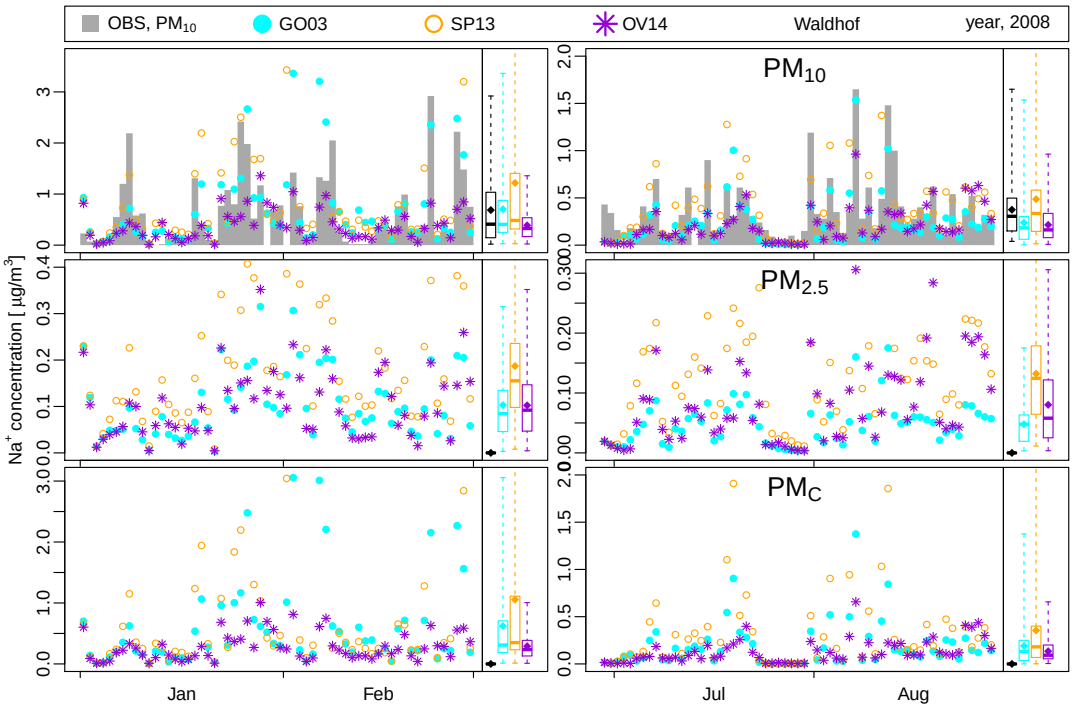

Figure 4.12: Similar to Fig. 4.10 but showing data for Waldhof. No $PM_{2.5}$ data were available nd no PM_C concentrations were calculated.

resolved measurements are of considerable importance in the validation process. Therefore, size-resolved sodium measurements in coastal regions will be necessary for the further evaluation of sea salt source functions.

For evaluating the evolution of the sodium size distributions, Figs. 4.11 and 4.12 depict similar data than Fig. 4.10 but at the stations Westerland and Waldhof, respectively. Figure 4.13 shows the modeled coarse-mode GMDs for all particles at Westerland, Waldhof and Melpitz.

At Westerland, PM_C sodium represents the predominant contribution to the total sodium mass in all three sea salt emission parameterizations (Fig. 4.11). The $PM_{2.5}$ and PM_C concentrations are twice as high during winter than summer. Similar as for the PM_{10} concentrations described above, the SP13 case yields the highest PM_C concentrations and OV14, the least. By contrast, the OV14 case yields higher $PM_{2.5}$ concentrations than the GO03 case in summer. In winter, the $PM_{2.5}$ concentrations of both cases are on the same level. At the station Waldhof (Fig. 4.12), the $PM_{2.5}$ concentrations are lower compared with the concentrations at Westerland but the ratio between the concentrations in the three cases is similar. By contrast, the PM_C concentrations in the three cases are closer to each other compared with Westerland. In particular, PM_C concentrations produced by OV14 are nearly as high as those produced by GO03. Additionally, the PM_C concentrations decrease stronger from Westerland to Waldhof than the $PM_{2.5}$ concentrations.

At Melpitz, the GO03 and OV14 cases yield quite similar PM_C concentrations. The PM_C concentrations are lower than at Waldhof and considerable lower than at Westerland, particularly the PM_C concentrations in the SP13 and GO03 cases. The decrease of the $PM_{2.5}$ concentrations from Westerland via Waldhof to Melpitz is lower compared to the decrease of PM_C. Consequently, $PM_{2.5}$ and PM_C concentrations are on a similar level at the station Melpitz. Therefore, the relevance of the $PM_{2.5}$ fraction increases with distance to the marine sea salt emission regions. Additionally, this analysis reveals that the deposition of coarse sea salt particles above 2.5 µm diameter is the predominant fraction of the total sea salt mass deposition. Thus, $PM_{2.5}$ sea salt is more relevant for the transport of attached species, which are condensed on the sea

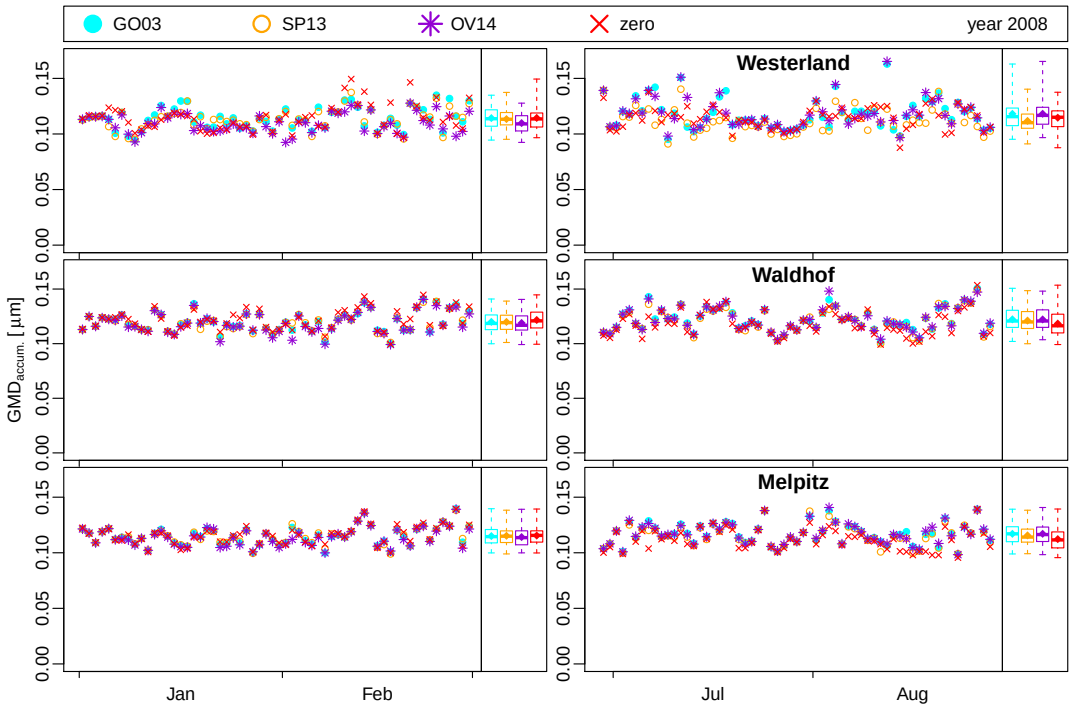

Figure 4.13: Similar to Fig. 4.9 but showing the GMDs of the modeled coarse-mode particle distributions. Not only sodium or sea salt but all coarse mode species are considered.

salt particle surface, over long distances than PM_C sea salt. The deposition of PM_C mass exhibits to be higher in the SP13 and GO03 cases than in the OV14 case. Therefore, sea salt emission parameterizations including more fine particles as OV14 can be expected to transport higher concentrations of those species over long distances than parameterizations as SP13 that yield a strong dry deposition close to source regions do. In order to understand why PM_C deposition velocities differ in the three emission cases, the GMDs of the modeled coarse mode are considered (Fig. 4.13). The GMD in the zero case represents the modeled GMD in the absence of sea salt emissions.

The sea salt particle emissions predicted in the SP13 and GO03 cases are larger in terms of the GMD than are those predicted in the OV14 case (Fig. D.6). Hence at the stations Westerland, SP13 yields the highest coarse-mode GMDs, followed by GO03 and then OV14 and zero. By contrast, at Waldhof, the GMDs for the different parameterizations are more similar to each other. On average, SP13 produces the highest GMDs, similar to the case of coastal stations. In summer, GMDs in the OV14 case exceed those in the GO03 case. At Melpitz, the GMDs are even closer to each other, whereby the GMDs in the GO03 case decrease below the GMDs in the zero case in some situations. The dry deposition behavior is dependent on particle size; therefore, coarse mass is deposited more rapidly in the SP13 and GO03 cases than in the OV14 case on the journey from the coast via Melpitz to Waldhof.

4.3.3 General Discussion

In this section, the shortcomings of and possible improvements to the individual sea salt emission parameterizations are discussed. The last paragraph contains technical remarks on the sea salt emission calculations.

Because the SP13 sea salt mass concentrations often considerably exceed the measured sea salt concentrations, it can be assumed that the SP13 emissions are too high. SP13 is based on a laboratory study [Mårtensson et al., 2003] in which SST-dependent sea salt emissions were measured directly after formation. The particle flux measured in Mårtensson et al. [2003] was

the gross particle flux, which is not necessarily equal to the net particle flux because some particles fall back into the ocean shortly after their emission. This may explain why SP13 overestimates sea salt emissions. The gross emission flux distribution of Mårtensson might need to be corrected by a size-dependent scaling function to accurately represent the net particle flux. The development of such a scaling function is beyond the scope of this study. Alternatively, the spume droplet production contributed by SM93, which is activated for wind speeds above a threshold of $9\,\mathrm{m\,s^{-1}}$, might be too high. This criterion is exceeded more frequently during winter than summer. This might yield the higher overestimations at coastal stations during winter compared with those during summer, which were noticed in Sect. 4.3.2.

The elevated overestimation at coastal stations during winter has also been observed in the GO03 case. Because both parameterizations depend on the same whitecap coverage parameterization [Monahan and Muircheartaigh, 1980], the increased overestimation during winter might originate from this whitecap coverage parameterization. Massel [2007b] discussed the sensitivity of the exponent in the whitecap coverage parameterization (Eq. (4.1)). A lower exponent would reduce the gradient of $W(u_{10})$ and the overestimation at high wind speeds. Additionally, GO03 does not include an SST dependence. As described by Mårtensson et al. [2003], Callaghan et al. [2014], and Salter et al. [2015], sea salt emissions decrease with decreasing SST. Thus, an emission reduction in winter due to a low SST might be missing from this model. Using CMAQ version 5.1, different modifications of the GO03 parameterization were compared. Among others, an SST scaling of GO03 emissions published by Jaeglé et al. [2011] was tested and found to improve the modeled sodium concentrations. Therefore, it is unclear whether the classical whitecap coverage dependence or deficiencies in the wind-independent part of the parameterization are responsible for the greater overestimation observed during winter.

In contrast to the GO03 and SP13 emission cases, the OV14 case yielded underestimations of the sodium PM_{10} concentrations at coastal stations. OV14 was fitted to data from the Northeastern Atlantic Ocean and to measurements from Mace Head, Ireland. The Atlantic Ocean is a deep and open ocean, in contrast to the North Sea, which is constrained by several coasts and is quite shallow in most areas. This allows waves to evolve differently; for example, the significant wave height is reduced near Dogger Bank. Hence, it might be necessary to refit the OV14 parameterization to the wave regime in the North Sea, e.g., by scaling $\mathrm{Re_{Hw}}$ with the wave period or wave length. An alternative approach that utilizes wave data is based on the energy dissipation caused by wave breaking, as reported by Long et al. [2011]. These authors related the volume of air entrained into the water via wave breaking to the dissipated energy. The volume of entrained air is considered to be proportional to the number of bursting bubbles and the number of sea salt particles produced. Salter et al. [2015] also employed this approach. However, Long et al. [2011] calculated the dissipated energy from u_{10} using a power-law relation, which is simply another fit similar to (Eq. (4.1)) and does not solve the problem of breaking waves in shallow water. Wave models can be used to calculate dissipative energy, as well. However, these estimations are rough because no dissipative energy measurements are available for validation purposes [Massel, 2007a].

Surf zone emissions are not the focus of this study. However, they must be briefly discussed because the three compared sea salt emission parameterizations allow the surf zone to be considered in different ways. The wind speed dependence adopted in GO03 and SP13 is the classical Monahan whitecap coverage parameterization [Monahan and Muircheartaigh, 1980]. Therefore, the CMAQ surf zone approach described by Kelly et al. [2010], namely, a 50 m wide surf zone in which the whitecap coverage is set to 1, was applied for these two parameterizations. However, OV14 does not incorporate the classical Monahan whitecap coverage treatment. Instead, a Reynolds number (Eq. (C.7)) is calculated for the sea surface and input into power laws for scaling the five log-normal particle number distributions. Unfortunately, the Reynolds number decreases toward the coast as a result of the decreasing wind speed and decreasing significant wave height (Fig. 4.4), which leads to reduced OV14 emissions at the coastline. Thus, the OV14

emissions are reduced in the surf zone, in contrast to the increase in surf zone emissions produced by the two other parameterizations. This may be a second reason why OV14 underestimates the sodium mass concentrations at coastal EMEP stations. An alternative approach that is instead based on the dissipative energy by wave breaking would imply enhanced sea salt emissions in the surf zone and would render a special treatment of the surf zone unnecessary.

The splitting of sea salt emissions into the three aerosol modes is a relevant step that affects the CTM calculations. According to Fig. 4.2, more coarse particles are produced by the SP13 parameterization than by the other two. However, the modal split is different for all three parameterizations (Fig. 4.3), leading to the emission of smaller but more numerous coarse-mode particles in the OV14 parameterization compared with the others. Consequently, the derived GMD for the OV14 coarse-mode emissions is smaller than those for the SP13 and GO03 coarse-mode emissions (Fig. D.6). This affects the modal distribution of the atmospheric particle concentrations (Figs. 4.10 to 4.13) as well as atmospheric processes such as dry deposition. Therefore, the technical aspects of the progression from the emission parameterization to the CTM affects the modeled sea salt particle behavior.

4.4 Conclusions

In a comparison of the sodium concentrations produced by three sea salt source parameterizations, the GO03 and OV14 parameterizations were identified to produce sodium mass concentrations closest to measurements. When comparing the modeled PM_{10} mass concentrations to observations, the correlation coefficients in all three cases are often similar to each other at individual stations and reveal no overall tendency (Table 4.3). The MNBs and RAEs indicate that the GO03 and OV14 parameterizations reproduce the measured data better than does the SP13 parameterization, which has the highest MNBs and generally overestimates the sodium concentrations. At coastal stations, OV14 underestimates and GO03 overestimates the sodium concentrations, whereas at inland stations, OV14 partially overestimates and GO03 partially underestimates (Fig. 4.9). This opposite trend between coastal and inland stations is due to the different dry deposition velocities of the parameterizations originating from their different particle size distributions (Fig. 4.13). Considering $PM_{2.5}$ and PM_{10} measurements from Melpitz station, the three parameterizations reproduce the concentrations in these two size classes with varying degrees of success: GO03 best reproduces the $PM_{2.5}$ mass concentrations, and OV14 best reproduces the PM_C mass concentrations. Unfortunately, no further size-resolved data were available, although measurements from closer to the coast would have been more informative. However, these results clearly indicate that size-resolved measurements are necessary for validating sea salt emission parameterizations. Because particles of different sizes have different deposition velocities, the particle distribution can be estimated based on speciated PM_{10} measurements recorded at different distances from the coast. However, this approach requires the CTMs to accurately reproduce the size distributions of the emitted sea salt particles and their dry deposition behavior.

The GO03 and OV14 emissions yielded the most accurate sodium mass concentrations. However, both parameterizations have certain shortcomings, and improvements to them should be considered. Enhancing GO03 by SST dependence, such as Jaeglé et al. [2011] did, might reduce overestimations, particularly during winter. OV14 was fitted based on wave data from the Northeast Atlantic Ocean to sea salt measurement data recorded at Mace Head, Ireland. However, the wave spectrum in the Atlantic Ocean is different from that in the North Sea; on the one hand, it may require a refit of the OV14 parameterization to the wave spectrum in the study region. Additionally, the possibility of enhancing OV14 with an appropriate representation of surf zone emissions should be considered. On the other hand, considering dissipative energy by wave breaking instead of Reynolds number of the sea surface would probably solve the surf zone and wave spectrum issues.

Acknowledgements

For the calculation of sea salt emissions, input data were obtained from the ECMWF, the German Federal Maritime and Hydrographic Agency (BSH), and the coastDatII database of Helmholtz-Zentrum Geesthacht (HZG). In particular, Beate Geyer and Nikolaus Groll supported this work by preparing the coastDatII meteorological and wave data, respectively, and by answering several questions about these data. We thank Matthias Karl and Jan Arndt for fruitful discussions and literature references as well as Markus Schultze and Joanna Staneva for providing additional information on the meteorological and wave data. Jim Kelly, Brett Gantt and Uma Shankar (U.S. EPA) answered questions about the implementation of the sea salt emission calculations in CMAQ, and Monica Mårtensson (Uppsala University), Astrid Manders-Groot (TNO) and Jurgita Ovadnevaite (National University of Ireland) provided helpful comments with respect to their sea salt studies and sea salt emission parameterizations. We offer our general gratitude to the U.S. EPA and the CMAQ development team for providing this high-quality chemistry transport model as an open-source product. The EMEP measurement data were extracted from the EBAS database, which is maintained and updated by the Norwegian Institute for Air Research (NILU). In particular, we thank Anne Hjellbrekke for answering questions about the EMEP data. The statistical evaluations and most plotting tasks were performed using R. The remaining plots were created using the Generic Mapping Tools (GMT) developed and maintained by Paul Wessel, Walter H. F. Smith, Remko Scharroo, Joaquim Luis and Florian Wobbe. The simulation data were processed using the Climate Data Operators (cdo) suite developed by Uwe Schultz-Weider from the Max-Planck-Institute for Meteorology and using the netCDF Operators (NCO) suite developed by Charlie Zender and Henry Butowsky. Finally, we thank American Journal Experts (AJE) for English language editing.

5 Comparing the impact of three sea salt emission parameterizations on atmospheric nitrate concentrations in the Northwestern European Region

5.1 Introduction

The impact of sea salt particles on atmospheric NO_3^-, sNO_3, and sNH_4 concentrations and on nitrogen deposition was assessed in Chap. 3. Chapter 4 dealt with a comparison of three sea salt emission parameterizations (GO03, OV14 and SP13). The GO03 and OV14 parameterizations were rated as appropriate but non of both was obviously more suitable than the other. Kelly et al. [2010] evaluated a new surf zone setup on the base of a comparison between modeled and measured particulate NO_3^- concentrations. In the first part of this chapter, the same approach is taken in order to identify whether the GO03 or OV14 parameterization yields better results in this respect. Since reliable NO_3^- were not available (see Chap. 3), sNO_3 (NO_3^- + HNO_3) was used for the validation.

In Chap. 4 it was shown that the sea salt particle distributions of the three sea salt emission cases expose different deposition patterns (Sect. 4.3.2). This fact indicates that particulate NO_3^-

Figure 5.1: EMEP stations considered for the evaluation of the model results. Atmospheric concentrations as well as wet deposition are evaluated. At stations indicated by orange dots only atmospheric NO_3^- and sNO_3 concentrations are evaluated, whereas at stations indicates by blue dots only nitrogen wet deposition and precipitation data are evaluated.

and, thus, total nitrogen deposition should also reveal different patterns when different sea salt emission parameterizations are employed. Hence, the nitrogen deposition in the three sea salt emission cases of Chap. 4 are assessed in the second part of this chapter.

No new materials and methods are introduced in this chapter. The sea salt emission cases are the same as used in Chap. 4, whereas the nitrogen-based evaluation equals the evaluation in Sects. 3.3.2 and 3.3.3. The EMEP stations considered for the evaluation are marked in Fig. 5.1. A similar analysis was presented under the same title at the Air Quality Conference 2016 in Milan. This chapter is an extended version of this talk.

5.2 Results and Discussion

5.2.1 Nitrate and Nitric Acid Concentrations

The impact of the sea salt emission parameterizations on particulate nitrate and sNO_3 (HNO_3 + NO_3^-) concentrations is first assessed in detail by regarding daily average concentrations at two stations (Fig. 5.2), one located at the coast (Westerland) and one inland (Melpitz). At Westerland station, the presence of sea salt leads to an increase of the nitrate PM_{10} and $PM_{2.5}$ concentrations at most days, whereby PM_{10} is increased stronger. The SP13 case yields the highest increase and GO03 the lowest. The zero case nitrate concentrations exceed the sea salt case nitrate concentrations in only a few situations. This is most notable for the $PM_{2.5}$ concentrations in winter. The exceedances commonly occur when peaks arise. In contrast, at Melpitz station, the nitrate $PM_{2.5}$ concentrations generally decreased in the sea salt cases compared to the zero case. Nitrate PM_{10} concentrations are maximized by the OV14 case followed by the zero case. The sNO_3 concentrations are similar in the zero and OV14 cases, and slightly lower in the SP13 and GO03 cases. In some situations, sNO_3 concentrations of the OV14 case exceed concentrations of the zero case and vice versa. In a nutshell, sea salt particles from the three sea salt emission parameterizations impact the nitrate PM_{10}, nitrate $PM_{2.5}$, and sNO_3 concentrations differently. They do not generally yield higher or lower concentrations than the zero case.

Two-month average particulate nitrate and sNO_3 concentrations of all stations are displayed in Fig. 5.3. It shows stations ordered according to increasing geographic distance to the coast from left to right. The average concentrations indicate that some patterns described for Westerland and Melpitz are present at all considered stations: Summer nitrate PM_{10} concentrations (Fig. 5.3, top row) are higher in the presence of sea salt emissions but, in contrast to Westerland, OV14 yields the highest nitrate concentrations at most stations. In winter, OV14 also leads to higher concentrations than GO03 and SP13 but they are exceeded by zero case nitrate concentrations at some stations. In contrast, nitrate $PM_{2.5}$ concentrations are highest in the SP13 and zero cases (Fig. 5.3, 2nd row). The zero case $PM_{2.5}$ exceeds that of SP13 in winter and both are balanced in summer. The variable influence of the three sea salt emissions parameterizations on the nitrate PM_{10} and $PM_{2.5}$ reflects the sea salt particle size distributions. The OV14 parameterization yields the highest coarse mode nitrate concentrations (not explicitly plotted but derived from the PM_{10} and $PM_{2.5}$ concentrations) because this parameterization's coarse mode particles have the longest atmospheric life time due to their low coarse mode geometric mean diameter (GMD) (Sect. 4.3.2, see also Fig. D.6). However, OV14 sea salt particles do not provide as much particle surface area as SP13 particles (Sect. 4.3.1, see also Fig. D.4). It is for this reason that relatively more HNO_3 condenses on freshly emitted SP13 particles than on OV14 particles. Hence, at the coastal station of Westerland, nitrate PM_{10} concentrations are highest in the SP13 case. The availability of particle surface area also governs the influence of the sea salt emission parameterizations on nitrate $PM_{2.5}$ concentrations, leading to highest $PM_{2.5}$ concentrations in the SP13 case.

The sNO_3 concentrations are lowest in the GO03 and SP13 cases (Fig. 5.3, 3rd row). They are highest in the zero case during winter and in the OV14 case during summer. None of the sea salt

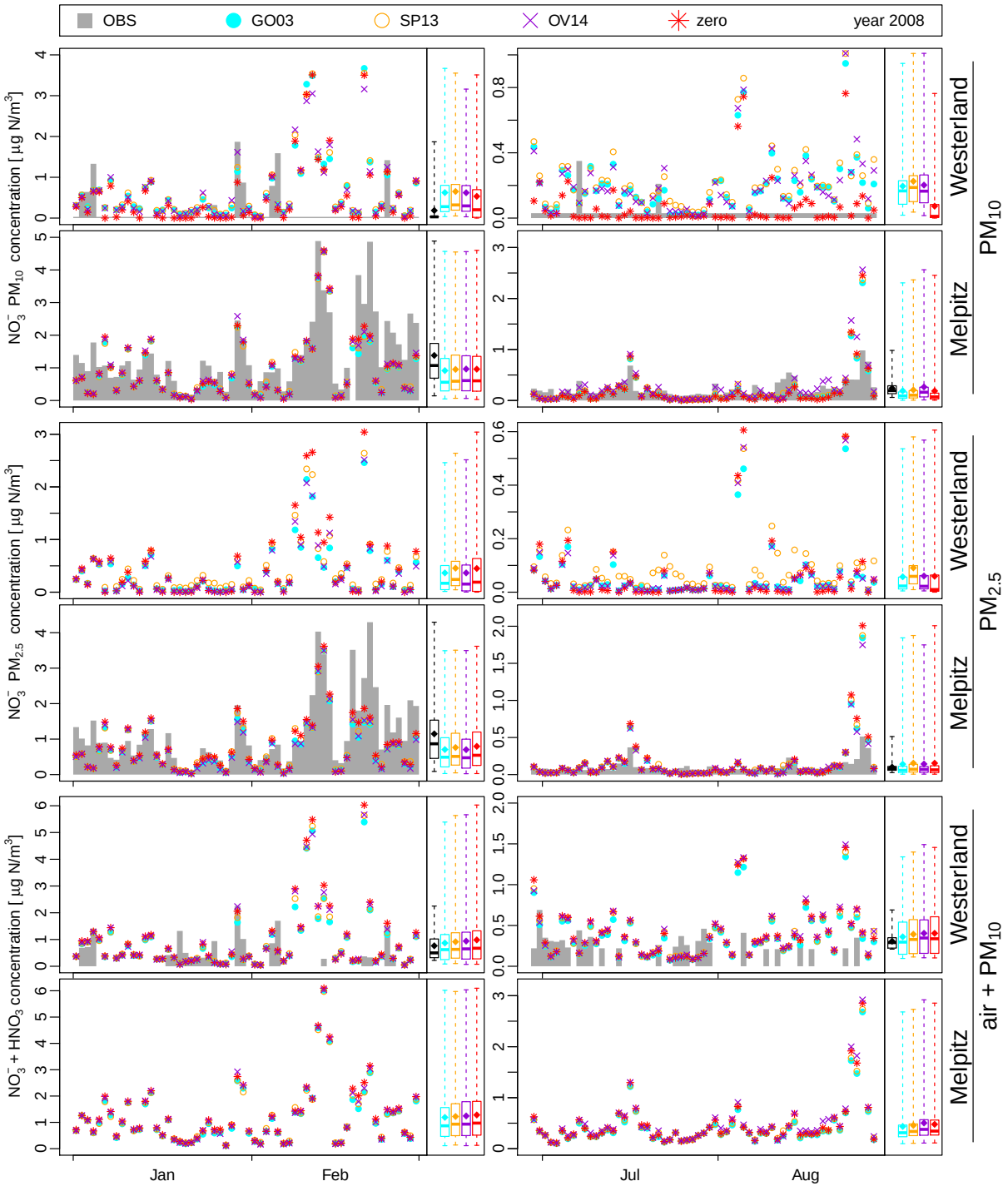

Figure 5.2: Particulate nitrate and sNO_3 concentrations at two EMEP stations in winter and summer. Similar to Figs. 3.7 and 3.8 with symbols of Chap. 4, such as Fig. 4.9. The NO_3^- PM_{10} (1st and 2nd row), NO_3^- $PM_{2.5}$ (3rd and 4th row), and sNO_3 (5th and 6th row) concentrations are displayed at Melpitz (top row of each set) and Melpitz (bottom row). Black box plots represent observational data. Only model data of days with measurements were considered for the model data box plots. When no oberservational data were available, the model box plots represent all model data points. Thus, the box plots are comparable within each plot but not necessarily between stations, seasons, and compounds.

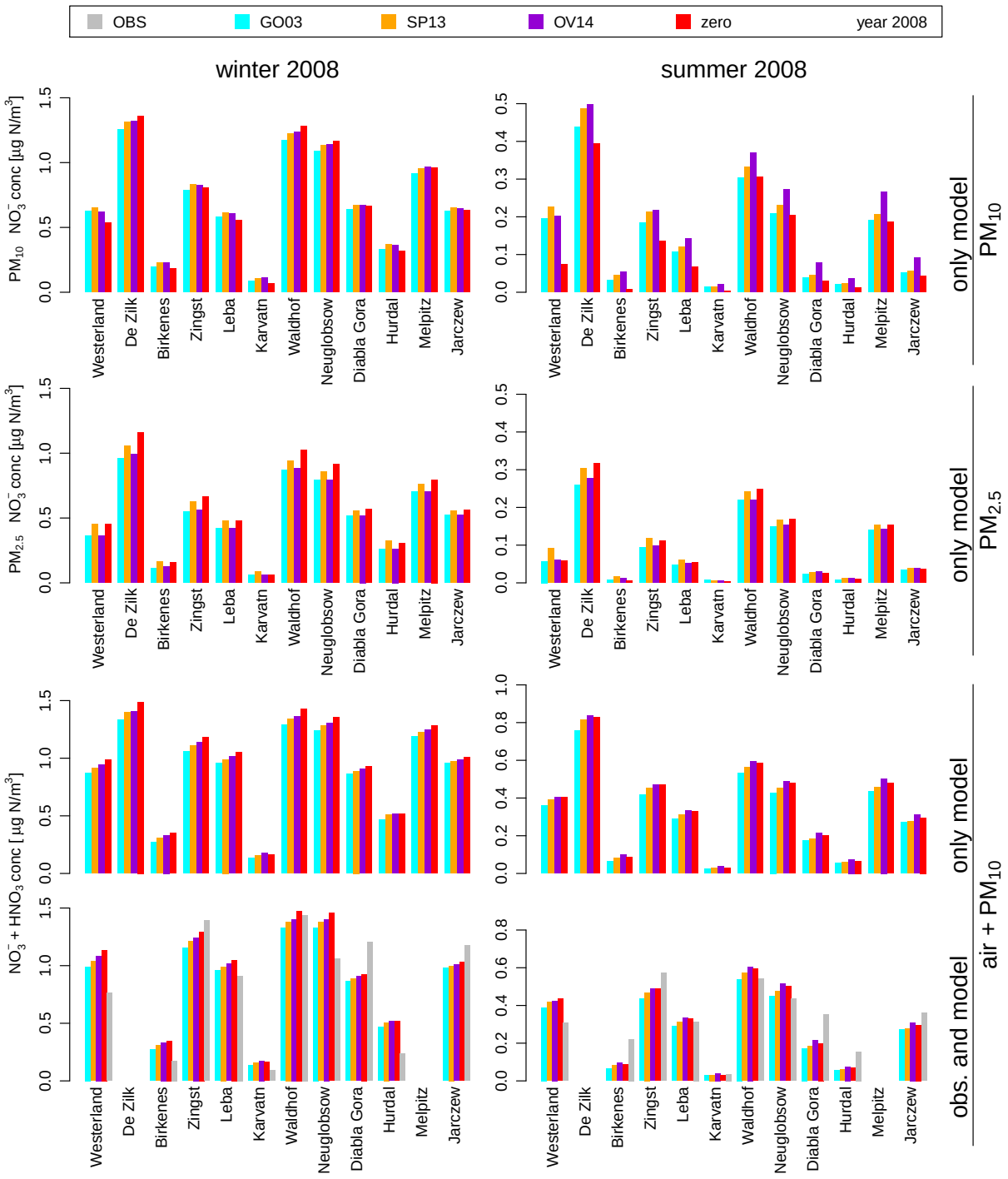

Figure 5.3: Similar to Fig. 5.2 but displaying two-month average concentrations at all stations. The modeled nitrate PM_{10} (1st row), nitrate $PM_{2.5}$ (2nd row), and sNO_3 (3rd row) concentrations are displayed in the first three rows. In the bottom row, modeled and measured average sNO_3 concentrations are displayed but only model values with corresponding measurements were considered for averaging. The EMEP stations are highlighted in Fig. 5.1 (black and orange dots).

Table 5.1: Similar to Table 3.4 but showing sNO_3 concentrations for the GO03, SP13, OV14, and zero sea salt emission cases.

sNO_3 concentration		Winter 2008				Winter 2008			
Station	Case	n	RAE	MNB	R	n	RAE	MNB	R
Westerland	GO03	21	0.76	1.17	0.10	26	0.25	0.41	-0.14
DE0001R	SP13	21	0.76	1.26	0.10	26	0.26	0.51	-0.11
Coast	OV14	21	0.76	1.36	0.11	26	0.27	0.54	-0.11
	zero	21	0.81	1.48	0.11	26	0.28	0.57	-0.13
Birkenes	GO03	60	0.19	1.24	0.45	52	0.17	-0.30	0.18
NO0001R	SP13	60	0.19	1.49	0.48	52	0.16	-0.14	0.11
mixed	OV14	60	0.23	1.73	0.45	52	0.15	-0.02	0.14
	zero	60	0.25	1.79	0.48	52	0.16	-0.11	0.17
Zingst	GO03	54	0.56	-0.17	0.76	56	0.26	-0.23	0.55
DE0009R	SP13	54	0.54	-0.12	0.76	56	0.25	-0.18	0.56
Coast	OV14	54	0.57	-0.10	0.75	56	0.25	-0.14	0.56
	zero	54	0.58	-0.08	0.77	56	0.26	-0.14	0.55
Leba	GO03	60	0.34	0.13	0.75	61	0.14	-0.03	0.51
PL0004R	SP13	60	0.33	0.20	0.76	61	0.14	0.04	0.51
Coast	OV14	60	0.36	0.20	0.76	61	0.16	0.12	0.51
	zero	60	0.37	0.24	0.75	61	0.16	0.10	0.52
Kårvatn	GO03	60	0.13	2.31	-0.07	47	0.02	-0.02	0.12
NO0039R	SP13	60	0.15	2.91	-0.13	47	0.02	0.11	0.15
Coast	OV14	60	0.16	3.35	-0.02	47	0.02	0.37	0.12
	zero	60	0.16	3.03	-0.06	47	0.02	0.02	0.11
Waldhof	GO03	50	0.67	0.00	0.64	59	0.31	0.05	0.34
DE0002R	SP13	50	0.65	0.04	0.65	59	0.31	0.12	0.33
Inland	OV14	50	0.68	0.05	0.65	59	0.33	0.18	0.33
	zero	50	0.68	0.10	0.67	59	0.32	0.16	0.34
Neuglobsow	GO03	53	0.59	0.39	0.63	54	0.25	0.04	0.39
DE0007R	SP13	53	0.58	0.45	0.65	54	0.24	0.11	0.41
Inland	OV14	53	0.62	0.45	0.63	54	0.26	0.18	0.43
	zero	53	0.62	0.50	0.65	54	0.26	0.16	0.41
Diabla Gora	GO03	59	0.56	-0.21	0.72	61	0.20	-0.47	0.36
PL0005R	SP13	59	0.55	-0.17	0.71	61	0.19	-0.44	0.38
Inland	OV14	59	0.56	-0.17	0.71	61	0.18	-0.36	0.38
	zero	59	0.55	-0.14	0.71	61	0.19	-0.39	0.36
Hurdal	GO03	60	0.34	1.86	0.44	52	0.11	-0.36	0.34
NO0056R	SP13	60	0.37	2.14	0.45	52	0.11	-0.31	0.34
Inland	OV14	60	0.39	2.17	0.43	52	0.10	-0.13	0.34
	zero	60	0.39	2.15	0.43	52	0.11	-0.22	0.34
Jarczew	GO03	58	0.45	-0.14	0.67	61	0.14	-0.19	0.49
PL0002R	SP13	58	0.44	-0.12	0.66	61	0.14	-0.18	0.51
Inland	OV14	58	0.44	-0.11	0.67	61	0.14	-0.10	0.51
	zero	58	0.44	-0.09	0.66	61	0.13	-0.13	0.50

emission parameterizations yields two-month average sNO_3 concentrations that clearly better reproduce the measurements (Fig. 5.3, bottom row).[a] The correlation coefficients (R) and the residual absolute errors (RAEs) of the four emission cases are close to each other at each station (Table 5.1): The highest and lowest values maximally differ by 0.7 (R) and 0.06 (RAE), respectively. The highest mean normalized biases (MNBs) arise in the OV14 and zero cases at most stations. This corresponds to the comparison of the two-month average sNO_3 concentrations. As a result, the OV14 case yields improved sNO_3 concentrations if they are underestimated in all cases at the particular station. In contrast, GO03 and SP13 yield improved sNO_3 concentrations if the concentrations are overestimated in all cases. None of the three sea salt emission parameterization leads to a general improvement of the sNO_3 concentrations and, therefore, no ranking of them can be performed on the basis of the evaluated sNO_3 concentrations.

[a]The difference between the 3rd and 4th row of Fig. 5.3 is that all model concentrations are averaged in the first case but only those at days with measurements in the second case.

Table 5.2: Similar to Table 3.7 but showing two-month nitrogen wet deposition in two alternative sea salt emission scenarios and, in addition, the statistical metrics MNB and RAE. The metrics are shown for all stations even if they are not reliable ($n < 10$). The mean values μ_{sim} and μ_{obs} are given in $\text{kg N ha}^{-1}\,\text{d}^{-1}$.

nitrogen wet deposition		Winter 2008						Summer 2008					
Station	Case	n	RAE	MNB	R	μ_{sim}	μ_{obs}	n	RAE	MNB	R	μ_{sim}	μ_{obs}
Westerland	GO03	7	0.01	-0.52	0.75	0.013	0.040	7	0.03	-0.55	0.32	0.009	0.020
DE0001R	SP13	7	0.01	-0.53	0.75	0.013	0.040	7	0.03	-0.56	0.32	0.009	0.020
Coast	OV14	7	0.01	-0.49	0.64	0.013	0.040	7	0.03	-0.53	0.32	0.010	0.020
	zero	7	0.01	-0.48	0.64	0.014	0.040	7	0.03	-0.53	0.32	0.010	0.020
Waldhof	GO03	19	0.04	-0.57	0.56	0.016	0.046	30	0.03	-0.35	0.20	0.023	0.059
DE0002R	SP13	19	0.04	-0.58	0.56	0.016	0.046	30	0.03	-0.36	0.19	0.023	0.059
Inland	OV14	19	0.04	-0.57	0.56	0.016	0.046	30	0.03	-0.34	0.20	0.024	0.059
	zero	19	0.04	-0.55	0.55	0.016	0.046	30	0.03	-0.35	0.19	0.024	0.059
Neuglobsow	GO03	22	0.02	-0.29	0.42	0.013	0.050	22	0.04	-0.56	0.10	0.017	0.034
DE0007R	SP13	22	0.02	-0.30	0.42	0.013	0.050	22	0.04	-0.57	0.11	0.017	0.034
Inland	OV14	22	0.02	-0.27	0.42	0.014	0.050	22	0.04	-0.55	0.10	0.018	0.034
	zero	22	0.02	-0.26	0.42	0.014	0.050	22	0.04	-0.56	0.11	0.018	0.034
Zingst	GO03	7	0.01	-0.32	0.82	0.016	0.019	7	0.01	0.08	0.39	0.008	0.014
DE0009R	SP13	7	0.01	-0.33	0.82	0.016	0.019	7	0.01	0.07	0.39	0.008	0.014
Coast	OV14	7	0.01	-0.29	0.82	0.017	0.019	7	0.01	0.11	0.39	0.008	0.014
	zero	7	0.01	-0.27	0.82	0.017	0.019	7	0.01	0.10	0.39	0.008	0.014
Melpitz	GO03	6	0.01	-0.53	0.77	0.014	0.032	8	0.02	-0.44	0.45	0.008	0.016
DE0044R	SP13	6	0.01	-0.54	0.77	0.014	0.032	8	0.02	-0.45	0.45	0.008	0.016
Inland	OV14	6	0.01	-0.53	0.77	0.015	0.032	8	0.02	-0.43	0.45	0.009	0.016
	zero	6	0.01	-0.51	0.77	0.014	0.032	8	0.02	-0.44	0.45	0.009	0.016
Keldsnor	GO03	3	0.00	-0.45	1.00	0.013	0.024	4	0.01	-0.35	1.00	0.006	0.010
DK0005R	SP13	3	0.00	-0.46	1.00	0.013	0.024	4	0.01	-0.36	1.00	0.006	0.010
Coast	OV14	3	0.00	-0.43	1.00	0.013	0.024	4	0.01	-0.33	1.00	0.006	0.010
	zero	3	0.00	-0.42	1.00	0.013	0.024	4	0.01	-0.33	1.00	0.006	0.010
Anholt	GO03	3	0.00	-0.10	1.00	0.018	0.015	4	0.00	0.23	1.00	0.011	0.013
DK0008R	SP13	3	0.00	-0.11	1.00	0.018	0.015	4	0.00	0.22	1.00	0.011	0.013
Coast	OV14	3	0.00	-0.05	1.00	0.019	0.015	4	0.00	0.27	1.00	0.011	0.013
	zero	3	0.00	-0.04	1.00	0.019	0.015	4	0.00	0.26	1.00	0.012	0.013
Ulborg	GO03	3	0.02	-0.72	0.50	0.013	0.018	4	0.01	-0.33	1.00	0.007	0.023
DK0031R	SP13	3	0.02	-0.73	0.50	0.013	0.018	4	0.01	-0.34	1.00	0.007	0.023
Coast	OV14	3	0.02	-0.71	0.50	0.013	0.018	4	0.00	-0.30	1.00	0.007	0.023
	zero	3	0.02	-0.70	0.50	0.013	0.018	4	0.00	-0.30	1.00	0.007	0.023
Virolahti II	GO03	7	0.01	-0.77	0.86	0.008	0.012	8	0.01	0.29	0.74	0.006	0.019
FI0017R	SP13	7	0.01	-0.77	0.86	0.008	0.012	8	0.01	0.25	0.74	0.006	0.019
Coast	OV14	7	0.01	-0.76	0.86	0.009	0.012	8	0.01	0.35	0.74	0.006	0.019
	zero	7	0.01	-0.76	0.86	0.008	0.012	8	0.01	0.33	0.74	0.006	0.019
Birkenes	GO03	36	0.07	-0.87	0.68	0.019	0.032	27	0.03	0.97	0.66	0.012	0.079
NO0001R	SP13	36	0.07	-0.87	0.68	0.019	0.032	27	0.03	0.92	0.66	0.011	0.079
mixed	OV14	36	0.07	-0.86	0.69	0.020	0.032	27	0.03	1.11	0.65	0.012	0.079
	zero	36	0.07	-0.85	0.68	0.020	0.032	27	0.03	1.11	0.65	0.013	0.079
Hurdal	GO03	25	0.05	-1.00	0.60	0.008	0.028	28	0.02	-0.70	0.54	0.000	0.054
NO0056R	SP13	25	0.05	-1.00	0.60	0.008	0.028	28	0.02	-0.71	0.55	0.000	0.054
Inland	OV14	25	0.05	-1.00	0.60	0.008	0.028	28	0.02	-0.67	0.52	0.000	0.054
	zero	25	0.05	-1.00	0.60	0.008	0.028	28	0.02	-0.68	0.54	0.000	0.054
Jarczew	GO03	24	0.03	-0.81	0.71	0.008	0.079	17	0.07	-0.82	-0.34	0.010	0.045
PL0002R	SP13	24	0.03	-0.81	0.71	0.008	0.079	17	0.07	-0.82	-0.34	0.010	0.045
Inland	OV14	24	0.03	-0.80	0.72	0.008	0.079	17	0.07	-0.82	-0.34	0.010	0.045
	zero	24	0.03	-0.79	0.69	0.008	0.079	17	0.07	-0.82	-0.34	0.011	0.045
Leba	GO03	31	0.02	-0.50	0.55	0.020	0.035	28	0.02	-0.49	0.59	0.013	0.030
PL0004R	SP13	31	0.02	-0.50	0.55	0.020	0.035	28	0.02	-0.50	0.59	0.013	0.030
Coast	OV14	31	0.02	-0.47	0.55	0.021	0.035	28	0.02	-0.47	0.58	0.014	0.030
	zero	31	0.02	-0.46	0.56	0.021	0.035	28	0.02	-0.48	0.59	0.014	0.030
Råö	GO03	38	0.03	-0.39	0.62	0.032	0.033	26	0.03	0.75	0.20	0.013	0.038
SE0014R	SP13	38	0.03	-0.41	0.63	0.031	0.033	26	0.03	0.71	0.21	0.013	0.038
Coast	OV14	38	0.03	-0.36	0.61	0.033	0.033	26	0.03	0.82	0.20	0.014	0.038
	zero	38	0.03	-0.35	0.62	0.033	0.033	26	0.03	0.83	0.20	0.014	0.038

5.2.2 Nitrogen Deposition

In contrast to Sect. 3.3.3, the nitrogen wet deposition is considered first and, after that, the total nitrogen deposition.

The modeled two-month average nitrogen wet deposition (Table 5.2, μ_{sim}) is below the measured nitrogen wet deposition (μ_{obs}) at most stations throughout the year. The highest deviations occur at inland stations, where μ_{obs} often is more than twice as high as μ_{sim}, such as at Jarczew and Melpitz stations. The MNBs are negative at most stations coinciding with the μ_{sim}-μ_{obs} comparison. Nevertheless, some stations have positive biases. The latter indicates that individual wet deposition values were considerably overestimated while the total nitrogen deposition was underestimated. At half of the stations, the number of observations was 7 and lower (Table 5.2, column n) due to a precipitation collection interval of one or two weeks. The statistical metrics are not reliable at these stations. The errors (RAE) were low at all stations. The correlation coefficients (Table 5.2, column R) were above 0.5 at most stations in winter, but only at half of the stations in summer. They were below 0.2 at four stations and even negative at Jarczew station. This is caused by poorly predicted temporal resolution of the precipitation at this station as indicated by a negative R of the precipitation data (Table 5.3).

The precipitation amount (Table 5.3, μ_{sim} and μ_{obs}) is slightly underestimated at most stations in summer and at half of the stations in winter. The fact that the precipitation is overestimated at the other half of the stations in winter indicates that the predictions of two-month total precipitation and of two-month average nitrogen deposition do not necessarily correlate with each other. In contrast, high correlation coefficients of precipitation time series often go along with high correlation coefficients of the nitrogen wet deposition time series. Hence, for correct predictions of nitrogen wet deposition, it is important to resolve the precipitation correctly in time.

The choice of the sea salt emission parameterization had a low effect on the nitrogen wet deposition. In winter, the correlation coefficients differ by ±0.01 at all stations apart from Westerland station. There the R is 0.64 for the OV14 and zero cases, but 0.74 for the other cases. The OV14 and zero cases also yield slightly larger MNBs which shifts most biases closer to 0. However, the magnitude of improvement is negligible. Hence, the sea salt emission scenario can be considered to have a negligible impact on the nitrogen wet deposition.

The total nitrogen deposition is higher in summer than in winter by about a factor of 2 (Fig. 5.4, top row). Spatial deposition peaks occur in the Netherlands, Northwestern Germany, and the Po Valley during both seasons and, additionally, in Denmark and along the northern foothills of the Alps during summer. The Netherlands, Northern Germany, and Denmark are known for extensive animal husbandry and agricultural activities which cause high emissions

Table 5.3: Similar to Table 5.2 but showing the two-month total precipitation in mm.

precipitation	Winter 2008						Summer 2008					
Station	n	RAE	MNB	R	μ_{sim}	μ_{obs}	n	RAE	MNB	R	μ_{sim}	μ_{obs}
Westerland	7	7.71	Inf	0.21	19.67	13.40	7	18.93	Inf	0.18	25.30	36.53
Waldhof	19	3.13	Inf	0.80	5.34	6.72	30	4.35	Inf	0.50	2.47	5.89
Neuglobsow	22	3.53	Inf	0.29	3.77	4.28	22	5.10	Inf	0.33	2.49	5.30
Zingst	7	2.29	Inf	1.00	9.71	8.66	7	10.29	0.31	0.68	17.03	14.20
Melpitz	6	3.74	Inf	0.83	15.36	12.75	8	11.18	0.16	0.29	14.30	16.59
Keldsnor	3	9.50	0.59	1.00	23.39	13.89	4	14.68	0.57	0.20	32.10	34.62
Anholt	3	13.07	0.67	1.00	32.14	19.07	4	20.58	0.02	0.80	45.59	56.44
Ulborg	3	11.84	-0.15	1.00	43.41	50.36	4	17.11	-0.16	0.80	48.93	58.30
Virolahti II	7	5.15	-0.47	0.50	6.32	11.17	8	13.26	1.38	0.81	22.70	15.81
Birkenes	36	8.67	Inf	0.57	6.32	14.04	27	10.95	Inf	0.54	6.84	13.60
Hurdal	25	8.96	Inf	0.58	0.12	9.01	28	8.22	Inf	0.59	4.52	8.84
Jarczew	24	2.01	Inf	0.66	2.67	3.48	17	7.40	Inf	-0.16	1.56	7.51
Leba	31	2.29	Inf	0.30	2.06	2.02	28	4.48	Inf	0.63	3.84	6.21
Råö	38	1.46	Inf	0.75	3.47	3.40	26	7.67	Inf	0.21	6.56	7.26

of NH_3. It either deposits close to its sources, condenses on particles, or nucleates (reactions R 2.3 to 2.1.1). Although, this region would have enhanced nitrogen deposition even without the North Sea in upwind direction, the sea salt from the North Sea significantly increases the nitrogen

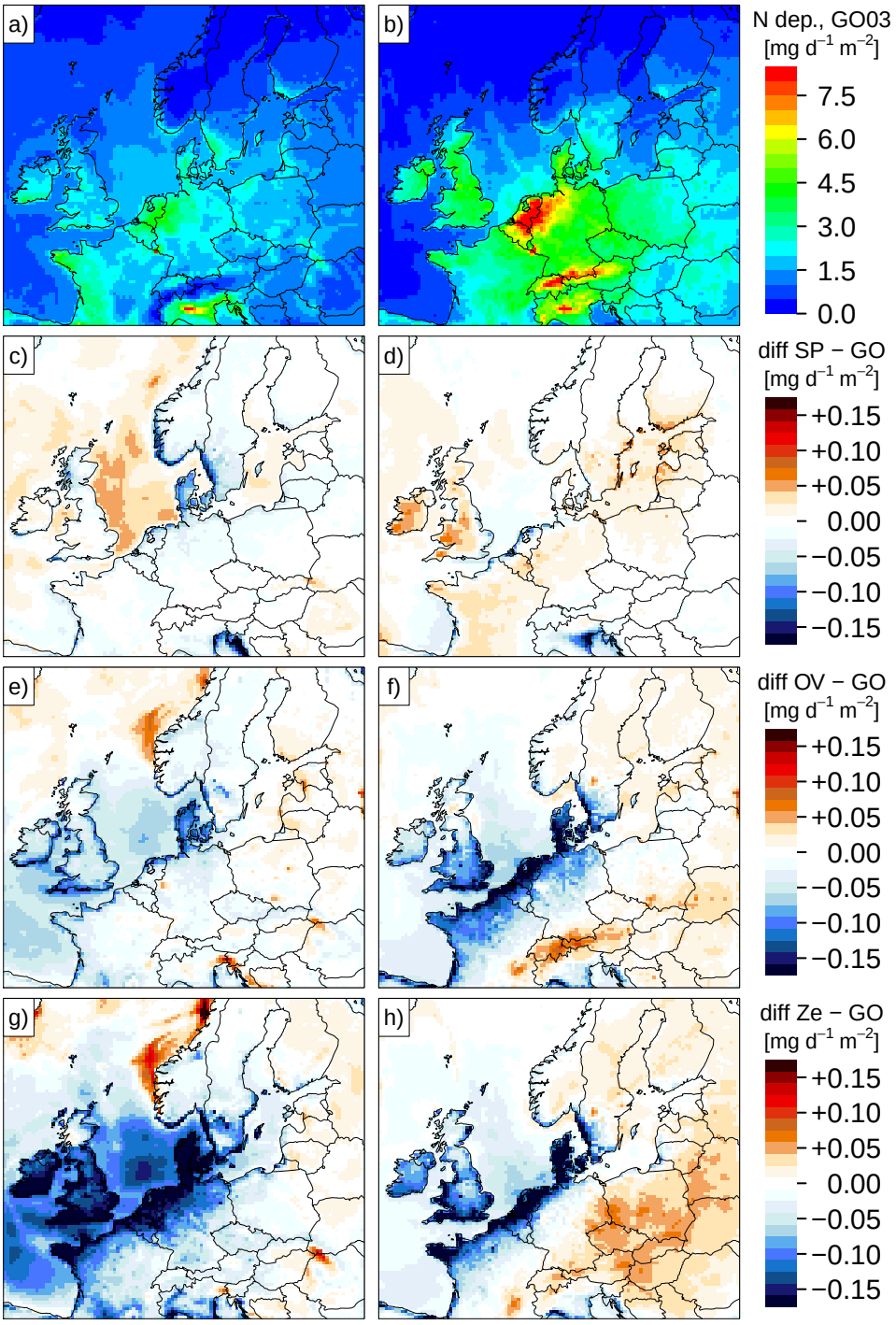

Figure 5.4: Similar to Fig. 3.9 but showing the nitrogen deposition of the cases of Chap. 4. **(a, b)** GO03 case (=Base) in the first row; **(c, d)** difference between SP13 and GO03 cases (SP13 – GO03) in the second; **(e, f)** difference between OV14 and GO03 cases (OV14 – GO03) in the third; **(g, h)** difference between zero and GO03 cases (zero – GO03) in the fourth. The plots in the first and fourth rows equal those in the first and third rows in Fig. 3.9 but the color bar is differently scaled.

Table 5.4: Similar to Table 3.6 but showing nitrogen deposition [$\mathrm{kt\,N\,d^{-1}}$] in the GO03 (=Base), SP13, OV14, and zero cases. The North Sea and Baltic Sea cover 6.50×10^{11} and $4.13 \times 10^{11}\,\mathrm{m^2}$, respectively, in this study's model setup. The exact regions considered are plotted in Apdx. B.5.

Region	Season	GO03	SP13	OV14	Zero	
North Sea	Winter 2008	1.007	1.021	0.973	0.938	$\mathrm{kt\,N\,d^{-1}}$
	Summer 2008	1.079	1.076	1.052	1.051	
Baltic Sea	Winter 2008	0.566	0.566	0.561	0.547	
	Summer 2008	0.602	0.608	0.603	0.602	
North Sea	Winter 2008	100.0 %	101.3 %	96.6 %	93.1 %	rel. to GO03
	Summer 2008	100.0 %	99.7 %	97.5 %	97.4 %	
Baltic Sea	Winter 2008	100.0 %	100.1 %	99.1 %	96.6 %	
	Summer 2008	100.0 %	101.0 %	100.2 %	100.0 %	

dry deposition and, hence, the total nitrogen deposition. Therefore, the nitrogen deposition is considerably reduced along the North Sea coast in the zero case compared to the Base (GO03) case (Fig. 5.4, bottom row). The difference is higher in winter due to higher sea salt emissions in this season. Instead of condensing on existing particles, the particle formation by NH_3, HNO_3, and H_2SO_4 is enhanced in the zero case leading to a higher number of fine particles which have lower dry deposition velocities than sea salt particles and are transported over longer distances. Therefore, the nitrogen deposition was increased in inland regions.

The OV14 sea salt emissions lead to a reduction of nitrogen deposition along the coastline, particularly in summer (Fig. 5.4, 3$^{\mathrm{rd}}$ row). The reason for this is that the accumulation and coarse mode GMDs of the OV14 parameterization are lower than those of the GO03 parameterization (Fig. D.6) yielding a lower dry deposition velocity and, hence, a longer transport distance. The absolute difference between OV14 and GO03 nitrogen deposition is stronger pronounced in summer due to higher total nitrogen deposition in this season. The relative reduction of nitrogen deposition along the coastline from the GO03 to OV14 case is similar in both seasons. The SP13 case also yields a slightly reduced nitrogen deposition in some coastal regions which might be counter intuitive because the SP13 coarse mode GMD considerably exceeds that of GO03 and OV14. However, the SP13 case provides less coarse particles and considerably more fine and ultra-fine sea salt particles (Fig. D.5) which, compared to GO03, have a longer atmospheric residence time and might induce the slight reduction of the nitrogen deposition in the vicinity of NH_3 and sea salt emission sources.

The total nitrogen deposition into the North Sea and Baltic Sea is considered in this paragraph. Table 5.4 shows it for the three sea salt emission cases and the zero case in winter and summer 2008. The absolute deposition is lower than in comparable studies [Bartnicki and Fagerli, 2008; Bartnicki et al., 2011; HELCOM, 2005; Hertel et al., 2002; Langner et al., 2009] as discussed in detail in Sect. 3.4.4. The differences between the four model cases are of interest in this Chapter. The CMAQ standard sea salt emissions (GO03) account for 2.5 % to 7 % and 0 % to 3.5 % of nitrogen deposition into the North Sea and Baltic Sea, respectively. The seasonal variation of the nitrogen deposition is low, as already noted in Sect. 3.3.3. Replacing the GO03 by the OV14 parameterization can reduce the sea salt related nitrogen deposition into the North Sea by approximately 50 % in winter and nearly 100 % in summer. In contrast, the usage of SP13 leads to a approximately 20 % increase in winter and a negligible decrease in summer. When the Baltic Sea is considered, the SP13 and OV14 parameterizations yield negligible differences.

Although, the choice of the sea salt emission parameterization can have a significant impact on the sea-salt-related nitrogen deposition into the North Sea, its impact is below 5 % with respect to the total nitrogen deposition into the North Sea. However, the relative contribution of sea salt is considerably higher in coastal regions as the differences in Fig. 5.4 indicate.

5.3 Conclusion

The variation of sea salt particle size distribution represented by the three sea salt emission cases GO03, SP13, and OV14 impacted the concentrations of particulate nitrate, its size distribution, and transport distance. Using the SP13 parameterization yielded the highest nitrate $PM_{2.5}$ concentrations. Using OV14 yielded the highest nitrate PM_C concentrations. Simulations without sea salt emissions (zero case) led to higher nitrate PM_{10} concentrations than simulations with sea salt in winter. These simulations generated the lowest nitrate PM_{10} concentrations in summer. In contrast, the ranking of the three sea salt emission parameterizations did not reveal any seasonal variations with respect to their impact on nitrate. Despite the fact that the parameterizations affect particulate nitrate concentrations differently, the evaluation of the sNO_3 concentrations with measurements (two-month mean concentrations and statistic metrics MNB, RAE, and R) did not identify one parameterization to be best suited for sNO_3 predictions.

On the one hand, the impact of sea salt emissions on nitrogen wet deposition was found to be negligible. On the other hand, the nitrogen dry deposition was influenced by the presence of sea salt particles and their size distribution. The latter was reflected by spatial changes in the total nitrogen deposition: The OV14 parameterization induced lower nitrogen depositions in coastal regions than the GO03 parameterization but slightly increased them in inland regions. As a result, the sea salt related nitrogen deposition of the Base case (GO03) into the North Sea was reduced by at least 50 % when the OV14 parameterizations is used. This corresponds to a reduction by 2.5 % to 3.5 % of the total nitrogen deposition into the North Sea. The impact of sea salt emissions on the nitrogen deposition into the Baltic Sea was low. Hence, the choice of the sea salt parameterization had a negligible impact. Since sea salt emissions are considerably lower in the Baltic Sea than in the North Sea (Fig. 3.3), a reduced impact of sea salt emissions is reasonable in the Baltic region.

In summary, sea salt was found to significantly impact the nitrogen deposition in coastal regions. However, non of the three sea salt emissions parameterizations was identified to reproduce sNO_3 concentrations and nitrogen deposition best.

6 Contribution of major anthropogenic emission sectors and sea salt emissions to fine and coarse particulate sulfate air pollution

Abstract

Fine sulfate particles pose a risk for human health when they are inhaled and atmospheric compounds, in general, yield acid deposition. In Europe, the major sources of sulfur air pollution are of anthropogenic origin but their contribution varies spatially. In order to assess which sources input air quality most at different locations, the contribution of the two dominant anthropogenic emission sectors energy production and shipping as well as of sea salt emissions to the atmospheric sulfate $PM_{2.5}$ and PM_{10} concentrations is modeled and evaluated at 22 locations in central and northern Europe. The modeling is performed with the chemistry transport model CMAQ. Each two months in winter and summer 2013 were considered. The sulfate PM_{10} concentrations well met with respect to the bias in summer, whereas they were generally overestimated in winter. In contrast, the correlation coefficients were higher in winter (> 0.5 at most stations). The sum of sulfate PM_{10} and SO_2 data yielded higher correlations throughout the year compared to pure sulfate PM_{10}, though the biases rose in summer. Particulate sulfate was significantly overestimated at two stations in northern Norway due to overestimated sea salt emissions along the Atlantic coast. The energy sector had the highest contributions to sulfate PM_{10} and PM_{25} concentrations amongst the considered sectors. However, the other not-considered anthropogenic source sectors contributed 50 % and more to the particulate sulfate at the most stations but considerably less to SO_2 concentrations. In summer, relevant amounts of particulate sulfate (10 % to 30 %) were accounted to the shipping sector. Two different sea salt emission parameterizations were used, which contributed up to 30 % and up to 10 % to sulfate PM_{10} concentrations but considerably less to $PM_{2.5}$. Along the coast, high shares of particulate sulfate were accounted to shipping and sea salt emissions becoming less relevant towards inland regions, although also inland stations were exposed to considerable shipping related sulfate in individual episodes. The method for calculating the sectoral contributions was validated by deriving sea salt sulfate with two methods and comparing their results with each other and with measurements. It was found that the uncertainty of the method rose when sea salt emissions had a lower contribution to the total sulfate concentrations. Vice versa, the higher the sea salt contribution was, the lower was the uncertainty and the higher the correlation between both methods and with the measurements. Further studies require a more detailed sectorization of the anthropogenic emission sources. Additionally, the overestimation of sulfur concentrations in winter need to be assessed in more detail. The available number of measured sulfate $PM_{2.5}$ time series was low but for the evaluation of health aspects as well as for model validation purposes, more sulfate $PM_{2.5}$ concentration time series would be valuable. The validation of the method for deriving sectoral contributions partly reveals high uncertainties. Therefore, it would be advantageous to evaluate the used method in further studies by a sulfur tagging scheme.

6.1 Introduction

Atmospheric sulfate particles have a negative impact on human health as their inhalation contributes to the development of respiratory and cardiovascular diseases [Brunekreef and Holgate,

2002] and they induce acid deposition – particularly acid rain [Seinfeld and Pandis, 2006a, Chap. 20.5]. Anthropogenic sulfur emissions have been significantly reduced in the last decades [EMEP, 2015; Smith et al., 2011], but there is still need for further reduction. Nowadays, the major sources for particulate sulfate air pollution in Europe are the shipping sector, the energy production sector (public and industrial), and natural sea salt emissions. However, the relevance of these source sectors varies spatially and seasonally. The identification of major local and regional contributors to particulate sulfate air pollution is important to plan and initiate further measures for reducing this type of air pollution. Depending on the considered threat, sulfate $PM_{2.5}$ (fine) and PM_{10} (fine plus coarse) air pollution need to be distinguished: The $PM_{2.5}$ concentrations are related to health impacts because they penetrate deep into the lung, whereas acid deposition is caused by fine and coarse sulfate particles as well as gaseous SO_2. Therefore, source receptor relationships with respect to fine and coarse particulate sulfate air pollution need consideration leading to the research question:

> What are the dominant contributors to fine and coarse air pollution by sulfate particles at different locations in Northwestern Europe?

This question will be evaluated by means of the CTM CMAQ employing different sulfur oxide emission scenarios distinguishing sulfate from the energy sector, shipping sector, sea salt and other sources. Here, sulfur oxides and not sulfate are named because most anthropogenic sources emit SO_2(g), H_2SO_4(g), and SO_4^{2-}(p). Gaseous SO_2 reacts via various pathways to H_2SO_4. H_2SO_4 is, in turn, considered to immediately condense or nucleate and, hence, deprotonize to particulate sulfate. In the real atmospheric chemistry, several gaseous intermediate products exist between SO_2 and H_2SO_4 but they are not represented explicitly in CMAQ and, hence, not considered. Two emissions cases, in which each one of the source sectors shipping and energy production was deactivated, were set up and used as input for CMAQ simulations. Comparing these simulations' results against one reference simulation including all emission sources provides these sectors' contributions to sulfate concentrations. Sea salt related sulfate concentrations were calculated from sodium concentrations.

Although sea salt emissions seem to be simple to parameterize compared to natural biogenic emissions and, although, the knowledge on these emissions has been considerably improved in the last three decades, modern sea salt emission parameterizations are still subject to large uncertainties [O'Dowd and de Leeuw, 2007; Spada et al., 2013; Ovadnevaite et al., 2014]. For estimating the uncertainty in the contribution of sea salt emissions to atmospheric particulate sulfate, two different sea salt emission cases were considered in this study.

6.2 Materials and Methods

6.2.1 Model Setup and Input Data

The presented simulations were performed with the CTM CMAQ version 5.0.1. The gas phase chemistry was represented by the cb05tump mechanism [Yarwood et al., 2005; Whitten et al., 2010; Sarwar et al., 2007] and the aerosol chemistry by the AERO6 mechanism. The latter is based on ISORROPIA v2.1 [Fountoukis and Nenes, 2007; Sarwar et al., 2011] and considers the condensation of H_2SO_4, HNO_3, HCl, and NH_3 onto particles and the re-volatilization of the latter three substances.

The simulations were performed on a $24 \times 24\,km^2$ grid covering Northwestern Europe that is one-way nested into a $72 \times 72\,km^2$ grid covering Europe and the northern coast of Africa. The boundary conditions of the outer grid domain were taken from GEOS-5/MOZART-4 model simulations [Emmons et al., 2010]. Two months in winter 2013 (January and February) and two months in summer 2013 (July and August) were simulated with a spin-up period of ten days.

Meteorological Input data were calculated with the regional climate model COSMO-CLM [Rockel et al., 2008] as set up by Geyer [2014]. Land-based emissions were calculated by SMOKE

for Europe [Bieser et al., 2011] based on reported sectorized EMEP emissions, shipping emissions according to Aulinger et al. [2016], and sea salt emissions according to Gong [2003] or Ovadnevaite et al. [2014] – depending on the emission case (see below).

Sea salt emissions by Gong include surf zone emission [Kelly et al., 2010]. The sea salt emissions were updated to depend on salinity (Sect. 3.2.4 and Apdx. H.4). The required salinity data were calculated by an advanced version of Hamburg Shelf Ocean Model (HAMSOM) [Schrum and Backhaus, 1999; Barthel et al., 2012]. Sea salt emissions by Ovadnevaite et al. [2014] do not include surf zone emission. Fields of SST, SAL, u_{10}, H_s, and C_D are necessary for calculating these emissions. SST data were taken from BSHcmod operational forecasts and from the ERA-Interim data set of the ECMWF, SAL data from BSHcmod operational forecasts, and H_s data from the ERA-Interim data set. In contrast to the year 2008 (Chaps. 3 and 4), no WAM data were available in the coastDatII database for 2013. The C_D was derived from u_{10} by Eq. (D.8) [Wu, 1982]. Figure E.1 in Sect. E.2 provides an overview of the input data. The procedure of calculating sea salt emissions by Ovadnevaite et al. [2014] is described in Chap. 4 and in Apdx. I. The emission parameterization by Gong is abbreviated as GO03 and the parameterization by Ovadnevaite as OV14.

6.2.2 Emissions

The contribution of major sulfur oxide sources to the atmospheric particulate sulfate budget was to be analyzed in this study. Namely, these sources are the anthropogenic energy production and shipping sectors as well as the natural sea salt emissions. Hence, the five emission cases *Base*, *NoShips*, *NoEnergy*, *NoSalt*, and *OV14* were defined (Table 6.1). The contribution of the shipping and the energy production sectors were calculated by subtracting the results of the *NoShips* and *NoEnergy* cases, respectively, from results of the *Base* case (Eqs. (6.1) and (6.2)). The contribution of sea salt emission was calculated from modeled Na^+ concentrations of *Base* and *OV14* cases with Eqs. (6.3) and (6.4), respectively. The numbers 0.3086 and 0.0776 are the mass fraction of Na^+ and $SO_4{}^{2-}$ in sea salt, respectively, as defined in the CMAQ code. Details are given in Sect. E.1. The remaining mass fractions is denoted as *OthrAnthr*.

$$\mathrm{P}_{\mathrm{Shipping},\mathrm{SO}_4^{2-}} = \mathrm{P}_{\mathrm{Base},\mathrm{SO}_4^{2-}} - \mathrm{P}_{\mathrm{NoShips},\mathrm{SO}_4^{2-}} \tag{6.1}$$

$$\mathrm{P}_{\mathrm{Energy},\mathrm{SO}_4^{2-}} = \mathrm{P}_{\mathrm{Base},\mathrm{SO}_4^{2-}} - \mathrm{P}_{\mathrm{NoEnergy},\mathrm{SO}_4^{2-}} \tag{6.2}$$

$$\mathrm{P}_{\mathrm{SeaSalt},\mathrm{GO03},\mathrm{SO}_4^{2-}} = \frac{\mathrm{P}_{\mathrm{Base},\mathrm{Na}^+} \times 0.0776}{0.3086} \approx \frac{\mathrm{P}_{\mathrm{Na}}}{4} \tag{6.3}$$

$$\mathrm{P}_{\mathrm{SeaSalt},\mathrm{OV14},\mathrm{SO}_4^{2-}} = \frac{\mathrm{P}_{\mathrm{OV14},\mathrm{Na}^+} \times 0.0776}{0.3086} \approx \frac{\mathrm{P}_{\mathrm{Na}}}{4} \tag{6.4}$$

$$\mathrm{P}_{\mathrm{OthrAnthr},\mathrm{SO}_4^{2-}} = \mathrm{P}_{\mathrm{Base},\mathrm{SO}_4^{2-}} - \mathrm{P}_{\mathrm{Shipping},\mathrm{SO}_4^{2-}} - \mathrm{P}_{\mathrm{Energy},\mathrm{SO}_4^{2-}} - \mathrm{P}_{\mathrm{SeaSalt},\mathrm{GO03},\mathrm{SO}_4^{2-}} \tag{6.5}$$

Turning emission sectors in simulations on and off, and calculating differences between these simulations adds uncertainty to the results due to non-linear processes taking place. This uncertainty is assessed as described in Sect. 6.2.3 based on sea salt sulfate concentrations calculated with the *NoSalt* emission case (Eqs. (6.6) and (6.7)), which does not contains sea salt but all other emissions.

$$\mathrm{P}_{\mathrm{SeaSalt},\mathrm{GO03},\mathrm{SO}_4^{2-},\mathrm{diff}} = \mathrm{P}_{\mathrm{Base},\mathrm{SO}_4^{2-}} - \mathrm{P}_{\mathrm{NoSalt},\mathrm{SO}_4^{2-}} \tag{6.6}$$

$$\mathrm{P}_{\mathrm{SeaSalt},\mathrm{SO}_4^{2-},\mathrm{diff}} = \mathrm{P}_{\mathrm{OV14},\mathrm{SO}_4^{2-}} - \mathrm{P}_{\mathrm{NoSalt},\mathrm{SO}_4^{2-}} \tag{6.7}$$

The construction of the *NoShips* and *NoSalt* emission cases is unambiguous because shipping and sea salt emissions are calculated separately and can be deactivated for simulations – the first

Table 6.1: Emission cases. Energy and shipping sector related emissions are calculated by the difference between the Base and the respective no-emission case.

Case	Description
Base	standard emissions, sea salt emissions by Gong [2003]
NoShips	like Base, no ship emissions
NoEnergy	like Base, no energy production sector emissions (see text)
NoSalt	like Base, no sea salt emissions
OV14	like Base but sea salt emissions according to Ovadnevaite et al. [2014]

are set up prior to the simulations and the latter are calculated inland on simulation run time. The *NoEnergy* emissions are not as simple to construct as they consist of public and industrial energy production emissions which are not explicitly given as described in the next paragraph.

The model emissions are calculated from the national emissions that were reported to EMEP for the year 2013 and categorized into the 11 SNAP sectors [European Environment Agency, 2001]. The annual sectoral SO_x, PM_{10}, and $PM_{2.5}$ emissions of the EU-28 countries are displayed in Table 6.2. The sector S2 represents the total public energy production sector emissions and only these. The industrial energy production emissions are included in the S3 and S4 sectors, which also aggregate non-energy-production related emissions. Hence, the S3 and S4 emissions

Table 6.2: Total emissions of SO_2, PM_{10}, and $PM_{2.5}$ reported to EMEP by the EU-28 countries. Sulfate $PM_{2.5}$ is derived according to split factors used in SMOKE for Europe [Bieser et al., 2011]. The *NoEnergy* case emissions are calculated by multiplying the reported SO_2 and sulfate $PM_{2.5}$ emissions by the vertical split factors of layers 1 to 3 (sum) in Table E.4. The raw data was obtained from the Webab Emission database of the Centre on Emission Inventories and Projections (CEIP) [CEIP, 2016] and is attached in the supplement as `supplement/paper3/emis/emep_emissions_snap_2013.csv`.

SNAP Sector		Reported Emissions			Sulfate in $PM_{2.5}$		*NoEnergy* emissions	
		SO_2 [Gg S a^{-1}]	PM_{10} [Gg a^{-1}]	$PM_{2.5}$ [Gg a^{-1}]	Split [-]	SO4 $PM_{2.5}$ [Gg S a^{-1}]	SO_2 [Gg S a^{-1}]	SO_4^{2-} $PM_{2.5}$ [Gg S a^{-1}]
S1	Combustion in energy and transformation industries	922.71	98.88	66.25	0.2127	4.70	0.00	0.00
S2	Non-industrial combustion plants	271.76	769.72	697.12	0.1736	40.34	271.76	40.34
S3	Combustion in manufacturing industry	327.60	95.99	75.11	0.2049	5.13	226.50	3.55
S4	Production processes	165.30	193.92	98.50	0.0986	3.24	94.22	1.85
S5	Extraction & distribution of fossil fuels and geothermal energy	1.08	66.63	12.52	0.2000	0.83	0.21	0.16
S6	Solvent and other product use	0.14	87.72	38.39	0.0000	0.00	0.14	0.00
S7	Road transport	2.98	226.41	167.46	0.0191	1.07	2.98	1.07
S8	Other mobile sources and machinery	43.44	86.25	80.07	0.0512	1.37	43.44	1.37
S9	Waste treatment and disposal	9.38	26.87	20.01	0.0652	0.43	0.22	0.01
S10	Agriculture	2.28	299.26	66.64	0.0502	1.12	2.28	1.12
S11	Other sources and sinks	0.00	0.00	0.00	0.0000	0.00	0.00	0.00
Sum		1746.67	1951.66	1322.06		58.22	641.75	49.45

need to be split into energy production and non-energy-production industrial emissions. As a standard procedure for model emission pre-processing, the emissions of all sectors are divided by predefined split factors (see Table E.4) into 15 vertical layers equaling the 15 lowest model grid layers. The splits are set according to the emission height of the individual sectors, i.e. stack height. The stacks of power plants are commonly higher than 120 m. Therefore, all emissions emitted into model layer 4, which starts at ≈ 126 m, are considered as energy production emissions and set to 0.0 in the *NoEnergy* case. A fraction of non-energy-production related emissions is removed by this procedure as well but this fraction is very low. The Table 6.2 shows the amounts of SO_2 and sulfate $PM_{2.5}$ that are emitted in the *Base* and *NoEnergy* cases per sector by the EU-28 countries. The EU-28 emissions do not equal the sum of all emissions in the domain but the relative distribution amongst the sectors and chemical compounds is comparable. This emission setup is briefly discussed in Sect. 6.3.5.

6.2.3 Evaluation Methodology

The modeled sulfate PM_{10} concentrations are compared with data from 22 EMEP measurement stations, whereas sulfate $PM_{2.5}$ concentrations are evaluated at four stations and gas phase SO_2 concentrations at 21 stations. The latter evaluation is performed in order to investigate whether discrepancies in the sulfate PM comparison are caused by inappropriate SO_2 to SO_4^{2-} conversion rates. The stations are listed in Table 6.3 and their locations are shown in Fig. 6.1.

Table 6.3: EMEP stations that were used for model evaluation. The column data indicates which measurement data were available for the respective station. PM_{10} and $PM_{2.5}$ mean sulfate PM_{10} and sulfate $PM_{2.5}$ concentrations, respectively.

Station ID	Station Name	Data	Lon	Lat	Height [m]	Location
DE0002R	Waldhof	PM_{10}, $PM_{2.5}$, SO_2	10.76	52.80	74	Inland
DE0007R	Neuglobsow	PM_{10}, $PM_{2.5}$, SO_2	13.03	53.17	62	Inland
DE0044R	Melpitz	PM_{10}, $PM_{2.5}$	12.93	51.53	86	Inland
DK0003R	Tange	PM_{10}, SO_2	9.60	56.35	13	Inland
DK0008R	Anholt	PM_{10}, SO_2	11.52	56.72	40	Coast
DK0012R	Risoe	PM_{10}, SO_2	12.09	55.69	3	Coast
DK0031R	Ulborg	PM_{10}, SO_2	8.43	56.28	10	Coast
FI0009R	Utö	PM_{10}, SO_2	21.38	59.78	7	Coast
FI0017R	Virolahti II	PM_{10}, SO_2	27.69	60.53	4	Coast
LT0015R	Preila	PM_{10}, SO_2	21.07	55.35	5	Coast
NL0091R	De Zilk	PM_{10}, SO_2	4.50	52.30	4	Coast
NO0002R	Birkenes II	PM_{10}, SO_2	8.25	58.39	219	Mixed
NO0015R	Tustervatn	PM_{10}, SO_2	13.92	65.83	439	Inland
NO0039R	Kårvatn	PM_{10}, SO_2	8.88	62.78	210	Coast
NO0056R	Hurdal	PM_{10}, SO_2	11.08	60.37	300	Inland
PL0002R	Jarczew	PM_{10}, SO_2	21.98	51.82	180	Inland
PL0004R	Leba	PM_{10}, SO_2	17.53	54.75	2	Coast
PL0005R	Diabla Gora	PM_{10}, $PM_{2.5}$, SO_2	22.07	54.15	157	Inland
SE0005R	Bredkälen	PM_{10}, SO_2	15.33	63.85	404	Inland
SE0011R	Vavihill	PM_{10}, SO_2	13.15	56.02	175	Coast
SE0012R	Aspvreten	PM_{10}, SO_2	17.38	58.80	20	Coast
SE0014R	Råö	PM_{10}, SO_2	11.91	57.39	5	Coast

The model and observational data sets are compared via the three statistical metrics residual absolute error (RAE), mean normalized bias (MNB), and Spearman's correlation coefficient (R), which are defined by the Eqs. (A.1), (A.2), and (A.3). The modeled concentrations of the grid cells, in which the EMEP stations are located, were used for the evaluation and no average values of neighboring grid cells were considered. The model data at the six stations Melpitz (DE0044R, inland), Ulborg (DK0031R, North Sea coast), Anholt (DK0008R, island, Kattegat), Virolahti II (FI0017R, coast, eastern Baltic Sea), Kårvatn (NO0039R, Norwegian Atlantic coast), and

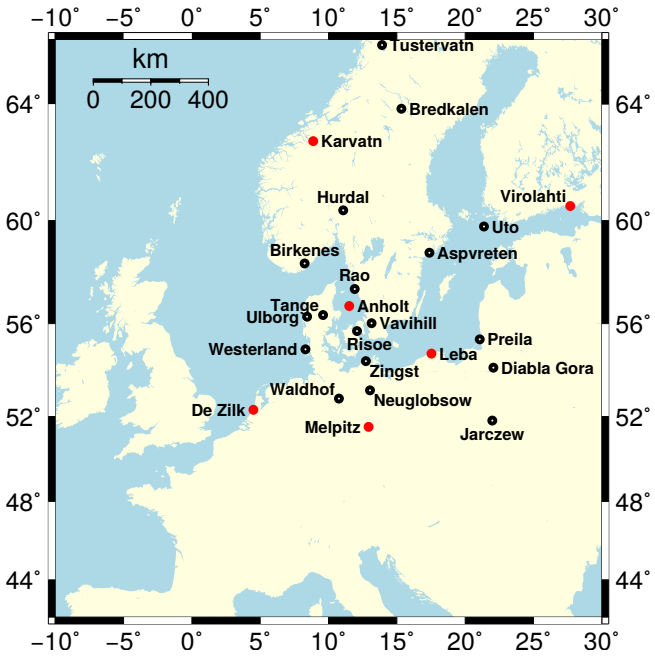

Figure 6.1: EMEP stations considered for the statistical evaluation of the model results. The stations indicated by red dots are evaluated in more detail (see text). The model domains are shown in Fig. 2.3

Leba (PL0004R, coast, southern Baltic Sea) are evaluated in more detail by considering time series plots of daily average sulfate PM_{10} concentrations. The stations represent geographically different located and, thus, represent different air quality regimes. The geographic locations are:

- Melpitz: inland station with low marine impact
- Anholt: station located on an island in the Kattegat, affected by shipping and sea salt emissions but also by emissions from the Danish mainland
- Virolahti II: coastal station located in the eastern Baltic Sea close to Helsinki
- De Zilk: coastal stations located at the Dutch North Sea coast, impacted by emissions of ships traveling from the English Channel to Hamburg or the Baltic Sea
- Kårvatn: remote station in mountainous territory in Northern Norway affected by coastal air from the North Atlantic
- Leba: station at the Polish Baltic Sea coast

The contribution of the energy production and shipping sectors to the particulate sulfate air pollution is calculated by subtracting the simulations results of the *NoEnergy* and *NoShips* cases from simulation results of the *Base* case. This procedure would be correct if all processes were linear.[a]. However, this situation does not prevail because the predominant number of chemical reaction and physical deposition processes are non-linear. Therefore, the sectoral separation applied in this study adds uncertainty to the results. If yonder uncertainty is on the same level or lower than the uncertainty inherent in the model, it can be ignored. Otherwise, the method should not be applied. In order to evaluate this, sea salt sulfate calculated by the same method as applied for the energy and shipping sector contributions (Eqs. (6.6) and (6.7)) is compared

[a]Even all processes affecting sulfate concentrations needed to be linear with respect to the current sulfate concentration and not linear with respect to other concentrations.

with sea salt sulfate concentrations derived from sodium concentrations (Eqs. (6.3) and (6.4)). To keep the textual descriptions legible, the first method is denoted as "subtraction method" and the second one as "sodium method". The results of the evaluation are presented and discussed in Sect. 6.3.4.

6.3 Results and Discussion

First, the sulfate PM_{10} and $PM_{2.5}$ predictions of the *Base* and *OV14* cases are validated against measurements. Second, SO_2 concentrations are briefly regarded in order to identify whether discrepancies in the sulfate concentrations were caused by inappropriate SO_2 to SO_4^{2-} conversion. Third, the contribution of the three source sectors shipping, energy production, and sea salt is analyzed in detail. Fourth, the subtraction method is evaluated by comparing sea salt sulfate calculated by the subtraction and sodium methods with each other and with measurements. Finally, the results are recapitulated in a summarizing discussion.

6.3.1 Particulate Sulfate Concentrations

Model sulfate PM_{10} concentrations are evaluated with EMEP measurements in this section. Before describing and discussing the simulation results, their representation should be briefly introduced: Table 6.4 contains RAE, MNB, and R of the *Base* and *OV14* emission cases for all stations during the winter and summer seasons. In addition, Fig. 6.2 shows daily averages of modeled and measured sulfate PM_{10} concentrations at the six stations Melpitz, Ulborg, Anholt, Virolahti II, Kårvatn, and Leba. The modeled concentrations are represented by colored stacked vertical bars, whereby each color indicates another emission source sector. In this section, the sectoral contribution is not relevant but the comparison of their sums with measurements (black symbols) is in focus.

The time series plots (Fig. 6.2) shows that the sulfate PM_{10} concentrations are considerably higher during winter. Such a seasonal variation is reasonable because (a) residential heating and heating related energy production and (b) increased sea salt emissions due to higher mean wind speeds lead to higher SO_2 and particulate sulfate emissions in winter. The temporal occurrence of peak concentrations is well met during most of that time. One episode with two peaks of very high concentrations is predicted at Virolahti II in mid-February. However, the measurements indicate a strong decline during that episode. One major sulfur emission source (Helsinki) is located at the Finnish coastline between the stations of Utö and Virolahti II, which impacts one of the stations during some episodes. In the specific episode no air pollution from Helsinki caused the peaks but air pollution was carried by southeasterly winds from the outer boundary towards Virolahti II yielding the first peak. This air pollution parcel was then transported counterclockwise by the wind over the eastern Baltic Sea to Helsinki and a second time to Virolahti II inducing the second peak. The station of Utö (not plotted) shows two similar peaks, which are slightly shifted in time because the air pollution parcel arrived that station several hours later. At Kårvatn in northern Norway, in turn, approximately half of the measured peaks are realized by the model but the predicted concentrations are apparently far too high, which is also indicated by high positive MNB values. At Melpitz, Anholt, Ulborg, and to some degree at Leba during winter and at Virolahti II during summer, the baseline and most peak concentration measurements are remarkably well captured by the model. Discrepancies in the magnitude of peak concentrations at the other stations and seasons might be caused by the spatial blurring of particulate sulfate concentrations by the grid resolution of 24 km. At Leba, for instance, sulfate PM_{10} concentrations are underpredicted at nearly every day during summer and in two episodes during winter. This is clearly reflected by negative MNBs throughout the year, whereas during winter, the MNBs are positive at all other stations indicating overpredictions of concentrations. They are, besides, particularly high at Ulborg, Utö, Bredkälen, Aspvreten and all Norwegian

Table 6.4: Statistical metrics for comparing modeled and measured sulfate PM_{10} concentrations: RAE, MNB, and R. Data for winter (left) and summer (right) for two emission cases (*Base* and *OV14*) are shown. The n indicates the number of daily average values considered.

		Winter 2013				Summer 2013			
Station	Case	n	RAE	MNB	R	n	RAE	MNB	R
Waldhof	Base	59	0.54	0.84	0.63	62	0.23	-0.14	0.43
DE0002R	OV14	59	0.54	0.73	0.64	62	0.23	-0.16	0.42
Neuglobsow	Base	58	0.44	0.37	0.67	62	0.21	0.13	0.55
DE0007R	OV14	58	0.44	0.27	0.68	62	0.21	0.11	0.56
Melpitz	Base	59	0.57	0.56	0.72	62	0.27	-0.08	0.11
DE0044R	OV14	59	0.56	0.46	0.74	62	0.28	-0.08	0.12
Tange	Base	44	0.37	0.47	0.47	62	0.23	-0.12	0.34
DK0003R	OV14	44	0.34	0.17	0.58	62	0.25	-0.26	0.34
Anholt	Base	59	0.33	0.61	0.59	29	0.23	-0.32	0.60
DK0008R	OV14	59	0.32	0.24	0.58	29	0.30	-0.44	0.58
Risoe	Base	54	0.46	0.81	0.48	62	0.15	-0.06	0.63
DK0012R	OV14	54	0.41	0.52	0.53	62	0.19	-0.24	0.61
Ulborg	Base	57	0.35	2.26	0.58	62	0.23	-0.15	0.36
DK0031R	OV14	57	0.26	1.13	0.61	62	0.29	-0.37	0.45
Utö	Base	59	0.46	1.48	0.59	57	0.19	-0.07	0.49
FI0009R	OV14	59	0.42	1.13	0.62	57	0.19	-0.13	0.49
Virolahti II	Base	59	0.43	1.04	0.55	62	0.12	0.07	0.64
FI0017R	OV14	59	0.42	0.94	0.54	62	0.12	0.06	0.63
Preila	Base	30	0.87	0.71	0.32	60	0.29	-0.36	0.29
LT0015R	OV14	30	0.87	0.60	0.33	60	0.30	-0.39	0.27
De Zilk	Base	28	0.49	0.46	0.60	31	0.29	0.03	-0.06
NL0091R	OV14	28	0.48	0.27	0.64	31	0.28	-0.07	-0.02
Birkenes II	Base	59	0.31	2.84	0.44	62	0.15	1.10	0.39
NO0002R	OV14	59	0.28	2.28	0.43	62	0.15	0.98	0.39
Tustervatn	Base	53	0.35	9.95	0.25	53	0.13	2.14	-0.36
NO0015R	OV14	53	0.22	5.74	0.29	53	0.09	1.23	-0.20
Kårvatn	Base	55	0.67	22.45	0.12	58	0.21	2.29	0.42
NO0039R	OV14	55	0.22	6.73	0.27	58	0.09	0.75	0.37
Hurdal	Base	59	0.75	9.19	0.30	62	0.12	0.94	0.61
NO0056R	OV14	59	0.73	8.79	0.31	62	0.12	0.94	0.61
Jarczew	Base	58	0.71	0.52	0.48	62	0.36	0.03	0.43
PL0002R	OV14	58	0.71	0.49	0.47	62	0.36	0.04	0.43
Leba	Base	59	0.53	-0.20	0.74	62	0.45	-0.29	0.30
PL0004R	OV14	59	0.56	-0.27	0.75	62	0.47	-0.32	0.29
Diabla Gora	Base	58	0.58	0.51	0.59	62	0.17	0.14	0.29
PL0005R	OV14	58	0.56	0.44	0.62	62	0.16	0.14	0.29
Bredkälen	Base	43	0.33	3.38	0.64	60	0.08	1.14	0.24
SE0005R	OV14	43	0.31	2.84	0.67	60	0.08	1.15	0.25
Vavihill	Base	59	0.36	0.97	0.73	53	0.13	0.23	0.55
SE0011R	OV14	59	0.33	0.72	0.73	53	0.12	0.12	0.56
Aspvreten	Base	59	0.37	1.40	0.69	60	0.11	0.50	0.59
SE0012R	OV14	59	0.33	1.14	0.68	60	0.11	0.44	0.57
Råö	Base	59	0.38	1.22	0.58	61	0.15	0.32	0.66
SE0014R	OV14	59	0.30	0.69	0.51	61	0.18	0.06	0.64

stations. Here, the MNBs were again lower in summer. Furthermore, they were demonstrably negative at most German and Danish stations and Leba, and positive at the Norwegian and Swedish stations. At most stations, the correlation coefficient (R) was strikingly found to be higher during winter taking values above 0.5 and partly even above 0.6. Exceptions in winter are Preila and most Norwegian stations which have considerably lower R values. During summer, the R of several Danish, German and Dutch stations falls below 0.5. De Zilk and Tustervatn even have negative R values. Thus, with respect to R values, the predicted concentrations are

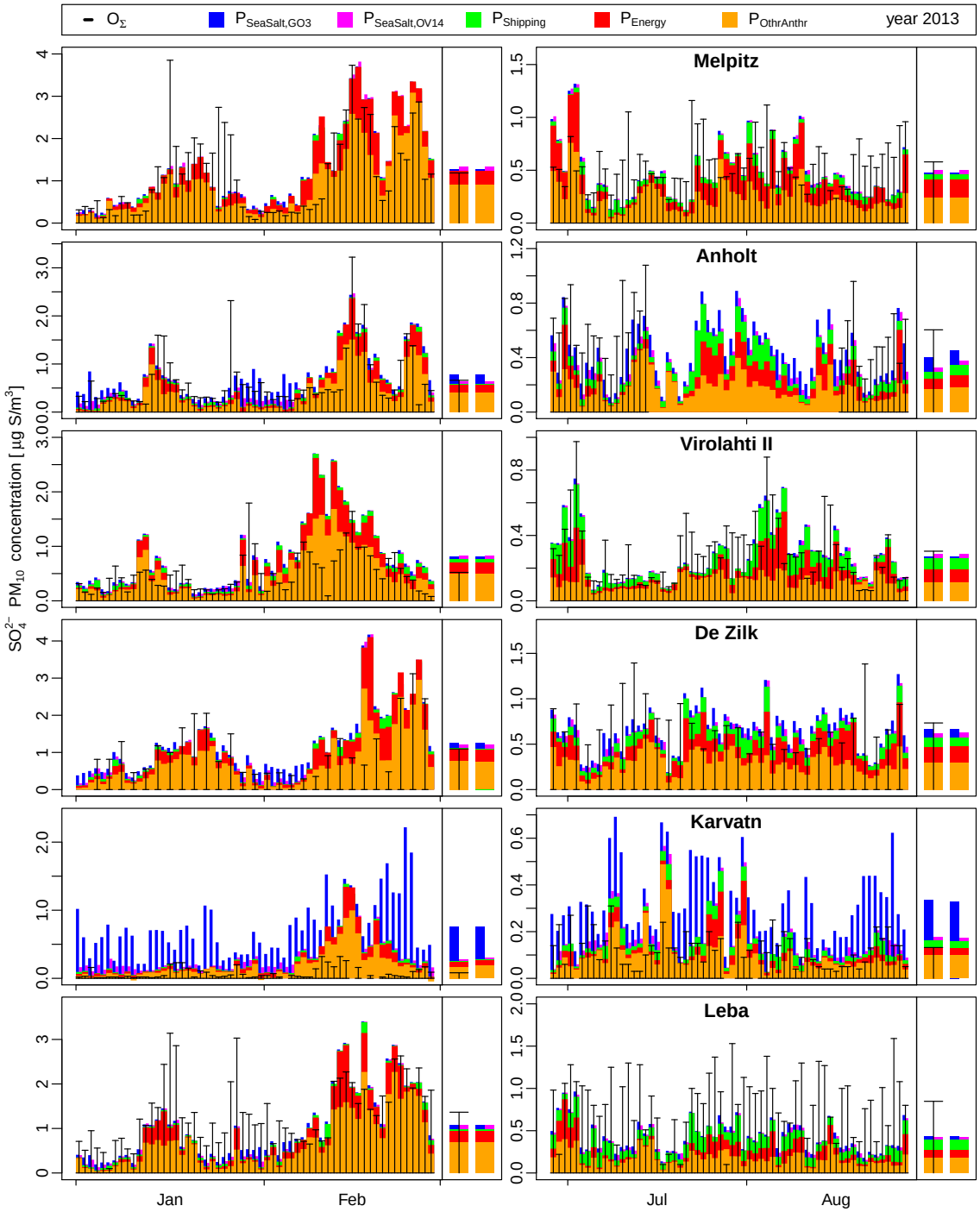

Figure 6.2: Time Series of daily average sulfate PM_{10} concentrations at six EMEP stations (top to bottom) in winter (left) and summer (right). The colored vertical bars represent modeled concentrations split into source sectors. The blue and magenta bars are not stacked because sea salt emissions are calculated either by the GO03 (*Base* case) or by the OV14 parameterization (*OV14* case). Measured concentrations are plotted as black horizontal lines. The vertical lines are included for a simplified visual comparison. Two-month average concentrations are shown to the right of each time series. Here, the left bar shows the average concentrations considering only days with measurements. The averages on the right are calculated from all model values.

closer to the measurements in winter, whereas, with respect to MNB values, they are closer in summer.

Comparing the *OV14* case with the *Base* case shows slight improvements of the MNBs and R during winter at most stations. During summer the MNBs are reduced as well. This has, however, a variable impact: The MNBs are improved at stations where SO_4^{2-} concentrations are overpredicted in the *Base* case – namely Norwegian and Swedish ones – and they get worse at stations where sulfate concentrations are underpredicted in the *Base* case – namely German and Danish stations.

The high MNBs at the Norwegian stations Tustervatn and Kårvatn are partly caused by overpredictions in the sea salt emissions of the standard CMAQ sea salt setup. Because numerous fjords along the Norwegian Atlantic coast reach far into inland regions, the number of grid cells containing the maximum amount of surf zone area is high (see Fig. H.1, Apdx. H). Thus, large amounts of sea salt are emitted within the fjords. However, in reality, the fjords are well protected against wind and waves and their salinity is lower than 35 ‰. Therefore, sea salt emissions are considerably overestimated along the Norwegian Atlantic coast leading to the described overpredictions. The OV14 parameterization does not include a special treatment of surf zone emissions which leads to considerably lower sea salt emissions and, hence, to reduced overpredictions of sulfate concentrations. However, it has to be noted that the sulfate PM_{10} concentrations are overestimated even in the *OV14* and *NoSalt* cases.

The low correlations and high overpredictions might also be caused by the mountainous area all over Norway which is still a challenge for meteorological and chemistry transport models, particularly at a resolution of 24 km: the resolution needed to be considerably finer. According to the EMEP site descriptions, the station Kårvatn is quite distantly located to most emission sources. Since the predicted sulfate concentrations are too high even after subtracting the sea salt related sulfate, one might assume that the deposition velocity of sulfate particles during their transport from sources to this EMEP station is too low. However, this theory cannot be validated or falsified in this study.

6.3.2 Sulfur Oxide Concentrations

Discrepancies between modeled and measured sulfate PM_{10} concentrations might result from shortcomings in the SO_2-SO_4^{2-} conversion rates. Hence, considering the sum of SO_2 and SO_4^{2-} concentrations might yield improved statistical metric compared to evaluating pure particulate sulfate. In a first step, SO_2 concentrations are regarded separately, followed by a second step in which the SO_4^{2-} concentrations are added. Since the results of the *Base* and *OV14* sea salt cases did not deviate much at most stations in Sect. 6.3.1, only *Base* case results are evaluated in this section.

Table 6.5 shows statistical metric of modeled and measured SO_2 concentrations at 21 of the EMEP stations (no SO_2 measurements at Melpitz). The correlation is very low at most of the Norwegian stations throughout the year. During summer, R is even negative at Tustervatn, Kårvatn, and Hurdal. At most German, Danish, and Swedish stations, R is close to 0.5 and above during winter. During summer, R is below 0.3 at half of the stations and only four stations' R values are above 0.5. A clear geographical pattern is not recognizable in the R values. Corresponding R values of sulfate PM_{10} concentrations (Table 6.4) are higher than those of SO_2 concentrations at most stations indicating that sulfate model results and measurements correlate better.

The biases are positive at all stations throughout winter and at nearly all stations during summer with the exceptions of three Norwegian and two Swedish stations. Three of these five stations – Kårvatn, Tustercatn and Bredkälen – are in the same mountainous region so that a similar pattern is likely. The MNB values were seasonally higher in winter than in summer and they were also higher than those of the corresponding sulfate PM_{10} concentrations. At Hurdal, the SO_2 concentrations were, besides, considerably stronger overestimated than at

Table 6.5: Statistical metrics for comparing modeled and measured SO_2 concentrations: RAE, MNB, and R. Data for winter (left) and summer (right) of the *Base* emission case are shown.

	Winter 2013				Summer 2013			
Station	n	RAE	MNB	R	n	RAE	MNB	R
Waldhof	59	1.43	2.68	0.48	62	0.34	0.52	0.36
Neuglobsow	59	1.41	1.29	0.51	62	0.28	0.23	0.56
Tange	44	0.61	6.51	0.61	54	0.16	1.23	0.28
Anholt	59	0.77	7.18	0.59	29	0.16	0.39	0.25
Risoe	58	1	7.36	0.61	62	0.19	0.66	0.57
Ulborg	57	0.67	10.39	0.67	62	0.13	0.4	0.22
Utö	59	0.61	4.2	0.56	57	0.16	0.22	0.5
Virolahti II	59	0.96	3.19	0.36	62	0.3	2.06	0.73
Preila	31	1.99	9.34	0.63	62	0.31	2.63	0.18
De Zilk	41	2.69	3.14	0.34	34	0.58	0.36	0.55
Birkenes II	50	0.39	5.14	0.53	48	0.08	-0.23	0.39
Tustervatn	35	0.22	5.69	0.33	11	0.04	-0.42	-0.11
Kårvatn	29	0.21	4.94	0.28	21	0.03	-0.39	-0.16
Hurdal	29	0.8	20.94	0.26	23	0.11	2.07	-0.01
Jarczew	58	5.58	3.58	0.49	62	1.07	3.97	0.21
Leba	59	1.6	1.75	0.65	62	0.34	0.48	0.41
Diabla Gora	58	2.59	2.39	0.72	62	0.3	0.54	0.11
Bredkälen	26	0.51	7.97	0.78	46	0.08	-0.86	0.13
Vavihill	58	0.73	5.65	0.53	53	0.15	0.65	0.57
Aspvreten	57	0.67	7.27	0.4	61	0.13	0.54	0.33
Råö	57	0.62	3.68	0.39	62	0.22	-0.31	0.36

Table 6.6: Statistical metrics for comparing total model and measurement SO_2+SO_4^{2-} concentrations (SO_2 + sulfate PM_{10}): RAE, MNB, and R. Data for winter (left) and summer (right) for the *Base* emission case are shown.

	Winter 2013				Summer 2013			
Station	n	RAE	MNB	R	n	RAE	MNB	R
Waldhof	59	1.62	1.08	0.79	62	0.42	0.10	0.44
Neuglobsow	58	1.50	0.44	0.76	62	0.34	-0.02	0.61
Tange	44	0.78	1.12	0.70	54	0.31	0.05	0.25
Anholt	59	0.95	1.58	0.63	29	0.26	-0.17	0.43
Risoe	54	1.27	1.93	0.68	62	0.23	0.13	0.62
Ulborg	57	0.93	2.13	0.67	62	0.28	-0.10	0.39
Utö	59	0.97	2.05	0.67	57	0.23	-0.06	0.66
Virolahti II	59	1.32	1.62	0.52	62	0.33	0.60	0.74
Preila	29	2.56	1.96	0.69	60	0.35	0.07	0.20
De Zilk	19	2.63	1.17	0.69	16	0.62	0.11	0.74
Birkenes II	50	0.62	2.66	0.62	48	0.15	0.02	0.64
Tustervatn	32	0.59	6.84	0.42	11	0.13	1.04	-0.58
Kårvatn	29	0.74	9.67	0.36	21	0.21	1.28	-0.04
Hurdal	29	1.43	8.23	0.49	23	0.10	0.20	0.83
Jarczew	58	5.77	1.99	0.46	62	1.07	1.12	0.31
Leba	59	1.63	0.42	0.77	62	0.58	-0.14	0.45
Diabla Gora	58	2.83	1.45	0.74	62	0.40	0.27	0.25
Bredkälen	22	1.05	4.51	0.75	44	0.10	0.16	0.06
Vavihill	58	1.03	1.76	0.75	53	0.23	0.30	0.60
Aspvreten	57	0.98	2.32	0.73	59	0.15	0.23	0.67
Råö	57	0.97	1.81	0.60	61	0.27	-0.14	0.62

other stations. The station at Hurdal is affected by air pollutants emitted in the vicinity of Oslo when southerly winds prevail. The meteorological situation at Hurdal is complicated to be reproduced by meteorological models due to its geographic location [Wang et al., 2015]. The variable transport of air pollution from Oslo to Hurdal might not be correctly reproduced causing

the observed deviations.

Particularly during winter, the modeled SO_2+SO_4^{2-} concentrations are expected to overestimate the measurements at most stations since modeled SO_2 as well as sulfate PM_{10} concentrations are already overestimated at these stations. In winter, this assumption is confirmed by the MNB values of SO_2+SO_4^{2-} (Table 6.6) which are positive and in between the MNB values of SO_2 and SO_4^{2-}. In summer, on the other hand, the MNBs improve at a few stations compared to the MNBs of sulfate PM_{10}. Therefore, particulate sulfate and SO_2 concentrations are under- and overestimated, respectively, – or vice versa. Exemplary stations are Birkenes II and Preila. The R values of SO_2+SO_4^{2-} are greater than 0.6 at several Danish, German, Swedish, and Polish stations during winter which is an improvement compared to R values of sulfate PM_{10}. During summer, the SO_2+SO_4^{2-} R values are also above sulfate R values at most stations but they are lower than winter values. At some stations, such as Bredkälen, the R value decreases (0.06) with respect to the values of SO_2 (0.13) and sulfate PM_{10} (0.24). Exemplary at Leba, combining sulfate PM_{10} and SO_2 data to total atmospheric sulfur (SO_2+SO_4^{2-}) leads to lower biases than the sulfate PM_{10} concentrations do (see Sect. 6.3.1).

Since the R values are improved at most stations – comparing SO_2+SO_4^{2-} to sulfate PM_{10} –, one might assume that the SO_2-SO_4^{2-} conversion is not correctly represented in the model. However, particularly during summer, atmospheric SO_2 and sulfate PM_{10} concentrations are overestimated and, thus, the SO_2+SO_4^{2-} concentrations are overestimated at most stations, as well. Hence, sulfur emissions are too high or sulfur depositions too low.

6.3.3 Sectoral Contribution

In this section, the contribution from the source sectors energy production, shipping, and sea salt is considered. Figure 6.2 shows time series of daily average measured and model sulfate PM_{10} concentrations at six stations. In Fig. 6.3, two-month average observed and modeled sulfate PM_{10} and $PM_{2.5}$ concentrations are given for all stations. Similar to Fig. 6.2, the modeled concentrations are split into the contribution from the source sectors energy production, shipping, OthrAnthr, and sea salt. Fig. 6.4 contains the relative sectoral contributions.

As discussed in Sect. 4.3.2, the sea salt emissions at the Norwegian Atlantic coast are considerably overestimated in the *Base* case. Resulting, the sea salt concentrations are overestimated at the Norwegian stations Tustervatn and Kårvatn leading to relative sulfate composition significantly different from other stations' compositions. For that reason, Tustervatn and Kårvatn are ignored in the following description. The absolute concentrations contributed by the non-sea-salt source sectors are similar at these two stations and the other stations.

In winter, the OthrAnthr sectors contributes 60 % and even more to the sulfate PM_{10} concentration at all stations. A quarter of the stations, it is even above 70 %. In the $PM_{2.5}$ fraction, the share is of similar magnitude. The contribution to sulfate PM_{10} from the energy sector is between 15 % and 30 %, that from the shipping sector below 10 %, and that from standard sea salt emissions (GO03) is between 3 % and 30 %. The $PM_{2.5}$ contribution of the anthropogenic sectors is similar to their PM_{10} contribution but sea salt share of the GO03 parameterization is considerably lower. The shipping related sulfate is at least twice as high at coastal stations – e.g. Virolahti II, Utö, and Leba – than at inland stations. In addition at these stations, the contribution of sea salt related sulfate by GO03 is three to four times as high. Sea salt emissions in the *OV14* case contribute less than 10 % and, hence, at coastal stations less than those in the GO03 case. However, the contribution by OV14 is approximately constant at coastal as well as at inland stations yielding higher sulfate PM_{10} concentration as GO03 at inland ones. The sulfate $PM_{2.5}$ share is similar to that of GO03 at coastal stations but considerably higher in the inland.

During summer, the contribution of the OthrAnthr sector is lower, namely 40 % to 50 % at most stations. The contribution from energy production is approximately on the same level as in winter and varies considerably between the stations. In contrast, the share of the shipping

sector is higher. Shipping emissions contribute 15 % to 30 % at coastal stations and 10 % to 20 % at inland stations. Moreover, the time series at Melpitz (Fig. 6.2 top-right panel) indicates that episodes with high shipping sector related sulfate concentrations exist at inland stations during summer. The relative contribution from sea salt is in summer similar to that in winter but

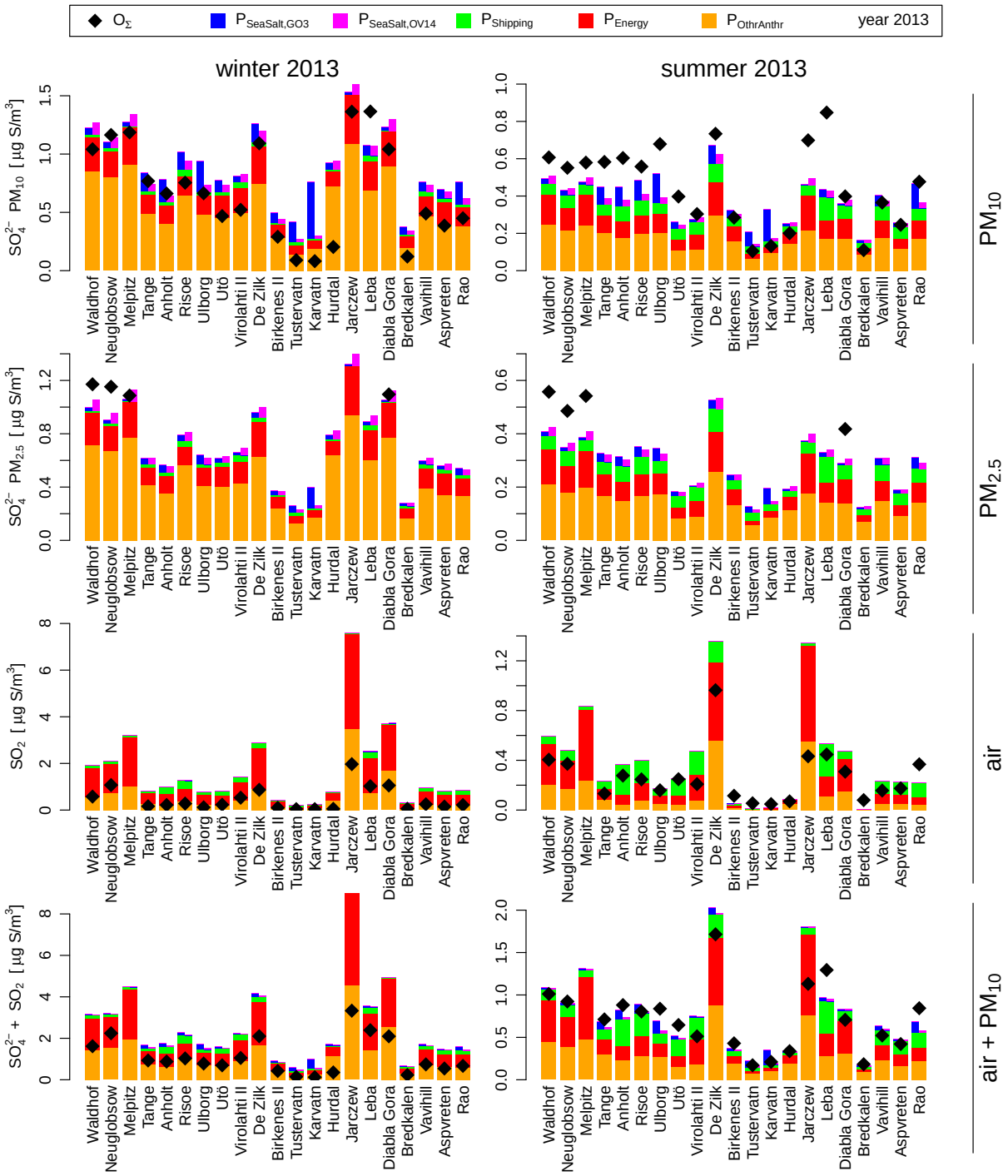

Figure 6.3: Stacked histograms showing the sectoral contributions to modeled two-month average sulfate PM_{10}, suflate $PM_{2.5}$, SO_2, and total atmospheric sulfur concentrations (top to bottom) in winter and summer (left to right). Measurements are drawn as black rhombi. Similar to Fig. 6.2 the base are split at the top differentiating between GO03 and OV14 sea salt sulfate.

the absolute contribution is considerably lower. The latter is due to a lower mean wind speed in summer. The absolute sulfur emissions from the energy production and OthrAnthr source sectors are reduced, too, which explains that the relative sea salt contribution to particulate sulfate is similar in both seasons. Contrary, the shipping related absolute sulfate concentrations approximately double during summer. Therefore, their relative contribution rises significantly from winter to summer.

Anholt and Virolahti II (Fig. 6.2, second and third panel from the top) are both coastal stations with a particularly high contribution from the shipping sector during summer. The salinity is

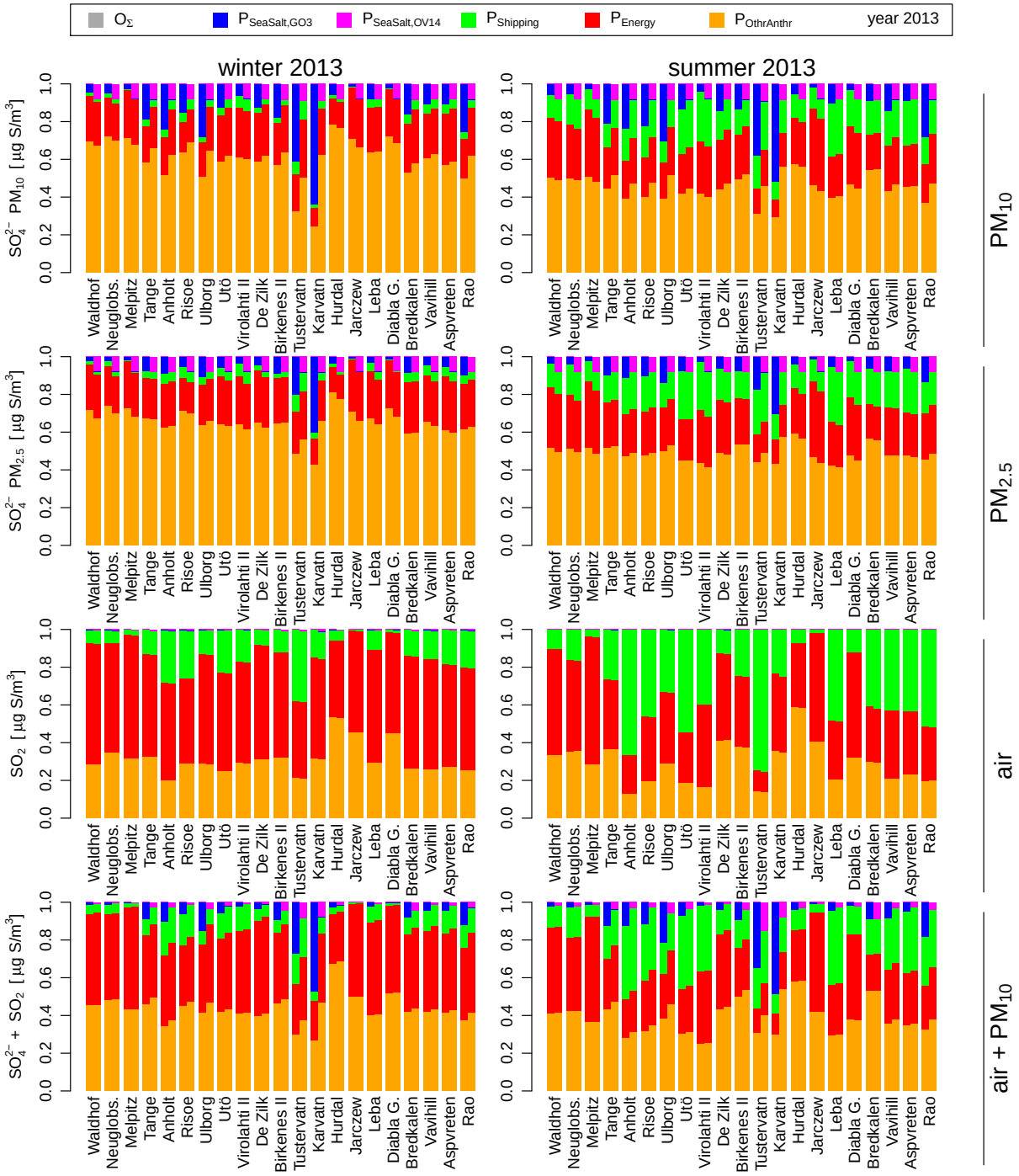

Figure 6.4: Similar to Fig. 6.3 but showing relative sectoral contributions.

Table 6.7: Ratio between sulfate $PM_{2.5}$ and PM_{10} concentrations of the considered sectors.

	$PM_{2.5}/PM_{10}$	Waldhof	Neuglobsow	Melpitz	Tange	Anholt	Risoe	Ulborg	Utö	Virolahti II	Preila	De Zilk	Birkenes II	Tustervatn	Kårvatn	Hurdal	Jarczew	Leba	Diabla Gora	Bredkälen	Vavihill	Aspvreten	Råö
winter	Salt, GO03	0.40	0.39	0.48	0.29	0.27	0.29	0.27	0.37	0.50	0.36	0.27	0.37	0.31	0.33	0.53	0.60	0.32	0.55	0.40	0.33	0.40	0.28
	Salt, OV14	0.49	0.49	0.55	0.39	0.40	0.44	0.36	0.45	0.57	0.46	0.39	0.44	0.41	0.45	0.57	0.69	0.40	0.64	0.47	0.47	0.49	0.40
	Shipping	0.86	0.85	0.95	0.84	0.86	0.86	0.84	0.85	0.84	0.87	0.82	0.84	0.85	0.88	0.85	0.69	0.86	0.90	0.78	0.83	0.84	0.85
	Energy	0.82	0.83	0.83	0.81	0.84	0.83	0.81	0.83	0.80	0.87	0.81	0.79	0.71	0.76	0.82	0.87	0.87	0.87	0.78	0.83	0.84	0.84
	OthrAnthr	0.84	0.84	0.85	0.85	0.88	0.87	0.86	0.88	0.85	0.88	0.84	0.85	0.94	0.92	0.89	0.86	0.88	0.86	0.84	0.84	0.87	0.87
summer	Salt, GO03	0.55	0.57	0.66	0.35	0.33	0.34	0.30	0.41	0.51	0.38	0.35	0.43	0.28	0.35	0.56	0.68	0.40	0.57	0.54	0.40	0.51	0.32
	Salt, OV14	0.58	0.59	0.61	0.47	0.45	0.51	0.43	0.42	0.57	0.38	0.52	0.52	0.32	0.48	0.58	0.61	0.43	0.52	0.50	0.52	0.58	0.45
	Shipping	0.84	0.82	0.80	0.81	0.77	0.80	0.81	0.73	0.72	0.77	0.86	0.81	0.82	0.85	0.78	0.81	0.78	0.80	0.79	0.80	0.72	0.78
	Energy	0.83	0.82	0.81	0.81	0.79	0.82	0.80	0.73	0.75	0.80	0.83	0.79	0.69	0.83	0.77	0.80	0.80	0.81	0.74	0.81	0.76	0.78
	OthrAnthr	0.85	0.84	0.83	0.84	0.83	0.85	0.84	0.75	0.79	0.80	0.87	0.82	0.85	0.87	0.79	0.82	0.82	0.82	0.79	0.84	0.78	0.82

considerably lower in the eastern Baltic Sea (Virolahti II) than in the Kattegat (Anholt, western Baltic Sea) leading to positive gradient in the sea salt emissions from East to West. This gradient in emissions is clearly reflected by lower sulfate concentrations at Virolahti II. The time series at De Zilk (Fig. 6.2 fourth row from the top) shows absolute shipping and sea salt related sulfate concentrations of similar magnitude as at Anholt. However, the relative contribution is lower at De Zilk because of higher anthropogenic emissions from the remaining sectors.

The ratio of $PM_{2.5}$ to PM_{10} (Table 6.7) shows that, during winter, approximately 80 % of energy production and OthrAnthr sulfate PM_{10} is $PM_{2.5}$. During summer, the fraction is slightly lower (75 % to 83 %) except at Diabla Gora where nearly 100 % of energy production and OthrAnthr sulfate PM_{10} is $PM_{2.5}$. Shipping related sulfate PM_{10} consists of nearly 100 % $PM_{2.5}$ during winter and of 73 % to 80 % $PM_{2.5}$ during summer.

At coastal stations, the OV14 parameterization leads to higher $PM_{2.5}/PM_{10}$ ratios than the GO03 parameterization. The ratios increase with increasing distance to coast, wherefore they are higher at inland stations, such as Melpitz, Jarczew, and Diabla Gora, compared to coastal ones. The highest $PM_{2.5}$ to PM_{10} ratios are yielded by OV14 at inland stations in winter. In contrast in summer, the ratios of both parameterizations are on the same level at most inland stations and at some stations GO03 yields even higher ratios. By definition, the OV14 parameterization produces a considerably higher number of fine sea salt particles compared to the GO03 parameterization. Hence, it is reasonable that it yields higher $PM_{2.5}/PM_{10}$ ratios at coastal stations. The lower share of coarse particles at inland stations for both parameterizations is caused by the long distance between coast and EMEP station: during advection, predominantly coarse particles deposit to the ground provoking a relative increase of the fine particle mass and of the $PM_{2.5}/PM_{10}$ ratio. In addition, the GO03 coarse mode has a higher GMD than the OV14 coarse mode. As a result, the dry deposition velocity of coarse particles by GO03 is higher and the enrichment of fine particles takes place faster. Since mean wind speed is lower in summer, the situation that $PM_{2.5}/PM_{10}$ ratios of OV14 and GO03 particles equal each other shifts closer to the coast in summer (see Sect. 4.3.2 for details).

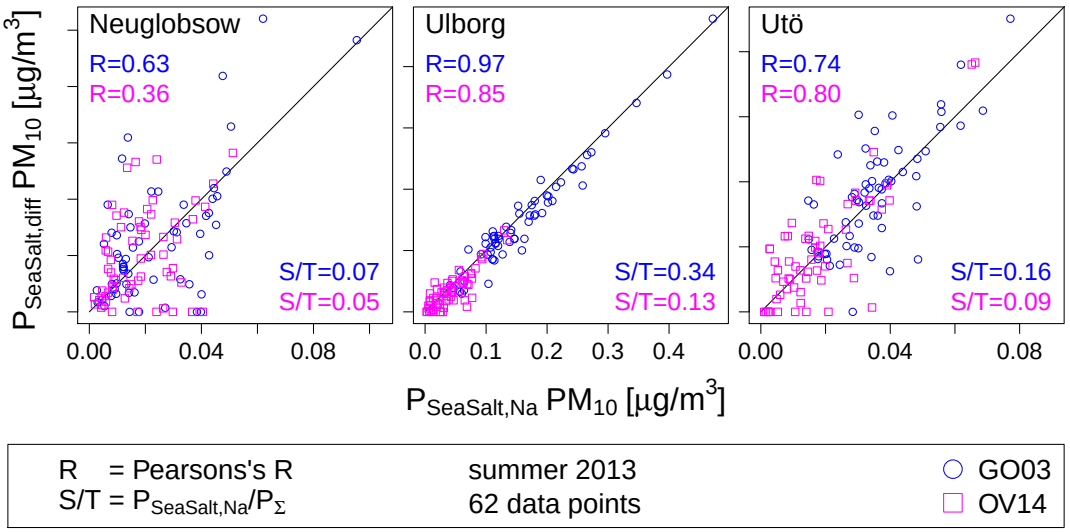

Figure 6.5: Scatter plot of the sea salt sulfate concentrations calculated from sodium concentrations ($P_{SeaSalt,Na}$, x-axis) as well as calculated by subtracting results of simulations without sea salt emissions from results of simulations with sea salt emissions ($P_{SeaSalt,diff}$, y-axis). Sea salt concentrations for summer 2013 obtained by the GO03 sea salt emission parameterization (*Base* case) and by the OV14 parameterization (*OV14* case) are plotted at three examplary stations: Neuglobsow, Ulborg, and Utö (left to right). The x- and y-axis within each plot are equally scaled but the axis scaling differs between the plots. The plots for all stations, both seasons (winter and summer), and both particle sizes ($PM_{2.5}$ and PM_{10}) are attached as Figs. E.5 to E.8 in the Appendix.

6.3.4 Uncertainty Estimation

The contribution of sulfate by individual anthropogenic emission sectors was calculated by subtracting results of simulations without these emissions from results of simulations where all emissions were considered (Eqs. (6.2) and (6.1)). This method adds uncertainty to the model results, as most atmospheric processes are non-linear (see Sect. 6.2.3).

The sea salt sulfate concentrations described in the previous sections were calculated from sea salt sodium concentrations (Eqs. (6.3) and (6.4); Apdx. E.1). This sodium method yields valid results because the sodium and sea salt sulfate mass ratios are assumed to be constant (Sect. E.1). It is commonly used in studies to split total sulfate into sea salt sulfate and non-sea-salt sulfate [e.g. Sorooshian et al., 2015; Udisti et al., 2016; EMEP, 2015]. Additionally, an emission case without sea salt emissions (*NoSalt*) was defined and the sea salt sulfate was calculated by subtracting *NoSalt* sulfate from *Base* and *OV14* sulfate (Eqs. (6.6) and (6.7)). The latter sea salt sulfate is denoted as $P_{SeaSalt,diff}$ and the sodium derived sea salt sulfate is called as $P_{SeaSalt,Na}$ in this section. The $P_{SeaSalt,diff}$ is assumed to be afflicted with uncertainty of unknown magnitude which is to be evaluated. The sea salt sulfate in measurements is abbreviated as $O_{SeaSalt}$.

Figure 6.5 displays scatter plots with $P_{SeaSalt,Na}$ PM_{10} and $P_{SeaSalt,diff}$ PM_{10} at three stations during summer 2013. The stations represent different sea salt concentration regimes. Both sea salt emission scenarios are considered. The correlation between $P_{SeaSalt,Na}$ PM_{10} and $P_{SeaSalt,diff}$ PM_{10} differs amongst the stations: It is highest at Ulborg and lowest at Neuglobsow – visually as well as indicated by the R values. The correlation is higher when the $\frac{P_{SeaSalt,Na}}{P_{\Sigma}}$ ratio (sea salt sulfate to total sulfate) is higher. In order to evaluate the correlation between $P_{SeaSalt,Na}$ and $P_{SeaSalt,diff}$ in more detail, the R, MNB, and fraction $P_{SeaSalt,Na}$ by $sulf_{tot}$ are displayed in

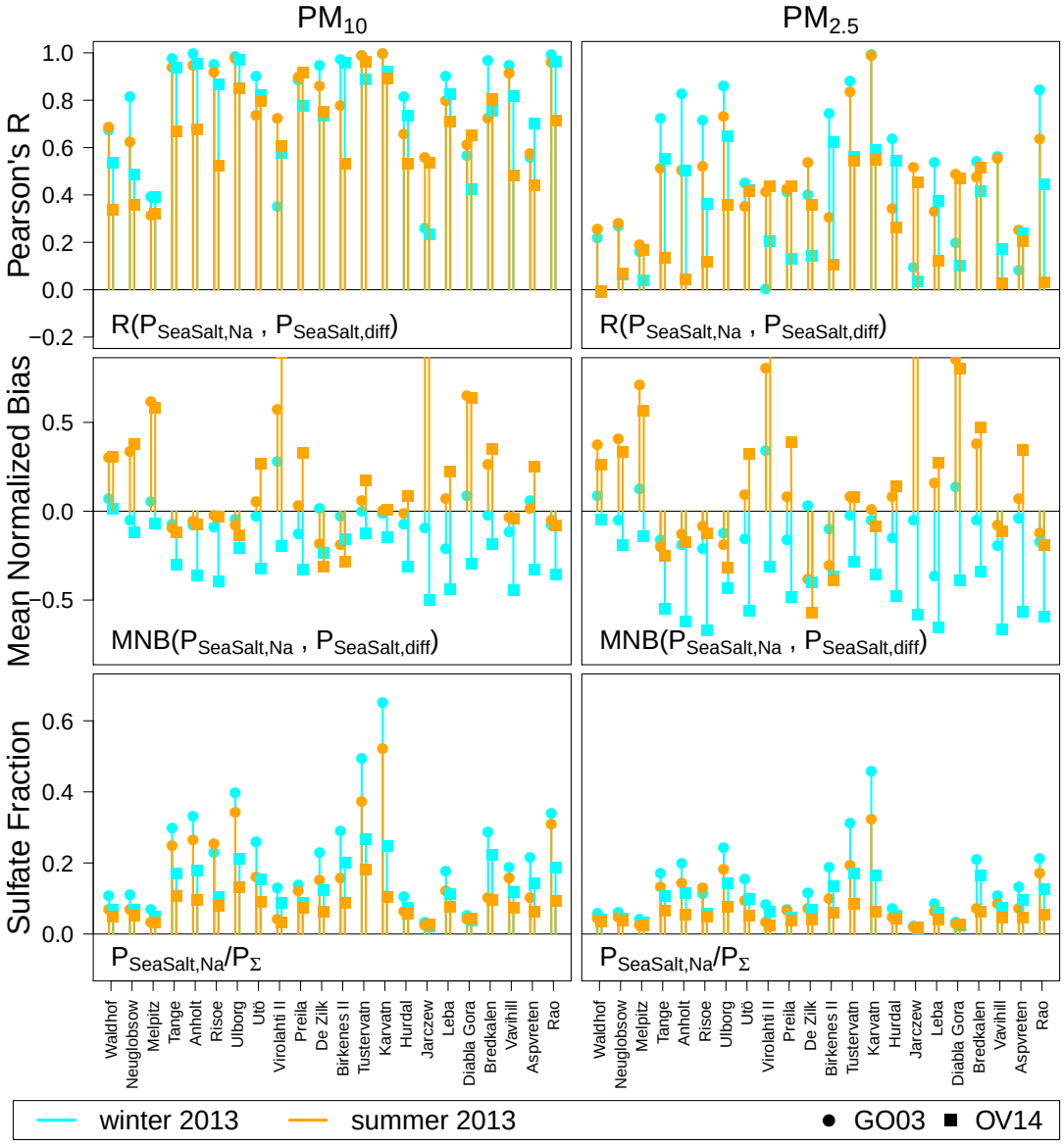

Figure 6.6: The R (top) and MNB (center) of modeled $P_{SeaSalt,Na}$ and $P_{SeaSalt,diff}$ PM_{10} (left) and $PM_{2.5}$ (right) concentrations of the GO03 (circles) and the OV14 parameterization (squares) during winter (cyan) and summer (orange) and corresponding $\frac{P_{SeaSalt,Na}}{P_{\Sigma}}$ (bottom). The vertical lines are for a facilitated visual comparison.

Fig. 6.6.

Comparing the plots in rows one and three shows that low $\frac{P_{SeaSalt,Na}}{P_{\Sigma}}$ values correlate with low R values, and that both values are higher during winter. The latter is caused by higher sea salt emission in winter. The first relationship is reasonable because high $\frac{P_{SeaSalt,Na}}{P_{\Sigma}}$ ratios imply relatively lower non-sea-salt sulfate concentrations that act as noise. During summer, on the other hand, low $\frac{P_{SeaSalt,Na}}{P_{\Sigma}}$ go along with high positive MNBs (row two) which means that $P_{SeaSalt,diff}$ concentrations are considerably larger than $P_{SeaSalt,Na}$ concentrations. In contrast, during winter, $P_{SeaSalt,Na}$ concentrations are greater than $P_{SeaSalt,diff}$ concentrations at most stations indicated by negative MNBs. All these statements are valid for PM_{10} and $PM_{2.5}$ concentrations. Comparing PM_{10} with $PM_{2.5}$ concentrations reveals that the R values of PM_{10} concentrations are higher and that the MNBs of PM_{10} concentrations are slightly closer to 0. This goes along with higher $\frac{P_{SeaSalt,Na}}{P_{\Sigma}}$ values for PM_{10}. Thus, sea salt sulfate calculated by the

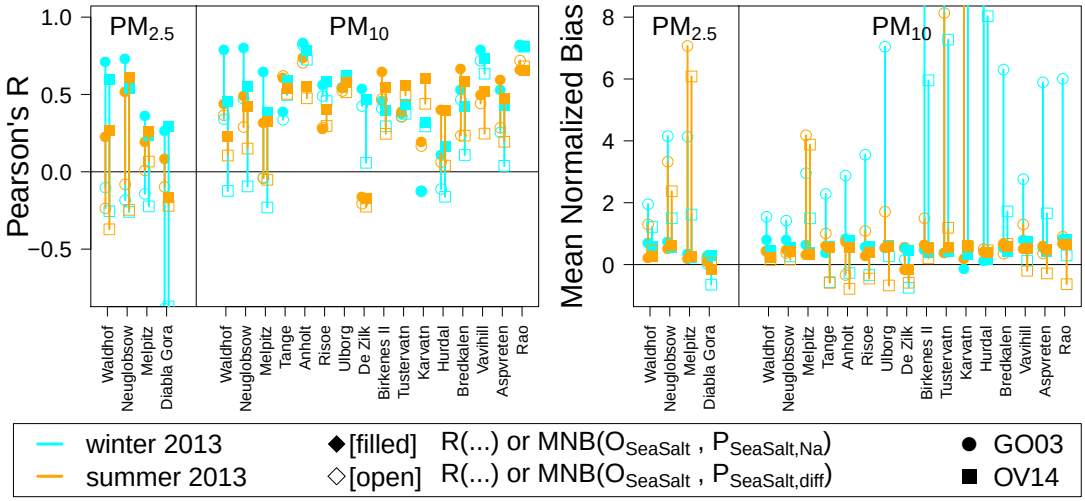

Figure 6.7: The R (left) and MNB (right) of $O_{SeaSalt}$ and $P_{SeaSalt,Na}$ (filled symbols) and of $O_{SeaSalt}$ and $P_{SeaSalt,diff}$ (non-filled symbols). The vertical line are for a facilitated visual comparison.

subtraction method ($P_{SeaSalt,diff}$) is closer to the actual sea salt sulfate ($P_{SeaSalt,Na}$) when the contribution of sea salt sulfate to total sulfate is higher. Therefore, the error of the sectoral sulfate concentrations is lower when the sectoral contribution to total sulfate is higher.

Based on this result and generalizing to the remaining emission sectors, one can assume that the calculated contribution by the shipping sector to total sulfate is afflicted with a higher uncertainty during winter than during summer because its contribution is very low in winter and considerably higher during summer. Moreover, one could assume that the uncertainty in the contribution of energy production to total sulfate is very low because this contribution is considerably higher than those by sea salt and shipping at most stations. However, the results on the inaccuracy in the sea salt sulfate contribution are not necessarily transferable to the inaccuracy in energy production related sulfate: First, sea salt sulfate consists only of primary sulfate, whereas anthropogenically related sulfate assembles of primary and secondary sulfate. The production of secondary sulfate might be differently impacted. Second, the sea salt sulfate concentrations, which are the base for the uncertainty estimations, are considerably lower than energy production sulfate concentrations at most stations and, hence, the results might not be applicable. The described uncertainties were introduced by the applied subtraction methods but are independent of uncertainties in the emissions, in the meteorology and in the CTM. A discussion of the latter uncertainties is beyond the scope, here.

Finally, the correlation between modeled sea salt sulfate ($P_{SeaSalt,Na}$ and $P_{SeaSalt,diff}$) and measured sea salt sulfate ($O_{SeaSalt}$) is evaluated (Fig. 6.7). The results clearly show that $R(P_{SeaSalt,diff}, O_{SeaSalt})$ is below $R(P_{SeaSalt,Na}, O_{SeaSalt})$ at nearly every station independent of the considered season, and that $R(P_{SeaSalt,diff}, O_{SeaSalt})$ is even negative for most $PM_{2.5}$ measurements. The MNBs of $O_{SeaSalt}$ and $P_{SeaSalt,Na}$ (Fig. 6.7, right) are considerably lower than the MNBs of $O_{SeaSalt}$ and $P_{SeaSalt,diff}$ and positive at most stations during winter. During summer, the MNBs to $P_{SeaSalt,Na}$ are in a similar size range. Moreover, the MNBs to GO03 $P_{SeaSalt,diff}$ are higher than the MNBs to GO03 $P_{SeaSalt,Na}$ at approximately half of the stations. Besides, the MNBs to OV14 $P_{SeaSalt,diff}$ are negative at eight stations but their absolute values are similar to the positive MNBs to $P_{SeaSalt,Na}$ of the GO03 and OV14 parameterizations. Summarizing, the subtraction method yields sea salt sulfate concentrations that lead to lower correlation coefficients and larger absolute bias values than those calculated from sodium.

6.3.5 Summarizing Discussion

The employment of the two sea salt emission parameterizations GO03 and OV14 leads to sulfate concentrations differing by a factor of approximately 2. In summer, sea salt sulfate concentrations are clearly lower than sulfate concentrations contributed by the remaining source sectors. Therefore, the choice of the parameterizations has a low impact in this season. In winter, however, it becomes more relevant for evaluations of anthropogenic and natural marine emissions because the shipping related sulfate concentrations are below the sea salt sulfate concentrations (GO03). Both sea salt emission parameterizations lead to considerably different sulfate concentrations in Northwestern Norway – stations Tustervatn and Kårvatn. This is caused by surf zone emissions that are activated in the *Base* case but that do not exist in the OV14 case. Repeating the *Base* case simulations without surf zone emissions (not shown) reduces the difference between the GO03 and OV14 sea salt sulfate concentrations. This fact clearly indicates either that the employed surf zone sea salt emission approach needs to be revised or that the surf zone input data have to be pre-processed region specific. Figure 6.7 displays higher R values for GO03 than for OV14 sea salt sulfate except at the stations with considerably overestimated sea salt concentrations. Both parameterizations are evaluated in Chap. 4 in more detail.

At most stations, sulfate PM_{10} from sea salt emissions consists of less than 50 % $PM_{2.5}$. The $PM_{2.5}$ to PM_{10} ratio rises with increasing distance from the sea but, nevertheless, sea salt has a very low contribution to $PM_{2.5}$ and PM_{10} air pollution. Instead, the anthropogenic sources, which have $PM_{2.5}$ to PM_{10} ratios of 80 % and above, are clearly dominating the atmospheric sulfate concentrations. The individual anthropogenic source sectors contribute differently in winter and summer. While the shipping related sulfate PM_{10} and $PM_{2.5}$ concentrations account for approximately $\frac{1}{4}$ of the sulfate concentrations at coastal stations in summer, they account for less than 5 % of the sulfate concentration – even in coastal regions. In contrast, the contributions of the energy sector are quite constant in both seasons – approximately a fifth to a third depending on the station. However, looking into SO_2+SO_4^{2-} concentrations shows considerably higher shares from the shipping and energy production sectors. This low share of the shipping sector in sulfate is due to the fact that the coastal stations are closely located to the shipping routes and, hence, measure fresh ship emissions, which are rich in SO_2 but have low primary and secondary sulfate concentrations. Comparing Melpitz to coastal stations (Figs. 6.2, E.3, and E.4) clearly shows that the sulfate to SO_2+SO_4^{2-} ratio is considerably higher at inland stations. Thus, most SO_2 reacted to secondary sulfate or was deposited.

Although, more than 60 % of the sulfur emissions are caused by the energy sector (Table 6.2), only 15 % to 30 % (at most stations) of the sulfate PM_{10} concentrations were accounted to the energy sector. Instead, the OthrAnthr sector contributed at least 40 % of particulate sulfate at most stations and even above 70 % at individual ones. First, power plant emissions are characterized by a lower SO_2:SO_4^{2-} ratio compared to OthrAnthr sulfur emissions and, vice versa, the energy sector contributes only approximately 15 % of the primary particulate sulfate emissions. Hence, the energy sector contributes a large fraction of SO_2 in freshly polluted air but a considerably lower fraction of particulate sulfate. The second reason is due to the height of emissions: Power plants are equipped with high stacks that facilitate the rise of the exhaust gas plume above the planetary boundary layer (PBL) in order to reduce the negative impact on local air quality. Thus, the energy sector contributes less SO_2 and SO_4^{2-} to the local and regional air pollution than it appears by considering its contribution to the sulfur emissions.

6.4 Conclusions

The energy production sector and the not further differentiated anthropogenic sectors (OthrAnthr) are the largest sources of particulate sulfate. Thereby, the OthrAnthr sector makes up 40–70 % of the sulfate, whilst the energy sector yields a quarter. A higher share of energy production related sulfate could be expect because more than 50 % of the anthropogenic sulfur

emissions in the study regions are accounted to the energy sector. However, emissions consists by approximately 99.5 % of SO_2. The other anthropogenic sources reveal a considerably higher proportion of particulate sulfate. The conversion from SO_2 to SO_4^{2-} takes time and is less effective in winter due to lower concentrations of oxidizing compounds produced by solar radiation. Additionally, power plants emit their exhaust gases in higher altitudes and, hence, have a lower impact on the local air quality. This leads to the lower contribution of the energy sector to sulfate concentrations as could be expected from the emissions. The shipping sector significantly contributes to sulfate concentrations in summer, particularly at coastal stations. Significant amounts of sulfate particles are also transported into regions far distant from their source locations as measurements at Melpitz indicate. Episodes with high shipping related sulfate concentrations were measured there. The contribution of sea salt particles emitted by GO03 accounts for up to a third of the sulfate PM_{10} concentration at one station and considerably decreases with increasing distance to the coast. The OV14 parameterization yielded considerably lower contributions at coastal stations as GO03 but it exceeded GO03 concentrations are some inland stations. Particles emitted by OV14 are smaller than GO03 particles and manifest a lower dry deposition velocity which lead to a significantly lower decrease as GO03 towards inland regions.

The analysis of total sulfate demonstrates that more than 50 % of sulfate PM_{10} is in the $PM_{2.5}$ fraction. Sea salt increases the coarse fraction of PM_{10} in marine and coastal regions. Since coarse particles deposit faster than fine ones, the $PM_{2.5}/PM_{10}$ ratios increased towards inland stations. Biases in the modeled sulfate concentrations were apparently not caused by shortcomings in the SO_2-SO_4^{2-} conversion rates because SO_4^{2-} as well as SO_2 concentrations are overestimated. However, correlation coefficients between model data and measurements are higher when SO_2+SO_4^{2-} instead of SO_4^{2-} or SO_2 are considered.

The employed method of calculating the contribution of the anthropogenic source sectors energy production and shipping was evaluated by calculating the sea salt sulfate concentrations by two different methods: One common accurate method based on sodium concentrations and another method equal to the procedure applied to anthropogenic source sectors. By comparing the sea salt sulfate concentrations determined by the two methods, deviations between both concentrations were identified that increased with lower ratio of sea salt sulfate to total sulfate. Moreover, the model results were compared with station measurements. This comparison demonstrated that the sodium based calculation method is more suitable than the subtraction method as it reflects the measurements in a more accurate way. Therefore, one has to assume that the applied method to determine the contribution of the anthropogenic source sectors shipping and energy production is not ideal because considerable uncertainties can be expected. Without implementing a sulfur tracking/tagging procedure, there is no alternative method to identify the contribution of different source sectors.

In a nutshell, the sectoral split of sulfur oxide (SO_x+SO_4^{2-}) emissions is not necessarily transferable to sulfate measurements at closely located measurements stations because it takes time and oxidizing compounds to convert the emitted SO_2 to sulfate. Additionally, exhaust gas is emitted into different heights by different sectors. The subtraction method applied in this thesis to determine the contribution from the energy production and shipping sectors is afflicted with uncertainty which could not be further isolated. However, that uncertainty decreases with increasing sectoral sulfate concentrations. Generally, it was shown that fine sulfate particulate matter is dominated by anthropogenically emitted sulfur compounds. In this context, the shipping sector is most relevant in summer but the energy production and OthrAnthr sectors are equally relevant in both seasons.

7 Summarizing Discussion

7.1 Sea Salt

A linear scaling of sea salt emissions by the ocean's salinity was introduced in this study and validated with measurements of sodium concentration. This scaling significantly reduced the bias of modeled sodium concentrations compared to measurements in the Baltic Sea region. The linear functional relation of the applied scaling $\frac{\mathrm{SAL}}{35\,‰}$ (Sect. D.3.2) is in line with the laboratory study results of Mårtensson et al. [2003] for fine sea salt particles emitted as film droplets. Jet droplet emissions exposed an ambiguous relation to salinity. From a mechanistical view, the linear scaling is reasonable: If salinity drops by 50 %, the film and jet droplet emissions are not affected, but the mass of salt per droplet decreases by 50 %.

The current technical implementation of surf zone emissions was found to increase sodium concentrations in coastal regions significantly. Although no general improvement or worsening of predicted concentrations was found, compared to simulations without surf zone emissions, surf zone emissions led to an improvement in modeled concentrations at several stations during summer but a deterioration in winter. The sea salt concentrations were considerably overpredicted at stations in northern Norway, which was even worsened by surf zone emissions. This deviation was caused by the following: Although the swell is less rough and the salinity in the fjords is lower than at the Atlantic Ocean, the water surface in all the fjords along the Norwegian coast was counted as sea surface and the fjords' coastlines were considered as surf zones leading to significant overestimations of sea salt emissions. Therefore, a special treatment of some coastal regions with bays or fjords, such as the Norwegian Atlantic coast, is necessary.

Kelly et al. [2010] used the same surf zone setup in CMAQ simulations in Tampa, Florida. They found improvements in the predicted particulate nitrate concentrations when surf zone emissions were activated. Similar results were reported by Nolte et al. [2008] who employed another surf zone emission parameterization [de Leeuw et al., 2000]. However, the results of Kelly et al. [2010] and Nolte et al. [2008] could not be reproduced for air quality at the European coast by the same type of comparison because of a lack of comparable nitrate measurement data. But, based on the performed sea salt sodium evaluation, users of CMAQ should be advised not to activate standard surf zone emissions if coastal regions like the Northwestern Norwegian coast are part of the model domain – unless they were tested for these regions.

The standard CMAQ sea salt emission setup (GO03) [Gong, 2003] was compared with two alternative sea salt emission parameterizations (SP13 and OV14) [Spada et al., 2013; Ovadnevaite et al., 2014], and all three were evaluated with particulate sodium measurements. GO03 and SP13 were extended by the salinity scaling discussed above while OV14 includes salinity as a parameter by definition. The bias of sodium PM_{10} concentrations of the SP13 parameterization considerably exceeded those of the two other parameterizations at most stations. The correlation coefficients of all three parameterizations were close to each other, but that of SP13 was slightly higher than the R values of the other two. The strong exceedance is reasonable because the MA03 parameterization, which is part of SP13, was determined by laboratory experiments and describes sea salt particle size distribution at the time of emission [Mårtensson et al., 2003; Mårtensson, 2015] – the gross emissions. In contrast, GO03 and OV14 compute the net emissions. Hence, the MA03 and SP13 emissions need to be reduced by a function or factor describing the relation between gross and net emission flux. The dry deposition parameterization incorporated in CMAQ could be used for calculating this reduction. In summing

up, SP13 is considered inappropriate as long as no reduction approach of these sea salt emissions is developed and applied. Spada et al. [2013], who compared different sea salt emission parameterizations and combinations of them on a global scale, also concluded that the SP13 parameterization greatly overestimates sea salt emissions.

The comparison between the CMAQ standard parameterization GO03 and OV14 did not yield clear results revealing which of the two parameterizations is preferable. OV14 number emissions exceed those of GO03 but particles from OV14 are considerably smaller implying lower mass emissions. Therefore, sodium PM_{10} concentrations of GO03 are above those of OV14 at coastal stations. The bias of GO03 sodium is positive at most coastal stations and that of OV14 sodium is negative. The deposition velocity of OV14 particles is lower due to their smaller size and, hence, the sea salt mass decreases more slowly during the transport towards inland regions. As a result, OV14 sodium PM_{10} concentrations partly exceed those of GO03 at inland stations, such as Melpitz, and have a positive bias. The GO03 sodium, in contrast, tends to have negative biases at inland stations.

The modeled sodium $PM_{2.5}$ concentrations were compared with measurements at Melpitz. Sodium concentrations by GO03 yielded the highest correlation coefficients and MNBs closest to 0. The MNBs in the OV14 case were higher, especially in summer. At the coastal station Westerland as well as at the inland station Waldhof, which is located closer to the coast than Melpitz, OV14 also exceeded GO03 with respect to sodium $PM_{2.5}$ concentrations. No comparison with measurements was performed at these two stations because further sodium $PM_{2.5}$ measurements were not available.

Size-resolved measurements of sea salt particles or of particulate sodium were not available in 2008 at European EMEP stations. Hence, no detailed evaluation of the sea salt size distributions of GO03 and OV14 was performed. Ovadnevaite et al. [2014] derived the OV14 parameterization from ECMWF model data and measurements performed at Mace Head, Ireland. It was compared with GO03 and Jaeglé et al. [2011] exposing significantly higher variability due to the larger number of input parameters. GO03 and Jaeglé et al. [2011] were not evaluated against the measurement data on which OV14 is based.

Based on the current status of the evaluation, both parameterizations are rated as valid despite their weaknesses. With respect to applicability, GO03 is favorable because setting up OV14 emissions requires considerably more input parameters that are not necessarily available. Both parameterizations have a different $PM_{2.5}/PM_{10}$ ratio and expose different deposition velocities. Hence, combined sodium PM_1, $PM_{2.5}$, and PM_{10} measurements at the coast as well as at various geographic distances to the coast would support the assessment of the two parameterizations.

7.2 Impact of Sea Salt on Atmospheric Nitrogen Concentrations and Deposition

The impact of sea salt on atmospheric nitrogen and nitrogen deposition has been studied with respect to the atmosphere. Sea salt particles primarily affect particulate NO_3^- and NH_4^+ concentrations, as well as the NO_3^--HNO_3 and NH_4^+-NH_3 equilibrium. Their deposition flux is modified by sea salt particles. However, the total nitrogen deposition is regarded here because it is of interest for eutrophication estimates.

The influence of sea salt particles on particulate NO_3^- concentrations was assessed by means of CMAQ. In 2008 the NO_3^-, NH_4^+, HNO_3, and NH_3 sampling was performed with three-stage filter packs at all EMEP stations in the model domain except at Melpitz. These filter packs do not reliably allow distinguishing between NO_3^- and HNO_3, and between NH_4^+ and NH_3 as described in Apdx. F. Hence, the impact of sea salt on nitrate was evaluated by the means of model data but HNO_3+NO_3^- (sNO_3) and NH_3+NH_4^+ (sNH_4) measurements were employed to validate the model results.

The NO_3^- concentrations of simulations with sea salt emissions clearly exceeded those of simulations without sea salt emissions at all stations in both simulated seasons with three exceptions. Thus, the presence of sea salt leads to an increase in atmospheric nitrate concentrations. This rise is stronger at coastal stations, as the difference between nitrate from simulations with and without sea salt emissions indicated (Table 3.5). Im et al. [2013] and Liu et al. [2015] describe the same effect in the Northwestern Mediterranean Sea and in the Pearl River Delta, China, respectively. This result is partly as expected because sea salt favors the condensation of HNO_3, which depends on the pH value of the liquid phase: Sea salt Cl^- is displaced by NO_3^- (see Sect. 2.1.1), leading to evaporation of HCl, which buffers the pH value. In the absence of sea salt particles, this pH-regulating function is performed by the NH_3-NH_4^+-equilibrium and, thus, the HNO_3 condensation is limited by NH_3. However, extensive animal husbandry practiced in Northwestern Europe contributes to significant NH_3 emissions. Hence, sea salt should be of lower relevance for NO_3^- formation compared to studies in regions with lower NH_3 emissions. However, NH_3, NH_4^+, or sNH_4 concentrations were not reported by Im [2013] and Liu et al. [2015], which would allow a comparison.

The alternative sea salt emission parameterizations SP13 and OV14 yielded atmospheric particulate NO_3^- concentrations that differed from the GO03 case concentrations. Nitrate $PM_{2.5}$ was generally reduced in the presence of sea salt, whereby SP13 produced the lowest and GO03 the highest reductions at all stations in both seasons. Nitrate PM_{10} concentrations took highest values in the OV14 case and lowest in the GO03 case among the three sea salt cases. The zero case, in contrast, yielded even lower concentrations in summer but concentrations higher than those of OV14 in winter. The differences between the three parameterizations is caused, on the one hand, by differing sea salt particle surface area that governs the amount of condensing HNO_3 and, on the other hand, by differently shaped sea salt particle size distributions yielding different dry deposition velocities of particle-bound nitrate.

The sNO_3 concentrations are reduced in the presence of sea salt particles (except for the OV14 case in summer) and HNO_3 too (Fig. 5.3). Hence, the HNO_3-NO_3^- equilibrium is clearly shifted towards NO_3^- by sea salt particles, particularly in summer. Im [2013] and Liu et al. [2015] found the same shift by considering the NO_3^-/sNO_3 fractions. The production of HNO_3 from NO_2 is not controlled by sea salt. Thus, the decline in sNO_3 concentrations in the presence of sea salt is not caused by a lower production of HNO_3 but by a higher NO_3^- deposition flux enhanced by sea salt particles. The fact that summer sNO_3 concentrations in the OV14 case exceed those in the zero case shows that sea salt particle distributions comprising high numbers of fine and ultra-fine particles might enhance the atmospheric life time of NO_3^-.

The sNO_3 concentrations yielded satisfactory correlation coefficients ($R > 0.5$) at all stations except at three German and the two Norwegian ones (Table 3.7). They were even above 0.7 at several stations during winter. The Norwegian stations have problematic locations with respect to predicted and modeled wind flows [Wang et al., 2015], which possibly induced the low correlation of the atmospheric concentrations. At the German stations Waldhof and Neuglobsow, high R values were produced in winter, but they fell below 0.4 in summer. This decrease is partly attributed to a one-week period of incorrectly predicted sNO_3 concentrations caused by northeasterly winds. Modeled concentrations generally yielded a low performance with respect to bias and R at the station of Westerland. The biases indicate an underestimation at most stations during summer and a mixture of under- and overestimations during winter with particularly high positive biases at Norwegian and Finnish stations. The negative biases, which particularly arose in summer, were not caused by incorrect predictions on individual days but by general underestimations of sNO_3 concentrations. Some possible reasons for this fact are (a) an overestimated dry deposition flux of NO_3^- and HNO_3, (b) too low NO_2-HNO_3 conversion rates, or (c) underestimated NO_2 concentrations. The dry deposition flux (a) probably did not induce this situation: The sNH_4 concentrations should behave similarly to the sNO_3 concentrations if the underestimation was related to particle dry deposition. However, the sNH_4 concentrations

yielded primarily positive biases (see next paragraph) and, as Table 3.8 displays, the MNBs of NO_2 concentrations are negative at all stations except at the Norwegian ones. Therefore, underestimations of NO_2 by the model led to reduced HNO_3 concentrations. None of the three sea salt emission cases reproduced measured sNO_3 concentrations significantly better than the others. Therefore, the decision on a preferable parameterization cannot be based on the available sNO_3 measurements.

The correlation coefficients of sNH_4 concentrations took mediocre values of above 0.5 at most stations in both seasons (Table 3.3), except at the Danish, Polish, and Norwegian stations in summer. In the latter situation, the concentrations yielded lower R values of approximately 0.4. Although the biases had mixed signs, they were predominantly positive (overestimation), particularly in summer. Remarkably, these overratings are opposed to the underestimated sNO_3 concentrations described above. The presence of sea salt emissions slightly reduces the model bias at Danish, Norwegian, Swedish, and Finnish stations in summer. Other than that, the sea salt scenario had no significant impact on the sNH_4 concentrations.

The two-month average nitrogen wet deposition was underestimated at all stations in winter and at most stations in summer (Fig. 3.7). It was slightly overestimated at the station Keldsnor and was balanced approximately at the station of Råö. Although statistical metrics are not reliable for small sample sizes, the metrics are displayed in Table 5.2 for all stations. The MNBs had positive values (overestimation) at five stations in summer (Table 5.2), which were caused by individually overestimated peak concentrations and contradict the comparison of the two-month mean wet depositions. The correlations were good with $R > 0.5$ in winter except at Neuglobsow. There the concentrations yielded the lowest R (0.4). In summer at this station, nitrogen wet deposition has a low correlation, too, but the R values at Waldhof, Jarczew, and Råö are low as well (0.2, -0.34, and 0.2). The low nitrogen deposition correlations at Neuglobsow (both seasons), Jarczew, and Råö are related to poorly correlating modeled precipitation events (Table 5.3): Particularly at Jarczew, some precipitation events were not predicted at all (time series plot not shown). The correlation of modeled and measured precipitation controlled the correlation of model and measured nitrogen wet deposition, whereas the quality of the predicted amount of precipitation (μ_{sim} and μ_{obs} in Table 5.3) had no clear impact on the predicted amount of nitrogen deposition (comparing μ_{sim} and μ_{obs} in Table 5.2): The precipitation amount was overpredicted at half of the stations in winter, but the nitrogen wet deposition was mostly underpredicted. The choice of the sea salt emission parameterization affects the MNBs of nitrogen wet deposition marginally, and no parameterization generally improves the deposition predictions.

Underestimations of the nitrogen wet deposition by CMAQ were also found by Appel et al. [2011], Im et al. [2013], and Matthias et al. [2008]. Im et al. [2013] studied the Northeastern Mediterranean Sea region and generated their meteorological data with the Weather Research and Forecast (WRF) model that underestimated the precipitation amounts. However, the nitrogen wet deposition was considerably more strongly underrated than precipitation. Matthias et al. [2008] considered the same region as in this study but modeled the year 2001 using an older CMAQ version and the Mesoscale Meteorology Model 5 (MM5) for generating meteorological data. The precipitation was well reproduced, but NH_4^+ and NO_3^- wet deposition had negative biases. Finally, Appel et al. [2011] ascribed their underratings to underrepresented agricultural emissions, to missing bi-directional flux of nitrogen species at the atmosphere-soil/plant interface, and to missing lightning NO_x production. However, not the whole bias was explained by these processes. In summary, it is not clear whether the meteorological input data or CMAQ yields the underestimations in the nitrogen wet deposition.

To sum up, well predicting the temporal occurrence of precipitation events correlated with high correlations of the nitrogen wet deposition. In contrast, low biases in the precipitation amounts did not necessarily yield low biases in the nitrogen wet deposition. These results are reasonable, because predicting rain fall at the wrong time might produce the correct monthly

precipitations amounts but possibly miss-predicts the nitrogen deposition.

Sea salt was found to increase the total nitrogen deposition (wet + dry) in coastal areas (Fig. 3.9), particularly in those downwind to the sea, and at the open sea. This led to a reduced nitrogen deposition in inland regions. Remarkably in the regarded winter episode, the nitrogen-dry deposition decreased along the Norwegian Atlantic coast. Surf zone emissions induced an increase in the nitrogen deposition in coastal areas as well, which was, though, stronger in summer than in winter. This seasonal variation is reasonable because the relative contribution by surf zone emissions to the total sea salt mass is larger in summer due to lower wind speeds and reduced open ocean sea salt emissions. These results are in agreement with those of Im [2013, Fig. 8] who considered PM_{10} deposition. The choice of the sea salt emission parameterization impacted the nitrogen deposition pattern (Fig. 5.4): With respect to the GO03 emissions, the OV14 parameterization, which emits more but finer particles than GO03, led to reduced nitrogen deposition along the coastline and at the open sea, producing a similar but less pronounced spatial pattern than the simulations without sea salt. In contrast, the SP13 parameterization led to an increased deposition at the open sea and along some shore lines, as well as to a decrease along the Danish and Dutch coasts.

Sea salt emissions accounted for 0 % to 7 % (Table 3.6) of the total nitrogen deposition into the North Sea and Baltic Sea, with the highest contributions into the North Sea (2.5 % to 7 %) and lowest into the Baltic Sea (up to 3.5 %). The impact of surf zone emissions was negligible, while alternative sea salt emission parameterizations significantly decreased (OV14) and increased (SP13) the sea-salt-related nitrogen deposition. Particularly, the OV14 parameterization induced a reduction of approximately 50 % into the North Sea in winter and by nearly 100 % in summer 2008 with respect to GO03 sea-salt-related nitrogen deposition. The nitrogen deposition values were lower than those in comparable studies focusing on the same oceanic region but using different models [de Leeuw et al., 2003; Hertel et al., 2002; Bartnicki and Fagerli, 2008; HELCOM, 2005; Langner et al., 2009; Bartnicki et al., 2011]. Detailed numbers are given in Sect. 3.4.4. The splitting of nitrogen deposition within coastal grid cells into oceanic and land deposition has major implications for the total nitrogen deposition into the ocean because the oceanic deposition has its maximum at the coast and decreases steadily towards the open ocean. Additionally, different years with different wind patterns and possibly higher atmospheric nitrogen concentrations were considered in other studies. Since the nitrogen wet deposition was underestimated in this study, the total nitrogen deposition into the sea might be underestimated. Since the modeled nitrogen dry deposition was not individually considered in this study due to a lack of measurement data, no statement with respect to the underrating of the total nitrogen deposition can be provided.

7.3 Sectoral Sulfate Evaluation

Sulfate particles generate acid deposition, and fine sulfate particles pose a threat to human health when they are inhaled. In order to identify the regionally most relevant contributors to these threats, the contribution of sulfur emissions from relevant source sectors to particulate sulfate air pollution was evaluated at different locations in Europe. The anthropogenic emission sectors such as energy production and shipping, along with natural sea salt emissions, were distinguished as individual contributors. The remaining anthropogenic emission sectors were regarded as a bulk and denoted as the OthrAnthr sector. The quality of the model results was assessed by comparing modeled sulfate PM_{10}, sulfate $PM_{2.5}$, SO_2, and SO_2+SO_4^{2-} concentrations with measurements at EMEP stations. The contribution for a specific sector was calculated by subtracting the results of a simulation without this sector's emissions from those of a base case simulation with all emissions. Additionally, this procedure, denoted as the subtraction method, was evaluated for sea salt sulfate. Sea salt sulfate was calculated with a reference method from Na^+ concentrations, which is considered to yield the correct sea salt sulfate concentrations. Both

model concentration sets were compared with each other and with measurements.

Atmospheric sulfate PM_{10} concentrations are overestimated at half of the stations in summer (Table 6.4 and Fig. 6.2) and at most stations in winter, with eight stations having MNBs larger than 1.0. Summer MNBs were considerably closer to 0.0 than those in winter, indicating that the magnitude of measured concentrations was better reproduced by the model in summer. Correlation coefficients were highest in winter with most R values above 0.5, indicating a good correlation. In contrast, only half of the R values were greater than 0.5 in summer. Sulfate concentrations were considerably overestimated at two Norwegian stations due to overestimated sea salt emissions in Norwegian fjords. A model case with the OV14 sea salt emission parameterization, which does not implement surf zone emissions, yielded considerably lower overestimations. This fact clearly points out that rugged coastline shapes require a special treatment particularly with respect to surf zone emissions. At the other stations, the OV14 parameterization produced correlation coefficients close to those of the base case (GO03). Positive MNBs were reduced by up to 50 % at several stations, but negative MNBs were further decreased.

Comparing model SO_2+SO_4^{2-} concentrations with the measurements produced significantly higher correlation coefficients (Table 6.6) than individual SO_2 and sulfate PM_{10} concentration did. However, the MNBs were higher than for sulfate PM_{10}. Inaccurate SO_2 to SO_4^{2-} conversion rates might be a reason for the high correlation of SO_2+SO_4^{2-} compared to the correlations of SO_2 and sulfate PM_{10} with measurements. Because the MNBs of SO_2+SO_4^{2-} were positive and higher than those of SO_4^{2-}, the total sulfate concentrations were overestimated, pointing to very high sulfur emissions, underestimated sulfur deposition or incorrect vertical transport in general. The exact reason for this was not identified in this study.

In winter the energy production and OthrAnthr sectors contributed more than 75 % of sulfate PM_{10} and $PM_{2.5}$, whereby the OthrAnthr sector had already made up more than 50 % at most stations (Tables E.6 and E.7). The shares of the shipping sector and of OV14 sea salt emissions were on a similar level and each below 10 %, without considering two Norwegian stations that were exposed to overpredicted sea salt emissions. The GO03 parameterization contributed as much as 30 % to total sulfate in winter. The total sulfur and sea salt emissions decreased as seasons changed from winter to summer, which kept the sea salt sulfate contribution unchanged throughout the year. In contrast, absolute sulfate concentrations related to shipping activities doubled from winter to summer, thereby yielding a significant increase in the relative shipping sector share. Hence, 10 % to 30 % of total sulfate was considered shipping-sector sulfur emissions in summer. In contrast, the contribution of energy production remained almost unchanged and that of the OthrAnthr sector was diminished. Coastal stations can be clearly distinguished from inland stations by a higher sulfate contribution from the shipping sector and sea salt. Sea salt's contribution is the highest along the North Sea coast and considerably lower along the Baltic Sea coast due to lower salinity in the Baltic Sea.

Approximately 80 % of the anthropogenically caused sulfate PM_{10} mass was found to be $PM_{2.5}$ mass. In contrast, only 50 % of the sea salt sulfate PM_{10} mass was situated in particles smaller than 2.5 µm. Hence, sea salt emissions led to a relative increase in the coarse particle fraction, which indirectly increased the dry deposition velocity of atmospheric sulfate and of compounds condensed on these particles. The OV14 parameterization yielded a slightly lower coarse particle fraction than the GO03 parameterization.

The high share of the OthrAnthr sector is surprising considering this sector's share in sulfur emissions: the concentrations should be lower. However, power plants emit their sulfur-containing exhaust gases into higher vertical layers than the emission sources of the OthrAnthr sector do. Therefore, primary and secondary particulate sulfate from power plants is transported over long distances in higher atmospheric layers, which reduces its impact on the local air quality. Moreover, the energy sector contributes nearly two thirds of the anthropogenic sulfur emissions (Table 6.2) in Europe, but it has a share of less than 20 % in the primary particulate sulfate emissions due to very efficient particle filter techniques. Therefore, the energy sector contributes

relatively more SO_2 but less SO_4^{2-} to ground-level sulfur concentrations (Fig. E.3) than other anthropogenic source sectors do. Because SO_2 is processed to sulfate, an evaluation of ground-level sulfate concentrations at locations away from individual power plants should find a shift from SO_2 dominated to SO_4^{2-} dominated energy sector sulfur concentrations. This processing is clearly visible for SO_2 and particulate sulfate of the shipping sector. While at coastal stations shipping-related contribution to SO_2 is considerably higher than that to particulate sulfate, the inland station Melpitz is mainly impacted by particulate sulfate.

The evaluation of the method for calculating the contribution from specified sources by subtraction was found to yield better results with higher sea salt concentrations and their ratio to total sulfate concentrations (Fig. 6.6). The correlation coefficients between the time series of both methods' particulate sulfate concentrations were greater than 0.6 for sulfate PM_{10} and considerably lower for $PM_{2.5}$. In winter the sulfate concentrations of the applied subtraction method fell below those of the reference method, whereas it was mixed in summer. Compared to observations (Fig. 6.7), the reference method yielded sulfur concentrations with MNBs closer to 0 and higher R values than the subtraction method. Thus, the applied subtraction method is definitely not the ideal one. Nevertheless, this method does not produce wrong results: Modeled emissions, chemical reactions, aerosol processes, and transport are not free of uncertainty. Hence, a perfect sectoral distinction technique would yield exact and correct sectoral contribution with respect to the model but not necessarily with respect to reality.

8 Conclusions

The impact of sea salt emissions on air quality and on nitrogen deposition in Northwestern Europe was evaluated in this thesis by means of the chemistry transport model CMAQ. The modeled sea salt sodium concentrations performed well in comparison with EMEP measurements. Salinity was introduced as an additional parameter for the sea salt emission calculations, which yielded a considerable improvement of modeled sodium PM_{10} concentrations in the Baltic Sea region. This result showed that sea salt scaling by salinity is very relevant over oceanic regions with salinity distinct from 35 ‰. Detailed coastline data were used to derive a gridded open ocean and surf zone data-set for calculating higher quality surf zone emissions. These emissions improved the atmospheric sodium concentrations at several stations in summer, but led to a significant overestimation of sea salt emissions along Norwegian fjords. A deactivation of surf zone sea salt emissions in the fjords is necessary for studies focusing on the Scandinavian region. This study refrained from dealing with this overestimation because it did not impact the atmospheric sea salt concentrations in the central model domain. Generally, it is important to include surf zone emissions parameterizations because sea salt emissions are considerably enhanced along the real world's coastlines. However, a distinct implementation of surf zone emissions in individual coastal regions is necessary in models. The salinity-improved CMAQ sea salt emission setup denoted as GO03 was evaluated against two alternative sea salt emission parameterizations. The first is a combination of three existing functions. It depends on u_{10} and SST but was extended by the same salinity dependence as GO03. The other parameterization is a state-of-the-art parameterization depending on wind, salinity, SST, and wave parameters. The first parameterization is abbreviated as SP13 and the second as OV14. The three parameterizations were chosen because they generate differently shaped particle size distributions and depend on different input parameters.

The comparison based on sodium PM_{10} concentrations showed that the modified CMAQ setup yielded concentrations of similar quality as the OV14 parameterization, while the SP13 parameterization produced considerable overestimations. At coastal stations, GO03 produced concentrations that best reproduced the measurements, but these concentrations decreased too fast during the advection from the coast toward inland stations. In contrast, concentrations by OV14 underestimated measurements at coastal stations but performed considerably better at inland stations. The particles of OV14 exhibited a lower dry deposition velocity than those of GO03, thereby yielding a spatial difference in deposition patterns. This shows that the size distribution of sea salt emissions is important to predict sodium concentrations at inland stations correctly and that the distribution impacts the medium range transport of sea salt particles and substances attached to them.

Sea salt particles influenced the atmospheric NO_3^--HNO_3 partitioning and enhanced dry nitrate deposition. The three sea salt emission parameterizations effected atmospheric nitrate concentrations differently, but none of the parameterizations clearly reproduced HNO_3+NO_3^- (sNO_3) and NH_3+NH_4^+ (sNH_4) concentrations significantly closer to the observations than the other two. The sNO_3 and sNH_4 and not the NO_3^- and NH_4^+ concentrations, respectively, were compared with measurements because no sufficient amount of reliable measurements of the latter two components were available. The GO03 case yielded the lowest particulate NO_3^- concentrations, whereas the OV14 case yielded the highest PM_{10} and the SP13 case yielded the highest $PM_{2.5}$ concentrations. The sNO_3 concentrations were influenced in the same manner as nitrate PM_{10}.

All three parameterizations yielded a decrease in nitrate $PM_{2.5}$ concentrations compared to

a situation without sea salt. This indicates that the increased nitrogen deposition through sea salt particles has a stronger impact than the enrichment of nitrate at the particle surfaces. In winter, nitrate PM_{10} concentrations revealed the same pattern but, in summer, the presence of sea salt particles considerably enhanced the nitrate PM_{10} concentrations. Thus, the NO_3^--HNO_3 equilibrium clearly shifted toward nitrate.

Up to 7 % and 3.5 % of the nitrogen deposition into the North Sea and Baltic Sea, respectively, were attributed to the presence of sea salt particles. The total nitrogen deposition into the sea revealed weak seasonal variations but the contribution from sea salt was found to be higher in winter. The alternative sea salt emission parameterization OV14 led to a considerable decrease in the sea-salt-related nitrogen deposition into the North Sea compared to the base case.

The contribution of emissions from the anthropogenic sectors energy production and shipping to the atmospheric particulate sulfate concentrations was assessed. The other anthropogenic sources, comprising mainly non-energy-producing industrial facilities, were summarized as a single sector denoted as OthrAnthr. The fine and coarse particulate sulfate concentrations at most stations were clearly dominated by emissions from the energy and OthrAnthr sectors. A discrepancy was found between the contribution of power plants to the total sulfur emissions and to the sulfate PM_{10} concentrations: The energy sector had the highest share in the anthropogenic sulfur emissions, while the OthrAnthr sector had the highest contribution to sulfate concentrations. Power plants emit into higher altitudes, thus leading to a stronger dispersion of exhaust gases. They also emit relatively more SO_2 than SO_4^{2-} compared to the sources of the OthrAnthr sector. Therefore, the energy sector contributed less particulate sulfate as expected earlier. In summer, the shipping sector had relevant contributions of up to 30 % at coastal stations. The processing of shipping-related SO_2 to SO_4^{2-} is enhanced in summer because stronger solar radiation leads to more oxidizing compounds in the atmosphere. Sea salt sulfate of the GO03 parameterization also contributed up to a third of the sulfate PM_{10} concentrations at coastal stations but contributed less at inland stations. The OV14 sea salt yielded considerably lower sea salt sulfate contributions. Sulfate $PM_{2.5}$ consisted of nearly no sea salt sulfate, whereas anthropogenic sources had similar shares in the respective $PM_{2.5}$ and PM_{10} fractions. Compared to sulfate PM_{10}, the SO_2 concentrations were differently composed with higher contributions from the energy and lower from the OthrAnthr sector. The shipping sector contributed more SO_2 than particulate sulfate at coastal stations and vice versa at inland stations, clearly indicating the processing of SO_2 into sulfate during transport.

The procedure for calculating the sectoral contributions was found to yield high deviations from the actual contributions in some situations: The uncertainty was higher in cases with low sea salt contributions than in cases with high sea salt contributions. Additionally, the reference sea salt sulfate concentrations correlated better with measurements and had lower biases than concentrations calculated by the evaluated method. It is unclear whether these findings can be transferred to the anthropogenic sectoral contributions.

Overall, it was shown that sea salt emissions are relevant for some atmospheric processes. A sea salt emission parameterization of low complexity as currently implemented in CMAQ and a first-order correction by salinity yielded results of similar quality as a complex state-of-the-art sea salt emission parameterization when PM_{10} mass concentrations are analyzed. The three compared emission parameterizations yielded different sea salt particle size distributions. These distributions differently impacted the HNO_3-NO_3^- equilibrium concentrations as well as the nitrogen deposition. Detailed size-resolved and speciated particle measurements are necessary for a proper validation of the sea salt emission parameterizations as well as for assessing the interaction between sea salt particles and atmospheric nitrogen species. Sea salt sulfate had a respectable contribution to the particulate sulfate mass in coastal regions, but it decreased toward inland regions. However, atmospheric sulfate and SO_2 concentrations were clearly dominated by emissions of energy production and non-energy-production industrial facilities (OthrAnthr sector). In coastal regions shipping emissions in summer also had a high contribution.

A Appendix of Paper 1

A.1 Statistical Evaluation

The statistical measures RAE, MNB, and R are calculated according to Eqs. (A.1), (A.2), and (A.3), respectively.

$$\mathrm{RAE} = \frac{1}{n} \times \sum_{i=1}^{n} |P_i - O_i| \tag{A.1}$$

$$\mathrm{MNB} = \frac{1}{n} \times \sum_{i=1}^{n} \frac{P_i - O_i}{O_i} \tag{A.2}$$

$$R = 1 - \frac{6}{n\,(n^2 - 1)} \times \sum_{i=1}^{n} (P_i - O_i)^2 \tag{A.3}$$

P_i is ith predicted value, p_i is the rank of the ith predicted value, O_i is the ith observed value, o_i is the rank of the ith observed value, and n is the number of observations.

A.2 Deposition Calculations

The nitrogen deposition is calculated from the dry and wet depositions of NO, NO_2, HNO_3, NO_3^-, NH_3, NH_4^+, NO_3, nitrous acide (HONO), peroxynitric acid (PNA), and peroxyacyl nitrate (PAN) according to Eqs. (A.4) to (A.6). HNO_3 and NO_3^- as well as NH_3 and NH_4^+ are separately listed in the CMAQ wet deposition output in order to distinguish the amount of particulate (ions) and gas compounds that were washed out.

$$\mathrm{WetDep_N} = M_\mathrm{N} \times \sum_{s \in \mathrm{species}} \frac{\mathrm{WetDep}_s}{M_s} \tag{A.4}$$

$$\mathrm{DryDep_N} = M_\mathrm{N} \times \sum_{s \in \mathrm{species}} \frac{\mathrm{DryDep}_s}{M_s} \tag{A.5}$$

$$\mathrm{Dep_N} = \mathrm{DryDep_N} + \mathrm{WetDep_N} \tag{A.6}$$

$$\mathrm{species} = \left\{\mathrm{NO}, \mathrm{NO_2}, \mathrm{HNO_3}, \mathrm{NO_3}^-, \mathrm{NH_3}, \mathrm{NH_4}^+, \mathrm{NO_3}, \mathrm{HONO}, \mathrm{PAN}, \mathrm{PNA}\right\}$$

DryDep_s is the dry deposition of species s, WetDep_s is the wet deposition of species s, Dep_s is the deposition of species s (sum of dry and wet deposition), and M_s is the molar mass of species s.

B Supplement of Paper 1

B.1 OCEAN file: ocean mask and surf zone definition

Please find an extended version of this supplement as Apdx. H.

B.2 Software for Data Evaluation

Please find an extended version of this supplement as Apdx. J

B.3 Model Input and Output Data and statistical Evaluation

Those model data which forms the base for plots and statistical evaluations are attached in post-processed format which allows the reproduction of all plots and figures (Table B.1). Data are attached as text (*.csv) and netCDF (*.nc) files. Concentration data are located in the subdirectory `supplement/paper1/conc`, sea salt emission data in the subdirectory `supplement/paper1/ssemis`, and nitrogen deposition data in the subdirectory `supplement/paper1/ndep`.

Table B.1: List of attached files containing model output data.

Type	Comment	Files	Corresp. Fig.
Sea Salt Emissions	averaged in time; resolved in space; one season (summer | winter) and one case (base |noSurf) per file;	`ssemis.area.timemean.*.nc` (four files)[1]	3.3 (sum of ANAJ, ANAK, ACLJ, ACLK, ASO4J, and ASO4K plotted)
Sea Salt Emissions	hourly resolved in time; one location (A |B |C), one season (summer |winter) and one case (base |noSurf) per file;	`ssemis.timeseries.*.csv` (12 files)	3.4 (MASST plotted)
Concentrations	hourly resolved in time; data on each station (Table B.3); one species (Na^+ | xSO4 |sNH_4 | sNO_3), one season (summer | winter) and one case (base | noSurf | full | zero) per file;	`conc.timeseries.*.csv` (32 files)	3.5, 3.6, 3.7, and 3.8
Nitrogen Wet Deposition	Nitrogen wet deposition averaged over the time intervals for which measurement data are available; one case (base |noSurf |full |zero) and one station per file	`wetdep.timeseries.*.csv` (56 files)	3.10
Nitrogen Deposition	averaged in time; resolved in spaces; one season (summer |winter) and one case (base |noSurf |zero |full) per file	`ndep.area.timemean.*.nc` (8 files)[1]	3.9

[1] The J and K in variable names indicate accumulation and coarse mode particle mass/number, respectively. The T indicates total mass/number (J + K). ANA, ACL and ASO4 denote Na^+, Cl^-, and SO_4^{2-} emissions, respectively.

Open ocean and surf zone fraction per grid cell are needed for calculating sea salt emissions in CMAQ (see Table B.2). Additionally, these data are needed for the simulation result evaluation. The files are located in the subdirectory `supplement/paper1/cmaq`.

Data on the statistical evaluation are in the file `supplement/paper1/conc/statistical.evaluation.conc.csv` and in `supplement/paper1/statistical.evaluation.wetdep.csv`. They contain

- n (number of considered values),

- RAE (residual absolute error),
- MNB (mean normalized bias),
- R (Spearman's correlation coefficient),
- MEAN.sim (mean of considered model values),
- MEAN.obs (mean of considered EMEP values),
- MEDIAN.sim (median of considered model values), and
- MEDIAN.obs (median of considered EMEP values).

Table B.2: Input files for CMAQ. Files are also needed for the data evaluation

Type	Comment	Files	Corresp. Fig.
Sea Surface Fraction	OCEAN file needed for sea salt emissions in CMAQ; contains OPEN (open ocean fraction), SURF (surf zone fraction), and MASK (0 = land; 1 = coast; 2 = open ocean)	`*sf050m*ubound_sal.nc` (base), `*sf000m*ubound.nc` (noSurf), `*noSalt*.nc` (zero), `*sf050m*ubound.nc` (full), `*sf050m*sal.nc` (no surf zone fraction capping)	H.3 and B.1

B.4 EMEP data

EMEP data for the comparison can be obtained from the EBAS database at `ebas.nilu.no`. Data for the year 2008 for the following stations were obtained for the evaluation of model data (Table B.3).

Table B.3: EMEP stations at which model and measurement data were compared statistically.

Station ID	Station Name	Data	Lon	Lat	Height [m]	Location
DE0001R	Westerland	Na^+, NO_3^-, sNO_3, sNH_4	8.31	54.93	12	Coast
DE0002R	Waldhof	Na^+, (NO_3^-,) sNO_3, sNH_4	10.76	52.8	74	Inland
DE0007R	Neuglobsow	Na^+, (NO_3^-,) sNO_3, sNH_4	13.03	53.17	62	Inland
DE0009R	Zingst	Na^+, (NO_3^-,) sNO_3, sNH_4	12.73	54.43	1	Coast
DE0044R	Melpitz	Na^+, NO_3^-	12.93	51.53	86	Inland
DK0003R	Tange	Na^+, sNO_3, sNH_4	9.6	56.35	13	Inland
DK0005R	Keldsnor	Na^+, sNO_3, sNH_4	10.73	54.73	10	Coast
DK0008R	Anholt	Na^+, sNO_3, sNH_4	11.52	56.72	40	Coast
DK0031R	Ulborg	Na^+, sNO_3, sNH_4	8.43	56.28	10	Coast
FI0009R	Utö	Na^+, sNO_3, sNH_4	21.38	59.78	7	Coast
FI0017R	Virolahti II	Na^+, sNO_3, sNH_4	27.69	60.53	4	Coast
NO0001R	Birkenes	Na^+, (NO_3^-,) sNO_3, sNH_4	8.25	58.38	190	Mixed
NO0056R	Hurdal	Na^+, (NO_3^-,) sNO_3, sNH_4	11.08	60.37	300	Inland
PL0002R	Jarczew	(NO_3^-,) sNO_3, sNH_4	21.98	51.82	180	Inland
PL0004R	Leba	(NO_3^-,) sNO_3, sNH_4	17.53	54.75	2	Coast
SE0014R	Røaö	sNO_3, sNH_4	11.91	57.39	5	Coast

B.5 Nitrogen Deposition

The nitrogen deposition per grid cell was multiplied by the sea surface fraction per grid cell for calculating the nitrogen deposition into the sea. Thus, in a coastal grid cell with 40 % sea surface and 60 % land, only 40 % of the nitrogen deposition is considered. Figure B.1 shows the sea surface fraction and the regions that are considered as North and Baltic Sea. The latter information is necessary to create Table 3.10.

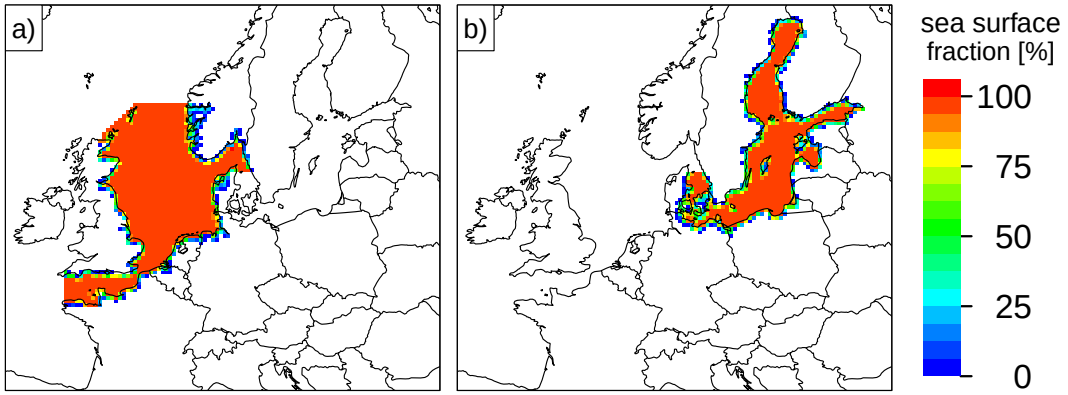

Figure B.1: Sea surface fraction of North (a) and Baltic Sea (b) that is considered for calculating the nitrogen deposition into both seas.

C Appendix of Paper 2

C.1 Abbreviations

Table C.1 shows the numbers and meaning of all abbreviations and variables used in the manuscript and in the supplement.

C.2 Sea Salt Emission Parameterizations

C.2.1 GO03

The sea salt emission parameterization GO03 published by Gong [2003] is given by Eq. (C.1).

$$\begin{aligned}\frac{dF_{\mathrm{GO03}}}{dr_{80}} &= W \times 3.576 \times 10^5 r_{80}^{-A} \left(1 + 0.057 \times r_{80}^{3.45}\right) \times 10^{1.607e^{-B^2}} \\ &= 1.373 \times u_{10}^{3.41} r_{80}^{-A} \left(1 + 0.057 \times r_{80}^{3.45}\right) \times 10^{1.607e^{-B^2}} \\ A &= 4.7 \times \left(1 + \Theta \times r_{80}\right)^{-0.017 \times r_{80}^{-1.44}} \\ B &= \left(0.433 - \log_{10} r_{80}\right) / 0.433 \\ \Theta &= 30\end{aligned} \tag{C.1}$$

The parameterization is valid on the size range $0.07\,\mu\mathrm{m} \leq r_{80} \leq 20\,\mu\mathrm{m}$.

C.2.2 SP13

The parameterization SP13 published by Spada et al. [2013] consists of MO86, SM93, and MA03. Below, all three formulas are given in Eqs. (C.2), (C.3), and (C.4), respectively. Equation (C.5) defines the combination of all three parameterizations.

$$\begin{aligned}\frac{dF_{\mathrm{MO86}}}{dr_{80}} &= W \times 3.576 \times 10^5 r_{80}^{-3} 10^{1.19e^{-B^2}} \\ &= 1.373 \times u_{10}^{3.41} r_{80}^{-3} 10^{1.19e^{-B^2}} \\ B &= \left(0.380 - \log_{10} r_{80}\right) / 0.650\end{aligned} \tag{C.2}$$

The parameterization is valid on the size range $0.8\,\mu\mathrm{m} \leq r_{80} \leq 20\,\mu\mathrm{m}$.

$$\begin{aligned}\frac{dF_{\mathrm{SM93}}}{dr_{80}} &= \sum_{k=1}^{2} \left(A_k\left(u_{10}\right) \times \exp\left(-f_k \left(\ln\left(\frac{r_{80}}{r_{0k}} \right) \right)^2 \right) \right) \\ \log_{10} A_1 &= 0.0676 \times u_{10} + 2.43 \\ \log_{10} A_2 &= 0.959 \times u_{10}^{0.5} - 1.476 \\ r_{01} &= 2.1\,\mu\mathrm{m}; \qquad r_{02} = 9.2\,\mu\mathrm{m} \\ f_1 &= 3.1; \qquad f_2 = 3.3\end{aligned} \tag{C.3}$$

Table C.1: Parameters, their units and their meaning.

Parameter	Unit	Explanation
r_{80}	µm	particle radius at 80 % relative humidity
D_{dry}	µm	dry particle diameter
PM_{10}	$\mu\mathrm{g\,m^{-3}}$	total particle mass
$\mathrm{PM}_{2.5}$	$\mu\mathrm{g\,m^{3}}$	fine particle ($\leq 2.5\,\mu$m) mass, $\neq \sum$ CMAQ Aitken- and accumulation-mode mass
PM_{C}	$\mu\mathrm{g\,m^{-3}}$	coarse particle mass: $\mathrm{PM}_{10}-\mathrm{PM}_{2.5}$, $\neq$ CMAQ coarse-mode mass
u_{10}	$\mathrm{m\,s^{-1}}$	10 m wind speed
SST	K	sea surface temperature
SAL	‰	sea surface salinity
W	-	whitecap coverage between 0 (0 %) and 1 (100 %)
u_*	$\mathrm{m\,s^{-1}}$	friction velocity at the sea surface
H_s	m	significant wave height
C_D	-	drag coefficient due to wind waves
ν_W	$\mathrm{m^2\,s^{-1}}$	sea water kinetic viscosity
$\mathrm{Re}_{\mathrm{Hw}}$	-	Reynolds number of the sea surface due to waves
RH	%	relative humidity
GMD	µm	geometric mean diameter
σ	-	standard deviation
$\frac{dF}{dr_{80}}$, $\frac{dF}{dD_{\mathrm{dry}}}$	$\mathrm{m^{-2}\,\mu m^{-1}\,s^{-1}}$	particle number flux
$\frac{dF}{d\log D_{\mathrm{dry}}}$	$\mathrm{m^{-2}\,s^{-1}}$	particle number flux
ρ_{ss}	$\mathrm{g\,cm^{-3}}$	density of dry sea salt

Spada et al. [2013] considers the parameterization to be valid on the size range $5\,\mu\mathrm{m} \leq r_{80} \leq 30\,\mu\mathrm{m}$.

$$\begin{aligned} \frac{dF_{\mathrm{MA03}}}{dD_{\mathrm{dry}}} &= W \times (A \times \mathrm{SST} + B) \\ A &= c_4 \times D_{\mathrm{dry}}^4 + c_3 \times D_{\mathrm{dry}}^3 + c_2 \times D_{\mathrm{dry}}^2 + c_1 \times D_{\mathrm{dry}} + c_0 \\ B &= d_4 \times D_{\mathrm{dry}}^4 + d_3 \times D_{\mathrm{dry}}^3 + d_2 \times D_{\mathrm{dry}}^2 + d_1 \times D_{\mathrm{dry}} + d_0 \end{aligned} \tag{C.4}$$

The parameterization is valid on the size range $0.02\,\mu\mathrm{m} \leq r_{80} \leq 2.8\,\mu\mathrm{m}$. The parameters c_i and d_i are provided in Table D.1.

$$\frac{dF_{\mathrm{SP13}}}{dD_{\mathrm{dry}}} = \begin{cases} \frac{dF_{\mathrm{MA03}}}{dD_{\mathrm{dry}}} & D_{\mathrm{dry}} \leq 2.8\,\mu\mathrm{m} \\ \frac{dF_{\mathrm{MO86}}}{dD_{\mathrm{dry}}} & D_{\mathrm{dry}} > 2.8\,\mu\mathrm{m} \\ & \quad \wedge\ u_{10} < 9\,\mathrm{m\,s^{-1}} \\ \max\left(\frac{dF_{\mathrm{MO86}}}{dD_{\mathrm{dry}}}, \frac{dF_{\mathrm{SM93}}}{dD_{\mathrm{dry}}}\right) & D_{\mathrm{dry}} > 2.8\,\mu\mathrm{m} \\ & \quad \wedge\ u_{10} \geq 9\,\mathrm{m\,s^{-1}} \end{cases} \tag{C.5}$$

SP13 is valid on the size range $0.02\,\mu\mathrm{m} \leq D_{\mathrm{dry}} \leq 30\,\mu\mathrm{m}$.

C.2.3 OV14

The sea salt emission parameterization OV14 published by Ovadnevaite et al. [2014] is given by Eq. (C.6).

$$\frac{dF_{\mathrm{OV14}}}{d\log_{10} D_{\mathrm{dry}}} = \sum_{i=1}^{5} \frac{F_i\left(\mathrm{Re_{Hw}}\right)}{\sqrt{2\pi} \times \log_{10}\sigma_i} \times \exp\left(-\frac{1}{2}\left(\frac{\log_{10}\frac{D_{\mathrm{dry}}}{\mathrm{GMD}_i}}{\log_{10}\sigma_i}\right)\right) \tag{C.6}$$

$$\mathrm{Re_{Hw}} = \frac{u_* \times H_S}{\nu_W} = \frac{\sqrt{C_D} \times u_{10} \times H_S}{\nu_W} \tag{C.7}$$

The kinetic viscosity ν_W is calculated according to Eqs. (22) and (8) in Sharqawy et al. [2010]. The source function is valid on the size range $0.015\,\mu\mathrm{m} < D_{\mathrm{dry}} < 6\,\mu\mathrm{m}$. The values for GMD_i, σ_i, and F_i are given in the supplement (Table D.2) and in Ovadnevaite et al. [2014].

C.3 Statistical Evaluation

The statistical figures residual absolute error (RAE), mean normalized bias (MNB), and Spearman's correlation coefficient (R) are calculated according to Eqs. (C.8), (C.9), and (C.10) , respectively.

$$\mathrm{RAE} = \frac{1}{n} \times \sum_{i=1}^{n} |P_i - O_i| \tag{C.8}$$

$$\mathrm{MNB} = \frac{1}{n} \times \sum_{i=1}^{n} \frac{P_i - O_i}{O_i} \tag{C.9}$$

$$\mathrm{R} = 1 - \frac{6}{n\left(n^2-1\right)} \times \sum_{i=1}^{n} \left(P_i - O_i\right)^2 \tag{C.10}$$

with

P_i	i^{th} predicted value
p_i	rank of the i^{th} predicted value
O_i	i^{th} observed value
o_i	rank of the i^{th} observed value
n	number of observations

D Supplement of Paper 2

D.1 Sea Salt Source functions

In order to combine, compare and integrate the functions introduced below some general assumptions and transformations are necessary that are described in Eqs. (D.1), (D.2), and (D.3). According to Lewis and Schwartz [2004] we assume

$$r_{80} = 2 \times r_{\mathrm{dry}} = D_{\mathrm{dry}} \tag{D.1}$$

Following the above relation and basic calculus we get

$$\frac{dF}{dr_{80}} = \frac{dF}{dD_{\mathrm{dry}}} \tag{D.2}$$

$$\frac{dF}{dD_{\mathrm{dry}}} = \frac{d\ln D_{\mathrm{dry}}}{dD_{\mathrm{dry}}} \times \frac{dF}{d\ln D_{\mathrm{dry}}} = \frac{1}{D_{\mathrm{dry}}} \times \frac{dF}{d\ln D_{\mathrm{dry}}} = \frac{1}{\ln 10 \times D_{\mathrm{dry}}} \times \frac{dF}{d\log_{10} D_{\mathrm{dry}}} \tag{D.3}$$

D.1.1 MO86, SM93, GO03, MA03, and SP13

Monahan and colleagues [Monahan and Muircheartaigh, 1980; Monahan et al., 1982] described the generation of sea salt particles from bursting bubbles. They fitted a power-law-shaped whitecap coverage function to the wind speed in 10 m height (Eq. (D.4)) [Monahan and Muircheartaigh, 1980]. A sea salt particle number flux distribution was estimated for 100 % whitecap coverage and multiplied by W [Monahan et al., 1986]. The resulting parameterization (Eq. D.5) is valid on the size range $0.8\,\mu\mathrm{m} < r_{80} < 20\,\mu\mathrm{m}$.

$$W = 3.84 \times 10^{-6} \times u_{10}^{3.41} \tag{D.4}$$

$$\begin{aligned} \frac{dF_{\mathrm{MO86}}}{dr_{80}} &= W \times 3.576 \times 10^{5} \times r_{80}^{-3} \times 10^{1.19 \times e^{-B^2}} \\ &= 1.373 \times u_{10}^{3.41} \times r_{80}^{-3} \times 10^{1.19 \times e^{-B^2}} \\ B &= \frac{0.380 - \log_{10}(r_{80})}{0.650} \end{aligned} \tag{D.5}$$

Gong [2003] updated Monahan et al. [1986] for smaller size ranges given by Eq. (C.1). The parameterization is valid on the size range $0.07\,\mu\mathrm{m} < r_{80} < 20\,\mu\mathrm{m}$. An adjustable dimensionless parameter θ was introduced and set to 30. However, a sensitivity study compared with observational data showed [Gantt et al., 2015] that setting θ to 8 improves Na^+ and $PM_{2.5}$ concentrations modeled with CMAQ. Hence in CMAQ v5.1, θ will be set accordingly.

Smith et al. [1993] fitted two log normal distributions given by Eq. (C.3) to coarse sea salt particle measurements of $0.09\,\mu\mathrm{m} < r_{\mathrm{RH}} < 23.5\,\mu\mathrm{m}$ performed on an island located 100 km off the north-west coast of the Scottish mainland. It was assumed that RH was approximately 80 % and that, based on preparation studies, surf zone emissions did not have a relevant contribution to the measured sea salt particles. Spada et al. [2013] considers the parameterization to be valid on the size range of $5\,\mu\mathrm{m} < r_{80} < 30\,\mu\mathrm{m}$.

Table D.1: Constants for Eq. (C.4). Values are taken from Mårtensson et al. [2003, Table 1] but given with more significant digits [Mårtensson, 2015, personal communication].

D_{dry} interval [µm]	c_4	c_3	c_2	c_1	c_0
0.020–0.145	−2.576 165 5e35	5.932 443 6e28	−2.867 174 3e21	−3.002 983 7e13	−2.880 813 5e6
0.145–0.419	−2.452 289 3e33	2.403 544 1e27	−8.147 834 1e20	1.182 850 3e14	−6.742 993 9e6
0.419–2.800	1.085 156 1e29	−9.841 434e23	3.132 359 3e18	−4.164 532 6e12	2.180 637 4e6
D_{dry} interval [µm]	d_4	d_3	d_2	d_1	d_0
0.020–0.145	7.188 465 6e37	−1.615 664 7e31	6.791 329 9e23	1.828 946 9e16	7.609 268 1e8
0.145–0.419	7.368 315 0e35	−7.310 214 9e29	2.528 340 4e23	−3.787 272 9e16	2.279 400 5e9
0.419–2.800	−2.859 476 2e31	2.601 213 7e26	−8.297 464 4e20	1.104 667 8e15	−5.800 388 0e8

Mårtensson et al. [2003] performed laboratory studies on SST and SAL dependence of sea salt emissions. They derived a SST dependent particle number flux parameterization based on two polynomial fits of the degree 4 (Eq. (C.4)). The whitecap coverage parameterization from Monahan and Muircheartaigh [1980] was employed (Eq. (D.4)). The polynomial coefficients (c_i and d_i) are given in Table D.1. Three sets of coefficients exist for three different intervals of Ddry. This parameterization is valid on the size range of $0.02\,\mu\mathrm{m} < D_{\mathrm{dry}} < 2.8\,\mu\mathrm{m}$ and on the temperature range of $271\,\mathrm{K} < SST < 298\,\mathrm{K}$. However, the polynomial is negative for some D_{dry} when the third set of coefficients is used and $SST < 275.6\,\mathrm{K}$. This situation needs special treatment when implemented.

Spada et al. [2013] compared several source functions and combinations of them on a global scale: They considered an extension of GO03 by SST [Jaeglé et al., 2011] and MA03/MO86/SM93 [Mårtensson et al., 2003; Monahan et al., 1986; Smith et al., 1993]. The latter one is used in this study and abbreviated as SP13 (Eq. (C.5)). Because of Eq. (D.2), we do not need to rewrite Eqs. (C.2) and (C.3). SP13 is valid on the size range $0.02\,\mu\mathrm{m} < D_{\mathrm{dry}} < 30\,\mu\mathrm{m}$.

D.1.2 OV14

Recently, Ovadnevaite et al. [2014] published a new parameterization depending on wave state, wind speed and sea water viscosity ν_W whereby the viscosity depends on SAL and SST (Eq. (C.6)). The formula can be transformed to Eq. (D.6) by using Eq. (D.3) to facilitate the numeric integration.

$$\frac{dF_{\mathrm{OV14}}}{dD_{\mathrm{dry}}} = \ln 10 \times D_{\mathrm{dry}} \times \sum_{i=1}^{5} \frac{F_i\left(\mathrm{Re_{Hw}}\right)}{\sqrt{2\pi} \times \log_{10}\sigma_i} \times \exp\left(-\frac{1}{2}\left(\frac{\log_{10}\frac{D_{\mathrm{dry}}}{\mathrm{GMD}_i}}{\log_{10}\sigma_i}\right)\right) \tag{D.6}$$

$$\mathrm{Re_{Hw}} = \frac{u_* \times H_S}{\nu_W} = \frac{\sqrt{C_D} \times u_{10} \times H_S}{\nu_W} \tag{D.7}$$

The factors GMD_i and σ_i and the functions $F_i\left(\mathrm{Re_{Hw}}\right)$ are given in Table D.2. The kinetic viscosity ν_W is calculated according to Eqs. (22) and (8) in Sharqawy et al. [2010]. The source function is valid for a diameter size range of $0.015\,\mu\mathrm{m} < D_{\mathrm{dry}} < 6\,\mu\mathrm{m}$.

In this study, the drag coefficient C_D was taken from WAM model runs of the coastDatII database (inside the North Sea) or was calculated according to Wu [1982] given in Eq. (D.8) (oceanic regions other than the North Sea). The friction velocity u_* is calculated from C_D by

$$C_D = \begin{cases} 1.2875 \times 10^{-3}, & \text{for } u_{10} < 7.5\,\mathrm{m\,s^{-1}} \\ \left(0.8 + 0.065\,\mathrm{s\,m^{-1}} \times u_{10}\right) \times 10^{-3}, & \text{for } u_{10} \geq 7.5\,\mathrm{m\,s^{-1}} \end{cases} \tag{D.8}$$

$$u_* = u_{10} \times \sqrt{C_D} \tag{D.9}$$

Table D.2: Values for Eqs. (C.6) and (D.6) but given with more significant digits than in the original parameterization [Ovadnevaite, 2015, personal communication]. When one wants to reconstruct Fig. 4 in Ovadnevaite et al. [2014], one gets slight deviations due to rounding.

Mode (i)	GMD_i [µm]	σ_i [µm]	$F_i\,(\mathrm{Re_{Hw}})$
1	0.018	1.37	$104.51 \times \left(\mathrm{Re_{Hw}} - 10^5\right)^{0.556}$
2	0.041	1.5	$0.044 \times \left(\mathrm{Re_{Hw}} - 10^5\right)^{1.08}$
3	0.09	1.42	$149.64 \times \left(\mathrm{Re_{Hw}} - 10^5\right)^{0.545}$
4	0.23	1.53	$2.96 \times \left(\mathrm{Re_{Hw}} - 10^5\right)^{0.79}$
5	0.83	1.85	$0.52 \times \left(\mathrm{Re_{Hw}} - 2 \times 10^5\right)^{0.87}$

D.2 Surf Zone Treatment

The surf zone is implemented in accordance with Kelly et al. (2010) by setting the whitecap coverage to 1 within it. For each grid cell, the fraction of open ocean and surf zone is calculated in accordance with Neumann et al. [2016] and denoted as OPEN and SURF, respectively. In Eqs. (D.5), (C.1), and (C.4) the W is replaced by Eq. (D.10).

$$(W \times \mathrm{OPEN} + \mathrm{SURF}) \times \frac{1}{W} \tag{D.10}$$

Exemplary, applying this to GO03 (Eq. (C.1)) leads to Eq. (D.11).

$$\begin{aligned} \frac{dF_{\mathrm{GO03,net}}}{dr_{80}} &= (W \times \mathrm{OPEN} + \mathrm{SURF}) \times \frac{1}{W} \times \frac{dF_{\mathrm{GO03}}}{dr_{80}} \\ \frac{dF_{\mathrm{GO03}}}{dr_{80}} &= (W \times \mathrm{OPEN} + \mathrm{SURF}) \times 3.576 \times 10^5 r_{80}^{-A} \left(1 + 0.057 \times r_{80}^{3.45}\right) \times 10^{1.607 e^{-B^2}} \end{aligned} \tag{D.11}$$

D.3 Salinity Dependence

For this study, the GO03 and SP13 parameterizations were enhanced by a salinity dependence. Figure D.1 shows the dependence for three exemplary salinities. We assumed that the sea salt emission parameterizations were derived for a sea surface salinity of 35 ‰.

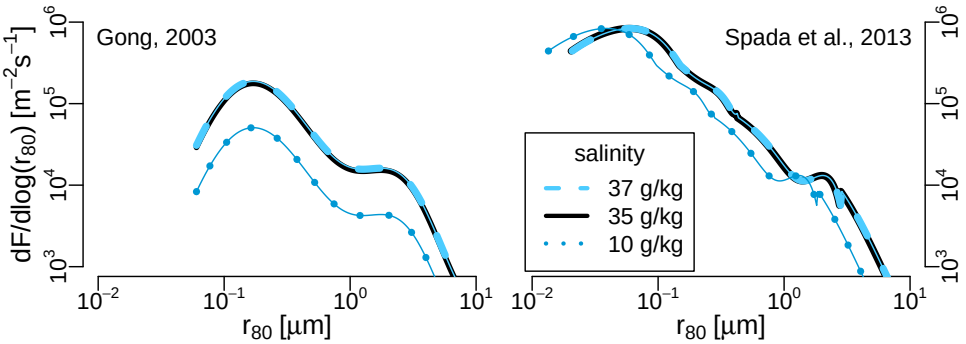

Figure D.1: Salinity dependence of the GO03 (left) and SP13 (right) parameterizations as implemented in this study. Parameters are chosen according to Fig. 4.2 in the main manuscript: $u_{10} = 8\,\mathrm{m\,s^{-1}}$, $\mathrm{SST} = 283\,\mathrm{K}$, $C_D = 2.15 \times 10^{-3}$, $H_s = 1.23\,\mathrm{m}$, and $\nu_W = 1.34 \times 10^{-6}\,\mathrm{m\,s^{-1}}$.

D.3.1 GO03

The sea salt number, surface area and mass (or volume) emissions are all scaled by the salinity SAL:

$$\frac{dF_{\mathrm{GO03,net}}}{dr_{80}} = \frac{\mathrm{SAL}}{35\,‰} \times (W \times \mathrm{OPEN} + \mathrm{SURF}) \times \frac{1}{W} \times \frac{dF_{\mathrm{GO03}}}{dr_{80}} \tag{D.12}$$

Because GO03 sea salt emissions are calculated within CMAQ, one solution for implementing the salinity dependence was to modify CMAQ code. Because OPEN and SURF are read in externally from the OCEANfile (see Appendix H), one can rewrite Eqs. (D.12) and (D.12) and scale OCEAN and SURF with SAL/35 ‰. Thus, no modifications in CMAQ are necessary.

$$\frac{dF_{\mathrm{GO03,net}}}{dr_{80}} = \left(W \times \frac{\mathrm{SAL}}{35\,‰} \times \mathrm{OPEN} + \frac{\mathrm{SAL}}{35\,‰} \times \mathrm{SURF}\right) \times \frac{1}{W} \times \frac{dF_{\mathrm{GO03}}}{dr_{80}} \tag{D.13}$$

This approach was chosen in this study. OPEN and SURF are considered to be constant in time. This approach does not allow including annual or diurnal variations of the salinity dependence.

D.3.2 SP13

We assume that (a) inorganic ions are homogeneously distributed in the water column (no enrichment at the sea surface or in deeper water layers) and that (b) the water droplet generation process is not affected by variable salinity. Then sea surface salinity and gross dry sea salt mass emissions are proportional to each other because the droplet emission distribution does not change but the sea salt concentration within them does change. Further we assume that we can apply the same relation to net sea salt emissions. This assumption is not completely correct. Thus, in a region with 17.5 ‰ salinity, the dry sea salt mass emissions should be half as high compared with the emissions in a region with 35 ‰ salinity. The sea salt number emissions should remain unchanged but the dry mass of sea salt per individual sea salt particle $m_{\mathrm{dry,SAL}}$ should vary as described:

$$m_{\mathrm{dry,SAL}} = \frac{\mathrm{SAL}}{35\,‰} \times m_{\mathrm{dry},35\,‰} \tag{D.14}$$

Dry sea salt particle volume and dry sea salt particle mass are proportional to each other. Therefore, for the volume (V), surface area (A), and diameter (D) of individual sea salt particles follows:

$$V_{\mathrm{dry,SAL}} = \frac{\mathrm{SAL}}{35\,‰} \times V_{\mathrm{dry},35\,‰} \tag{D.15}$$

$$A_{\mathrm{dry,SAL}} = \left(\frac{\mathrm{SAL}}{35\,‰}\right)^{2/3} \times A_{\mathrm{dry},35\,‰} \tag{D.16}$$

$$D_{\mathrm{dry,SAL}} = \left(\frac{\mathrm{SAL}}{35\,‰}\right)^{1/3} \times D_{\mathrm{dry},35\,‰} \tag{D.17}$$

If Eq. (D.17) is applied to the particle emission size distribution in Eq. (C.5) then the particle diameter needs to be scaled accordingly yielding a shift of the distribution by $\left(\sqrt[3]{\mathrm{SAL}/35\,‰} - 1\right) \times D_{\mathrm{dry}}$ to the right. If SAL < 35 ‰ then the shift is performed to the left (Figure D.1).

D.4 Integrating SP13 and OV14

The two sea salt source functions SP13 (Eqs. (C.5) and (D.20)) and OV14 (Eq. (D.6)) were integrated as described in Sect. 4.2.2, in Table D.3, and in Fig. 4.3. Equation (D.20) shows how the SAL dependence described in Sect. D.3 is applied to Eq. (C.5).

Table D.3: Overview of the integration of SP13 and OV14. This table should be considered in combination with Fig. 4.3 in the main manuscript. $D_{\mathrm{dry,min,SAL}}$ and $D_{\mathrm{dry,max,SAL}}$ denote the minimum and maximum diameters, respectively, for those the SP13 parameterization is defined (see Sect. D.3.2). $D_{\mathrm{dry,Aa}}$ and $D_{\mathrm{dry,ac}}$ are the integration boundaries between the Aitken and accumulation mode (index **Aa**) and between the accumulation and coarse mode (index **ac**), respectively.

Size mode	SP13	OV14
Aitken	Whole function integrated from $D_{\mathrm{dry,min,SAL}}$ [1] to $D_{\mathrm{dry,Aa}}$ (= 0.1 µm)	Modes 1 and 2 integrated from 0.015 µm to 6 µm
accumulation	Whole function integrated from $D_{\mathrm{dry,Aa}}$ to $D_{\mathrm{dry,ac}}$ [2]	Modes 3 and 4 integrated from 0.015 µm to 6 µm
coarse	Whole function integrated from $D_{\mathrm{dry,ac}}$ [2] to $D_{\mathrm{dry,max,SAL}}$ [1]	Mode 5 integrated from 0.015 µm to 6 µm

[1] see Sect. D.4.1; [2] see Table D.4 for appropriate values

The water content of wet sea salt – compared to dry – was calculate in accordance with Lewis and Schwartz [2004, p.54] (or Lewis and Schwartz [2006] for exactly this formulation):

$$\frac{D_{\mathrm{RH}}}{D_{80}} = 0.54 \times \left(\frac{2-\mathrm{RH}}{1-\mathrm{RH}}\right)^{\frac{1}{3}} \tag{D.18}$$

D.4.1 Integration boundaries for SP13

Values for the integration boundaries $D_{\mathrm{dry,min,SAL}}$, $D_{\mathrm{dry,Aa}}$, $D_{\mathrm{dry,ac}}$, and $D_{\mathrm{dry,max,SAL}}$ are needed for calculating Aitken, accumulation, and coarse mode emissions of the SP13 parameterization. The values for $D_{\mathrm{dry,min,SAL}}$ and $D_{\mathrm{dry,max,SAL}}$ are derived from the definition range of the parameterization and the value for $D_{\mathrm{dry,Aa}}$ is given in Table D.18. The integration boundary between accumulation and coarse mode ($D_{\mathrm{dry,ac}}$) is not defined yet. It was set equal to the intersection between accumulation and coarse mode distributions of the GO03 sea salt emission parameterizations as implemented in CMAQ: Both modal distributions are discrete functions of RH. For this study, the intersection wet diameter was calculated for each discrete RH value and converted into the corresponding dry diameter (Table D.4). The resulting dry diameter depends on RH which is an artifact. However, this dependency was kept in order to be consistent with CMAQ sea salt emissions.

Table D.4: RH dependent integration boundary between accumulation and coarse mode as dry diameter $D_{\mathrm{dry,ac}}$ for integrating the SP13 parameterization.

RH [%]	$D_{\mathrm{dry,ac}}$ [µm]	RH [%]	$D_{\mathrm{dry,ac}}$ [µm]
45	1.276076	...	...
50	1.324269	80	1.498309
55	1.347672	85	1.49023
60	1.388263	90	1.514228
65	1.415549	93	1.550082
70	1.45391	95	1.578587
75	1.479312	97	1.577349
...	...	99	1.361808

Including SAL dependence into the integration of SP13 is not straightforward. Therefore, it is described in detail. We define a function f_{sp}

$$f_{sp}\left(D_{\mathrm{dry}}\right) = \frac{dF_{\mathrm{SP13}}}{dD_{\mathrm{dry}}} \tag{D.19}$$

in order to express the SAL dependence mathematically by

$$\frac{dF_{\mathrm{SP13,SAL}}}{dD_{\mathrm{dry}}} = f_{\mathrm{sp,\,SAL}}\left(D_{\mathrm{dry}}\right) = f_{\mathrm{sp}}\left(D_{\mathrm{dry}} \times \left(\frac{35\,‰}{\mathrm{SAL}}\right)^{1/3}\right) \tag{D.20}$$

The SAL dependent source function as defined by Eq. (D.20) is not valid on the same interval as Eq. (C.5) anymore; that was

$$D_{\mathrm{dry,min}} = 0.02\,\mu\mathrm{m} < D_{\mathrm{dry}} < 30\,\mu\mathrm{m} = D_{\mathrm{dry,max}}$$

But rather it is valid on the interval

$$D_{\mathrm{dry,min,SAL}} = 0.02\,\mu\mathrm{m} \times \left(\frac{\mathrm{SAL}}{35\,‰}\right)^{1/3} < D_{\mathrm{dry}} < 30\,\mu\mathrm{m} \times \left(\frac{\mathrm{SAL}}{35\,‰}\right)^{1/3} = D_{\mathrm{dry,max,SAL}}$$

Further, we define that the boundaries between Aitken and accumulation mode ($D_{\mathrm{dry,Aa}}$) and between accumulation and coarse mode ($D_{\mathrm{dry,ac}}$) remain unaffected by changes in SAL. $D_{\mathrm{dry,ac}}$ depends on RH (Table D.4).

$$D_{\mathrm{dry,Aa}} = 0.1\,\mu\mathrm{m}$$
$$D_{\mathrm{dry,ac}} = D_{\mathrm{dry,ac}}\left(\mathrm{RH}\right)$$

The dry sea salt number, surface area, and volume emissions are integrated based on these definitions and assumptions (Table D.5). Dry mass emissions are calculated from the volume emissions by multiplication with $\rho_{\mathrm{sea\ salt}}$ which is considered to be $2.2\,\mathrm{g\,cm^{-3}}$.

Table D.5: Integrals for calculating SAL dependent SP13 sea salt emissions.

	Number Emissions	Surface area Emissions	Volume Emissions
Aitken	$\int_{D_{\mathrm{min}}\sqrt[3]{\frac{S}{35\,‰}}}^{D_{\mathrm{Aa}}} f_{\mathrm{sp}}\left(\frac{D}{\sqrt[3]{\frac{S}{35\,‰}}}\right)\mathrm{d}D$	$\int_{D_{\mathrm{min}}\sqrt[3]{\frac{S}{35\,‰}}}^{D_{\mathrm{Aa}}} \pi D^2 \times f_{sp}\left(\frac{D}{\sqrt[3]{\frac{S}{35\,‰}}}\right)\mathrm{d}D$	$\int_{D_{\mathrm{min}}\sqrt[3]{\frac{S}{35\,‰}}}^{D_{\mathrm{Aa}}} \frac{\pi}{6} D^3 \times f_{sp}\left(\frac{D}{\sqrt[3]{\frac{S}{35\,‰}}}\right)\mathrm{d}D$
acc.	$\int_{D_{\mathrm{Aa}}}^{D_{ac}} f_{sp}\left(\frac{D}{\sqrt[3]{\frac{S}{35\,‰}}}\right)\mathrm{d}D$	$\int_{D_{\mathrm{Aa}}}^{D_{ac}} \pi D^2 \times f_{sp}\left(\frac{D}{\sqrt[3]{\frac{S}{35\,‰}}}\right)\mathrm{d}D$	$\int_{D_{\mathrm{Aa}}}^{D_{ac}} \frac{\pi}{6} D^3 \times f_{sp}\left(\frac{D}{\sqrt[3]{\frac{S}{35\,‰}}}\right)\mathrm{d}D$
coarse	$\int_{D_{ac}}^{D_{\mathrm{max}}\sqrt[3]{\frac{S}{35\,‰}}} f_{sp}\left(\frac{D}{\sqrt[3]{\frac{S}{35\,‰}}}\right)\mathrm{d}D$	$\int_{D_{ac}}^{D_{\mathrm{max}}\sqrt[3]{\frac{S}{35\,‰}}} \pi D^2 \times f_{sp}\left(\frac{D}{\sqrt[3]{\frac{S}{35\,‰}}}\right)\mathrm{d}D$	$\int_{D_{ac}}^{D_{\mathrm{max}}\sqrt[3]{\frac{S}{35\,‰}}} \frac{\pi}{6} D^3 \times f_{sp}\left(\frac{D}{\sqrt[3]{\frac{S}{35\,‰}}}\right)\mathrm{d}D$

D.5 Input Data

Figure D.2 shows the regions that are covered by different sets of input data. The COSMO-CLM meteorological data set covers the whole study region and is not marked in the map. ERA-Interim wave and ocean data were used outside of the blue and orange colored regions except for SAL. SAL was set to 35 ‰ in the Atlantic Ocean, 37 ‰ in the Mediterranean Sea, and 18 ‰ in the Black Sea. Table D.6 shows the source and resolution of the input data that were used for calculation sea salt emissions for the five sea regions – North Sea, Baltic Sea, Atlantic Ocean, Mediterranean Sea, and Black Sea.

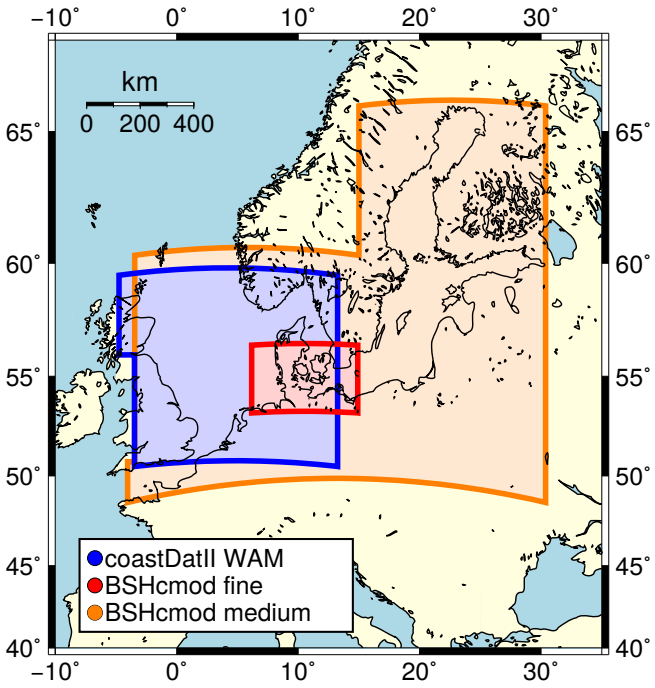

Figure D.2: Map showing the locations corresponding to the input data from each source. **Wave data:** In the blue region, wave data from coastDatII were used. Outside this region, the significant wave height data were acquired from ERA-Interim and the friction velocity data were calculated based on meteorological input data. **SST and SAL data:** In the orange and red regions, SST and SAL data were acquired from BSHcmod with medium and fine grid resolutions, respectively. Outside the orange region, the SST data were acquired from ERA-Interim and the SAL was set to a fixed value (see text). **Meteorological data:** The same meteorological data were used for the entire map region.

Table D.6: Overview of the input data used for calculating sea salt emissions.

Parameter	Resolution	Region	Model [Database]	Reference
Meteorology	$0.22° \times 0.22°$ lon x lat, rotated	Whole model domain	COSMO-CLM v4.8 [coastDatII]	Geyer and Rockel [2013] Geyer [2014]
Waves (H_s, C_D)	$0.075° \times 0.05°$ lon $\times$ lat	North Sea (southward of 59.2° N and eastward of 4.75° W)	WAM 4.5.3 [coastDatII]	Groll et al. [2014]
Waves (H_s)	$1° \times 1°$	Atlantic Ocean, Baltic Sea, Mediterranean Sea, Black Sea	WAM [ERA-Interim]	Dee et al. [2011]
Waves (C_D)	see Meteorology	Atlantic Ocean, Baltic Sea, Mediterranean Sea, Black Sea	derived from u_{10} [coastDatII]	Wu [1982]
SST, SAL	$5' \times 3'$ lon $\times$ lat	North and Baltic Sea	BSHcmod4, coarse grid	Dick et al. [2001], BSH*
SST, SAL	$50'' \times 30''$ lon $\times$ lat	German waters in North and Baltic Sea	BSHcmod4, fine grid	Dick et al. [2001], BSH*
SST	$1° \times 1°$	Atlantic Ocean, Mediterranean Sea, Black Sea	ERA input only [ERA-Interim, NCEP]	
SAL	–	Atlantic Ocean, Mediterranean Sea, Black Sea	Atlantic: 35 ‰, Med. Sea: 37 ‰, Black Sea: 18 ‰	

*`www.bsh.de/en/Marine_data/Forecasts/Prediction_models/index.jsp`

D.6 Setup of CMAQ runs

The $24 \times 24\,\mathrm{km}^2$ and $72 \times 72\,\mathrm{km}^2$ grids are denoted as CD24 and CD72 grids (Fig. 4.1) and defined in the attached GRIDDESC file.

Six OCEAN files are attached – three for each grid. The identifier _sf050m indicates that a surf zone of 50 m width is assumed. The identifier _sal indicates that the OPEN and SURF variables are scaled by the salinity as described in Sect. D.3.1. The identifier _noSalt indicates that OPEN and SURF are set to 0 (zero) so that no sea salt is emitted. The identifier _GIS_ubound indicates that the coastline data were extracted via ArcGIS and that the SURF variable has an upper bound as described in Sects. H.1 and H.3, respectively. Table D.7 shows which OCEAN file was used for each emission case.

Table D.7: Usage of the three OCEAN files in the four sea salt emission cases. The asterisks replace CD24 and CD72.

Case	OCEAN file
zero	OCEAN_*_noSalt_GIS.nc
GO03	OCEAN_*_sf050m_GIS_ubound_sal.nc
SP13	OCEAN_*_sf050m_GIS_ubound.nc
OV14	OCEAN_*_sf050m_GIS_ubound.nc

D.7 Modifications in CMAQ

D.7.1 Changes in the CMAQ Code

The modules AERO_EMIS.F (minor changes) and SSEMIS.F were modified. All other modules were kept unchanged. The modified source code files are attached in the supplement. Modifications in the modules and subroutines/functions are documented in the beginning of each one by "[DATE] Neumann: ..." and indicated in the code by "NEUMANND". There are four types of comments indicating modifications:

1. new variables
   ! NEW VARIABLES BY NEUMANND
   [VARIABLE DEFINITION]
2. long new code passages
   ! START NEUMANND
   [CODE]
   ! END NEUMANND
3. individual new code lines
   ! NEW NEUMANND: [DESCRIPTION]
   [CODE] ! NEW
4. individual modified code lines
   ! MODIFIED NEUMANND: [DESCRIPTION]
   [CODE] !

D.7.2 Changes in the Namelist files

Commonly, sea salt emissions consist of accumulation and coarse mode emissions. The SP13 and OV14 parameterizations were implemented to emit Aitken, accumulation, and coarse mode sea salt particles. However, if Aitken mode sea salt emissions are considered, they should be displayed in the output files. For this purpose the aerosol namelist file (AE_cb05tucl_ae5_aq.nml) needs to be modified. In the line starting with ANAI, the columns DDEP, WDEP and CONC have to be set to Yes. Alternatively, one can replace the line

'ANAI:23.0:ANAI:1.0:VMASSI:1.0:NA_AITKEN:1.0:::NA_AITKEN:Yes:::',

by the line

'ANAI:23.0:ANAI:1.0:VMASSI:1.0:NA_AITKEN:1.0:::NA_AITKEN:Yes:Yes:Yes:Yes',

D.7.3 Additions in the CMAQ Run Script

Two new environment variables need to be set in the CMAQ run script in order to read in sea salt emissions externally. Below, a code example is given (Listing D.1).

Listing D.1: New variables which need to be added to the CMAQ start scripts when external sea salt emissions should be imported.

```
#> read sea-salt emissions from external file [ N|F ]
setenv CTM_READSSEMIS Y

#> Sea Salt emissions
set SS_FILE = SSEMIS.${STDATE}  # example file name
set SS_DIR  = /example/ssemis    # example directory name

#> file containing the sea-salt emissions
setenv SSEMIS_1 ${SS_DIR}/${SS_FILE}
```

D.8 Emissions

The Figs. D.3 to D.5 show sea salt mass, surface area, and number emissions, respectively, at one location in the German Bight. Figure D.6 shows the GMD of the emissions at the same locations. In each figure, Aitken-, accumulation- and coarse-mode emissions are plotted (top to bottom). The plots show winter (left) and summer emissions (right).

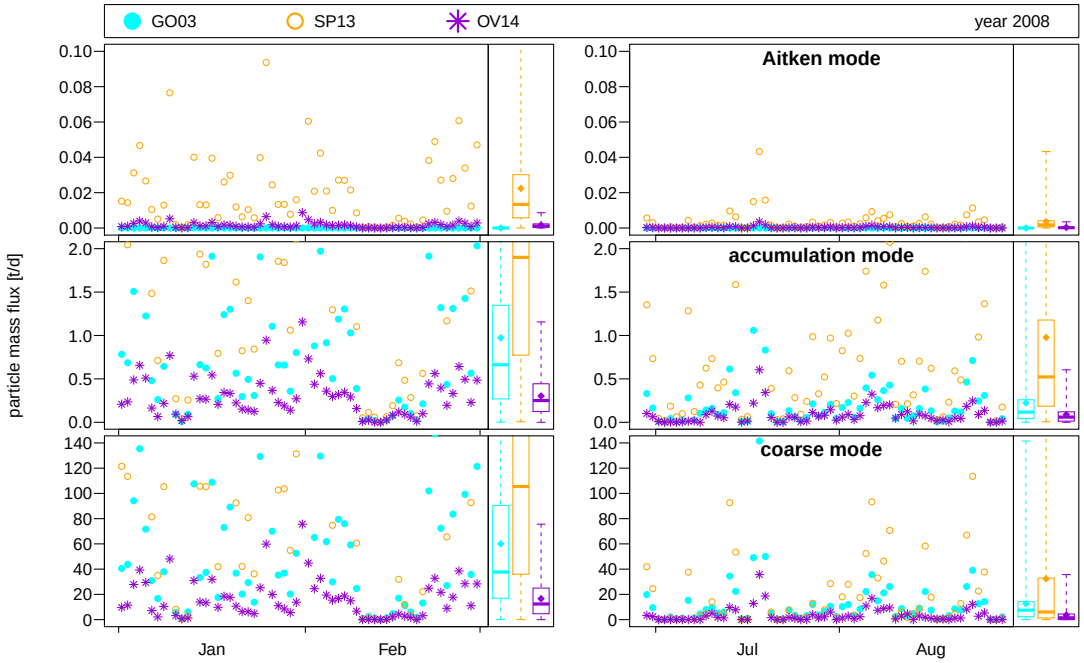

Figure D.3: Sea salt mass emissions [$\mathrm{t\,d^{-1}}$] into the Aitken, accumulation, and coarse modes (top to bottom) at one location in the German Bight in winter (left) and summer (right) 2008.

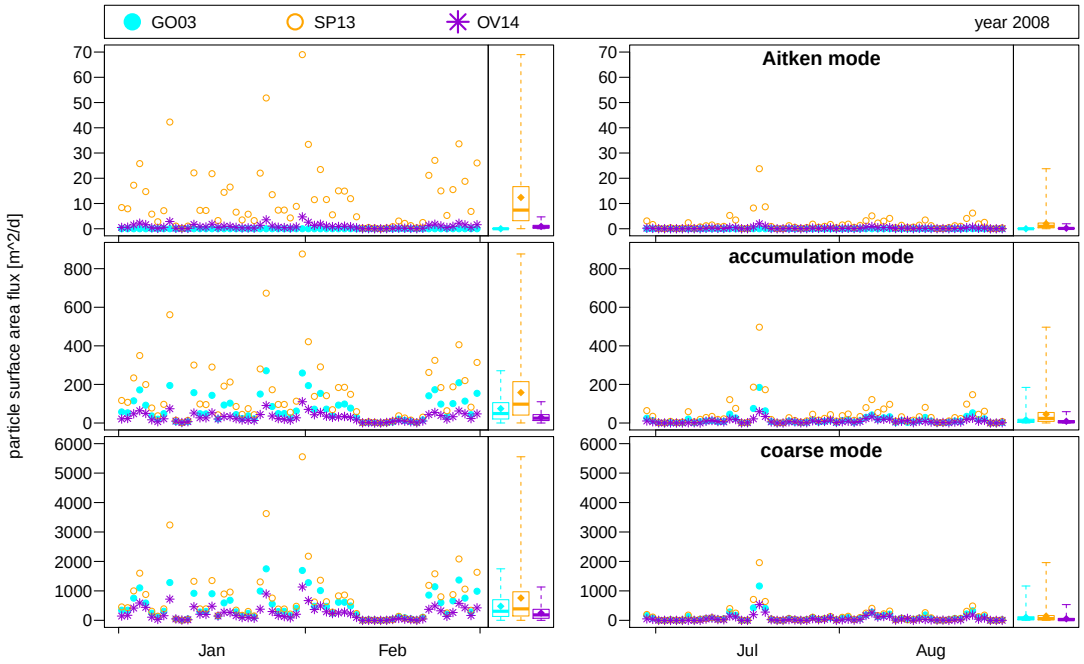

Figure D.4: Similar to Fig. D.3 but showing sea salt particle surface area emissions [$\mathrm{m^2\,d^{-1}}$].

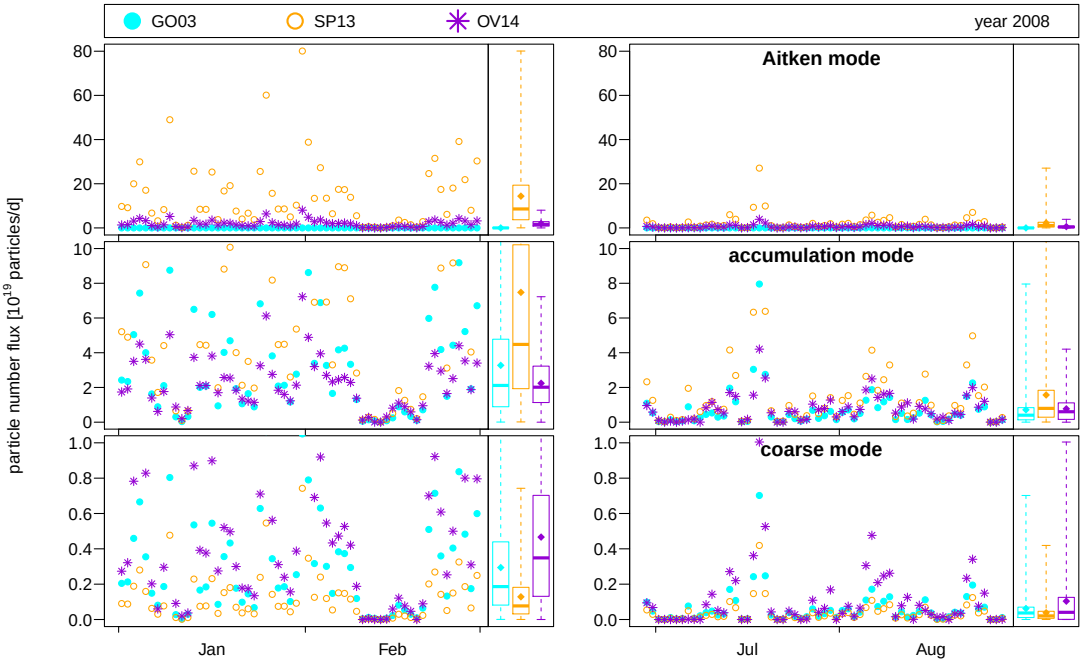

Figure D.5: Similar to Fig. D.3 but showing sea salt particle number emissions $[1 \times 10^{19}\,\text{particles}\,\text{d}^{-1}]$.

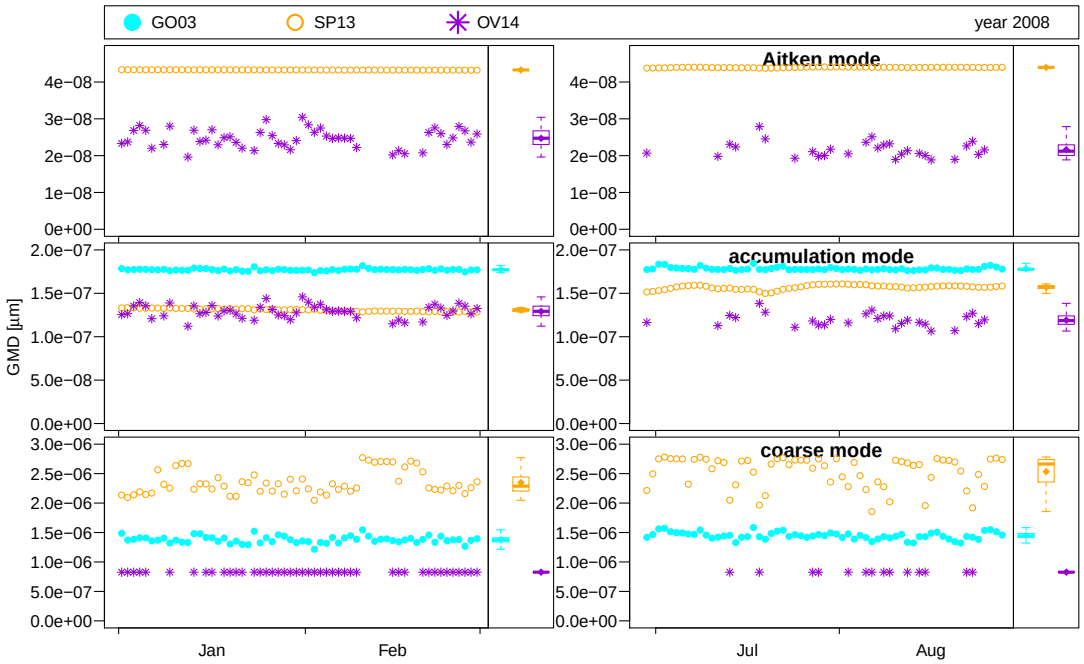

Figure D.6: Similar to Fig. D.3 but showing the GMD of the emitted sea salt particle Aitken, accumulation and coarse mode distributions (top to bottom). Log-normal distributed modes are assumed in order to calculate the GMD (Binkowski and Roselle, 2003). As Fig. 4.2 (Paper) shows, this assumption is not justified. However, log-normal shaped emissions and concentrations are assumed in CMAQ.

E Supplement of Draft Paper 3

E.1 Sea Salt Composition

E.1.1 General Composition

The six ions most abundant ions in oceanic saline water by mass are Cl^- (55.38 $\%_m$), Na^+ (30.77 $\%_m$), SO_4^{2-} (7.83 $\%_m$), Mg^{2+} (3.71 $\%_m$), Ca^{2+} (1.18 $\%_m$), and K^+ (1.14 $\%_m$) [calculated from Culkin and Cox, 1976; Feistel et al., 2010].[a] The composition does not vary significantly among the large oceans, the North Sea, and the Baltic Sea [Riley and Tongudai, 1967; Culkin and Cox, 1976; Feistel et al., 2010]. Slight variations in the Ca^{2+}/Cl^- ratio have been found in the Baltic Sea due to anthropogenic activities [Kremling and Wilhelm, 1997]. However, these variations do not have a relevant extend. The increased usage of scrubbers, particularly those with open water cycles, might lead to an increased input of sulfate into North and Baltic Sea waters [Lange, 2013], but the amounts are too low to change the sea water SO_4^{2-} concentrations in near future. It is commonly accepted that the mass ratios of ions in sea water and sea salt particles are equal and that no enrichment of individual ions occurs [e.g. Lewis and Schwartz, 2004, Sect. 2.5.2, and references therein]. Measured enrichments of individual ions in the 1960s and 70s were accounted to background air pollution [Duce and Hoffman, 1976; Junge, 1972; MacIntyre, 1974]. However recently, Zieger et al. [2015] found an enrichment of Ca^{2+} concentrations in laboratory-generated film droplets which might be caused by calcium containing compounds in the SML. The results are not published, yet.

E.1.2 CMAQ

The sea salt mass emissions in CMAQ are split into Cl^-, Na^+, and SO_4^{2-} (AERO5) and into Cl^-, Na^+, SO_4^{2-}, Mg^{2+}, Ca^{2+}, and K^+ (AERO6) by the speciation factors given in Table E.1. Na^+ summarizes all sea salt cations in the AERO5 mechanism. The split factors are chosen according to the abundance of these ions in sea water assuming that not separation of individual ions takes place.

Table E.1: Sea salt speciation factors used for CMAQ sea salt emissions [Kelly et al., 2010]. In the AERO6, sea salt cation are represented by Na^+, Mg^{2+}, Ca^{2+}, and K^+ in the accumulation mode but only by one variable (ASEACAT) in the coarse mode. In the AERO5, Na^+ represented all sea salt cations.

Ion	AE05		AE06	
	accum.	coarse	accum.	coarse
Cl^-	0.5389	0.5389	0.5538	0.5538
Na^+	0.3856	0.3856	0.3086	0.0000
SO_4^{2-}	0.0755	0.0755	0.0776	0.0776
Mg^{2+}	0.0000	0.0000	0.0368	0.0000
Ca^{2+}	0.0000	0.0000	0.0118	0.0000
K^+	0.0000	0.0000	0.0114	0.0000
Cations	0.0000	0.0000	0.0000	0.3686

[a] Commonly, the composition is defined as the mass-ratio of the individual constituents to Cl^-: 0.5555 for Na^+, 0.1413 for SO_4^{2-}, 0.0669 for Mg^{2+}, 0.0213 for Ca^{2+}, and 0.0206 for K^+. The ratios between the ionic compounds differ slightly from publication to publication; e.g. Seinfeld and Pandis [2006a, Table 8.8] and Lewis and Schwartz [2004, Table 6]

E.1.3 Sea Salt Tracers

The Na^+ concentrations are considered as the most appropriate tracer for sea salt particles. Cl^- might evaporate as HCl when stronger acids, such as H_2SO_4 and HNO_3 condense, condense on sea salt particles. ${SO_4}^{2-}$ does not evaporate but anthropogenic combustion process emit considerable amounts of SO_2 which leads to the formation of particulate sulfate that exceeds the sea salt sulfate concentrations. The concentrations of Ca^{2+} and K^+ are not reliable for the quantification of sea salt concentrations because both compounds may be emitted from other processes, too. The non-sea-salt emissions of Na^+ can also be extensive by particular processes and events, such as industrial facilities and street salt in spring [Tsyro et al., 2011]. However, these processes and events are spatially and temporally limited making Na^+ to the best available tracer for particulate sea salt.

E.1.4 Deriving Sea Salt Sulfate

In model studies and measurements it might be of interest to determine the amount of sulfate originating from sea salt. Since ${SO_4}^{2-}$ does not evaporate and Na^+ is the most reliable trancer for sea salt, sea salt sulfate can be calculated according to Eq. (E.1). The particular constants in the equation are chosen according to the sea salt emissions in CMAQ's AERO6 mechanism. The factor 4 for converting between sea salt sodium and sulfate concentrations is a good first order approximation.

$$\mathrm{P}_{\mathrm{seaSalt},\mathrm{SO_4^{2-}}} = \frac{\mathrm{P}_{\mathrm{Na}} \times 0.0776}{0.3086} \approx \frac{\mathrm{P}_{\mathrm{Na}}}{4} \tag{E.1}$$

In EMEP, sea salt sulfate and corrected sulfate (non-sea-salt sulfate) are calculated by Na^+, Mg^{2+}, or Cl^- as described in the pseudo code below [EMEP, 2015; Hjellbrekke, 2016].

```
# Definitions:
#  Na:  measured sodium concentration
#  Mg:  measured magnesium concentration
#  Cl:  measured chloride concentration
#  SO4: measured sulfate concentration
#
# All concentrations in mg/l, SO4 in mg S/l.

# First calculate the ratios between Na, Cl and Mg normalized by the
# expected ratios in sea water:
a = 8.40 * Mg/Na
b = 1.80 * Na/Cl
c = 14.90 * Mg/Cl

# If the ratios are close to the expected ratios, a, b and c will be close
# to 1. If all three components are measured, we try to pick the best one:
if ( 0.75 <= a <= 1.25)
    # Mg/Na in expected ratio:
    use Na
    # else: possible problem with Na or Mg measurement
else if ( (0.75 <= c <= 1.25) && (b < 0.75 or 1.25 < b) )
    # Mg/Cl in expected ratio but Na/Cl not
    use Mg
else if ( (0.75 <= b <= 1.25) && (c < 0.75 or 1.25 < c) )
    # Na/Cl in expected ratio but Mg/Cl not
    use Na
else if ( abs(b-1) < abs(c-1) )
    # the Na/Cl ratio is closer to 1 than the Mg/Cl ratio
    use Na
else
    # the Mg/Cl ratio is closer to 1 than the Na/Cl ratio
```

```
    use Mg
end if

# If one component is missing, use Na, Mg or Cl for the correction in that
# order. Cl is used only if both, Na and Mg, are missing.

# The excess sulphate is calculated as:
if ( 'use Na' or (no Mg but Na is available )
    XSO4 = SO4 - 0.0837 * Na
else if ( 'use Mg' or (no Na but Mg is available) )
    XSO4 = SO4 - 0.695 * Mg
else
    # if neither Na nor Mg are available
    XSO4 = SO4 - 0.0466 * Cl
end if
```

E.2 Input Data

E.2.1 Sea Salt Emissions

Figure E.1 shows the regions that are covered by different sets of input data. The COSMO-CLM meteorological and ERA-Interim data sets cover the whole study region and their coverage is not drawn into the map. While ERA-Interim wave data were used for the whole domain, the ERA-Interim SST data were only used outside of the orange colored region. SAL and SST data

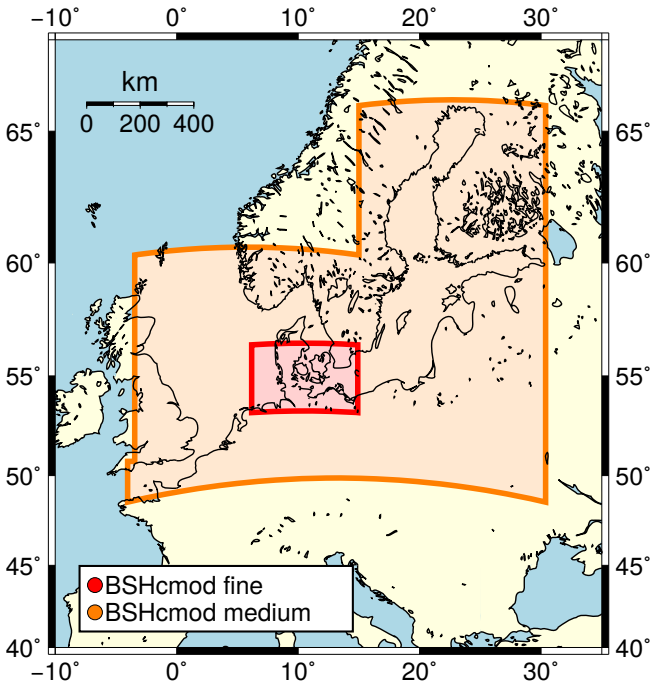

Figure E.1: Map showing the coverage of input data from different sources. **SST and SAL data:** In the orange and red regions, SST and SAL data were acquired from BSHcmod with medium and fine grid resolutions, respectively. Outside the orange region, the SST data were acquired from ERA-Interim and the SAL was set to constant values (see text). **Meteorological data:** The same meteorological data were used for the entire map region. **Wave data:** The significant wave height data were acquired from ERA-Interim and the friction velocity data were calculated based on meteorological input data.

Table E.2: Overview of the input data used for calculating sea salt emissions for the year 2013.

Parameter	Resolution	Region	Model [Database]	Reference
Meteorology	0.22° × 0.22° lon × lat, rotated	Whole model domain	COSMO-CLM v4.8 [coastDatII]	Geyer and Rockel [2013] Geyer [2014]
Waves (H_s)	1° × 1°	Whole model domain	WAM [ERA-Interim]	Dee et al. [2011]
Waves (C_D)	see Meteorology	Whole model domain	derived from u_{10} [coastDatII]	Wu [1982]
SST, SAL	5′ × 3′ lon × lat	North and Baltic Sea	BSHcmod4, coarse grid	Dick et al. [2001], BSH*
SST, SAL	50″ × 30″ lon × lat	German waters in North and Baltic Sea	BSHcmod4, fine grid	Dick et al. [2001], BSH*
SST	1° × 1°	Atlantic Ocean, Mediterranean Sea, Black Sea	ERA input only [ERA-Interim, NCEP]	
SAL	–	Atlantic Ocean, Mediterranean Sea, Black Sea	Atlantic: 35 ‰, Med. Sea: 37 ‰, Black Sea: 18 ‰	

*`www.bsh.de/en/Marine_data/Forecasts/Prediction_models/index.jsp`

for the North Sea and Baltic Sea were taken from operational BSHcmod runs of the BSH. SAL was set to 35 ‰ in the Atlantic Ocean, to 37 ‰ in the Mediterranean Sea, and to 18 ‰ in the Black Sea. Table E.2 shows the source and resolution of the input data that were used for calculating sea salt emissions in the five marine regions – North Sea, Baltic Sea, Atlantic Ocean, Mediterranean Sea, and Black Sea.

Open ocean and surf zone fraction per grid cell are needed for calculating sea salt emissions in CMAQ (see Table E.3). Additionally, these data are needed for the simulation result evaluation. The files are located in the subdirectory `supplement/paper1/cmaq` because they were used in Chaps. 3 and listed in Table B.2.

E.2.2 Anthropogenic Emissions

Signing parties (countries) of the European Monitoring and Evaluation Programme (EMEP) have to report their annual emissions of CO, NH_3, non-methane volatile organic compounds (NMVOCs), NO_x (as NO_2), SO_x (as SO_2), black carbon (BC), PM_{10}, $PM_{2.5}$, total suspended particulate matter (TSP), a list of heavy metals and a list of persistent organic pollutants (POPs) split into 11 SNAP sectors (Selected Nomenclature for sources of Air Pollution, two most left columns in Table E.4) to EMEP. These emissions are publicly available at the Centre on Emission Inventories and Projections (CEIP) via `www.ceip.at`.

The emissions used in this study are partly based on these reported emissions. In the employed CMAQ setup, they are not emitted as bulk into the model's bottom layer but they are split up into the 15 lowest model layers (Table E.4). The employed split factors are displayed in Table E.4. Each SNAP sector has its own set of split factors: Road transport emissions occur only in the bottom layer, whereas power plants have stacks above 120 m height which forces emissions into higher model layers.

The reported SO_x emissions are supplied as SO_2 into the model. The PM_{10} and $PM_{2.5}$ emissions are split up into their components, such as SO_4^{2-}. The species split also depends on the SNAP sectors (Table 6.2): particulate emissions by cars and by power plants have different composition.

Table E.3: OCEAN files that were used as input files in CMAQ simulations.

Type	Comment	Files	Corresp. Fig.
Sea Surface Fraction	OCEAN file needed for sea salt emissions in CMAQ; contains OPEN (open ocean fraction), SURF (surf zone fraction), and MASK (0 = land; 1 = coast; 2 = open ocean)	`*sf050m*ubound_sal.nc` (Base), `*sf000m*ubound.nc` (SALT_OV14), `*noSalt*.nc` (NoSalt)	H.3 and B.1

Table E.4: Split factors for the vertical distributions of the emissions of the 11 SNAP sectors. Layer 1 is the bottom layer. Numbers are given in % and sum up to 100 % in each row.

SNAP Sector		Emission split for each model layer [%]														
		1	2	3	4	5	6	7	8	9	10	11	12	13	14	15
S1	Combustion in energy and transformation industries	0.00	0.00	0.00	0.04	9.29	31.18	31.21	15.40	6.81	2.85	2.95	0.21	0.02	0.02	0.02
S2	Non-industrial combustion plants	100.00	0.00	0.00	0.00	0.00	0.00	0.00	0.00	0.00	0.00	0.00	0.00	0.00	0.00	0.00
S3	Combustion in manufacturing industry	0.00	18.05	51.09	24.31	6.02	0.48	0.04	0.01	0.00	0.00	0.00	0.00	0.00	0.00	0.00
S4	Production processes	0.10	16.79	40.10	27.90	12.74	2.16	0.16	0.03	0.01	0.00	0.00	0.00	0.00	0.00	0.00
S5	Extraction & distribution of fossil fuels and geothermal energy	0.06	6.55	12.71	33.46	41.66	5.10	0.41	0.03	0.01	0.00	0.00	0.00	0.00	0.00	0.00
S6	Solvent and other product use	100.00	0.00	0.00	0.00	0.00	0.00	0.00	0.00	0.00	0.00	0.00	0.00	0.00	0.00	0.00
S7	Road transport	100.00	0.00	0.00	0.00	0.00	0.00	0.00	0.00	0.00	0.00	0.00	0.00	0.00	0.00	0.00
S8	Other mobile sources and machinery	100.00	0.00	0.00	0.00	0.00	0.00	0.00	0.00	0.00	0.00	0.00	0.00	0.00	0.00	0.00
S9	Waste treatment and disposal	0.00	0.00	2.31	25.94	56.10	13.20	2.00	0.34	0.07	0.02	0.02	0.00	0.00	0.00	0.00
S10	Agriculture	100.00	0.00	0.00	0.00	0.00	0.00	0.00	0.00	0.00	0.00	0.00	0.00	0.00	0.00	0.00
S11	Other sources and sinks	100.00	0.00	0.00	0.00	0.00	0.00	0.00	0.00	0.00	0.00	0.00	0.00	0.00	0.00	0.00

E.3 Model Output Data and statistical Evaluation

The model data that forms the base for plots and statistical evaluations are attached in post-processed format which allows the reproduction of all plots and figures (see Table E.5). Data are attached as text (*.csv) and netCDF (*.nc) files. Concentration data are located in the subdirectory `supplement/paper3/conc`. The full model output and the OV14 sea salt emission data can be provided on request.

Table E.5: List of attached files containing model output data.

Type	Comment	Files	Corresp. Fig.
Concentrations	hourly resolved in time; data on each station (Table B.3); one species (Na^+ | xSO4 |sNH_4 | sNO_3), one season (summer | winter) and one case (base | noSurf | full | zero) per file;	`conc.timeseries.*.csv` (32 files)	6.2, 6.3, 6.4, 6.5, 6.6, 6.7, and all in this Appendix

Data on the statistical evaluation are in the file `supplement/paper3/conc/stat.sulfScen.evaluation.conc.csv` and two-month mean concentrations divided into source sectors are in the file `supplement/paper3/conc/data.sulfScen.means.sectors.csv`. The statistical evaluation file contains

- n (number of considered values),
- RAE (residual absolute error),
- MNB (mean normalized bias),
- R (Spearman's correlation coefficient),
- MEAN.sim (mean of considered model values),
- MEAN.obs (mean of considered EMEP values),
- MEDIAN.sim (median of considered model values), and
- MEDIAN.obs (median of considered EMEP values).

E.4 Modeled SO_2, SO_x and sulfate $PM_{2.5}$ concentrations and uncertainty evaluation of subtraction method

Figure 6.2 shows time series of sulfate PM_{10} concentrations at six stations. Here, the corresponding time series of sulfate $PM_{2.5}$, SO_2, and sulfate PM_{10} + SO_2 concentrations are shown in Figs. E.2 to E.4.

Tables E.6 and E.7 host similar data to those, which are plotted in Figs. 6.3 and 6.4, respectively. All model concentrations were considered for calculating the two-month average values in the figures, whereas the averages in the Tables consist only of model values of days with corresponding measurements. The fact that two-month average model concentrations (considering all model values) were compared with averages of partly patchy measurements might bias the comparison in Figs. 6.3 and 6.4 if particularly high or particularly low concentrations were not measured. Therefore, the fraction between the "*model data average considering only values with corresponding measurements*" ($P_{\Sigma,obs}$) and the "*model data average considering all values*" ($P_{\Sigma,all}$) is given in Table E.6. The comparison between modeled and measured values should be critically treated if this fraction considerably diverges from 1.0.

The uncertainty introduced through using the subtraction method (e.g. Eq. (6.1)) was evaluated in Sect. 6.3.4 being motivated by Fig. 6.5, which shows scatter plots of sea salt sulfate PM_{10} concentrations at three stations in summer. The scatter plots of sulfate $PM_{2.5}$ and PM_{10} concentrations at all stations in both seasons are displayed in Figs. E.5 to E.8.

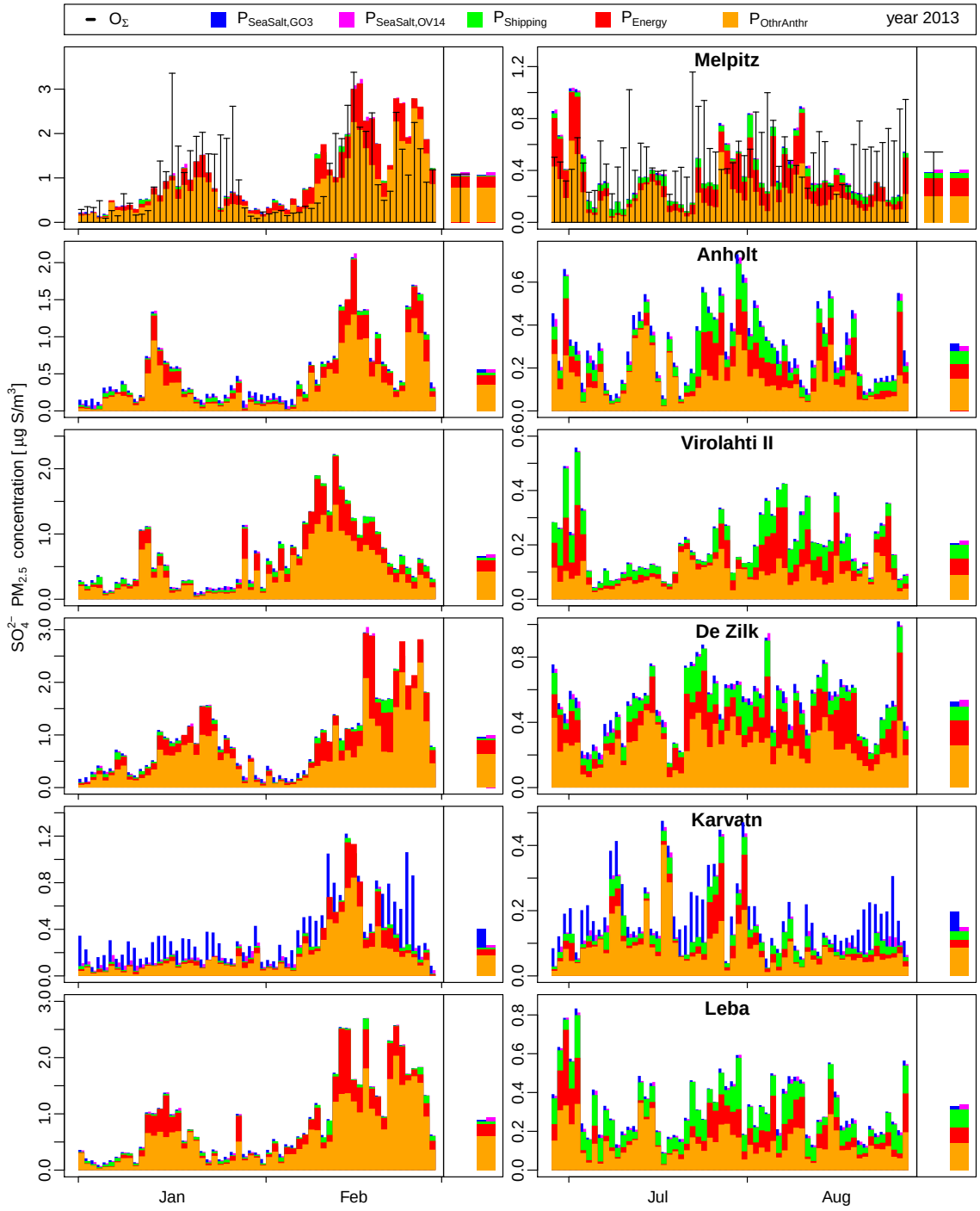

Figure E.2: Similar to Fig. E.3 but showing sulfate $PM_{2.5}$ concentrations.

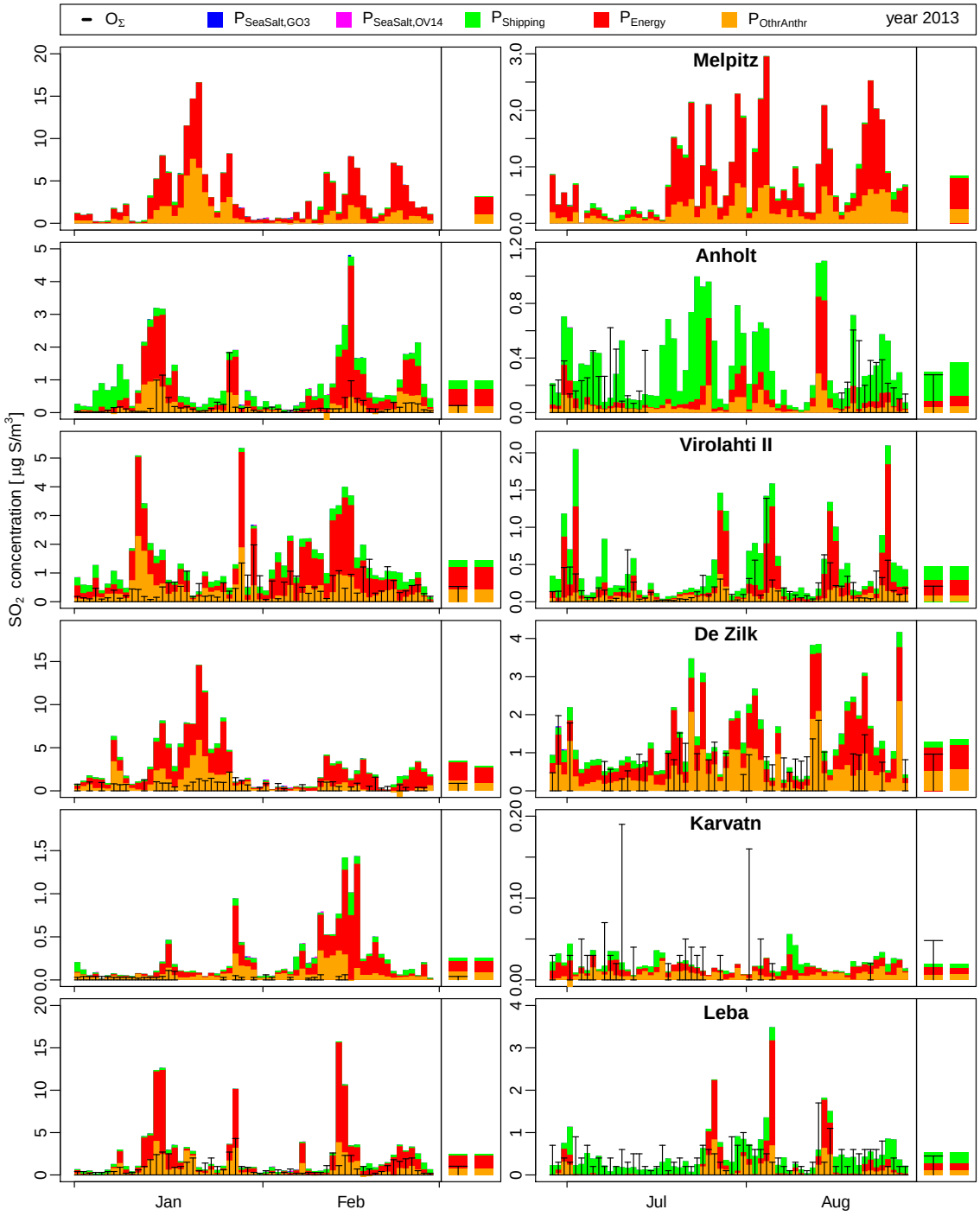

Figure E.3: Similar to Fig. 6.2 but showing SO_2 concentrations.

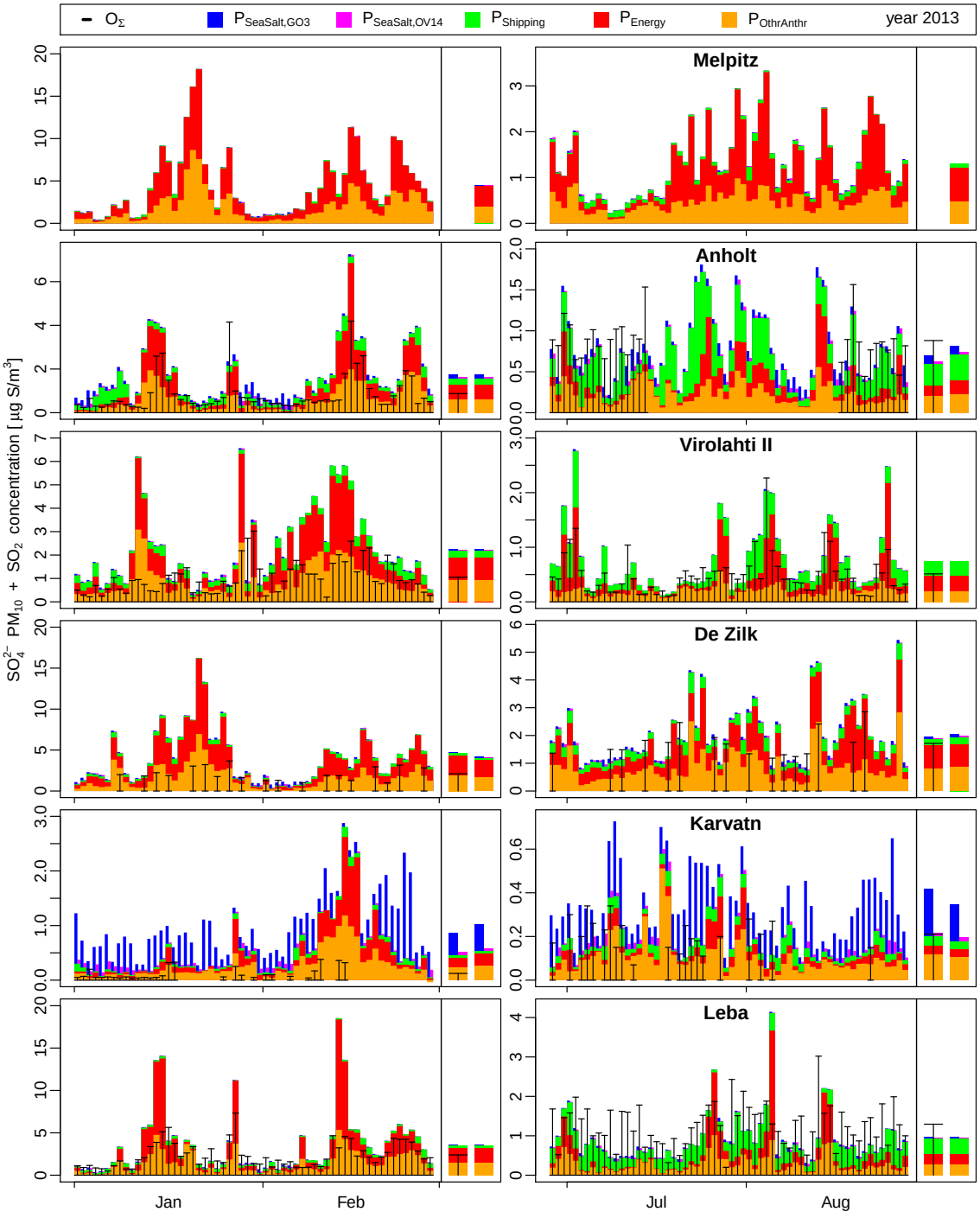

Figure E.4: Similar to Fig. E.3 but showing sulfate PM_{10} + SO_2 concentrations.

Table E.6: Absolute measured and modeled two-month average PM_{10} and $PM_{2.5}$ sulfate concentrations. The modeled concentrations are split into the source sectors energy production, shipping, sea salt (GO03 and OV14), and OthrAnthr. Only model values at days at which measurements are available were considered except for the calculation of $P_{\Sigma,all}$, which is the average concentration over all model values. The number of considered values is given in the column 'Number'.

Station	Type	Winter 2013, values in [µg m^{-3}] except last column									Summer 2013, values in [µg m^{-3}] except last column								
		Number	O_Σ	$P_{\Sigma,obs}$	P_{Energy}	$P_{Shipping}$	$P_{OthrAnthr}$	$P_{SeaSalt,GO03}$	$P_{SeaSalt,OV14}$	$\frac{P_{\Sigma,obs}}{P_{\Sigma,all}}$	Number	O_Σ	$P_{\Sigma,obs}$	P_{Energy}	$P_{Shipping}$	$P_{OthrAnthr}$	$P_{SeaSalt,GO03}$	$P_{SeaSalt,OV14}$	$\frac{P_{\Sigma,obs}}{P_{\Sigma,all}}$
Waldhof	PM_{10}	59	1.04	1.22	0.29	0.02	0.85	0.06	0.03	1.00	62	0.61	0.49	0.16	0.06	0.25	0.03	0.02	1.00
Neuglobsow	PM_{10}	58	1.16	1.12	0.23	0.03	0.81	0.05	0.03	1.01	62	0.55	0.43	0.12	0.07	0.22	0.02	0.02	1.00
Melpitz	PM_{10}	59	1.19	1.27	0.32	0.01	0.91	0.04	0.02	1.00	62	0.58	0.47	0.17	0.05	0.24	0.01	0.01	1.00
Tange	PM_{10}	44	0.77	0.92	0.20	0.04	0.52	0.16	0.04	1.09	62	0.58	0.45	0.10	0.06	0.20	0.09	0.03	1.00
Anholt	PM_{10}	59	0.66	0.78	0.16	0.03	0.40	0.19	0.05	1.00	29	0.60	0.40	0.07	0.05	0.17	0.11	0.03	0.89
Risoe	PM_{10}	54	0.75	0.99	0.16	0.05	0.63	0.15	0.04	0.97	62	0.56	0.49	0.10	0.08	0.20	0.11	0.03	1.00
Ulborg	PM_{10}	57	0.66	0.92	0.16	0.03	0.46	0.27	0.06	0.97	62	0.68	0.52	0.10	0.06	0.20	0.16	0.04	1.00
Utö	PM_{10}	59	0.47	0.77	0.19	0.03	0.46	0.10	0.04	1.00	57	0.40	0.27	0.06	0.06	0.11	0.03	0.02	1.02
Virolahti II	PM_{10}	59	0.52	0.81	0.21	0.05	0.50	0.05	0.03	1.00	62	0.30	0.27	0.08	0.07	0.11	0.01	0.01	1.00
Preila	PM_{10}	30	1.16	1.60	0.43	0.03	1.06	0.07	0.03	1.35	60	0.63	0.37	0.08	0.09	0.15	0.04	0.02	1.00
De Zilk	PM_{10}	28	1.09	1.27	0.32	0.03	0.77	0.14	0.05	1.00	31	0.73	0.67	0.17	0.10	0.30	0.10	0.03	1.00
Birkenes II	PM_{10}	59	0.29	0.50	0.11	0.01	0.28	0.09	0.04	1.00	62	0.28	0.32	0.08	0.04	0.16	0.04	0.02	1.00
Tustervatn	PM_{10}	53	0.09	0.44	0.09	0.03	0.14	0.18	0.05	1.04	53	0.10	0.21	0.03	0.04	0.07	0.08	0.02	1.00
Kårvatn	PM_{10}	55	0.08	0.75	0.06	0.01	0.17	0.51	0.05	0.99	58	0.13	0.34	0.03	0.03	0.10	0.17	0.02	1.02
Hurdal	PM_{10}	59	0.20	0.92	0.13	0.01	0.72	0.06	0.03	1.00	62	0.20	0.25	0.06	0.03	0.15	0.01	0.01	1.00
Jarczew	PM_{10}	58	1.36	1.53	0.42	0.00	1.09	0.03	0.02	1.00	62	0.70	0.46	0.19	0.05	0.22	0.01	0.01	1.00
Leba	PM_{10}	59	1.37	1.08	0.25	0.05	0.69	0.09	0.04	1.00	62	0.85	0.44	0.10	0.12	0.17	0.04	0.03	1.00
Diabla Gora	PM_{10}	58	1.04	1.23	0.30	0.00	0.90	0.03	0.02	1.00	62	0.40	0.36	0.11	0.07	0.17	0.01	0.01	1.00
Bredkälen	PM_{10}	43	0.12	0.45	0.12	0.02	0.25	0.06	0.03	1.20	60	0.11	0.17	0.03	0.03	0.09	0.01	0.01	1.00
Vavihill	PM_{10}	59	0.49	0.76	0.18	0.04	0.46	0.08	0.03	1.00	53	0.36	0.41	0.10	0.08	0.18	0.06	0.02	1.01
Aspvreten	PM_{10}	59	0.39	0.69	0.19	0.04	0.40	0.07	0.04	1.00	60	0.25	0.26	0.06	0.06	0.12	0.02	0.01	1.01
Råö	PM_{10}	59	0.45	0.76	0.16	0.03	0.38	0.20	0.05	1.00	61	0.48	0.47	0.10	0.07	0.17	0.13	0.03	1.00
Waldhof	$PM_{2.5}$	20	1.17	0.96	0.24	0.02	0.68	0.02	0.02	0.96	20	0.56	0.37	0.12	0.05	0.19	0.01	0.01	0.91
Neuglobsow	$PM_{2.5}$	20	1.15	0.86	0.18	0.03	0.62	0.02	0.01	0.95	20	0.49	0.32	0.09	0.05	0.16	0.01	0.01	0.92
Melpitz	$PM_{2.5}$	59	1.09	1.06	0.27	0.01	0.77	0.02	0.01	1.00	62	0.54	0.39	0.14	0.04	0.20	0.01	0.01	1.00
Diabla Gora	$PM_{2.5}$	9	1.10	1.03	0.29	0.00	0.71	0.02	0.02	0.97	9	0.42	0.33	0.11	0.05	0.17	0.01	0.01	1.16

Table E.7: Relative contribution of the energy production, shipping, sea salt (GO03 and OV14), and OthrAnthr source sectors to the PM_{10} and $PM_{2.5}$ particulate sulfate concentration. Only model values with corresponding measurements are considered.

Station	Type	Winter 2013, values in [%]						Summer 2013, values in [%]					
		Number	P_{Energy}	$P_{Shipping}$	$P_{OthrAnthr}$	P_{GO03}	P_{OV14}	Number	P_{Energy}	$P_{Shipping}$	$P_{OthrAnthr}$	$P_{SeaSalt,GO03}$	$P_{SeaSalt,OV14}$
Waldhof	PM_{10}	59	0.24	0.02	0.70	0.05	0.03	62	0.32	0.12	0.50	0.06	0.04
Neuglobsow	PM_{10}	58	0.20	0.02	0.73	0.05	0.03	62	0.28	0.16	0.50	0.06	0.04
Melpitz	PM_{10}	59	0.25	0.00	0.71	0.03	0.02	62	0.36	0.11	0.51	0.03	0.03
Tange	PM_{10}	44	0.22	0.04	0.57	0.17	0.05	62	0.22	0.13	0.45	0.21	0.08
Anholt	PM_{10}	59	0.20	0.04	0.52	0.24	0.08	29	0.18	0.13	0.42	0.26	0.10
Risoe	PM_{10}	54	0.16	0.05	0.63	0.15	0.04	62	0.21	0.17	0.40	0.22	0.06
Ulborg	PM_{10}	57	0.18	0.03	0.51	0.29	0.09	62	0.19	0.11	0.39	0.31	0.10
Utö	PM_{10}	59	0.24	0.04	0.59	0.12	0.06	57	0.22	0.24	0.42	0.13	0.07
Virolahti II	PM_{10}	59	0.26	0.06	0.61	0.06	0.04	62	0.28	0.26	0.42	0.04	0.03
Preila	PM_{10}	30	0.27	0.02	0.66	0.05	0.02	60	0.22	0.25	0.41	0.11	0.06
De Zilk	PM_{10}	28	0.25	0.02	0.61	0.11	0.04	31	0.26	0.15	0.44	0.15	0.06
Birkenes II	PM_{10}	59	0.22	0.02	0.57	0.18	0.09	62	0.24	0.13	0.49	0.14	0.07
Tustervatn	PM_{10}	53	0.20	0.06	0.33	0.40	0.16	53	0.14	0.18	0.32	0.37	0.15
Kårvatn	PM_{10}	55	0.09	0.02	0.22	0.67	0.17	58	0.09	0.09	0.30	0.52	0.09
Hurdal	PM_{10}	59	0.14	0.02	0.78	0.06	0.04	62	0.25	0.12	0.58	0.06	0.05
Jarczew	PM_{10}	58	0.28	0.00	0.71	0.02	0.01	62	0.40	0.11	0.46	0.02	0.02
Leba	PM_{10}	59	0.23	0.04	0.64	0.08	0.04	62	0.22	0.28	0.40	0.10	0.06
Diabla Gora	PM_{10}	58	0.24	0.00	0.73	0.02	0.02	62	0.31	0.19	0.47	0.03	0.03
Bredkälen	PM_{10}	43	0.28	0.04	0.56	0.13	0.08	60	0.19	0.18	0.54	0.09	0.09
Vavihill	PM_{10}	59	0.23	0.05	0.61	0.11	0.05	53	0.24	0.19	0.44	0.14	0.06
Aspvreten	PM_{10}	59	0.27	0.05	0.57	0.11	0.05	60	0.22	0.23	0.46	0.09	0.05
Råö	PM_{10}	59	0.21	0.03	0.50	0.26	0.08	61	0.21	0.14	0.37	0.28	0.08
Waldhof	$PM_{2.5}$	20	0.25	0.03	0.71	0.02	0.02	20	0.32	0.12	0.52	0.04	0.03
Neuglobsow	$PM_{2.5}$	20	0.21	0.04	0.73	0.03	0.02	20	0.29	0.16	0.51	0.04	0.03
Melpitz	$PM_{2.5}$	59	0.25	0.00	0.73	0.02	0.01	62	0.36	0.10	0.52	0.02	0.02
Diabla Gora	$PM_{2.5}$	9	0.28	0.00	0.69	0.02	0.02	9	0.33	0.15	0.50	0.02	0.02

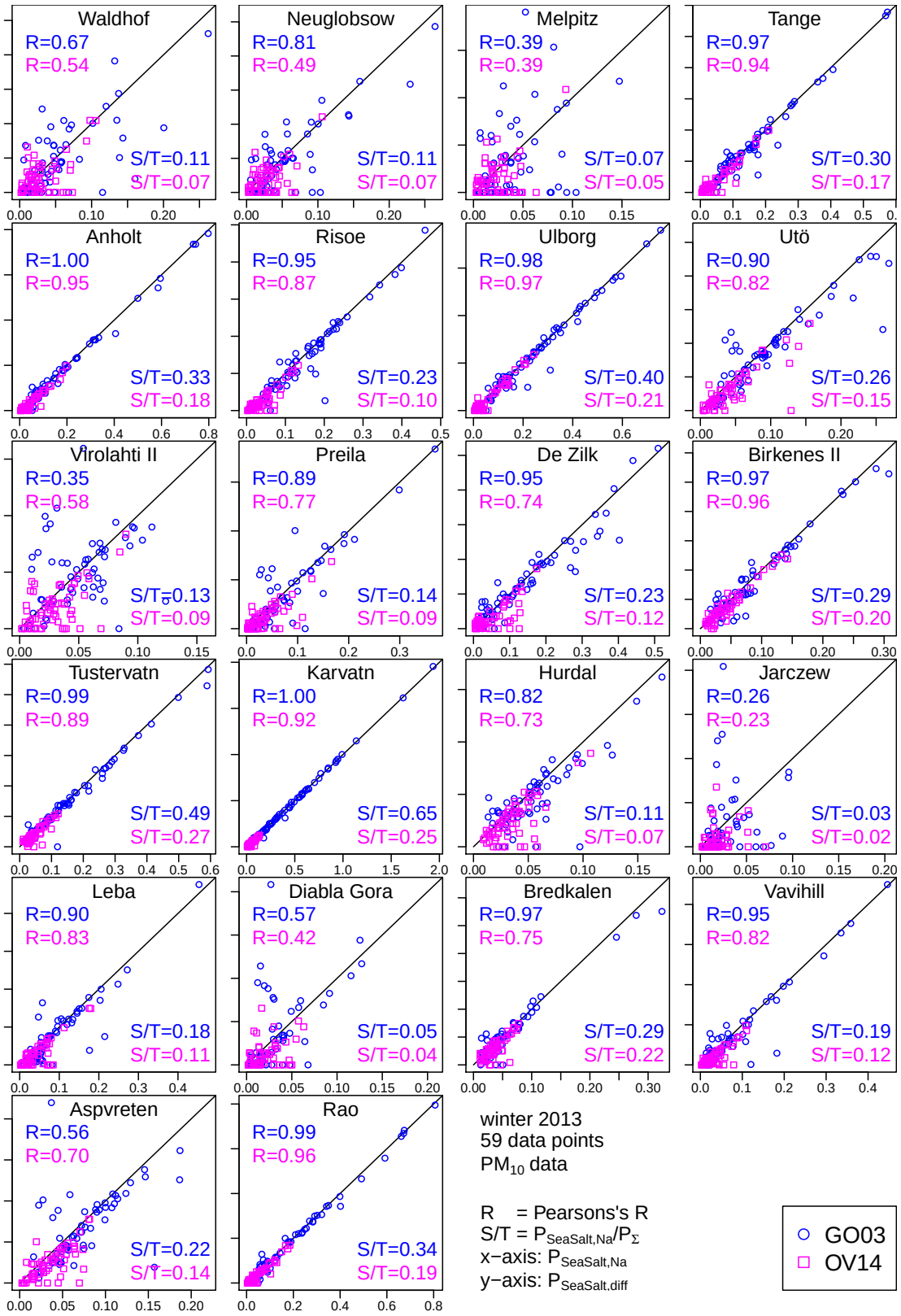

Figure E.5: Similar to Fig. 6.5 but showing sulfate PM_{10} concentrations of all stations in winter 2013

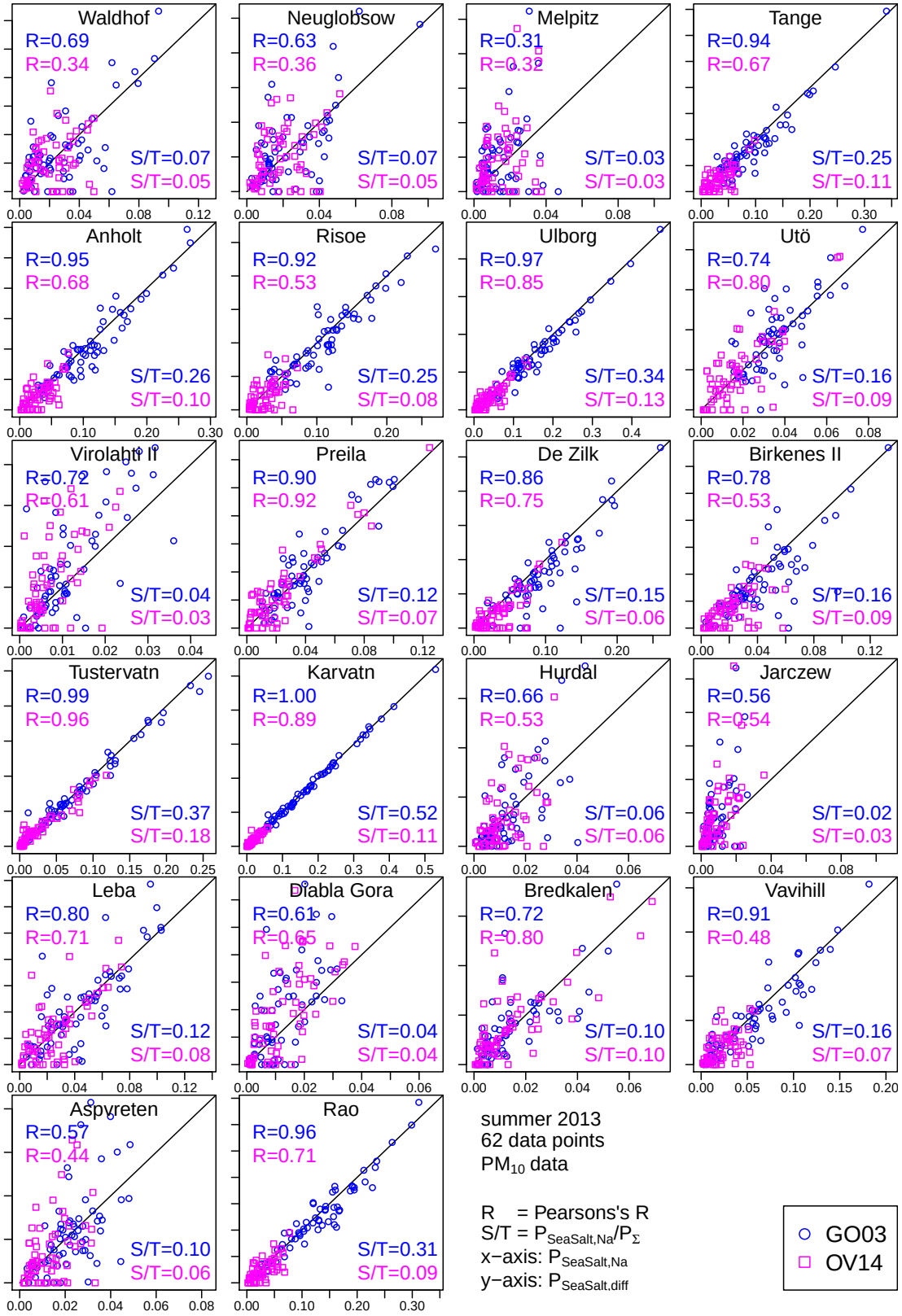

Figure E.6: Similar to Fig. E.5 but showing sulfate PM_{10} concentrations in summer 2013

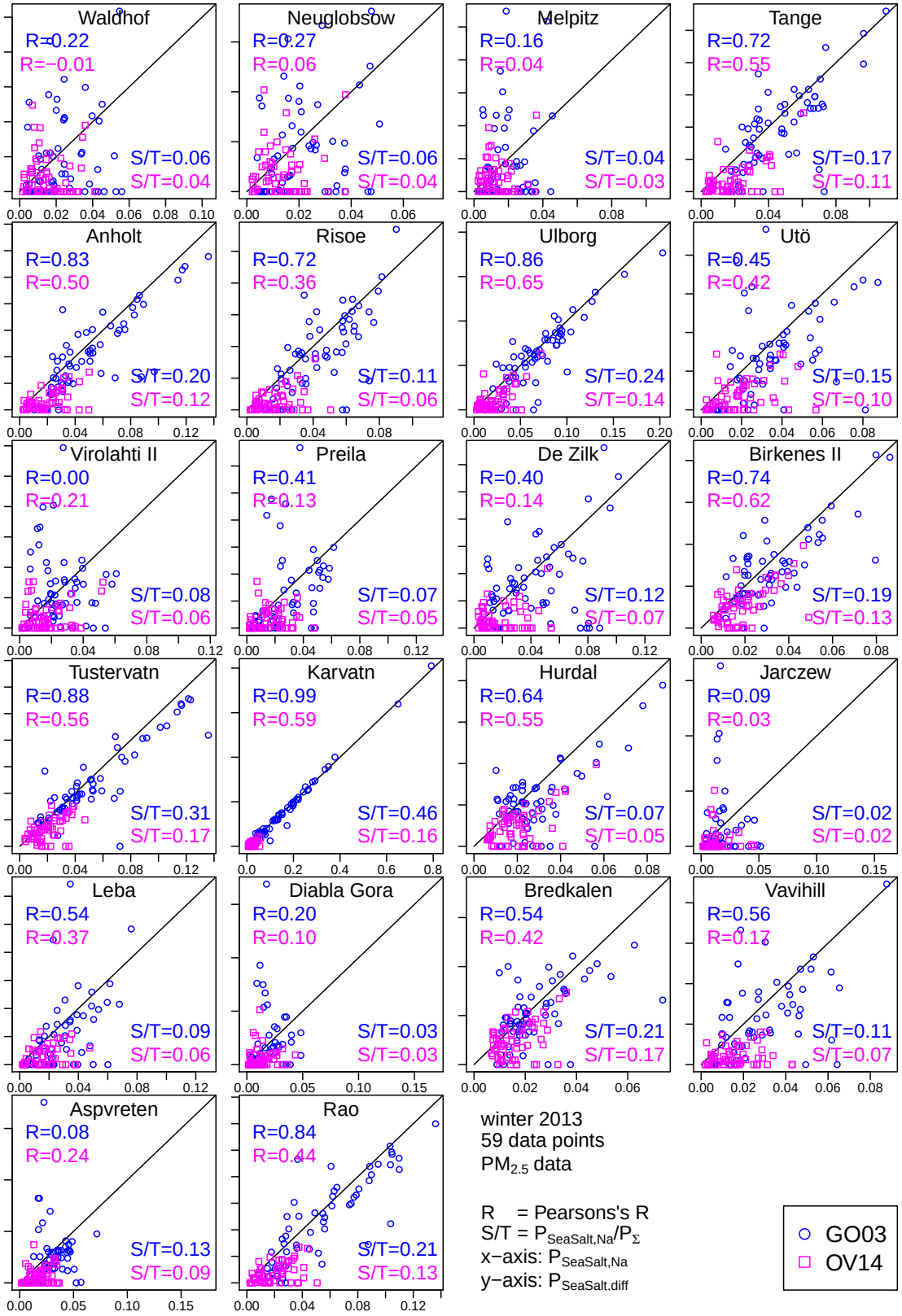

Figure E.7: Similar to Fig. E.5 but showing sulfate $PM_{2.5}$ concentrations in winter 2013

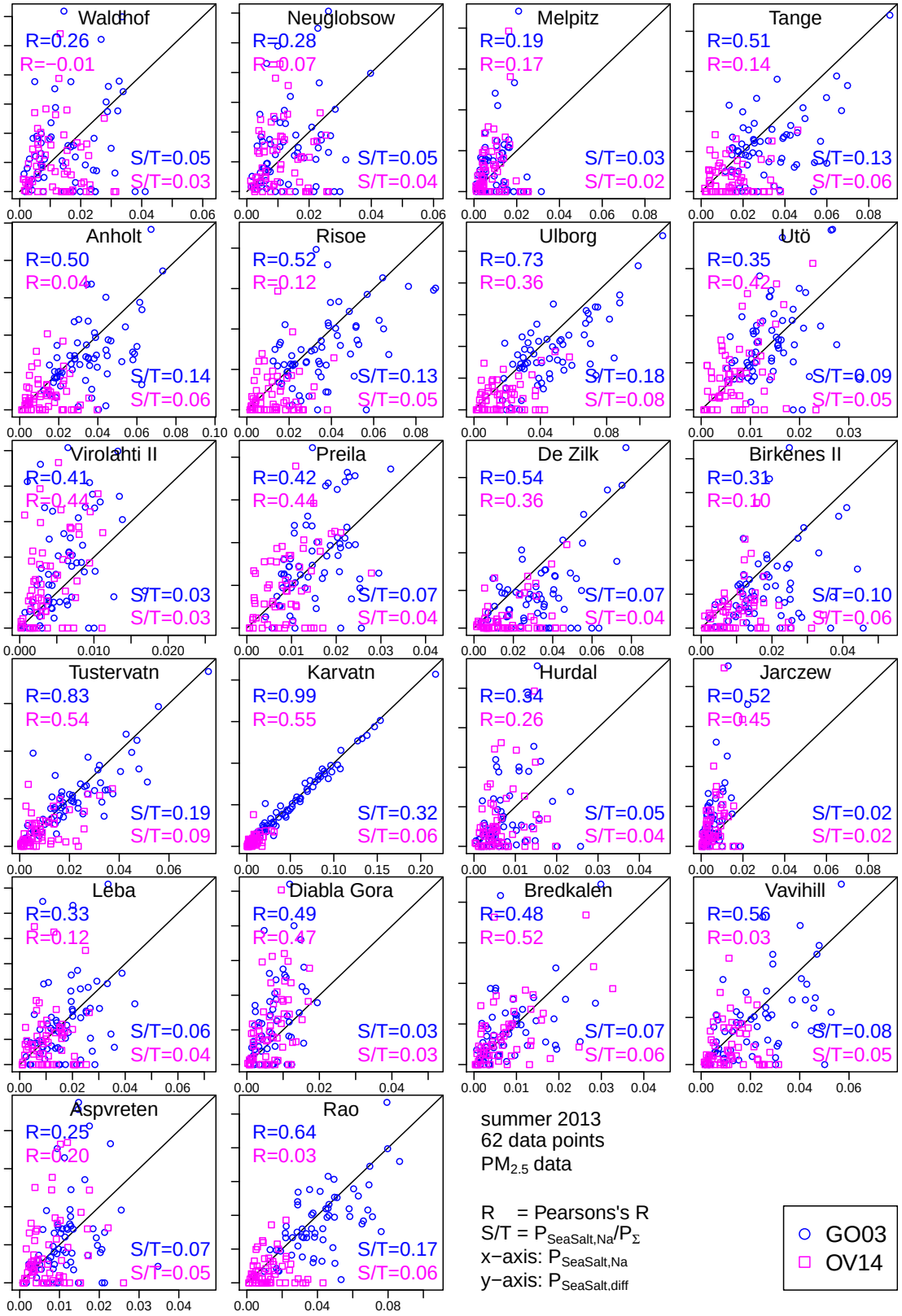

Figure E.8: Similar to Fig. E.5 but showing sulfate $PM_{2.5}$ concentrations in summer 2013

F Filter Packs: Sampling Atmospheric Nitrogen Compounds

Atmospheric NO_3^-, HNO_3, NH_4^+, and NH_3 can be sampled via denuders or via filter packs. The measurements are performed in a second step. The Filter packs that are commonly used at EMEP stations consist of three filters (see Fig. F.1 and EMEP [2014, Sect. 3.2]): a particle filter, an alkaline impregnated filter, and an acidic impregnated filter. The filter packs are denoted as 3-filter packs or three-stage filter packs. The functioning of denuders is briefly described in the quotation below. It is described in EMEP [2014, Sect. 3.4] in detail.

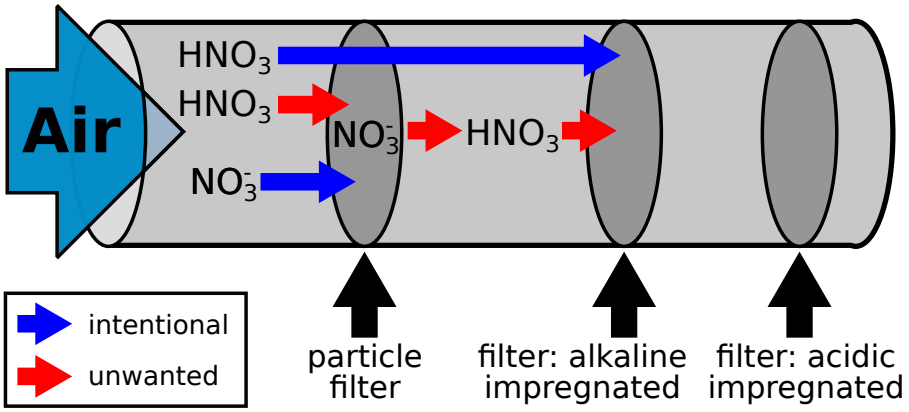

Figure F.1: Schematic cross section of a 3-filter pack. Air flows in from the left and passes a particle filter, an alkaline impregnated filer, and an acidic impregnated filter. Gaseous acids and SO_2 condense on the 2nd filter and gaseous bases on the 3rd filter. Particulate NH_4^+ and NO_3^- might evaporate as NH_3 and HNO_3, respectively, from the particle filter and condense on the other filters. Additionally, gaseous NH_3 and HNO_3 might condense on the particle filter. These processes – indicated by red arrows – are unwanted. Blue arrows identify intentional processes. Particulate SO_4^{2-} and gaseous SO_2 are not affected. See text for details.

Filter packs are simpler in their handling than denuders and, hence, commonly used at EMEP stations. However, they do not allow to distinguish between NO_3^- and HNO_3 and between NH_4^+ and NH_3. The reason for this is given in the quotation hereafter that is from EMEP [2014, Sect. 3.2.1] and illustrated by Fig. F.1.

> Nitric acid in the gaseous state readily reacts with other atmospheric constituents to form nitrates in the form of atmospheric particles. If ammonium nitrate is formed, the reaction is reversible, and its presence requires a dissociation product of gaseous nitric acid and ammonia, which in turn depends on temperature and relative humidity (Stelson and Seinfeld, 1982). Sampling artefacts due to the volatile nature of ammonium nitrate, and possibly due to interaction with other atmospheric constituents make separation of these gases and particles by a simple aerosol filter unreliable. This can be achieved using denuders where one takes advantage of the different diffusion velocities of gas and aerosol particles in a sampling device, which is simply a tube coated on the inside by an absorbing reagent, usually sodium chloride or sodium

> carbonate. The same sampling principle may also be used for sampling of ammonia, using citric, oxalic, or phosphoric acid as the absorbent. Because the diffusion speed of ammonia in air is about twice that of nitric acid, a shorter diffusion tube will achieve >95 % absorption. If the flow is laminar, minimal deposition of particles occur, and if the tube has proper dimensions in relation to the flow rate and the diffusion speed of gaseous nitric acid in air, nitric acid is efficiently deposited to the walls of the tube.
>
> [...]
>
> Denuders can be rather impractical and are relatively expensive, and as filter packs are mostly more reliable and less demanding in terms of sampling and sample preparation, this procedure is often chosen. However, since the filter pack technique is poorer when it comes to separate gas and particle phase, only the sum of nitric acid and nitrate and for the sum of ammonium and ammonia are obtained. Information on the partition between the gaseous and the particle formed may sometimes be inferred also from filter pack data. This may be the situation in areas where the concentration of gaseous ammonia is usually high, or where the concentrations of both nitric acid and ammonia gas concentrations are so low that the partial pressure product necessary for ammonium nitrate to be present is not reached. The separation of SO2/SO42- is good in both techniques.

In this study, the sum of NO_3^- and HNO_3 is denoted as sNO_3 and the sum of NH_4^+ and NH_3 as sNH_4. In the year 2008, 3-filter packs were used at nearly every European EMEP measurement station in the considered model region. Therefore, the validation of model NO_3^- and NH_4^+ concentrations was primarily based on sNO_3 and sNH_4 data. At Melpitz, NO_3^- was sampled and measured by a Monitor for AeRosols and GAses in ambient air (MARGA) which allows individual NO_3^- measurements [Makkonen et al., 2012; Rumsey et al., 2014]. However, no comparison to filter pack sampling data was possible because no parallel filter pack and HNO_3 samplings were set up.

G EMEP data

G.1 File Format

The EBAS database was originally set up at the NILU in the 1970s and is currently improved in the course of the EBAS online project which was started in 2012.[a] One action of the project was to introduce the EBAS version 1.0 file format for the data provided by EBAS. It is derived from the NASA Ames 1001 data format (Listing G.1).[b] Files in this format consist of a header containing meta data (header section) and a body containing the actual data (data section).

Listing G.1: NASA Ames 1001 data file format

line number	content
1	[NLHEAD = number of lines till data section starts] 1001
2	[creator of the file]
3	[affiliation of the originator]
4	[source of the measurements/model results]
5	[name of the mission or campaign]
6	1 1
7	[start date of data] [revision date]
8	[length of a measurement time step in unit (next line)]
9	[time unit of measurement time steps]
10	[NV = number of data variables (including time)]
11	[scaling factor for each variable]
12	[quantity indicating a missing or bad value]
13	[variable definition 1 (time)]
14	[variable definition 2]
...	...
12+NV	[variable definition NV]
13+NV	[NS = number of lines with special comments]
14+NV	[special comment 1]
...	...
13+NV+NS	[special comment NS]
14+NV+NS	[NN = number of lines with normal comments]
15+NV+NS	[normal comment 1]
...	...
14+NV+NS+NN	[normal comment NN]
15+NV+NS+NN	starttime endtime [head var 2] ... [head var NV]
16+NV+NS+NN	[start 1] [end 1] [var 1 at 1] ... [var NV at 1]
17+NV+NS+NN	[start 2] [end 2] [var 1 at 2] ... [var NV at 2]
...	...
15+NV+NS+NN+NT	[start NT] [end NT] [var 1 at NT] ... [var NV at NT]

In 2015, the format was updated to EBAS version 1.1 (Listing G.2).[c] It explicitly defines a set of the normal comments (28), bans special comments, and dictates variable name and variable

[a] see `http://www.nilu.no/projects/ccc/ebas_online/index.html`, last access: 19 April 2016

[b] format description: `cloud1.arc.nasa.gov/solve/archiv/archive.tutorial.html`, last access: 19 April 2016

[c] overview: ebas-submit.nilu.no/SubmitData/RegularAnnualDataReporting/Aerosolchemcompfilterbased.aspx
example NO_x: ebas-submit.nilu.no/SubmitData/RegularAnnualDataReporting/NOsubxsubregular.aspx
example inorganic aerosol chemistry:
ebas-submit.nilu.no/SubmitData/RegularAnnualDataReporting/Inorganicairaerosolchemistryfilterbased.aspx

definition conventions. The data section contains measurement and quality flag variables in pairs[d]. In the case of long term measurements, one file holds data for one year of measurements. Data of measurement campaigns shorter than one year are also available is this format.

Listing G.2: EBAS 1.1 data file format. EMEP data that is exported from the EBAS database is provided in this format.

line number	content
1	[NLHEAD = number of lines till data section starts] 1001
2	[creator of the file]
3	[affiliation of the originator]
4	[source of the measurements/model results]
5	EMEP
6	1 1
7	[start date of data] [revision date]
8	[length of a measurement time step in unit (next line)]
9	[time unit of measurement time steps]
10	[NV = number of data variables (including time)]
11	1 ... 1
12	[quantity indicating a missing or bad value]
13	[time definition (variable 1)]
14	[measurement 1 definition (variable 2)]
15	[flag to measurement 1 definition (variable 3)]
16	[measurement 2 definition (variable 4)]
17	[flag to measurement 2 definition (variable 5)]
...	...
11+NV	[measurement (NV−1)/2 definition (variable NV−1)]
12+NV	[flag to measurement (NV−1)/2 definition (variable NV)]
13+NV	0
14+NV	28
15+NV	[normal comment 1]
...	...
42+NV	[normal comment 28]
43+NV	starttime endtime [head measurement 1] [head flag 1] ...
44+NV	[start 1] [end 1] [measurement 1 at 1] [flag 1 at 1] ...
45+NV	[start 2] [end 2] [measurement 1 at 2] [flag 1 at 2] ...
...	...
43+NV+NT	[start NT] [end NT] [measurement 1 at NT] [flag 1 at NT] ...

G.2 Quality Flags

Quality flags are assigned to all EMEP measurements by quality assurance officials.[e] Each flag is a three digit number, such as 000, 557, 567, 657, or 999, and it states whether a measurement value as valid (V), invalid (I), missing (M), or hidden and invalid (H). The flag holds information on the exact reason of the validity or invalidity of a measurement. Exemplary, 657 means 'Precipitation collector overflow' (V), 567 means 'Insect contamination, considered invalid' (I), and 557 means 'Insect contamination, but considered valid' (V). The flags 000 and 999 are most common, meaning "everything is fine" and "missing measurement, unspecified reason", respectively. The flag variable in EBAS 1.1 files consist of up to three flags per time step forming a number of three, six, or nine digits.

[d] In EBAS 1.0 format, one flag variable was mapped to one or more measurement variable, i.e. when several measurements were performed with one instrument, such as parallel sodium and chloride measurements by an ion chromatograph.

[e] The flags are listed at `http://www.nilu.no/projects/ccc/flags/index.html`; last access: 19 April 2016

G.3 Local Database for EMEP Data

The EMEP measurement data were used in this study for the evaluation of model results. A set of R functions, denoted as emep_file_parser, were programmed to read EBAS data files, parse the data including the meta data, and write them into R variables (Fig. G.3). In order to simplify the handling of the measurement data, a PostgreSQL database was set up. Measurement data from EBAS files can be imported into this database and easily exported when needed. A R function (emep_database_importer) was written for the importing procedure (described below). Armin Aulinger programmed the ctmeval R package that exports data from the database and allows comparing the data against CMAQ modeling results. Data from the database can be also directly accessed, e.g. with the R RODBC package. For the case that data is missing in the database but available as EBAS data file, the R function emep_data2ctmeval was programmed to convert the output of the emep_file_parser into variable structures needed by functions of the ctmeval package. The functions emep_file_parser, emep_database_importer, and emep_data2ctmeval are attached in the supplement DVD.

The local PostgreSQL database to host EMEP measurement data was set up at a database server of the IT department of the HZG. The keyword "local" distinguishes this database from the the EBAS database at NILU. It is not run locally on an office computer as the keyword might suggest. The database structure is given in Fig. G.1. The structure is fitted to the EBAS data file structure and to the procedure of downloading and importing individual data files. The idea behind the structure is described below:

- files holds meta data that remains constant over several years (e.g. instrument).
- sgl_files holds meta data of the individual EBAS data files that changes in each file: one record (row) per EBAS data file.
- The table f_substances holds the variable names and matrices of the measurement variables per EBAS data file: one record per measurement variable and per EBAS data file.
- The table data contains individual measurements and the associated flags: one row per time step, per variable, and EBAS data file.
- The table flags contains all flags and their status of validity (V, I, M, and H).
- The table stations contains the detailed station information: name, id, location, altitude.

The emep_database_importer attempts to import the measurement data and meta data provided by the emep_file_parser into the local database. Prior to writing the data into the database, the tools tests whether the measurements or parts of it are already present in the database in order to avoid duplicate entries (Fig. G.2). Three cases can occur:

a) the file has never been imported before

b) the file has already been imported completely

c) the file has already been important but not all measurement variables

Case (a) should be the standard situation. Case (b) occurs if a user tries to import a file a second time. Case (c) is explained with a short example: A EBAS data file with three measurement variables is given. One variable is correctly imported but two variables are not due to incorrect quality flags. The user fixes the problem with one of the two defective variables (e.g. corrects typos in quality flags). He restarts the importing procedure, which (z) ignores the already correctly imported measurement variable, (y) imports the corrected one, and (x) does not import the still defective one. The exact testing procedure is presented in Fig. G.2.

This complicated testing-procedure was a design decision. Other designs were: (1) A file with at least one defective measurement variable is not imported at all. (2) A file can be imported only once but defective measurement variables are not imported and cannot be imported a second time. Both alternative designs would have led to a lower amount of available data sets.

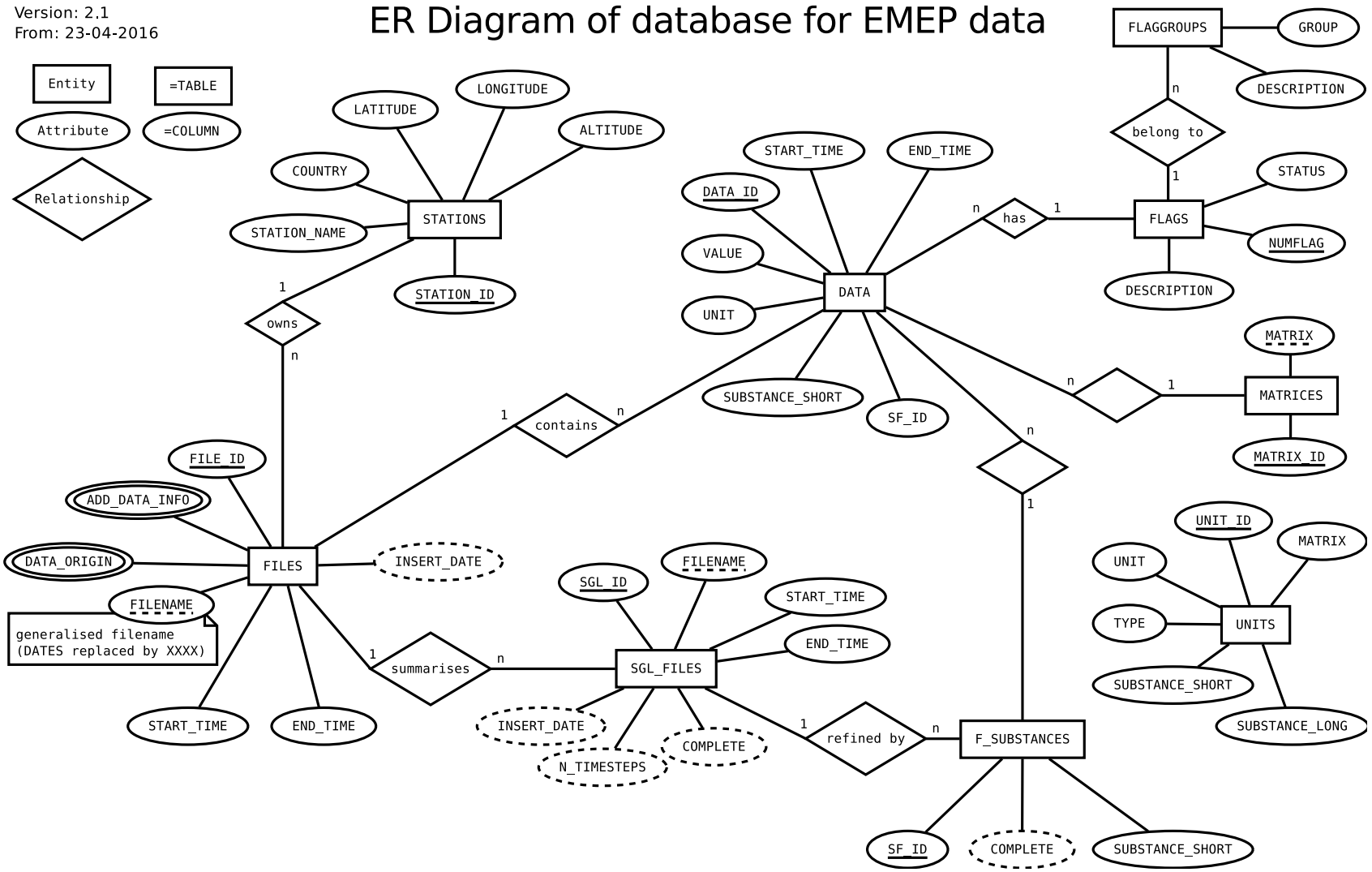

Figure G.1: ER diagram showing the database structure (tables and columns) of the local EMEP database. Continuous underlined attribute names indicate primary keys and attributes with dashed underlined names have unique values but are no official primary keys. Some attributes are not shown in the diagram to keep it readible. Attributes surrounded by a dashed ellipse contain meta data for error correction activities and no EMEP data.

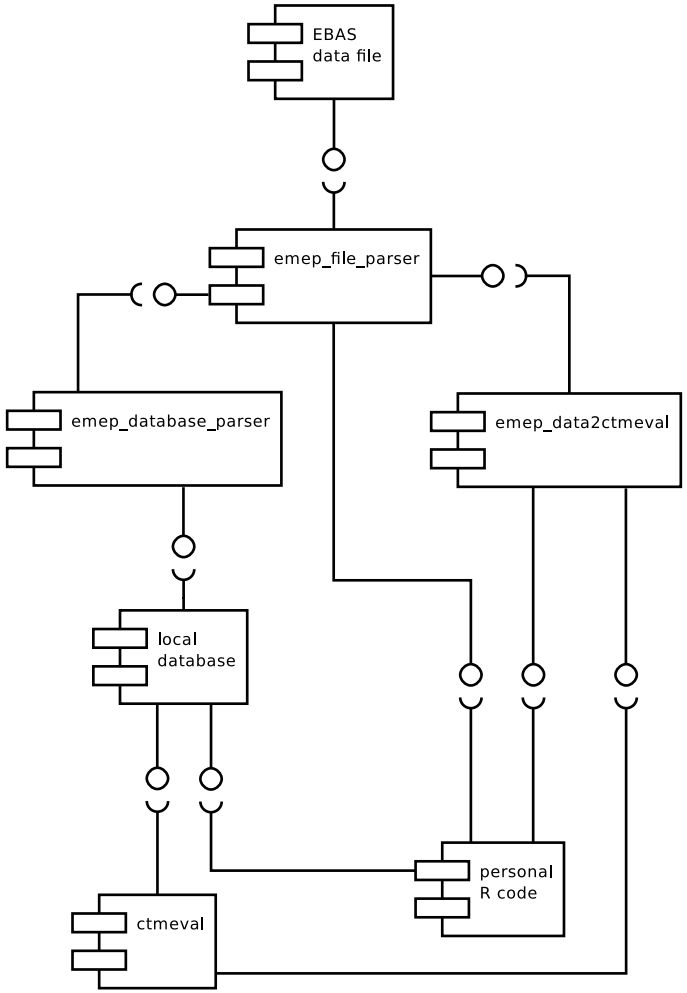

Figure G.2: UML component diagram of accssing EMEP data (emep_file_parser) that are imported into the local database (emep_database_importer) or processed by the user. The ctmeval package either exports EMEP data from the database or obtains them via emep_file_parser and emep_data2ctmeval directly from EBAS data files.

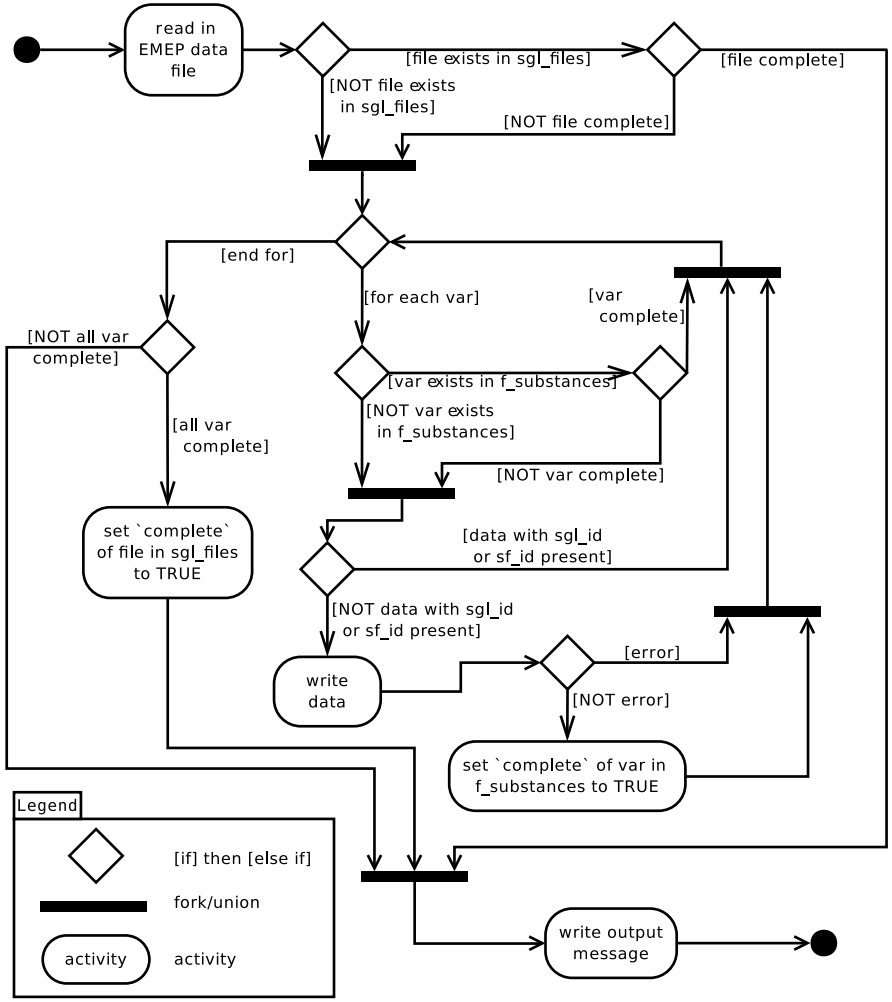

Figure G.3: UML activity diagram on the import of EMEP data into the local EMEP database by the emep_database_importer function. The start of the procedure is indicate by the black sphere (bull's eye) in the top left corner of the diagram. The meanings of the diagram symbols is shown in the legend bottom left. The diagram should be regarded in combination with the source code.

H The OCEAN file

H.1 Introduction

CMAQ's land-ocean mask and the fraction of surf zone and open ocean (per grid cell) are read in from a netCDF file denoted as OCEAN file. For the four sea salt emissions cases base, noSurf, zero, and full four OCEAN files were created. The necessary data were extracted via ArcGIS from the Natural Earth large scale data set (Sect. H.5.2). They were post-processed which is commonly not the case for CMAQ OCEAN files: First, the surf zone area was limited by a threshold (Sect. H.3). Second, the OCEAN file was scaled linearly with the salinity (Sect. H.4). Since this method via ArcGIS is complicated, a second simplified method that works solely on the command line is presented in Sect. H.5.1. However, OCEAN files generated by the latter approach do not include a surf zone.

This appendix chapter is structured as follows: First, the structure of CMAQ OCEAN files is presented (Sect. H.2), followed by the approaches for capping the surf zone area (Sect. H.3) and for salinity scaling (Sect. H.4). Finally, the different methods for creating new OCEAN files are described (Sect. H.5)

H.2 Structure

The OCEAN file employed by CMAQ consists of a variable TFLAG and data variables SURF, OPEN, and MASK (see Listing H.1). The variable MASK is the land-coast-ocean mask which defines whether a grid cell is coastline, open ocean or land by taking the values 1, 2 or 0, respectively. SURF and OPEN contain the surf zone and open ocean fractions per grid cell taking values between 0.0 and 1.0. The data variables need to have LAY (layer) and TSTEP (time) dimensions even though they are 1. The time and date given in TFLAG should exist but they do not needed to be consistent with time and date of the simulation. The variable TFLAG needs to be the first variable The order of the data variables is not specified but is has to equal the order of variable names in the global attribute VAR-LIST. The global attributes and the variable's attributes need to be properly set according to the IOAPI conventions. This means, particularly, that the time and all data variables need to have the attributes units, long_name, and var_desc properly set.

Listing H.1: NetCDF header of an OCEAN file of the CD24 grid.

```
netcdf OCEAN_CD24_sf050m {
dimensions:
        DATE-TIME = 2 ;
        VAR = 3 ;
        TSTEP = UNLIMITED ; // (1 currently)
        COL = 112 ;
        ROW = 106 ;
        LAY = 1 ;
variables:
        int TFLAG(TSTEP, VAR, DATE-TIME) ;
                TFLAG:units = "<YYYYDDD,HHMMSS>" ;
                TFLAG:long_name = "TFLAG               " ;
                TFLAG:var_desc = "" ;
        float MASK(TSTEP, LAY, ROW, COL) ;
                MASK:units = "none" ;
```

```
                MASK:long_name = "MASK                " ;
                MASK:var_desc = "2=open ocean, 1=coastline, 0=other" ;
        float SURF(TSTEP, LAY, ROW, COL) ;
                SURF:units = "none" ;
                SURF:long_name = "SURF                " ;
                SURF:var_desc = "surf zone area / total area" ;
        float OPEN(TSTEP, LAY, ROW, COL) ;
                OPEN:units = "none" ;
                OPEN:long_name = "OPEN                " ;
                OPEN:var_desc = "open ocean area / total area" ;

// global attributes:
                :FTYPE = 1 ;
                :CDATE = 2014136 ;
                :CTIME = 172931 ;
                :WDATE = 2014136 ;
                :WTIME = 172931 ;
                :SDATE = 0 ;
                :STIME = 0 ;
                :TSTEP = 0 ;
                :NTHIK = 1 ;
                :NCOLS = 112 ;
                :NROWS = 106 ;
                :NLAYS = 1 ;
                :NVARS = 3 ;
                :GDTYP = 2 ;
                :P_ALP = 30. ;
                :P_BET = 60. ;
                :P_GAM = 10. ;
                :XCENT = 10. ;
                :YCENT = 55. ;
                :XORIG = -1398000. ;
                :YORIG = -1191000. ;
                :XCELL = 24000. ;
                :YCELL = 24000. ;
                :VGTYP = 2 ;
                :VGTOP = 10000.f ;
                :VGLVLS = 1.f, 0.98f ;
                :GDNAM = "CD24" ;
                :UPNAM = "" ;
                :VAR-LIST = "MASK            SURF            OPEN            " ;
                :FILEDESC = "OCEANfile" ;
                :HISTORY = "" ;
                :EXEC_ID = "0.45535579521348" ;
}
```

H.3 Limited surf zone

All bights and fjords are included in the ArcGIS calculations. However, in protected bights and fjords there is no surf zone. A maximum effective surf zone shape was arbitrarily defined as plotted in Fig. H.1 (c). The maximum surf zone area fraction in the 24 km grid is calculated in Eq. (H.1). The surf zone area fraction was capped at this value and the excess area fraction was added to the open ocean area fraction.

$$\mathrm{SURF}_{\max} = \frac{\sqrt{5} \cdot 50\,\mathrm{m} \cdot 24\,\mathrm{km}}{(24\,\mathrm{km})^2} = \frac{\sqrt{5} \cdot 50\,\mathrm{m}}{24\,\mathrm{km}} \approx 0.004658 \approx 0.47\,\% \tag{H.1}$$

Figure H.1 (a) shows the surf zone fraction after applying the capping (salinity scaling as described in sect. H.4 is already applied). The surf zone fraction that was removed and added

to the open ocean is shown in Fig. H.1 (b). Figure H.2 shows the impact of the capping on atmospheric sodium concentrations: cyan cross indicates concentrations without applying the capping. In contrast to Figs. 3.5 to 3.8, the Waldhof station was exchanged against the Ulborg station, which is located at the Danish North Sea coast.

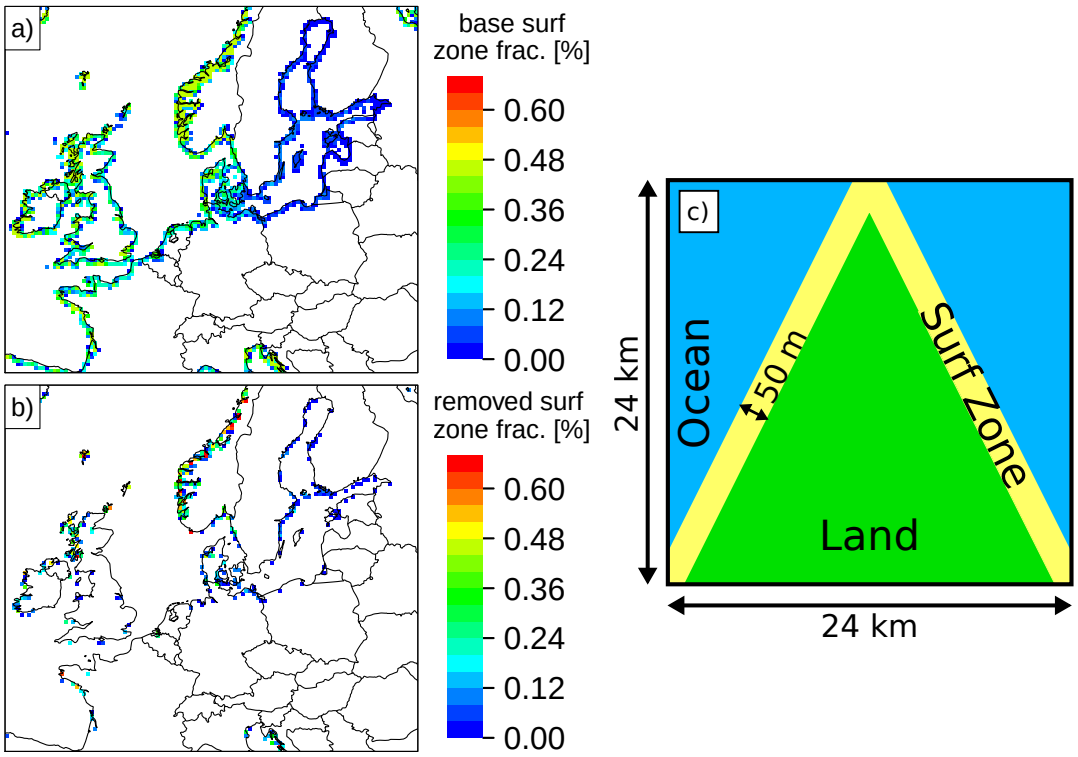

Figure H.1: **left:** Surf zone fraction per grid cell in %. (a) Surf zone fraction in the base case (capped according to Eq. (H.1)). (b) Surf zone fraction that was removed: [surf zone fraction, no capping] - [surf zone fraction, capping]. **right:** (c) Maximum effective surf zone.

H.4 Salinity Scaling

Mårtensson et al. [2003] found an effect of salinity on sea salt emissions. Working in the European domain, makes salinity correction of sea salt emissions necessary because the salinity in most parts of the Baltic Sea is below 10 ‰. In order to reduce sea salt emissions according to local salinity, the values of OPEN and SURF were linearly scaled by the salinity SAL: each value multiplied by SAL/35 ‰. Although Mårtensson et al. [2003] showed that a linear downscaling of the emitted mass, surface and number is not appropriate for the whole size range, this linear scaling is applied because it is the simplest way to add salinity dependence to CMAQ's sea salt emissions without modifying CMAQ program code. One of the results of Chap. 3 was that salinity scaled sea salt emission (linear scaling as described here) improved modeled sodium PM_{10} concentrations in the Baltic Sea region compared to non-salinity-scaled sea salt emissions. Therefore, it is reasonable, to include salinity scaling when oceanic regions with low salinity (SAL) are included in the model domain.

Figure H.3 (a) shows the sea surface fraction without being scaled by the salinity. It is 100 % above most oceanic regions. Figure H.3 (b), in contrast, shows the OCEAN file's sea surface fraction after scaling the actual fraction by SAL/35 ‰. The red color indicates grid cells with a sea surface fraction above 100 % (slightly). This is because the modeled salinity was slightly

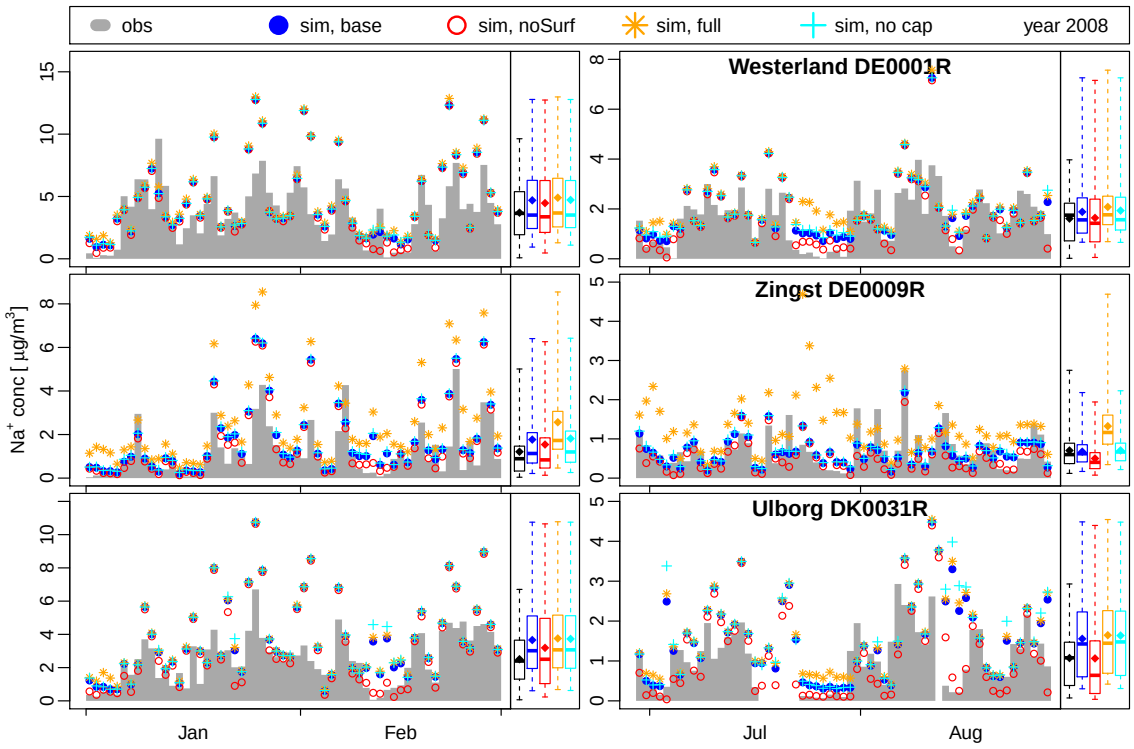

Figure H.2: Similar to Fig. 3.5 but with the addition of sodium concentrations without surf zone capping (cross, cyan) and showing Ulborg instead of Waldhof.

above 35 ‰ in the North Sea. The red area in the Atlantic Ocean is an extrapolation artifact. The salinity data for the North and Baltic Sea were taken from ECOSMO simulations [Schrum and Backhaus, 1999; Barthel et al., 2012].

H.5 Create new OCEAN files

Two different procedures of creating OCEAN files are described below. The first procedure employs the GRIDCRO2D files of the meteorology data set as a source for ocean, land, and coastline data. It is described in the Sect. H.5.1. The second procedure uses data that were

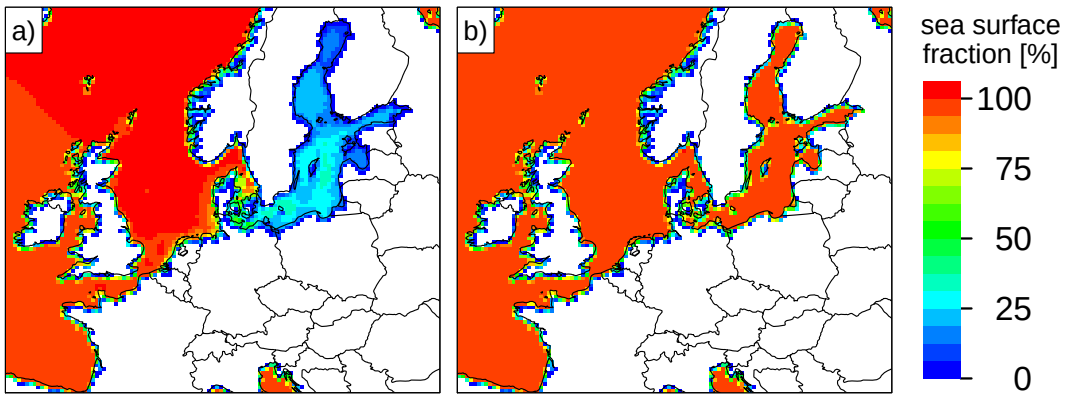

Figure H.3: Sea surface fraction (OPEN + SURF) in % per grid cell as defined in this study's OCEAN files. (a) Sea surface fraction is scaled by the salinity of the underlying ocean. (b) The original sea surface fraction without salinity scaling.

extracted via ArcGIS. This approach is described in the Sect. H.5.2. The preparation of the necessary data in ArcGIS is time consuming and the resulting coastlines do not necessarily agree with the meteorology's coast lines because the spatial resolution in the ArcGIS data is higher. Hence for practical reasons, the first procedure is more sensible for most applications.

Both approaches optionally employ salinity data (see Sect. H.4). For historical reasons, salinity data from BSHcmod operational forecasts [Dick et al., 2001] were used for the procedure described in Sect. H.5.1, whereas salinity data from ECOSMO runs [Schrum and Backhaus, 1999; Barthel et al., 2012] were used for the procedure described in Sect. H.5.2.

All OCEAN files used in simulations for this thesis were created by the advanced procedure described in Sect. H.5.2. These OCEAN files are located in the folder `supplement/TOOLS/OCEAN_gis/` on the attached DVD. The OCEAN files created by the basic approach are located in the folder `supplement/TOOLS/OCEAN_basic/`.

H.5.1 Basic Approach

The basic approach for creating an OCEAN file utilizes an existing GRIDCRO2D file of the meteorology data set. Particularly, the variables LUFRAC_16 (Land use category 16; water fraction, float: $0.0 \leq \ldots \leq 1.0$) and LWMASK (land-water mask; land, boolean: TRUE/FALSE) are be used to create the variables OPEN and MASK for the new OCEAN file. The variable SURF is set to 0.0 everywhere in this approach. The netCDF Operators (NCO) and Climate Data Operators (cdo) are employed to the tasks. Depending on whether salinity data or not are available, a salinity-scaled OCEAN file or a non-salinity-scaled OCEAN file can be created.

Basic Approach without salinity data

Firstly, the creation of a non-salinity-dependent OCEAN file is described (Listing H.2). Exemplary, a GRIDCRO2D file for the CN06 grid on day 1 of the year 2013, denoted as `GRIDCRO2D_cn06_2013001`, is used. It is assumed that the file is located in the directory `../../GRIDCRO`.

Listing H.2: Bash script for creating a non-salinity-dependent OCEAN file from a GRIDCRO2D file for a model grid named CN06.

```
1  #!/bin/bash
2
3  ## create calculated script file for a call of 'ncap2':
4  echo 'defdim("LAY",1);' > addLAY_dim.nco
5  echo 'XMASK[$time,$LAY,$y,$x]=MASK;' > addLAY_dim.nco
6  echo 'YSURF[$time,$LAY,$y,$x]=SURF;' > addLAY_dim.nco
7  echo 'ZOPEN[$time,$LAY,$y,$x]=OPEN;' > addLAY_dim.nco
8
9  ## Copy the GRIDCRO2D file and make TSTEP to the record dimension
10 ncks -O --mk_rec_dmn TSTEP ../../GRIDCRO/GRIDCRO2D_cn06_2013001 cn06.nc
11
12 ## Calculate the OPEN varianle from the LUFRAC_16 and LWMASK variables
13 # OPEN = LUFRAC_16 * ((-1) * (LWMASK - 1))
14 cdo chname,LUFRAC_16,OPEN -mul -selname,LUFRAC_16 cn06.nc -mulc,-1 -subc,1 -
       selname,LWMASK cn06.nc tmp01.nc
15
16 ## Remove some water grind cells from the new OPEN variable
17 # Otherwise, large lakes and river deltas who we open ocean regions.
18 cdo setcindexbox,0,1,90,55,100 -setcindexbox,0,1,68,0,100 -setcindexbox
       ,0,90,100,1,10 -setcindexbox,0,110,115,10,24 -setcindexbox,0,125,140,84,100
       tmp01.nc tmp02.nc
19
20 ## Create SURF and MASK variables from the OPEN variables
21 # SURF = 0.0 * OPEN
22 # MASK(i,j) = IF( OPEN(i,j) == 0 )       0.0 * OPEN(i,j)
23 #              ELSE IF( OPEN(i,j) == 1 ) 2.0 + 0.0 * OPEN(i,j)
```

```
24 #                ELSE                              1.0 + 0.0 * OPEN(i,j)
25 cdo -O merge -chname,OPEN,SURF -mulc,0 -selname,OPEN tmp02.nc -selname,OPEN tmp02.
       nc -chname,OPEN,MASK -ifthenelse -eqc,0 -selname,OPEN tmp02.nc -mulc,0 -
       selname,OPEN tmp02.nc -ifthenelse -eqc,1 -selname,OPEN tmp02.nc -addc,2 -mulc
       ,0 -selname,OPEN tmp02.nc -addc,1 -mulc,0 -selname,OPEN tmp02.nc tmp03.nc
26
27 ## Copy the TFLAG variable from the modified GRIDCRO2D file into an extra files
28 ncks -O -v TFLAG -d VAR,0,2 cn06.nc tmp04.nc
29 cp tmp04.nc tmp08.nc
30
31 ## Copy MASK, OPEN, and SURF into new variables which have the additional
32 ## dimension LAY (=1). Then remove the old variables and rename some dimensions.
33 ncap2 -O -S addLAY_dim.nco tmp03.nc tmp05.nc
34 ncks -O -x -v MASK,OPEN,SURF tmp05.nc tmp06.nc
35 ncrename -O -d x,COL -d y,ROW -d time,TSTEP tmp06.nc tmp07.nc
36
37 ## Copy the copied variables (with extra dimension) into the TFLAG file and
38 ## rename the MASK, SURF, and OPEN variables to their old names.
39 ncks -A -v XMASK,YSURF,ZOPEN tmp07.nc tmp08.nc
40 ncrename -O -v XMASK,MASK -v YSURF,SURF -v ZOPEN,OPEN tmp08.nc tmp09.nc
41
42 ## Finally, add some global attributes.
43 ncatted -O -a 'VAR-LIST',global,m,c,'MASK                SURF                OPEN
                ' -a FILEDESC,global,m,c,'\gls{OCEANfile}' -a units,MASK,o,c,'none
                ' -a long_name,MASK,o,c,"MASK                " -a var_desc,MASK,o,c,"2=
    open ocean, 1=coastline, 0=other" -a units,OPEN,o,c,'none                ' -a
    long_name,OPEN,o,c,"OPEN                " -a var_desc,OPEN,o,c,"open ocean area /
    total area" -a units,SURF,o,c,'none                ' -a long_name,SURF,o,c,"SURF
                " -a var_desc,SURF,o,c,"surf zone area / total area" -a GDNAM,
    global,m,c,"CN06" -a UPNAM,global,o,c,"OCEAN" -a NVARS,global,o,i,3 tmp09.nc
    OCEAN_CN06_sf000m.nc
```

This code can be found on the DVD in the folder `supplement/TOOLS/makeOCEAN/ocean_basic`.

Basic Approach with salinity data

When salinity data are available, the OPEN variable should be scaled by these data (see Sect. H.5). For this purpose the OPEN variable is multiplied by the SALINITY variable and divided by 35 (see also Eq. (D.12)). If the salinity data do not cover the whole considered area, some special cases need to be set up for oceanic regions outside of the covered area. Since the necessary code is quite long, it is not displayed here but attached on the supplement DVD in the folder `supplement/TOOLS/makeOCEAN/ocean_basic_sal`.

H.5.2 Advanced Approach

The basic approaches lack the information on the exact coast line shape. Hence, no surf zone could be defined (SURF variable is 0.0). In order to overcome this problem, coastlines of the Natural Earth large scale data set version 3.1.0 were imported into ArcGIS 10.2.1, a stripe of 50 m width was attached to the outer side of the coast with the ArcGIS buffer tool, and the area within the stripe was calculated per grid cell. Overlapping areas of two and more stripes were not counted twice. It is assumed that the Natural Earth coastlines are represented in sufficient resolution. Open ocean area and land area per grid cell were calculated by ArcGIS, as well, and written out as Excel files – including the surf zone fraction data. In a R script, these data were combined with salinity data [Schrum and Backhaus, 1999; Barthel et al., 2012, ECOSMO], the surf zone fraction was capped (Sect. H.3), and a new OCEAN files was created. The script is available on the attached DVD in the folder `supplement/TOOLS/makeOCEAN/ocean_gis_sal/`.

The generated OCEAN files were used for the studies presented in Chaps. 3, 4, 5, and 6. The base case OCEAN file was created according to this description. The salinity scaling was not

performed for the full case OCEAN file. For the noSurf case OCEAN file, SURF was added to OPEN and set to 0 afterwards. The OPEN and SURF variables were set to 0 in the zero OCEAN file.

I Externally Calculated Sea Salt Emissions

I.1 Calculation Routines

The routines for calculating sea salt emissions were written in the R scripting language. R is widely used for data post-processing and pre-processing tasks by the scientific community. The tasks for generating sea salt emissions are divided into individual functions, such as for (a) numeric integration of sea salt emission parameterizations, (b) the speciation of bulk sea salt mass emissions, and (c) writing calculated sea salt emissions into netCDF files. All functions, except those for integration, are independet of the sea salt emission parameterization. This setup simplifies the extension of the routines by new sea salt emission parameterizations. The integration routines are fitted to each parameterizations because (z) different input data are needed by different parameterizations and (y) because the routines should be optimized for the function type of the parameterization – e.g. polynomial or log-normal.

The functions are attached on the supplement DVD as supplement to Paper 2.[a] The code is commented and the basic usage is described in a readme file (`README_PRODUCE_SSEMIS`).

I.2 File Format

In the unmodified CMAQ version the user can choose to write the inline-calculated sea salt emissions into diagnostic files. The same format and file structure was chosen for the externally calculated sea salt emissions in order to be consistent with CMAQ and the IOAPI standard.

I.3 Necessary Modifications to CMAQ

Please see Sect. D.7.

[a] `supplement/paper2/ssemis`

J Software and Documentation

J.1 Software for Data Evaluation and Visualization

Data pre- and post-processing was performed with the Climate Data Operators (cdo) versions 1.5.3 and 1.6.9, with the netCDF Operators (NCO) versions 4.0.8, 4.0.9, and 4.4.8, with R versions 2.15.1 and 3.1.2 and by Fortran 95 programs. Major plotting work and statistical evaluation were performed with R using the packages ncdf4, maps, mapdata, RODBC, cmaqtools and ctmeval. The latter two packages are in-house developments by Armin Aulinger of the Institute of Coastal Research at the HZG. The maps that show the study region, the model domains and the EMEP stations – but show no data – were created with Generic Mapping Tools (GMT) versions 4.5.2 and 5.1.2. The UML and ER diagrams were created with dia version 0.97.2. The figures produced by R, GMT and dia were post-processed with Inkscape version 0.91.

J.2 Unified Modeling Language

Data flows and structures of programs are described in Sects. 2.4 and G.3. Textual descriptions of these are often lengthy and difficult to read. Therefore, these flows and structures are represented by Unified Modeling Language (UML) diagrams [e.g. Balzert, 2005]. UML defines a set of symbols and diagram types to describe parts of software, software systems, hardware configurations, and user interactions from different views. UML is widely used in the field of software development and documentation. The current version of the UML standard is version 2.5, released in June 2015. The UML diagrams in this thesis are based on the UML version 1.x standard.

J.3 Relational Databases and Entity Relationship Modeling

The purpose of a database is to store data. The purpose of a relational database is to store data but to avoid redundancy by linking data: Data that are needed at two or more "locations" in the database should be stored only once. Table J.1 shows an example data set with redundant information (should not be found in a relational database): the instrument and station information is duplicated in several lines. This table provides a overview of all available data but it consumes unnecessary storage space. Before looking into another way of storing that information, some nomenclature is introduced: Each row is denoted as *record* and each column is denoted as *attribute*.

Table J.1 can be split into three separate tables (Tables J.2 to J.4) that are interconnected by the attributes *Instr.ID* and *Stat.ID* denoted as *Keys*. The attribute *Instr.ID* in table *Instruments* and the attribute *Stat.ID* in the table *Stations* are denoted as *Primary Keys* because each *ID* uniquely identifies one record [Harrington, 2009, Chap. 5]. Table J.2 was extended by an *Attribute Meas.ID* that holds the *Primary Key* for *Measurement records*. Although it is not necessary in this example, every table should have a *Primary Key*. The attributes that hold *Keys* of other tables are denoted as *Foreign Keys*. The instrument information for each *Measurement* record is provided via the *Foreign Key Inst.ID* in *Measurements*.[a].

[a] Station information to *Measurement records* is obtained by: *measurement* record with *Instr.ID* → *instrument* record with *Stat.ID* → *Station* record

Relational databases store data as described by Tables J.2 to J.4. If the stored data should be printed out as shown in Table J.1, The data of several tables can be summarized by *views*. *Views* show data like tables do but they do not store it. Table J.1 could be a *view* on the relational database. If *records* in the actual tables are modified, the modifications are immediately visible in the *View*.

The relational database formulated by Tables J.2 to J.4 can be represented by Entity Relationship (ER) diagrams (Fig. J.1), which were defined for exactly this purpose [Harrington, 2009, Chap. 4]. The tables are represented by squares and denoted as *Entities*. The connection

Table J.1: Examplary database table showing measurements (*Val.*) of different substances (*Subst.*) that were obtained by three instruments (*Inst. Name*) at two separate stations (*Stat.ID*/*Station Name*). Each instrument and each station hold additional information, such as the manufacturer of the instrument or the latitude of the station. The latitude and longitude coordinates are fictive and do not exist. The table holds redundant information. It is split into three separate tables (Table J.2 to J.4) without the loss of information.

Time	Val.	Subst.	Instr. Name	Manufacturer	Technician	Stat.ID	Station Name	Lat	Lon	Alt
10	0.3	A	CounterA	MuellerInstr.	M. Schmidt	DE99	Musterstadt	92° N	362° E	5 m
11	0.29	A	CounterA	MuellerInstr.	M. Schmidt	DE99	Musterstadt	92° N	362° E	5 m
12	0.31	A	CounterA	MuellerInstr.	M. Schmidt	DE99	Musterstadt	92° N	362° E	5 m
12	1.4	B	MultiSpec	MuellerInstr.	M. Meyer	DE99	Musterstadt	92° N	362° E	5 m
12	0.9	C	MultiSpec	MuellerInstr.	M. Meyer	DE99	Musterstadt	92° N	362° E	5 m
12	1.7	B	MultiSpec	MuellerInstr.	P. Silie	DE80	Hamburg	97° N	361° E	2 m
12	1.2	C	MultiSpec	MuellerInstr.	P. Silie	DE80	Hamburg	97° N	361° E	2 m
13	0.29	A	CounterA	MuellerInstr.	M. Schmidt	DE99	Musterstadt	92° N	362° E	5 m
14	0.27	A	CounterA	MuellerInstr.	M. Schmidt	DE99	Musterstadt	92° N	362° E	5 m
15	0.28	A	CounterA	MuellerInstr.	M. Schmidt	DE99	Musterstadt	92° N	362° E	5 m
16	0.28	A	CounterA	MuellerInstr.	M. Schmidt	DE99	Musterstadt	92° N	362° E	5 m
16	1.5	B	MultiSpec	MuellerInstr.	M. Meyer	DE99	Musterstadt	92° N	362° E	5 m
16	0.95	C	MultiSpec	MuellerInstr.	M. Meyer	DE99	Musterstadt	92° N	362° E	5 m
16	1.6	B	MultiSpec	MuellerInstr.	P. Silie	DE80	Hamburg	97° N	361° E	2 m
16	1.1	C	MultiSpec	MuellerInstr.	P. Silie	DE80	Hamburg	97° N	361° E	2 m

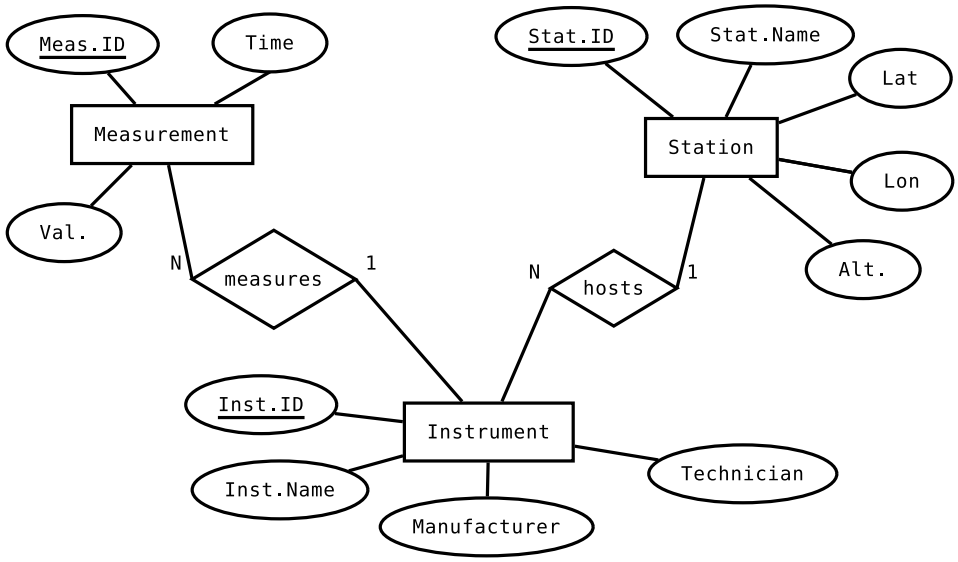

Figure J.1: ER diagram of the relational database represented by Tables J.2 to J.4. The squares are *Entities* (Tables), the ovals are *Attributes*, and the diamonds are *Relations* [Harrington, 2009, Chap. 4]. The underlined *Attributes* are the *Primary Keys*.

Table J.2: Table *Measurements* which holds measurement-related columns of Table J.1. The attribute (column) *Instr.ID* refers to records (rows) in the table *Instruments* (Table J.3).

Measurements				
Meas.ID	Time	Val.	Subst.	Instr.ID
M1	10	0.3	A	I1
M2	11	0.29	A	I1
M3	12	0.31	A	I1
M4	12	1.4	B	I2a
M5	12	0.9	C	I2a
M6	12	1.7	B	I2b
M7	12	1.2	C	I2b
M8	13	0.29	A	I1
M9	14	0.27	A	I1
M10	15	0.28	A	I1
M11	16	0.28	A	I1
M12	16	1.5	B	I2a
M13	16	0.95	C	I2a
M14	16	1.6	B	I2b
M15	16	1.1	C	I2b

Table J.3: Table *Instruments* which holds instrument-related attributes of Table J.1. The attribute textitStat.ID refers to records in the table *Stations* (Table J.4).

Instruments				
Instr.ID	Instr.Name	Manufacturer	Technician	Stat.ID
I1	CountA	MuellerInstr.	M. Schmidt	DE99
I2a	MultiSpec	MuellerInstr.	M. Meyer	DE99
I2b	MultiSpec	MuellerInstr.	P. Silie	DE80

Table J.4: Table *Stations* which holds station-related attributes of Table J.1.

Stations				
Stat.ID	Stat.Name	Lat	Lon	Alt.
DE99	Musterstadt	92° N	362° E	5 m
DE80	Hamburg	97° N	361° E	2 m

via *Foreign* and *Primary Keys* are denoted as *Relations* and represented by diamonds. The *Attributes* are represented by ovals. The *Foreign Keys* are not explicitly shown. The two numbers at the *Relation* named *measures* indicate that an *Instrument* can *measure* a substance *N* times (= several times), whereas a *Measurement* can *be measured* by only *1 Instrument*. Equally, a *Station* can *host N Instruments* but an *Instrument* can *be hosted* by only *1 Station*.

Danksagung

Zuallererst möchte ich meiner Abteilung danken: Allen voran Volker Matthias meinem Betreuer und Markus Quante. Ich konnte immer zu euch kommen, wenn ich fachliche Fragen hatte, und Ihr habt mich sehr beim Schreiben der Dissertation und in der Zeit davor unterstützt. Johannes Bieser hat mir viele Dinge zu CMAQ und zu Emissionsberechnungen beigebracht und Armin Aulinger hat seine R Packages bereit gestellt und sehr viel Ruhe ausgestrahlt, die ich sich zum Teil auf mich übertragen hat. Zu euch beiden konnte ich auch immer mit Fragen kommen. Anna Backes hat einige Dinge in ArcGIS für mich aufbereitet und Jan Arndt war für Fragen zum Schwefelkreislauf immer offen. Zuletzt ist Matthias Karl in unsere Abteilung und in "mein" Büro gekommen. Wir konnten uns seit dem gut fachlich austauschen und ich habe viel von Dir gelernt und viele Publikationshinweise bekommen. Andreas Weigelt, Jan, Martin Ramacher und Matthias waren (in dieser Reihenfolge) meine Büronachbarn und ich habe mich mit euch zusammen immer sehr wohl in einem Büro gefühlt. Neben fachlichen Aspekten gibt es in der Abteilung ein schönes soziales Miteinander mit Kaffeepausen und wechselseitigen Einladung zu sich nach Hause. Das fand ich sehr schön, auch wenn ich oft nicht an Kaffeepausen teilgenommen habe.

Weiterer Dank gebührt auch Kay Emeis meinem zweiten Betreuer, der zusammen mit Felix Ament während der Doktoranden Panel Treffen meine Forschungsfragen und Zeitplanung hinterfragte und mich so voran brachte. Andreas Richter hat während der Panel Treffen, aber auch außerhalb, Wissen zu meiner Doktorarbeit beigesteuert. Vielen Dank, Andreas. Und vielen Dank an Corinna Schrum, die sich bereit erklärt hat, zusammen mit den drei oben genannten Panelmitgliedern und Volker, Mitglied der Prüfungskommission meiner Verteidigung zu werden.

Ein besonderer Dank gebührt meinen Eltern für die ideelle, moralische, soziale und finanzielle Förderung über viele Jahre hinweg. Die finanzielle Förderung ist seit ein paar Jahren vorbei aber die übrige Förderung geht weiter. Ich bin froh euch gehabt zu haben und weiterhin zu haben. Danke. Seit etwa zwei Jahren unterstützt mich auch meine Freundin Franzi moralisch und sozial. Es hat mir sehr viel Kraft gegeben, mit Dir einen Teil meiner Freizeit zu verbringen. Schafi und Pandi waren auch oft dabei. Besonders Schafi hat mir beim Einarbeiten der letzten Korrekturen bis zum Morgengrauen tapfer zur Seite gestanden.

Ein sehr großer Dank geht an die Korrekturleser und leserinnen dieser Arbeit: allen voran Alexandra Gorontzi, die etwa 1/3 des Hauptteils der Arbeit Korrektur gelesen und sehr detaillierte Rückmeldung geben hat. Detailliertere Rückmeldungen kamen nur von Volker und Markus Q. Man muss Alexandra sehr hoch anrechnen, dass sie jetzt schon bei drei von drei meiner Abschlussarbeiten das Korrekturlesen übernommen hat. Super Leistung! Super Nerven! In alphabetischer Reihenfolge waren weiterhin Korrekturleser: Jan Arndt, Anna Backes, Franziska Heydebreck, Andre Schemschadt, Markus Schulze, Maria Schwab, Peer Wagner und Jochen Wollschläger. Ihr habt viele kleine und große Korrekturen beigetragen, die die Arbeit deutlich verbessert haben.

Die große gemeinsame Mittagessensrunde hat mir immer gut gefallen, auch wenn ich die letzten Monate vor Abgabe der Doktorarbeit immer seltener daran teilgenommen habe. Es passte zeitlich leider schlecht.

Jens Meywerk und Hartmut Kapitza halfen bei Problemen auf dem Gruppenserver und auf dem Cluster und halten alle Server ganz gut am Laufen. Antworten auf Fragen zur Verarbeitung von netCDF Dateien mit cdo und zu COSMO-CLM Daten hat Beate Geyer immer ausführlich und geduldig beantwortet. Nikolaus Groll stellte Wellendaten für meine Seesalzberechnungen zur Verfügung und war für Fragen immer offen. Salinitäts- und SST Daten habe ich vom BSH

bezogen auch wenn hier kein konkreter Ansprechpartner zu nennen ist: Vielen Dank.

Ohne die ehrenamtliche Arbeit vieler Programmierer an Open Source Projekten and die Förderung von Open Source Software durch einige Einrichten wäre meine Arbeit wesentlich aufwendiger gewesen. Die verwendete Software hier aufzuliste würde den Rahmen sprengen. Sie ist in Anhang J aufgelistet. Viele Antworten auf Fragen rund um Programmiertätigkeiten, zu LaTeXund zu weiteren technischen Dingen habe ich auf den Seiten des StackExchange Q&A Netzwerkes, speziell den Unterseiten Super User, Stack Overflow, TeX LaTeX und Ask Ubuntu, gefunden. Den vielen nicht genannten Fragenstellern und Antwortengebern: Vielen Dank.

Darüber hinaus habe ich sehr viel bei ERCA (European Research Course on Atmospheres) und bei den internen Fortbildungen des HZG gelernt.

Ein großer Dank gebührt weiterhin den Leuten, die die (verwaltungs-)technische Infrastruktur bereit stellen: die IT Abteilung – keine Telefonnummber habe ich in den letzten drei Jahren häufiger gewählt –, die Druckerei, die Bibliothek, die Cantine, die Fortbildungsabteilung, die Institutsassistentinnen und -assistenten und die Bereiche, die ich hier vergessen habe. Namentlich sind dies speziell in alphabetischer Reihenfolge Dirk Hellriegel, Martin König, Beate Meiners, Alexander Schneider und Sybille Ziemann.

Zu meinem körperlichen Wohl haben die Fit@Work Kurse des VfL Geesthacht von Maren, das morgendliche Schwimmen im Freibad mit Henrike Thomas (aber auch mit Martina und Michael) und die Rücken- und Beinmassagen bei Jörg Tietje beigetragen. Nach letzteren fiel das Joggen am nächsten Tag gleich viel leichter. Das wichtigste für mein körperliches und geistiges Wohl war mein Garten, in dem ich nach der Arbeit und am Wochenende bei der Gartenarbeit abschalten konnte. Außerdem fand ich es sehr toll, dass Beate es immer wieder versucht hat, mich zum Erarbeiten des Sportabzeichen zu motivieren.

Diese Doktorarbeit wurde auf einem Xubuntu System mit LaTeX gesetzt und es wurden das KOMA Script und viele nützliche LaTeX Pakete verwendet.

Meine Stelle am HZG wurde zu unterschiedlichen Teilen aus dem Projekt MeSmarT (Measurements of shipping emissions in the marine troposphere) gemeinsam mit dem BSH (Bundesamt für Seeschifffahrt und Hydrographie) und der Universitä Bremen, aus dem EU Interreg IV B Nordsee Projekt Sail und aus der Grundförderung PACES II (Polar Regions and Coasts in a Changing Earth System) finanziert. Während meiner Doktorarbeit war ich Mitglied in der SICSS Doktorandenschule (School of Integrated Climate System Sciences), die mich durch jährliche Retreats ideell und die meine Reise zu ERCA finanziell unterstützt hat.

Bibliography

AERONET: AOD data, URL http://aeronet.gsfc.nasa.gov/data_menu.html, available at: http://aeronet.gsfc.nasa.gov/data_menu.html, last access: 3 August 2016, 2016.

Allan, J. D., Williams, P. I., Najera, J., Whitehead, J. D., Flynn, M. J., Taylor, J. W., Liu, D., Darbyshire, E., Carpenter, L. J., Chance, R., Andrews, S. J., Hackenberg, S. C., and McFiggans, G.: Iodine observed in new particle formation events in the Arctic atmosphere during ACCACIA, Atmos. Chem. Phys., 15, 5599–5609, doi:10.5194/acp-15-5599-2015, 2015.

Appel, K. W., Foley, K. M., Bash, J. O., Pinder, R. W., Dennis, R. L., Allen, D. J., and Pickering, K.: A multi-resolution assessment of the Community Multiscale Air Quality (CMAQ) model v4.7 wet deposition estimates for 2002-2006, Geosci. Model Dev., 4, 357–371, doi:10.5194/gmd-4-357-2011, 2011.

Athanasopoulou, E., Tombrou, M., Pandis, S. N., and Russell, A. G.: The role of sea-salt emissions and heterogeneous chemistry in the air quality of polluted coastal areas, Atmos. Chem. Phys., 8, 5755–5769, doi:10.5194/acp-8-5755-2008, 2008.

Aulinger, A., Matthias, V., Zeretzke, M., Bieser, J., Quante, M., and Backes, A.: The impact of shipping emissions on air pollution in the greater North Sea region Part 1: Current emissions and concentrations, Atmos. Chem. Phys., 16, 739–758, doi:10.5194/acp-16-739-2016, 2016.

Backes, A., Aulinger, A., Bieser, J., Matthias, V., and Quante, M.: Ammonia emissions in Europe, part I: Development of a dynamical ammonia emission inventory, Atmos. Environ., 131, 55–66, doi:10.1016/j.atmosenv.2016.01.041, 2016a.

Backes, A. M., Aulinger, A., Bieser, J., Matthias, V., and Quante, M.: Ammonia emissions in Europe, part II: How ammonia emission abatement strategies affect secondary aerosols, Atmos. Environ., 126, 153–161, doi:10.1016/j.atmosenv.2015.11.039, 2016b.

Balzert, H.: Lehrbuch der Objektmodellierung: Analyse und Entwurf mit der UML 2, Elsevier, Spektrum Akad. Verl., Heidelberg, 2005.

Barrett, K.: Oceanic ammonia emissions in Europe and their transboundary fluxes, Atmos. Environ., 32, 381–391, doi:10.1016/S1352-2310(97)00279-3, 1998.

Barthel, K., Daewel, U., Pushpadas, D., Schrum, C., Årthun, M., and Wehde, H.: Resolving frontal structures: on the payoff using a less diffusive but computationally more expensive advection scheme, Ocean Dynam., 62, 1457–1470, doi:10.1007/s10236-012-0578-9, 2012.

Bartnicki, J. and Fagerli, H.: Airborne load of nitrogen to European seas, Ecol. Chem. Eng. S, 15, 297–313, 2008.

Bartnicki, J., Semeena, V. S., and Fagerli, H.: Atmospheric deposition of nitrogen to the Baltic Sea in the period 1995–2006, Atmos. Chem. Phys., 11, 10 057–10 069, doi:10.5194/acp-11-10057-2011, 2011.

Behnke, W., George, C., Scheer, V., and Zetzsch, C.: Production and decay of ClNO2 from the reaction of gaseous N2O5 with NaCl solution: Bulk and aerosol experiments, J. Geophys. Res. Atmos., 102, 3795–3804, doi:10.1029/96JD03057, 1997.

Bieser, J., Aulinger, A., Matthias, V., Quante, M., and Builtjes, P.: SMOKE for Europe - adaptation, modification and evaluation of a comprehensive emission model for Europe, Geosci. Model Dev., 4, 47–68, doi:10.5194/gmd-4-47-2011, 2011.

Binkowski, F. S. and Roselle, S. J.: Models-3 Community Multiscale Air Quality (CMAQ) model aerosol component 1. Model description, J. Geophys. Res. Atmos., 108, 4183, doi:10.1029/2001JD001409, 2003.

Binkowski, F. S. and Shankar, U.: The Regional Particulate Matter Model: 1. Model description and preliminary results, J. Geophys. Res. Atmos., 100, 26 191–26 209, doi:10.1029/95JD02093, 1995.

Blanchard, D. C.: Sea-to-Air Transport of Surface Active Material, Science, 146, 396–397, doi:10.1126/science.146.3642.396, 1964.

Blanchard, D. C. and Woodcock, A. H.: The Production, Concentration, and vertical Distribution of the Sea-Salt Aerosol, Ann. NY. Acad. Sci., 338, 330–347, doi:10.1111/j.1749-6632.1980.tb17130.x, 1980.

Bowyer, P. A., Woolf, D. K., and Monahan, E. C.: Temperature dependence of the charge and aerosol production associated with a breaking wave in a whitecap simulation tank, J. Geophys. Res. Oceans, 95, 5313–5319, doi:10.1029/JC095iC04p05313, 1990.

Brunekreef, B. and Holgate, S. T.: Air pollution and health, The Lancet, 360, 1233–1242, doi:10.1016/S0140-6736(02)11274-8, 2002.

Byun, D. and Schere, K. L.: Review of the Governing Equations, Computational Algorithms, and Other Components of the Models3 Community Multiscale Air Quality (CMAQ) Modeling System, Appl. Mech. Rev., 59, doi:10.1115/1.2128636, 2006.

Cai, X., Ziemba, L. D., and Griffin, R. J.: Secondary aerosol formation from the oxidation of toluene by chlorine atoms, Atmos. Environ., 42, 7348–7359, doi:10.1016/j.atmosenv.2008.07.014, 2008.

Callaghan, A. H., Stokes, M. D., and Deane, G. B.: The effect of water temperature on air entrainment, bubble plumes, and surface foam in a laboratory breaking-wave analog, J. Geophys. Res. Oceans, 119, 7463–7482, doi:10.1002/2014JC010351, 2014.

Carlton, A. G., Bhave, P. V., Napelenok, S. L., Edney, E. O., Sarwar, G., Pinder, R. W., Pouliot, G. A., and Houyoux, M.: Model Representation of Secondary Organic Aerosol in CMAQv4.7, Environ. Sci. Technol., 44, 8553–8560, doi:10.1021/es100636q, 2010.

Cavalli, F., Facchini, M. C., Decesari, S., Mircea, M., Emblico, L., Fuzzi, S., Ceburnis, D., Yoon, Y. J., O'Dowd, C. D., Putaud, J.-P., and Dell'Acqua, A.: Advances in characterization of size-resolved organic matter in marine aerosol over the North Atlantic, J. Geophys. Res. Atmos., 109, doi:10.1029/2004JD005137, 2004.

CEIP: WebDab Emission Export of the EU-28 countries divided into SNAP sectors, Accessed on 14 April 2016, URL `webdab.umweltbundesamt.at/scaled_country_year.html`, 2016.

Chen, Y., Cheng, Y., Ma, N., Wolke, R., Nordmann, S., Schüttauf, S., Ran, L., Wehner, B., Birmili, W., Denier van der Gon, H. A. C., Mu, Q., Barthel, S., Spindler, G., Stieger, B., Müller, K., Zheng, G.-J., Pöschl, U., Su, H., and Wiedensohler, A.: Sea salt emission, transportation and influence on nitrate simulation: a case study in Europe, Atmos. Chem. Phys. Discussions, 2016, 1–26, doi:10.5194/acp-2016-309, 2016.

Chomka, M. and Petelski, T.: Sea spray emission over the coastal zone, J. Aerosol Sci., 28, 103–104, doi:10.1016/S0021-8502(97)85052-5, 1997.

Crippa, M., Janssens-Maenhout, G., Dentener, F., Guizzardi, D., Sindelarova, K., Muntean, M., Van Dingenen, R., and Granier, C.: Forty years of improvements in European air quality: the role of EU policy-industry interplay, Atmos. Chem. Phys. Discussions, 15, 20 245–20 285, doi:10.5194/acpd-15-20245-2015, 2015.

Crisp, T. A., Lerner, B. M., Williams, E. J., Quinn, P. K., Bates, T. S., and Bertram, T. H.: Observations of gas phase hydrochloric acid in the polluted marine boundary layer, J. Geophys. Res. Atmos., 119, 6897–6915, doi:10.1002/2013JD020992, 2014.

Cuevas, E., Camino, C., Benedetti, A., Basart, S., Terradellas, E., Baldasano, J. M., Morcrette, J. J., Marticorena, B., Goloub, P., Mortier, A., Berjón, A., Hernández, Y., Gil-Ojeda, M., and Schulz, M.: The MACC-II 2007–2008 reanalysis: atmospheric dust evaluation and characterization over northern Africa and the Middle East, Atmos. Chem. Phys., 15, 3991–4024, doi:10.5194/acp-15-3991-2015, 2015.

Culkin, F. and Cox, R.: Sodium, potassium, magnesium, calcium and strontium in sea water, Deep-Sea Res.: Oceanogr. Abstr., 13, 789–804, doi:10.1016/0011-7471(76)90905-0, 1976.

de Leeuw, G., Neele, F. P., Hill, M., Smith, M. H., and Vignati, E.: Production of sea spray aerosol in the surf zone, J. Geophys. Res. Atmos., 105, 29 397–29 409, doi:10.1029/2000JD900549, 2000.

de Leeuw, G., Skjøth, C. A., Hertel, O., Jickells, T., Spokes, L., Vignati, E., Frohn, L., Frydendall, J., Schulz, M., Tamm, S., Sørensen, L., and Kunz, G.: Deposition of nitrogen into the North Sea, Atmos. Environ., 37, 145–165, doi:10.1016/S1352-2310(03)00246-2, 2003.

de Leeuw, G., Andreas, E. L., Anguelova, M. D., Fairall, C. W., Lewis, E. R., O'Dowd, C. D., Schulz, M., and Schwartz, S. E.: Production flux of sea spray aerosol, Rev. Geophys., 49, doi:10.1029/2010RG000349, 2011.

Dee, D. P., Uppala, S. M., Simmons, A. J., Berrisford, P., Poli, P., Kobayashi, S., Andrae, U., Balmaseda, M. A., Balsamo, G., Bauer, P., Bechtold, P., Beljaars, A. C. M., van de Berg, L., Bidlot, J., Bormann, N., Delsol, C., Dragani, R., Fuentes, M., Geer, A. J., Haimberger, L., Healy, S. B., Hersbach, H., Hólm, E. V., Isaksen, L., Kållberg, P., Köhler, M., Matricardi, M., McNally, A. P., Monge-Sanz, B. M., Morcrette, J.-J., Park, B.-K., Peubey, C., de Rosnay, P., Tavolato, C., Thépaut, J.-N., and Vitart, F.: The ERA-Interim reanalysis: configuration and performance of the data assimilation system, Q. J. Roy. Meteor. Soc., 137, 553–597, doi:10.1002/qj.828, 2011.

Déqué, M., Jones, R. G., Wild, M., Giorgi, F., Christensen, J. H., Hassell, D. C., Vidale, P. L., Rockel, B., Jacob, D., Kjellström, E., Castro, M. d., Kucharski, F., and Hurk, B. v. d.: Global high resolution versus Limited Area Model climate change projections over Europe: quantifying confidence level from PRUDENCE results, Climate Dynamics, 25, 653–670, doi:10.1007/s00382-005-0052-1, 2005.

Dick, S., Mueller-Navarra, S., Klein, H., Komo, H., and Kleine, E.: The operational circulation model of BSH (BSHcmod) - model description and validation, Techreport, Bundesamt fuer Seeschiffahrt und Hydrographie, URL `http://hdl.handle.net/10068/186797`, 2001.

Doms, G., Schttler, U., Steppeler, J., and Wicker, L.: Development of the Nonhydrostatic Regional Model LM at DWD, Res. Act. in Atmos. and Oceanic Model., 27, WMO/TD-No.865, 5.17–5.18, 1998.

Doms, G., Förstner, J., Heise, E., Herzog, H.-J., Mironov, D., Raschendorfer, M., Reinhardt, T., Ritter, B., Schrodin, R., Schulz, J.-P., and Vogel, G.: A Description of the Nonhydrostatic Regional COSMO Model - Part II: Physical Parameterization, Tech. Rep. LM F90 4.20, Deutscher Wetterdienst, Deutscher Wetterdienst, P.O. Box 100465, 63004 Offenbach, Germany, URL `http://www.cosmo-model.org/content/model/documentation/core/cosmoPhysParamtr.pdf`, 2011.

Donaldson, D. J., , and Vaida, V.: The Influence of Organic Films at the Air - Aqueous Boundary on Atmospheric Processes, Chem. Rev., 106, 1445–1461, doi:10.1021/cr040367c, 2006.

Duce, R. A. and Hoffman, E. J.: Chemical Fractionation at the Air/Sea Interface, Ann. Rev. Earth Planet. Sci., 4, 187–228, doi:10.1146/annurev.ea.04.050176.001155, 1976.

EBAS: EMEP measurements (atmospheric concentrations, wet deposition, precipitation), URL `http://ebas.nilu.no`, available at: `http://ebas.nilu.no`, last access: 3 August 2016, 2016.

ECMWF MARS: ERA-Interim reanalysis, 6-hourly, URL `http://apps.ecmwf.int/datasets/data/interim-full-daily/levtype=sfc/`, available at: `http://apps.ecmwf.int/datasets/data/interim-full-daily/levtype=sfc/`, last access: 3 August 2016., 2016.

EMEP: EMEP Manual for Sampling and Analysis, EMEP, available at: `http://www.nilu.no/projects/ccc/manual/index.html` (last access: 30 October 2015), 2014.

EMEP: EMEP Status Report 1/2015 "Transboundary particulate matter, photo-oxidants, acidifying and eutrophying components", Joint msc-w & ccc & ceip report, MSC-W & CCC & CEIP, URL `http://emep.int/publ/reports/2015/EMEP_Status_Report_1_2015.pdf`, 2015.

Emmons, L. K., Walters, S., Hess, P. G., Lamarque, J.-F., Pfister, G. G., Fillmore, D., Granier, C., Guenther, A., Kinnison, D., Laepple, T., Orlando, J., Tie, X., Tyndall, G., Wiedinmyer, C., Baughcum, S. L., and Kloster, S.: Description and evaluation of the Model for Ozone and Related chemical Tracers, version 4 (MOZART-4), Geosci. Model Dev., 3, 43–67, doi:10.5194/gmd-3-43-2010, 2010.

Erickson, D. J., Merrill, J. T., and Duce, R. A.: Seasonal estimates of global atmospheric sea-salt distributions, J. Geophys. Res. Atmos., 91, 1067–1072, doi:10.1029/JD091iD01p01067, 1986.

EU: Directive 2000/60/EC of the European Parliament and of the Council of 23 October 2000 establishing a framework for Community action in the field of water policy, Official Journal of the European Union, URL `http://eur-lex.europa.eu/legal-content/EN/TXT/?uri=CELEX:32000L0060`, 2000.

EU: Directive 2008/56/EC of the European Parliament and of the Council on establishing a framework for community action in the field of marine environmental policy (Marine Strategy Framework Directive), Official Journal of the European Union, URL `http://eur-lex.europa.eu/legal-content/EN/TXT/?qid=1456311260639&uri=CELEX:32008L0056`, 2008.

European Environment Agency: EMEP/CORINAIR Emission Inventory Guidebook - 3rd edition 2001, Tech. Rep. Technical Report No 30/2001, European Energy Agency, Copenhagen, Denmark, URL `http://www.eea.europa.eu/publications/technical_report_2001_3`, 2001.

Fairall, C. W., Davidson, K. L., and Schacher, G. E.: An analysis of the surface production of sea-salt aerosols, Tellus B, 35B, 31–39, doi:10.1111/j.1600-0889.1983.tb00005.x, 1983.

Feistel, R., Weinreben, S., Wolf, H., Seitz, S., Spitzer, P., Adel, B., Nausch, G., Schneider, B., and Wright, D. G.: Density and Absolute Salinity of the Baltic Sea 20062009, Ocean Sci., 6, 3–24, doi:10.5194/os-6-3-2010, 2010.

Fountoukis, C. and Nenes, A.: ISORROPIA II: a computationally efficient thermodynamic equilibrium model for K^+-Ca^{2+}-Mg^{2+}-NH_4^+-Na^+-SO_4^{2-}-NO_3^--Cl^--H_2O aerosols, Atmos. Chem. Phys., 7, 4639–4659, doi:10.5194/acp-7-4639-2007, 2007.

Fuentes, E., Coe, H., Green, D., de Leeuw, G., and McFiggans, G.: On the impacts of phytoplankton-derived organic matter on the properties of the primary marine aerosol - Part 1: Source fluxes, Atmos. Chem. Phys., 10, 9295–9317, doi:10.5194/acp-10-9295-2010, 2010.

Gantt, B., Meskhidze, N., Facchini, M. C., Rinaldi, M., Ceburnis, D., and O'Dowd, C. D.: Wind speed dependent size-resolved parameterization for the organic mass fraction of sea spray aerosol, Atmos. Chem. Phys., 11, 8777–8790, doi:10.5194/acp-11-8777-2011, 2011.

Gantt, B., Kelly, J. T., and Bash, J. O.: Updating sea spray aerosol emissions in the Community Multiscale Air Quality (CMAQ) model version 5.0.2, Geosci. Model Dev., 8, 3733–3746, doi:10.5194/gmd-8-3733-2015, 2015.

Gathman, S. G. and Hoppel, W. A.: Surf electrification, J. Geophys. Res., 75, 4525–4529, doi:10.1029/JC075i024p04525, 1970.

Geyer, B.: High-resolution atmospheric reconstruction for Europe 1948-2012: coastDat2, Earth Syst. Sci. Data, 6, 147–164, doi:10.5194/essd-6-147-2014, 2014.

Geyer, B. and Rockel, B.: coastDat-2 COSMO-CLM Atmospheric Reconstruction, World Data Center for Climate (WDCC), Hamburg, Germany, doi:10.1594/WDCC/coastDat-2_COSMO-CLM, 2013.

Geyer, B., Weisse, R., Bisling, P., and Winterfeldt, J.: Climatology of North Sea wind energy derived from a model hindcast for 1958-2012, J. Wind Eng. Ind. Aerod., 147, 18–29, doi:10.1016/j.jweia.2015.09.005, 2015.

Gong, S. L.: A parameterization of sea-salt aerosol source function for sub- and super-micron particles, Global Biogeochem. Cycles, 17, 1097, doi:10.1029/2003GB002079, 2003.

Groll, N. and Weisse, R.: coastDat-2 North Sea wave hindcast for the period 1949–2014 performed with the wave model WAM, World Data Center for Climate (WDCC), Hamburg, Germany, doi:10.1594/WDCC/coastDat-2_WAM-North_Sea, 2016.

Groll, N., Grabemann, I., and Gaslikova, L.: North Sea wave conditions: an analysis of four transient future climate realizations, Ocean Dynam., 64, 1–12, doi:10.1007/s10236-013-0666-5, 2014.

Grythe, H., Ström, J., Krejci, R., Quinn, P., and Stohl, A.: A review of sea-spray aerosol source functions using a large global set of sea salt aerosol concentration measurements, Atmos. Chem. Phys., 14, 1277–1297, doi:10.5194/acp-14-1277-2014, 2014.

Harrington, J. L.: Relational Database Design (Third Edition), Morgan Kaufmann, Boston, Boston, third edition edn., URL `http://www.sciencedirect.com/science/book/9780123747303`, 2009.

HELCOM: Airborne nitrogen loads to the Baltic Sea, Tech. rep., Helsinki Commission, Baltic Marine Environment Protection Commission, URL `http://www.helcom.fi/Lists/Publications/Airborne%20nitrogen%20loads%20to%20the%20Baltic%20Sea.pdf`, 2005.

Hertel, O., Skjøth, C. A., Frohn, L., Vignati, E., Frydendall, J., de Leeuw, G., Schwarz, U., and Reis, S.: Assessment of the atmospheric nitrogen and sulphur inputs into the North Sea using a Lagrangian model, Phys. Chem. Earth, Pt A/B/C, 27, 1507–1515, doi:10.1016/S1474-7065(02)00153-5, 2002.

Hjellbrekke, A.-G.: personal communication, 2016.

Holmes, N.: A review of particle formation events and growth in the atmosphere in the various environments and discussion of mechanistic implications, Atmos. Environ., 41, 2183–2201, doi:10.1016/j.atmosenv.2006.10.058, 2007.

Huijnen, V., Williams, J., van Weele, M., van Noije, T., Krol, M., Dentener, F., Segers, A., Houweling, S., Peters, W., de Laat, J., Boersma, F., Bergamaschi, P., van Velthoven, P., Le Sager, P., Eskes, H., Alkemade, F., Scheele, R., Nédélec, P., and Pätz, H.-W.: The global chemistry transport model TM5: description and evaluation of the tropospheric chemistry version 3.0, Geosci. Model Dev., 3, 445–473, doi:10.5194/gmd-3-445-2010, 2010.

Im, U.: Impact of sea-salt emissions on the model performance and aerosol chemical composition and deposition in the East Mediterranean coastal regions, Atmos. Environ., 75, 329–340, doi:10.1016/j.atmosenv.2013.04.034, 2013.

Im, U., Christodoulaki, S., Violaki, K., Zarmpas, P., Kocak, M., Daskalakis, N., Mihalopoulos, N., and Kanakidou, M.: Atmospheric deposition of nitrogen and sulfur over southern Europe with focus on the Mediterranean and the Black Sea, Atmos. Environ., 81, 660–670, doi:10.1016/j.atmosenv.2013.09.048, 2013.

Inness, A., Baier, F., Benedetti, A., Bouarar, I., Chabrillat, S., Clark, H., Clerbaux, C., Coheur, P., Engelen, R. J., Errera, Q., Flemming, J., George, M., Granier, C., Hadji-Lazaro, J., Huijnen, V., Hurtmans, D., Jones, L., Kaiser, J. W., Kapsomenakis, J., Lefever, K., Leitão, J., Razinger, M., Richter, A., Schultz, M. G., Simmons, A. J., Suttie, M., Stein, O., Thépaut, J.-N., Thouret, V., Vrekoussis, M., Zerefos, C., and the MACC team: The MACC reanalysis: an 8 yr data set of atmospheric composition, Atmos. Chem. Phys., 13, 4073–4109, doi:10.5194/acp-13-4073-2013, 2013.

Jaeglé, L., Quinn, P. K., Bates, T. S., Alexander, B., and Lin, J.-T.: Global distribution of sea salt aerosols: new constraints from in situ and remote sensing observations, Atmos. Chem. Phys., 11, 3137–3157, doi:10.5194/acp-11-3137-2011, 2011.

Jiang, W., Smyth, S., Éric Giroux, Roth, H., and Yin, D.: Differences between {CMAQ} fine mode particle and PM2.5 concentrations and their impact on model performance evaluation in the lower Fraser valley, Atmos. Environ., 40, 4973 – 4985, doi:10.1016/j.atmosenv.2005.10.069, special issue on Model Evaluation: Evaluation of Urban and Regional Eulerian Air Quality Models, 2006.

Junge, C. E.: Our knowledge of the physico-chemistry of aerosols in the undisturbed marine environment, J. Geophys. Res., 77, 5183–5200, doi:10.1029/JC077i027p05183, 1972.

Kampa, M. and Castanas, E.: Human health effects of air pollution, Environ. Pollut., 151, 362–367, doi:10.1016/j.envpol.2007.06.012, 2008.

Karl, M., Leck, C., Gross, A., and Pirjola, L.: A study of new particle formation in the marine boundary layer over the central Arctic Ocean using a flexible multicomponent aerosol dynamic model, Tellus B, 64, URL `http://www.tellusb.net/index.php/tellusb/article/view/17158`, 2012.

Kelly, J. T.: personal communication, 2014.

Kelly, J. T., Bhave, P. V., Nolte, C. G., Shankar, U., and Foley, K. M.: Simulating emission and chemical evolution of coarse sea-salt particles in the Community Multiscale Air Quality (CMAQ) model, Geosci. Model Dev., 3, 257–273, doi:10.5194/gmd-3-257-2010, 2010.

Kelly, J. T., Baker, K. R., Nowak, J. B., Murphy, J. G., Markovic, M. Z., VandenBoer, T. C., Ellis, R. A., Neuman, J. A., Weber, R. J., Roberts, J. M., Veres, P. R., de Gouw, J. A., Beaver, M. R., Newman, S., and Misenis, C.: Fine-scale simulation of ammonium and nitrate over the South Coast Air Basin and San Joaquin Valley of California during CalNex-2010, J. Geophys. Res. Atmos., 119, 3600–3614, doi:10.1002/2013JD021290, 2014.

Knipping, E. M. and Dabdub, D.: Impact of Chlorine Emissions from Sea-Salt Aerosol on Coastal Urban Ozone, Environ. Sci. Technol., 37, 275–284, doi:10.1021/es025793z, 2003.

Kremling, K. and Wilhelm, G.: Recent increase of the calcium concentrations in Baltic Sea waters, Mar. Pollut. Bull., 34, 763–767, doi:10.1016/S0025-326X(97)00048-9, 1997.

Kulmala, M., Vehkamäki, H., Petäjä, T., Maso, M. D., Lauri, A., Kerminen, V.-M., Birmili, W., and McMurry, P.: Formation and growth rates of ultrafine atmospheric particles: a review of observations, J. Aerosol Sci., 35, 143–176, doi:10.1016/j.jaerosci.2003.10.003, 2004.

Lana, A., Bell, T. G., Simó, R., Vallina, S. M., Ballabrera-Poy, J., Kettle, A. J., Dachs, J., Bopp, L., Saltzman, E. S., Stefels, J., Johnson, J. E., and Liss, P. S.: An updated climatology of surface dimethlysulfide concentrations and emission fluxes in the global ocean, Global Biogeochem. Cycles, 25, doi:10.1029/2010GB003850, 2011.

Lange, B.: Auswirkungen von Abgasnachbehandlungsanlagen (Scrubbern) auf die Umweltsituation in Häfen und Küstengewässern, Tech. Rep. TEXTE 83/2014, UBA, Dessau-Roßlau,, URL `http://www.umweltbundesamt.de/publikationen/auswirkungen-von-abgasnachbehandlungsanlagen`, projektnummer 33913, UBA-FB 002015, 2013.

Langner, J., Andersson, C., and Engardt, M.: Atmospheric input of nitrogen to the Baltic Sea basin: present situation, variability due to meteorology and impact of climate change, Boreal Environ. Res., 14, 226–237, URL `http://smhi.diva-portal.org/smash/record.jsf?pid=diva2%3A806944&dswid=5707`, 2009.

Lavender, S., Jackson, T., and Sathyendranath, S.: The Ocean Colour Climate Change Initiative - Merging ocean colour observations seamlessly, Ocean Challenge, 21, 29–31, URL `http://www.esa-oceancolour-cci.org/?q=webfm_send/531`, 2015.

Lewis, E. R. and Schwartz, S. E.: Sea Salt Aerosol Production: Mechanisms, Methods, Measurements and Models - A Critical Review, vol. 152, AGU, Washington, D. C., doi:10.1029/GM152, 2004.

Lewis, E. R. and Schwartz, S. E.: Comment on "size distribution of sea-salt emissions as a function of relative humidity", Atmos. Environ., 40, 588–590, doi:10.1016/j.atmosenv.2005.08.043, 2006.

Liu, Y., Zhang, S., Fan, Q., Wu, D., Chan, P., Wang, X., Fan, S., Feng, Y., and Hong, Y.: Accessing the Impact of Sea-Salt Emissions on Aerosol Chemical Formation and Deposition over Pearl River Delta, China, Aerosol Air Qual. Res., 15, 2232–2245, doi:10.4209/aaqr.2015.02.0127, 2015.

Long, M. S., Keene, W. C., Kieber, D. J., Erickson, D. J., and Maring, H.: A sea-state based source function for size- and composition-resolved marine aerosol production, Atmos. Chem. Phys., 11, 1203–1216, doi:10.5194/acp-11-1203-2011, 2011.

Lövblad, G., Tarrasón, L., Tørseth, K., and Dutchak, S.: EMEP Assessment Part I - European Perspective, Tech. rep., Norwegian Meteorological Institute, Oslo, Norway, P.O. Box 43, N-313, URL `http://emep.int/publ/reports/2004/assessment_2004.html`, 2004.

MacIntyre, F.: Chemical fractionation and sea-surface microlayer processes, in: The Sea, edited by Goldberg, E. D., pp. 245–299, John Wiley & Sons, New York, 1974.

Makkonen, U., Virkkula, A., Mäntykenttä, J., Hakola, H., Keronen, P., Vakkari, V., and Aalto, P. P.: Semi-continuous gas and inorganic aerosol measurements at a Finnish urban site: comparisons with filters, nitrogen in aerosol and gas phases, and aerosol acidity, Atmos. Chem. Phys., 12, 5617–5631, doi:10.5194/acp-12-5617-2012, 2012.

Malm, W. C., Sisler, J. F., Huffman, D., Eldred, R. A., and Cahill, T. A.: Spatial and seasonal trends in particle concentration and optical extinction in the United States, J. Geophys. Res. Atmos., 99, 1347–1370, doi:10.1029/93JD02916, 1994.

Manders, A., Schaap, M., Querol, X., Albert, M., Vercauteren, J., Kuhlbusch, T., and Hoogerbrugge, R.: Sea salt concentrations across the European continent, Atmos. Environ., 44, 2434–2442, doi:10.1016/j.atmosenv.2010.03.028, 2010.

Massel, S. R.: Ocean Waves Breaking and Marine Aerosol Fluxes, vol. 38 of *Atmospheric and Oceanographic Sciences Library*, Springer New York, doi:10.1007/978-0-387-69092-6, 2007a.

Massel, S. R.: Ocean Waves Breaking and Marine Aerosol Fluxes, vol. 38 of *Atmospheric and Oceanographic Sciences Library*, chap. 7, pp. 183–206, Springer New York, doi:10.1007/978-0-387-69092-6, 2007b.

Matthäus, W., Nehring, D., Lass, H. U., Nausch, G., Nagel, K., and Siegel, H.: Hydrographisch-chemische Zustandseinschätzung der Ostsee 1996, Marine Science Reports 24, Leibniz Institute for Baltic Sea Research Warnemünde, URL `http://www.io-warnemuende.de/tl_files/forschung/meereswissenschaftliche-berichte/mebe24_1997-zustand-hc.pdf`, 1997.

Matthias, V.: The aerosol distribution in Europe derived with the Community Multiscale Air Quality (CMAQ) model: comparison to near surface in situ and sunphotometer measurements, Atmos. Chem. Phys., 8, 5077–5097, doi:10.5194/acp-8-5077-2008, 2008.

Matthias, V., Aulinger, A., and Quante, M.: Adapting CMAQ to investigate air pollution in North Sea coastal regions, Environ. Modell. Softw., 23, 356–368, doi:10.1016/j.envsoft.2007.04.010, 2008.

Matthias, V., Aulinger, A., Bieser, J., Cuesta, J., Geyer, B., Langmann, B., Serikov, I., Mattis, I., Minikin, A., Mona, L., Quante, M., Schumann, U., and Weinzierl, B.: The ash dispersion over Europe during the Eyjafjallajökull eruption – Comparison of CMAQ simulations to remote sensing and air-borne in-situ observations, Atmos. Environ., 48, 184–194, doi:10.1016/j.atmosenv.2011.06.077, 2012.

Matthias, V., Aulinger, A., Backes, A., Bieser, J., Geyer, B., Quante, M., and Zeretzke, M.: The impact of shipping emissions on air pollution in the greater North Sea region Part 2: Scenarios for 2030, Atmos. Chem. Phys., 16, 759–776, doi:10.5194/acp-16-759-2016, 2016.

Miao, J.-F., Wyser, K., Chen, D., and Ritchie, H.: Impacts of boundary layer turbulence and land surface process parameterizations on simulated sea breeze characteristics, Ann. Geophys., 27, 2303–2320, doi:10.5194/angeo-27-2303-2009, 2009.

Monahan, E. C. and Muircheartaigh, I. O.: Optimal Power-Law Description of Oceanic Whitecap Coverage Dependence on Wind Speed, J. Phys. Oceanogr., 10, 2094–2099, doi:10.1175/1520-0485(1980)010⟨2094:OPLDOO⟩2.0.CO;2, 1980.

Monahan, E. C., Davidson, K. L., and Spiel, D. E.: Whitecap aerosol productivity deduced from simulation tank measurements, J. Geophys. Res. Oceans, 87, 8898–8904, doi:10.1029/JC087iC11p08898, 1982.

Monahan, E. C., Spiel, D. E., and Davidson, K. L.: A Model of Marine Aerosol Generation via Whitecaps and Wave Disruption, pp. 167–174, Oceanographic Sciences Library, Springer, Dordrecht, Netherlands, doi:10.1007/978-94-009-4668-2_16, 1986.

Mårtensson, E. M.: personal communication, 2015.

Mårtensson, E. M., Nilsson, E. D., de Leeuw, G., Cohen, L. H., and Hansson, H.-C.: Laboratory simulations and parameterization of the primary marine aerosol production, J. Geophys. Res. Atmos., 108, 4297, doi:10.1029/2002JD002263, 2003.

Nausch, G., Feistel, R., Umlauf, L., Nagel, K., and Siegel, H.: Hydrographisch-chemische Zustandseinschätzung der Ostsee 2008, Marine Science Reports 77, Leibniz Institute for Baltic Sea Research Warnemünde, URL `http://www.io-warnemuende.de/tl_files/forschung/meereswissenschaftliche-berichte/mebe77_2008-zustand-hc-und-schwermetalle.pdf`, 2009.

Nenes, A., Pandis, S. N., and Pilinis, C.: ISORROPIA: A New Thermodynamic Equilibrium Model for Multiphase Multicomponent Inorganic Aerosols, Aquat. Geochem., 4, 123–152, doi:10.1023/A:1009604003981, 1998.

Nenes, A., Pandis, S. N., and Pilinis, C.: Continued development and testing of a new thermodynamic aerosol module for urban and regional air quality models, Atmos. Environ., 33, 1553–1560, doi:10.1016/S1352-2310(98)00352-5, 1999.

Neumann, D., Matthias, V., Bieser, J., Aulinger, A., and Quante, M.: Sensitivity of modeled atmospheric nitrogen species and nitrogen deposition to variations in sea salt emissions in the North Sea and Baltic Sea regions, Atmos. Chem. Phys., 16, 2921–2942, doi:10.5194/acp-16-2921-2016, 2016.

Nolte, C. G., Bhave, P. V., Arnold, J. R., Dennis, R. L., Zhang, K. M., and Wexler, A. S.: Modeling urban and regional aerosols - Application of the CMAQ-UCD Aerosol Model to Tampa, a coastal urban site, Atmos. Environ., 42, 3179–3191, doi:10.1016/j.atmosenv.2007.12.059, 2008.

Norman, M. and Leck, C.: Distribution of marine boundary layer ammonia over the Atlantic and Indian Oceans during the Aerosols99 cruise, J. Geophys. Res. Atmos., 110, doi:10.1029/2005JD005866, 2005.

O'Dowd, C. D. and de Leeuw, G.: Marine aerosol production: a review of the current knowledge, Philos. T. Roy. Soc. A, 365, 1753–1774, doi:10.1098/rsta.2007.2043, 2007.

O'Dowd, C. D. and Hoffmann, T.: Coastal New Particle Formation: A Review of the Current State-Of-The-Art, Environ. Chem., 2, 245–255, doi:10.1071/EN05077, 2005.

O'Dowd, C. D., Facchini, M. C., Cavalli, F., Ceburnis, D., Mircea, M., Decesari, S., Fuzzi, S., Yoon, Y. J., and Putaud, J.-P.: Biogenically driven organic contribution to marine aerosol, Nature, 431, 676–680, doi:10.1038/nature02959, 2004.

Otte, T. L. and Pleim, J. E.: The Meteorology-Chemistry Interface Processor (MCIP) for the CMAQ modeling system: updates through MCIPv3.4.1, Geosci. Model Dev., 3, 243–256, doi:10.5194/gmd-3-243-2010, 2010.

Ovadnevaite, J.: personal communication, 2015.

Ovadnevaite, J., Manders, A., de Leeuw, G., Ceburnis, D., Monahan, C., Partanen, A.-I., Korhonen, H., and O'Dowd, C. D.: A sea spray aerosol flux parameterization encapsulating wave state, Atmos. Chem. Phys., 14, 1837–1852, doi:10.5194/acp-14-1837-2014, 2014.

Paulot, F., Jacob, D. J., Johnson, M. T., Bell, T. G., Baker, A. R., Keene, W. C., Lima, I. D., Doney, S. C., and Stock, C. A.: Global oceanic emission of ammonia: constraints from seawater and atmospheric observations, Global Biogeochem. Cycles, doi:10.1002/2015GB005106, 2015.

Petelski, T., Markuszewski, P., Makuch, P., Jankowski, A., and Rozwadowska, A.: Studies of vertical coarse aerosol fluxes in the boundary layer over the Baltic Sea*, Oceanologia, 56, 697–710, doi:10.5697/oc.56-4.697, 2014.

Pitchford, M., Malm, W., Schichtel, B., Kumar, N., Lowenthal, D., and Hand, J.: Revised Algorithm for Estimating Light Extinction from IMPROVE Particle Speciation Data, J. Air Waste Manage., 57, 1326–1336, doi:10.3155/1047-3289.57.11.1326, 2007.

Pleim, J., Venkatram, A., and Yamartino, R.: ADOM/TADAP model development program 4: The dry deposition module, Tech. rep., Ontario Ministry of the Environment Toronto, Canada, 1984.

Pleim, J. E.: A Combined Local and Nonlocal Closure Model for the Atmospheric Boundary Layer. Part I: Model Description and Testing, J. Appl. Meteor. Climatol., 46, 1383–1395, doi:10.1175/JAM2539.1, 2007a.

Pleim, J. E.: A Combined Local and Nonlocal Closure Model for the Atmospheric Boundary Layer. Part II: Application and Evaluation in a Mesoscale Meteorological Model, J. Appl. Meteor. Climatol., 46, 1396–1409, doi:10.1175/JAM2534.1, 2007b.

Pleim, J. E. and Chang, J. S.: A non-local closure model for vertical mixing in the convective boundary layer, Atmos. Environ. A-Gen., 26, 965–981, doi:10.1016/0960-1686(92)90028-J, 1992.

Riley, J. and Tongudai, M.: The major cation/chlorinity ratios in sea water, Chem. Geol., 2, 263–269, doi:10.1016/0009-2541(67)90026-5, 1967.

Robinson, N.: Synthetic aerosol distribution in number area and volume space, Online, URL `https://commons.wikimedia.org/wiki/File:Synthetic_aerosol_distribution_in_number_area_and_volume_space.svg`, 2012.

Rockel, B., Will, A., and Hense, A.: The Regional Climate Model COSMO-CLM (CCLM), Meteorol. Z., 17, 347–348, doi:10.1127/0941-2948/2008/0309, 2008.

Rumsey, I. C., Cowen, K. A., Walker, J. T., Kelly, T. J., Hanft, E. A., Mishoe, K., Rogers, C., Proost, R., Beachley, G. M., Lear, G., Frelink, T., and Otjes, R. P.: An assessment of the performance of the Monitor for AeRosols and GAses in ambient air (MARGA): a semi-continuous method for soluble compounds, Atmos. Chem. Phys., 14, 5639–5658, doi:10.5194/acp-14-5639-2014, 2014.

Salter, M. E., Zieger, P., Acosta Navarro, J. C., Grythe, H., Kirkevåg, A., Rosati, B., Riipinen, I., and Nilsson, E. D.: An empirically derived inorganic sea spray source function incorporating sea surface temperature, Atmos. Chem. Phys., 15, 11 047–11 066, doi:10.5194/acp-15-11047-2015, 2015.

Sarwar, G., Luecken, D., and Yarwood, G.: Chapter 2.9 Developing and implementing an updated chlorine chemistry into the community multiscale air quality model, in: Air Pollution Modeling and Its Application XVIII, edited by Borrego, C. and Renner, E., vol. 6

of *Developments in Environmental Science*, pp. 168–176, Elsevier, Amsterdam, Netherlands, doi:10.1016/S1474-8177(07)06029-9, 2007.

Sarwar, G., Fahey, K., Napelenok, S., Roselle, S., and Mathur, R.: Examining the impact of CMAQ model updates on aerosol sulfate predictions, in: 10th Annual CMAS Conference, October 24-26, 2011 Chapel Hill, NC, URL `http://www.cmascenter.org/conference/2011/slides/sarwar_examining_impact_2011.pdf`, 2011.

Schlünzen, K. H. and Sokhi, R. S.: Joint Report of COST Action 728 and GURME. Overview of Tools and Methods for Meteorological and Air Pollution Mesoscale Model Evaluation and User Training, WMO TD No 1457, WMO, Geneva, Switzerland, URL `ftp://ftp.wmo.int/Documents/PublicWeb/arep/gaw/gaw181final_18dec08.pdf`, 2008.

Schrum, C. and Backhaus, J. O.: Sensitivity of atmosphere-ocean heat exchange and heat content in the North Sea and the Baltic Sea, Tellus A, 51, 526–549, doi:10.1034/j.1600-0870.1992.00006.x, 1999.

Schultze, M.: personal communication, 2015.

Seinfeld, J. H. and Pandis, S. N.: Atmospheric Chemistry and Physics: From Air Pollution to Climate Change, Wiley-Interscience, Hoboken, New Jersey, 2nd edn., URL `http://eu.wiley.com/WileyCDA/WileyTitle/productCd-0471720186.html`, 2006a.

Seinfeld, J. H. and Pandis, S. N.: Atmospheric Chemistry and Physics: From Air Pollution to Climate Change, chap. 10, Wiley-Interscience, Hoboken, New Jersey, 2nd edn., URL `http://eu.wiley.com/WileyCDA/WileyTitle/productCd-0471720186.html`, 2006b.

Sharqawy, M. H., Lienhard, J. H., and Zubair, S. M.: Thermophysical properties of seawater: a review of existing correlations and data, Desalin. Water Treat., 16, 354–380, doi:10.5004/dwt.2010.1079, 2010.

Slinn, S. and Slinn, W.: Predictions for particle deposition on natural waters, Atmos. Environ., 14, 1013–1016, doi:10.1016/0004-6981(80)90032-3, 1980.

Smith, M. H., Park, P. M., and Consterdine, I. E.: Marine aerosol concentrations and estimated fluxes over the sea, Q. J. Roy. Meteor. Soc., 119, 809–824, doi:10.1002/qj.49711951211, 1993.

Smith, S. J., van Aardenne, J., Klimont, Z., Andres, R. J., Volke, A., and Delgado Arias, S.: Anthropogenic sulfur dioxide emissions: 18502005, Atmos. Chem. Phys., 11, 1101–1116, doi:10.5194/acp-11-1101-2011, 2011.

Smith, V., Tilman, G., and Nekola, J.: Eutrophication: impacts of excess nutrient inputs on freshwater, marine, and terrestrial ecosystems, Environ. Pollut., 100, 179–196, doi:10.1016/S0269-7491(99)00091-3, 1999.

Sorooshian, A., Crosbie, E., Maudlin, L. C., Youn, J.-S., Wang, Z., Shingler, T., Ortega, A. M., Hersey, S., and Woods, R. K.: Surface and airborne measurements of organosulfur and methanesulfonate over the western United States and coastal areas, J. Geophys. Res. Atmos., 120, 8535–8548, doi:10.1002/2015JD023822, 2015.

Spada, M., Jorba, O., Pérez García-Pando, C., Janjić, Z., and Baldasano, J. M.: Modeling and evaluation of the global sea-salt aerosol distribution: sensitivity to size-resolved and sea-surface temperature dependent emission schemes, Atmos. Chem. Phys., 13, 11 735–11 755, doi:10.5194/acp-13-11735-2013, 2013.

Sutton, M. A., Howard, C. M., Erisman, J. W., Billen, G., Bleeker, A., Grennfelt, P., van Grinsven, H., and Grizzetti, B., eds.: The European Nitrogen Assessment, Cambridge University Press, New York, URL `http://www.nine-esf.org`, 2011.

Tanaka, P. L., Allen, D. T., McDonald-Buller, E. C., Chang, S., Kimura, Y., Mullins, C. B., Yarwood, G., and Neece, J. D.: Development of a chlorine mechanism for use in the carbon bond IV chemistry model, J. Geophys. Res. Atmos., 108, 4145, doi:10.1029/2002JD002432, 2003.

Tang, I. N., Tridico, A. C., and Fung, K. H.: Thermodynamic and optical properties of sea salt aerosols, J. Geophys. Res. Atmos., 102, 23 269–23 275, doi:10.1029/97JD01806, 1997.

Tian-Kunze, X., Kaleschke, L., Weller, R., König-Langlo, G., Wagenbach, D., Rast, S., Santos, G., Richter, A., and Begoin, M.: Sea ice as a source of sea salt aerosol: A trajectory study of 25 years of year-round sea salt aerosol record at Neumayer, Antarctica, in: Geophysical Research Abstracts Vol. 11, p. p.8934, EGU 2009, EGU, Vienne, Austria., URL `http://epic.awi.de/19730/1/Tia2008b.pdf`, 2009.

Tørseth, K., Aas, W., Breivik, K., Fjæraa, A. M., Fiebig, M., Hjellbrekke, A. G., Lund Myhre, C., Solberg, S., and Yttri, K. E.: Introduction to the European Monitoring and Evaluation Programme (EMEP) and observed atmospheric composition change during 1972-2009, Atmos. Chem. Phys., 12, 5447–5481, doi:10.5194/acp-12-5447-2012, 2012.

Tsyro, S., Aas, W., Soares, J., Sofiev, M., Berge, H., and Spindler, G.: Modelling of sea salt concentrations over Europe: key uncertainties and comparison with observations, Atmos. Chem. Phys., 11, 10 367–10 388, doi:10.5194/acp-11-10367-2011, 2011.

Udisti, R., Bazzano, A., Becagli, S., Bolzacchini, E., Caiazzo, L., Cappelletti, D., Ferrero, L., Frosini, D., Giardi, F., Grotti, M., Lupi, A., Malandrino, M., Mazzola, M., Moroni, B., Severi, M., Traversi, R., Viola, A., and Vitale, V.: Sulfate source apportionment in the Ny-Ålesund (Svalbard Islands) Arctic aerosol, Rendiconti Lincei, pp. 1–10, doi:10.1007/s12210-016-0517-7, 2016.

Wang, Y., Zhang, J., Marcotte, A. R., Karl, M., Dye, C., and Herckes, P.: Fog chemistry at three sites in Norway, Atmos. Res., 151, 72 – 81, doi:j.atmosres.2014.04.016, 2015.

Weisse, R., Bisling, P., Gaslikova, L., Geyer, B., Groll, N., Hortamani, M., Matthias, V., Maneke, M., Meinke, I., Meyer, E. M., Schwichtenberg, F., Stempinski, F., Wiese, F., and Wöckner-Kluwe, K.: Climate services for marine applications in Europe, Earth Perspectives, 2, 1–14, doi:10.1186/s40322-015-0029-0, 2015.

Whitby, K. T. and Cantrell, B.: Fine particles, in: Proc. Int. Conf. Environ. Sens. and Asses, Las Vegas, BV, Institute of Electrical and Electronic Engineers, 1976.

Whitten, G. Z., Heo, G., Kimura, Y., McDonald-Buller, E., Allen, D. T., Carter, W. P., and Yarwood, G.: A new condensed toluene mechanism for Carbon Bond: CB05-TU, Atmos. Environ., 44, 5346–5355, doi:10.1016/j.atmosenv.2009.12.029, 2010.

Wu, J.: Wind-stress coefficients over sea surface from breeze to hurricane, J. Geophys. Res. Oceans, 87, 9704–9706, doi:10.1029/JC087iC12p09704, 1982.

Yang, X., Pyle, J. A., and Cox, R. A.: Sea salt aerosol production and bromine release: Role of snow on sea ice, Geophys. Res. Lett., 35, L16 815, doi:10.1029/2008GL034536, 2008.

Yarwood, G., Rao, S., Yocke, M., and Whitten, G. Z.: Updates to the Carbon Bond Chemical Mechanism: CB05, Final report to project rt-04-00675, U.S. Environmental Protection Agency, Research Triangle Park, NC 27703, URL `http://www.camx.com/files/cb05_final_report_120805.aspx`, 2005.

Zhang, K. M., Knipping, E. M., Wexler, A. S., Bhave, P. V., and Tonnesen, G. S.: Size distribution of sea-salt emissions as a function of relative humidity, Atmos. Environ., 39, 3373–3379, doi:10.1016/j.atmosenv.2005.02.032, 2005.

Zhang, Y., Pun, B., Vijayaraghavan, K., Wu, S.-Y., Seigneur, C., Pandis, S. N., Jacobson, M. Z., Nenes, A., and Seinfeld, J. H.: Development and application of the Model of Aerosol Dynamics, Reaction, Ionization, and Dissolution (MADRID), J. Geophys. Res. Atmos., 109, doi:10.1029/2003JD003501, 2004.

Zieger, P., Salter, M., Acosta, J., Corbin, J., Gysel, M., Hamacher-Barth, E., Johnson, M., Leck, C., Nilsson, D., Partridge, D., Rastak, N., Riipinen, I., Rosati, B., Ström, J., Väisänen, O., Virtanen, A., and J., W.: On the hygroscopicity of laboratory generated inorganic sea spray aerosol, Conference Presentation, European Aerosol Conference 2015, Milan, talk `48AAP_0047`, 2015.

Eidesstattliche Versicherung

Hiermit erkläre ich an Eides statt, dass ich die vorliegende Dissertationsschrift selbst verfasst und keine anderen als die angegebenen Quellen und Hilfsmittel benutzt habe.

Hamburg, den 27. April 2016

(Daniel Neumann)